INCREASING ESTIMATION PRECISION
IN LOCALIZATION MICROSCOPY

by

Carl G. Ebeling

A dissertation submitted to the faculty of
The University of Utah
in partial fulfillment of the requirements for the degree of

Doctor of Philosophy

in

Physics

Department of Physics and Astronomy

The University of Utah

May 2015

The University of Utah Graduate School

STATEMENT OF DISSERTATION APPROVAL

The dissertation of **Carl G. Ebeling**

has been approved by the following supervisory committee members:

Jordan M. Gerton , Chair	**12/05/2014** Date Approved	
Erik M. Jorgensen , Member	**12/05/2014** Date Approved	
Saveez Saffarian , Member	**12/05/2014** Date Approved	
Stephan Lebohec , Member	**12/05/2014** Date Approved	
Paolo Gondolo , Member	**12/05/2014** Date Approved	

and by **Carleton DeTar** , Chair/Dean of

the Department/College/School of **Physics and Astronomy**

and by David B. Kieda, Dean of The Graduate School.

ABSTRACT

This dissertation studies detection-based methods to increase the estimation precision of single point-source emitters in the field of localization microscopy. Localization microscopy is a novel method allowing for the localization of optical point-source emitters below the Abbe diffraction limit of optical microscopy. This is accomplished by optically controlling the active, or bright, state of individual molecules within a sample. The use of time-multiplexing of the active state allows for the temporal and spatial isolation of single point-source emitters. Isolating individual sources within a sample allows for statistical analysis on their emission point-spread function profile, and the spatial coordinates of the point-source may be discerned below the optical response of the microscope system. Localization microscopy enables the identification of individual point-source emitter locations approximately an order of magnitude below standard, diffraction-limited optical techniques.

The precision of localization microscopy methods is limited by the statistical uncertainty in which the location of these sources may be estimated. By utilizing a detection-based interferometer, an interference pattern may be super-imposed over the emission signal. Theoretical analysis and Monte-Carlo simulations by means of Fisher information theory demonstrate that the incorporation of a modulation structure over the emission signal allow for a more precise estimation when compared to conventional localization methods for the same number of recorded photons.

These theoretical calculation and simulations are demonstrated through the use of two proof-of-concept experiments utilizing a modified Mach-Zehnder interferometer. The first methodology improves the localization precision of a single nanoparticle over the theoretical limit for an Airy-disk point-spread function by using self-interference to spatially modulate the recorded point-spread function. Experimental analysis demonstrates an improvement factor of ≈ 3 to 5 over conventional localization methods. A related method employs the phase induced onto the Fourier domain signal due to path

length differences in the Mach-Zehnder interferometer to improve localization precision. The localization capability of a modified Fourier domain signal generated by self-interference is utilized to yield a two-fold improvement in the localization precision for a given number of photons compared to a standard Gaussian intensity distribution of the corresponding point-spread function.

To my wife Megan. To the next journey!

CONTENTS

APPENDICES

LIST OF FIGURES

ACKNOWLEDGMENTS

This work owes many people a word of gratitude. I have had what some may consider an unconventional graduate school career, and my collection of academic mentors have all had a hand in making this dissertation a reality. Firstly, I must thank Dr. Jordan Gerton for giving me the chance years ago of starting a project in his lab that has morphed into my current project. I had no idea during our initial discussions where things would lead, but I can honestly say that if not for Jordan providing the initial opportunity and years of support, I would not be in the place I am today. I would like to say thank you for your continuously positive and optimistic demeanor, and providing a welcoming lab to work in.

Secondly, I would like to thank Dr. Rajesh Menon of the Department of Electrical and Computer Engineering, whom I have worked in collaboration with over the bulk of my graduate career. Rajesh's relentless push forward is a welcome motivation, and helped me get through those long days in the lab. His discussions, insight, and support were always welcome, and always appreciated. And the last of my academic advisors, Dr. Erik Jorgensen of the Department of Biology, deserves a special thank you. It is not only for financial support over the past four years of my career, but for his willingness to take a chance on my skills being useful for him and his lab. Erik carries his passion for his science, and for life in general, on his sleeve more so than perhaps any person I have ever met, and to say that it is not infectious would be a lie. Erik's lab is a joy to work in, and that joy certainly starts at the top.

I must also thank the various members of the three labs that I straddle. First, within Jordan's lab, I must thank Dr. Ben Mangum and Dr. Eyal Shafran, who both were patient enough with me when I first began in the lab, and put me on a solid foundation. I must also thank Dr. Analia Dall'asén, Dr. Anil Ghimire, Ben Martin, Lauren Simonsen, Yuchen Young, Jessica Johnston, and Charles McGuire, who were always around for discussions, help, and the refinement of ideas and welcoming critique. You made the lab a fun and

enjoyable place to work. And lastly from Jordan's lab, I must thank Jason Martineau, who spent both a class as an undergraduate with me as a teacher's assistant, and fortunately for everyone, came back years later to take over my project. I thank you for your hours sitting in the dark taking the data for our papers, always with a cheerful and upbeat manner.

Within the Menon lab, I must thank Peng Wang, for his hard work on a couple of projects we were involved in together; to say that I learned a lot from you is an under-statement. And most importantly, I need to thank Dr. Amihai Meiri, who joined the lab at the perfect time to help me push through the end of this project, and to help me immensely with his simulations and complicated data analysis. A large portion of this work deserves as much credit to Amihai as to myself. It has been great to work with you, even if we had to be confined to that perpetually dark room together.

Within the Jorgensen lab, I must give a blanket acknowledgment to the entire lab - Dr.'s Wayne Davis, Manasa Gudheti, Patrick Allaire, Eric Bend, Cathy Dy, Christian Frøkjær-Jensen, Hsiao-Fen Han, Rob Hobson, Gunther Hollopeter, Randi Rawson, Matt Schwartz, Shigeki Watanabe, and students Eddie Hujber, Matt Labella, Patrick Mac, Sean Merrill, and Leo Parra. You all made the Jorgensen lab one of a kind, and as a physics out-sider, welcomed me in with open arms. Lastly, I must thank Becky McKean for keeping the Jorgensen lab running smoothly, and dealing with the myriad of orders and requests I placed through her.

Finally, I must thank all the friends and family whose support made this work pos-sible. To my parents, who instilled a love of learning at an early age, and who gave me the foundation to make the academic achievements of my life possible. To my friends within the Department and across campus, for making the Univeristy of Utah a great place to be a part of. To my office buddy Alex, for dealing with the incessant click of the keyboard, and giving me lots of figure advice. To my amazing mother and father-in-law, who made life in Salt Lake a joy, and showed me a much larger world. And finally, to my amazing wife Megan, who put up with my long days in the lab without complaint, and saved my sanity by taking me on adventures around the world. May they never stop.

CHAPTER 1

INTRODUCTION TO OPTICAL MICROSCOPY

Perhaps unconventionally, this dissertation will take a longer introductory form than commonly employed. My graduate career existed in an intersection between three different labs, one each from physics, biology, and electrical and computer engineering. The overall goal of my project was to further expand upon the work in the field of localization microscopy, and I will attempt to explain this field in the broader context of microscopy as a whole. However, microscopy is a multidiscipline endeavor. The instrument itself is designed and operated under the laws of optics and physics, and in today's current forms, relies heavily on computational control and analysis. The interaction of the sample, namely the use of markers within the sample tagged to a target, involve photo-physics and quantum mechanics in the understanding of their behaviors. The fields are very physics and optics intensive.

Moreover, the main goal of microscopy is focused upon investigating the world of the very small, and perhaps in its most visual form, in the world of biological research and investigation. While microscopy has branched out to other fields of science, its early days primarily dealt with the biological world, and led to the discovery of the cellular theory of biology, single-celled organisms, and subcellular components. Overall technological innovations have allowed for microscopes to become more complex and an even more integral part of biological research as they become integrated into such fields as diagnostic research, studies on cellular dynamics and function, and along with the use of fluorescence markers to serve as beacons, determining the spatial distribution of proteins in the cellular environment.

Much of the first three chapters deals with the background required to allow the reader to see the research presented in the latter chapters in its broader context. This is intended not to take away from the content of the latter chapters, but rather to present

it in its proper contextual framework. Specifically, this dissertation will discuss in detail my work investigating the concept of localization microscopy, a new form of optical microscopy that offers the ability to probe the location of individual fluorescent emitters in spatial detail below the conventional diffraction limit. This is a relatively new form of optical microscopy, and even in the short amount of time that is has been a part of the field, it has helped usher in a new era of research interest and development in the field of optical microscopy. These advancements have in fact spurred a large interest in optical microscopy techniques, which is in turn having a large impact mainly within the biological community. This chapter will provide an introduction to the field of optical microscopy, its context within the larger field of imaging and its various modalities, and both its strengths and critical limitations.

1.1   Motivation

Optical microscopy in its various iterations has been around since the days of Galileo, when he fashioned an *occhiolino*, or compound microscope with simple convex and concave lenses [1]. The ability to magnify an object may be achieved with only a single lens, a property known for thousands of years. The word microscope stems from the Greek, meaning "small" (micro) and "to look" or "see" (scope), as the primary purpose of such an instrument is to allow for the visualization of objects or details that are too small for the human eye to see unaided. To a large extent, microscopy is a tool for the world of biology. While certainly useful in a host of other scientific disciplines, such as material science, engineering, and geology to name a few, the biological sciences heavily rely on microscopy methods to gain contextual and quantitative information regarding the organization and construction of biological systems. Antonie van Leeuwenhoek used his self-ground lenses in the late 1600's to construct a simple microscope and discovered bacteria, starting the field of microbiology [2]. In 1838, Matthias Schleiden and Theodor Schwann, using newly developed optical microscopes, were able to resolve individual cells for the first time, formulating the theory of cell biology [3].

Today, microscopy in its various iterations is a fundamental tool of biology, allowing researchers to investigate the fundamental components that make up biological systems. The scale of investigations runs from whole or partial examinations of plants or

animals, individual single cellular organisms, subcellular organelles, and finally, down to the individual components of the cell. The range of scales is vast as well. Single cells are $\approx$ 10-20 μm in diameter, while individual organelles inside of a cell can be anywhere from tens of nanometers in size to a few microns. The fundamental building blocks of the cell, such as proteins, and the genetic information carriers, such as DNA and RNA, are macromolecular complexes that can be a few nanometers in size or smaller.

Perhaps the most important of these are the proteins of a cell. Proteins constitute the majority of a cell's mass, and are responsible for such functions in the cell as catalyzing metabolic reactions, replicating DNA, transporting molecules from one part of the cell to another, responding to stimuli, perform structural functions, cell-to-cell signaling, immune responses, and cell replication, to name a few. Due to their myriad number of roles, proteins also are a challenge to study. They are ubiquitous in the cell, and the ability to isolate and investigate single types of proteins is an extremely powerful tool in helping to understanding a particular protein's functionality within the cellular environment. The scientific pursuit of the study of cellular systems has led to the development of numerous types of microscopy.

1.2   Types of Microscopy

In general, the term "microscope" is usually associated with light, since these were first to be developed and remain the most common. The simplest optical microscopes, compound microscopes, allow for the user to place the object under a series of lenses, and the image of the object is magnified. Numerous, more complicated, optical modalities have been developed to allow for the discrimination of internal structures within biological samples. For further reading on the various types of optical methods in microscopy, the reader is referred to reference [4]. Furthermore, there are classes of microscopes that avoid the use of light altogether. For example, large amounts of imaging done within the biological sciences are performed by electron microscopy, where beams of electrons are used to image a sample, and avoid the use of light altogether [5]. In scanning electron microscopy, a focused beam of electrons is scanned over a sample, and the electrons that scatter off of the sample are recorded, building up the image pixel by pixel. In transmission electron microscopy, electrons are transmitted through

an ultrathin sample, and the electrons are focused onto an imaging device to generate an image. The electron microscope has proven to be a hugely powerful diagnostic tool, and is capable of generating images with extremely high levels of detail regarding the cellular structure, as shown in Figure 1.1, with resolution down to a few nanometers. Finally, there are scanning probe microscopes [6], which measure an "image" by scanning a probe, on the order of tens of nanometers, over the sample. Examples of these include atomic force microscopy (AFM) [7] and near-field scanning optical microscopy (NSOM) [8].

1.2.1   Optical Microscopy

Optical microscopy, as described above, was instrumental in developing the modern theoretical and experimental framework of biology. However, cells are colorless and transparent, making it impossible to differentiate between the various components of a cell. Cells, by weight, are close to 70% water, and there is little in the cell that can naturally absorb large amounts of visible light. Without further techniques to distinguish various structures of the cell, optical microscopy lacks the ability to provide any sort of contrast that would enable distinct features to be resolved. Like electron microscopy, optical microscopy has benefitted as much from various techniques to stain and introduce contrast to the sample as much as it has from improvements in the instruments themselves.

A general method for creating contrast within a cell is by the introducing an organic dye to the cellular environment, which will have a natural affinity for a particular subcellular feature. For instance, the dye *hematoxylin* is attracted to negatively charged molecules, and will bind to DNA and RNA, revealing the location of these molecules throughout the cellular environment [3]. If a particular dye has a natural affinity for a single cellular component, then the distribution of the target component can be visualized easily, since sufficient contrast exists between the target and the remainder of the cellular components.

1.2.2   Fluorescence Microscopy

While organic dyes produce contrast within the cellular environment, their ability to target and bind to individual components within the cell, or their specificity, is lim-
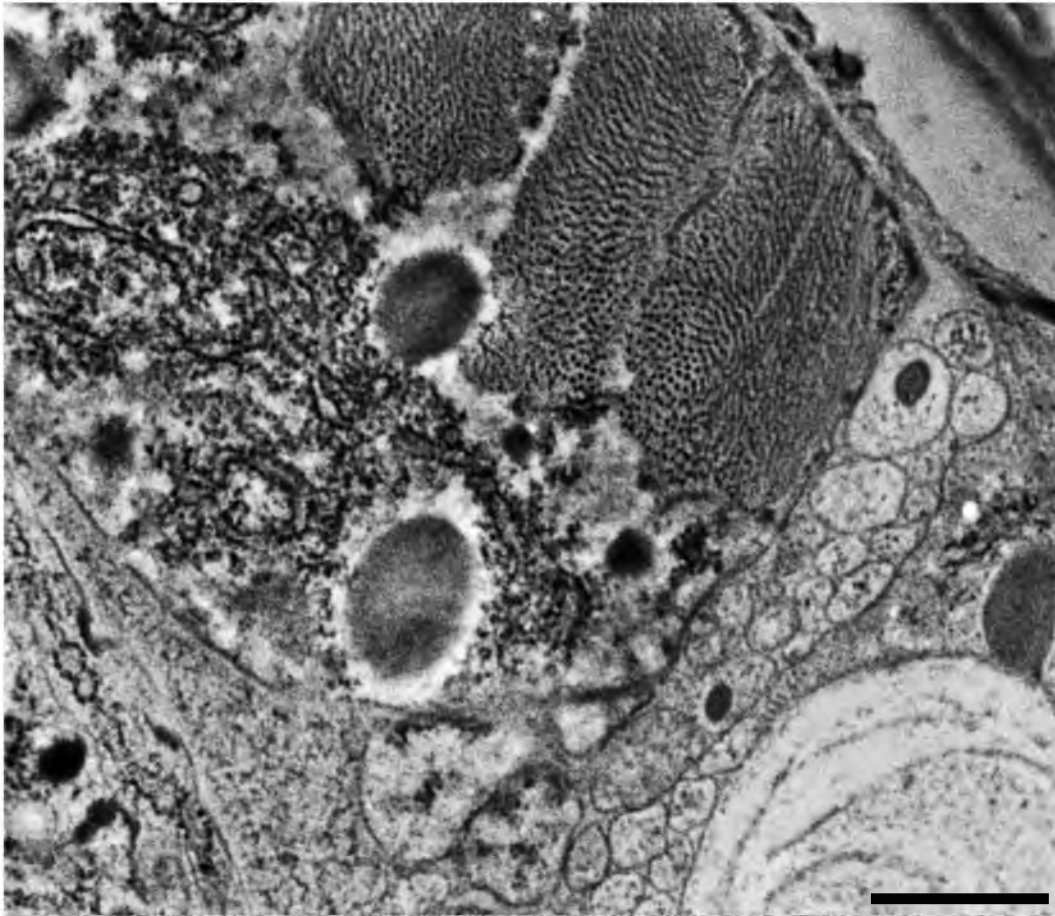
Figure 1.1. Example of an electron microscope (micrograph) image, showing a high degree of structural resolution. The image shows a small portion of a cross section of the nematode worm *Caenorhabditis elegans.* The reader is able to see structural detail linked to internal organelles, membranes, and compartmentalization. What is not possible to discern from this image, however, is the distribution of specific proteins within the image. Scale bar, 1 μm. Sample preparation and data collection by the Jorgensen Lab, University of Utah.

ited. These techniques generally operate by shining white light onto the sample, and recording the image onto a camera. The contrast of the image is a function of the overall absorption of incident white light by the organic dye. Fluorescence microscopy offers an advantage over these methods both in the level of contrast, and the specificity of the technique.

The incorporation of fluorescence molecules as the method of contrast enhancement allows for targeting of specific proteins, or the DNA and RNA [9] within the cell. The fluorescent molecules are either introduced into the cellular environment through

the genetic introduction of fluorescent proteins [10] or through immunofluorescence techniques [11]. These techniques are extremely chemically specific, meaning that only a certain protein or proteins will be marked with a fluorescent molecule, while the rest of the cell or sample remains the unaltered. In this way, only the proteins under investigation are labeled. Fluorescent molecules are extremely powerful markers because they will absorb light at one wavelength, and emit light at a longer wavelength (these details will be further explained in Chapter 2). This allows for the selective separation of excitation and emission light by the use of wavelength selective mirrors (called dichroics) and emission filters. An example of a generic fluorescence microscope is shown in Figure 1.2.

The branch of optical microscopy that incorporates fluorescent markers is called, appropriately, fluorescence microscopy. Fluorescence microscopes are distinct from simpler conventional optical microscopes in that they have a high-power excitation source, usually either a number of high-power lasers, LEDs, or a broad-band lamp. The excitation light is directed onto the sample, where fluorescent molecules within the sample absorb this light and give off emission of a different wavelength. This emission is collected by the objective, passes through both the dichroic mirror[1] and emission filters (to remove any residual excitation light), and focused onto a camera or photo-counting device. Since only the emitted photons from the fluorescent molecules reach the detector, even a small number of photons can be imaged to produce a quality image.

An example of the advantages of fluorescence microscopy is shown in Figure 1.3. Part **(a)** of the figure shows a conventional optical microscopy image of the nematode worm *Caenorhabditis elegans*. The general outline of the worm is clearly visible, as well as a few internal structures. Part **(b)** of the figure is a fluorescent image, where only certain neurons within the worm have been labeled with the first isolated fluorescent protein, Green Fluorescent Protein (GFP). This allows for an easily visualized mapping of the neurons in question, and their distribution throughout the organism.

---

[1]Dichroic mirrors come in many variants. Some, called long-pass dichroics, are transparent to wavelengths above a certain threshold, while reflective to those below. Short-pass dichroics are the opposite. Others only pass a very narrow spectral band, while others are called multiband and are reflective and transparent to multiple regions of the visible spectrum. Interestingly, many of the best specialized optical component companies are located in Rochester, NY, where a little company called Kodak was formed in 1888.
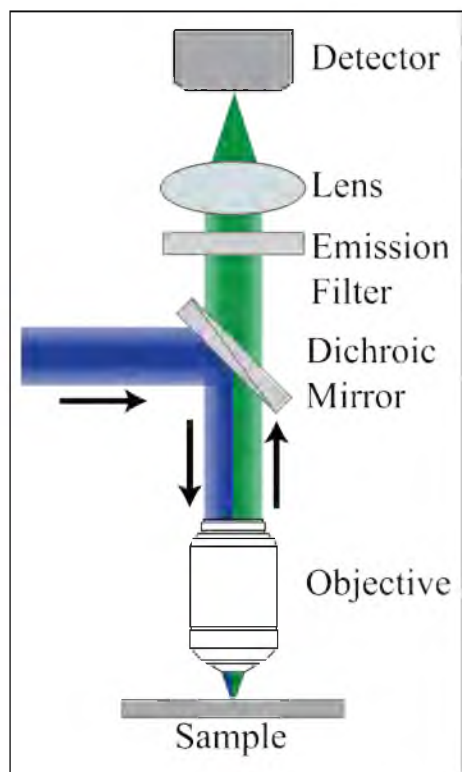
Figure 1.2. Basic illustration of the design of a fluorescence microscope. The excitation light, shown in blue, is directed onto the sample by the use of a dichroic mirror (see main text) and microscope objective. The source can be a laser (or lasers), a high-powered LED, broad-band lamp. The emitted fluorescence, shown in green, is collected by the same objective. Since dichroic mirrors are wavelength specific, the emission photos will pass through the dichroic, separating the excitation from the emission. An emission filter will further suppress any remaining excitation light from the optical path, and the light is then focused onto some form of detector, such as a camera or photon counting device.

While fluorescence microcopy offers a tremendous advantage in terms of chemical specificity and the ability to view only the desired target proteins or cellular component of interest, it is subject to the resolving power of optical methods. The diffraction-limit is the fundamental limit of the resolving power of an optical system, and is given as $\approx \lambda/2$. Fluorescence microscopy operates in the visible region of the electromagnetic spectrum, meaning that the fundamental resolution of fluorescent microscopes is 200-300 nm. For studies of whole organisms, such as demonstrated in Figure 1.3, where the length scale is over hundreds of microns, the resolution limit does not generally limit the information content of the image. In studies involving protein localization within the cellular environment, or protein-protein interaction studies, this poses a fundamental
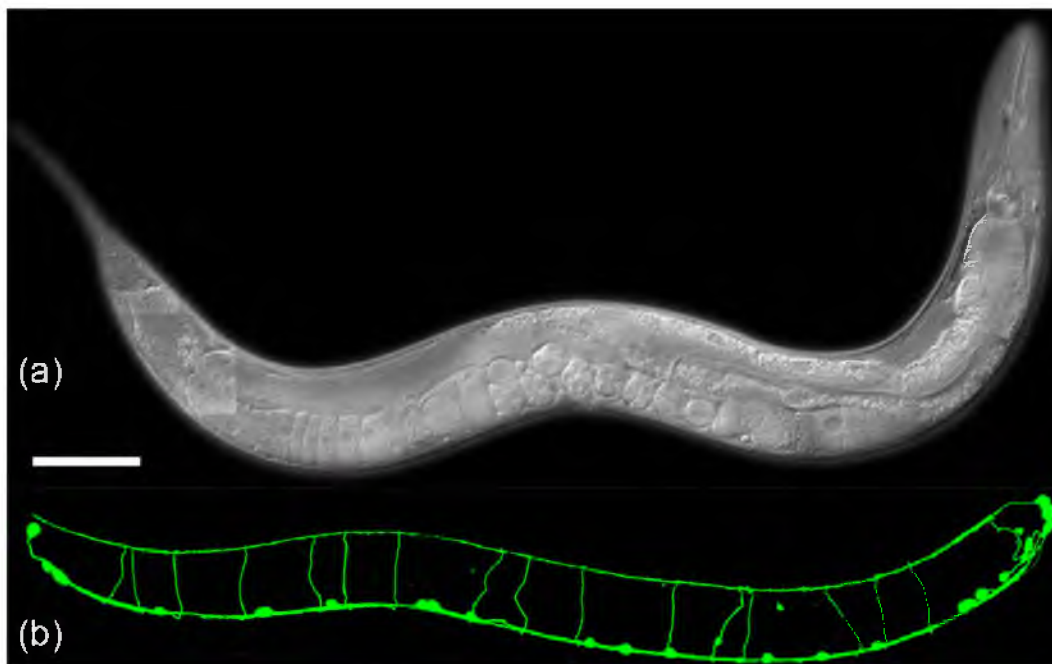
Figure 1.3. Composite image showing one of the most utilized biological model organisms, the nematode worm *Caenorhabditis elegans* (*C. elegans*). Top section **(a)** shows a transmitted light image of the worm using differential interference contrast. While large structural features may be discerned, no further information regarding protein expressions or distributions is available. Publicly available image by Ian D. Chin-Sang, Queen's University, Kingston, ON, Canada. Bottom image **(b)** gives an example of fluorescence microscopy, showing the specificity of the technique. In this specimen, only particular neurons within the worm (GABA neurons[2]) were genetically modified to express green fluorescent protein (GFP, discussed further in Chapter 2) in the cytoplasm of the cells. As a result, the only optical signal from the worm upon excitation are cells expressing GFP, showing the neuronal network throughout the organism. Image by Dr. Randi Rawson, Jorgensen Lab, University of Utah. Scale bar, 100 μm.

obstacle. The size of individual proteins is in the 2-5 nm range, meaning that the best possible resolution of an optical system is two orders of magnitude larger than the protein being studied.

1.3   Microscopy, Specificity, and Resolution

Each of the variants of microscopy has its inherent strengths and weaknesses. A qualitative illustration of various methods and their relation to chemical specificity and

---

[2]GABA neurons are neurons within the worm that make and release the neurotransmitter gamma-aminobutyric acid, abbreviated GABA. In the nematode worm *C. elegans*, the neurotransmitter GABA primarily acts at neuromuscular junctions.

resolving power may be seen in Figure 1.4. Optical microscopes offer a high degree of chemical specificity, or the ability to distinguish between specific types of molecules and proteins within a biological sample, along with the ability to image live specimens. The major downside is their relatively poor resolution. Electron microscopy offers the ability to resolve detail on the nanometer scale, yet offers limited chemical specificity, and cannot be performed on live samples. Scanning probe methods achieve nearly the same resolving power as electron microscopy, yet can only probe the surface of a biological structure, and so are inadequate for studies requiring any imaging within the interior of a sample.

An ideal instrument would be one that has both a high degree of chemical specificity as well as high resolution. Recall that in Figure 1.4, the further to the right an imaging modality is placed on the chart, the higher its resolving power. What would be ideal for biologists is an optical method that can combine the chemical specificity of optical microscopy methods with the high spatial resolution of electron microscopy [12]. A first step in this direction can be seen in Figure 1.5, which illustrates how it is possible to combine an optical image of a sample with the image of the same sample from an electron microscope. However, the dissimilarity between the resolving scales of the two methods is abundantly clear in this image. Each method has its own strengths and weaknesses, gives a different conceptual understanding of the sample in question, but is ultimately hampered by the drastic resolution disparity between the two methods, namely due to the diffraction limit of optical systems.

1.4   Summary and Outline

The remainder of this dissertation is outlined out as follows. Chapter 2 will give an in-depth analysis of some of the main strengths and weakness of optical microscopy. The first half of the chapter will focus one of optical microscopy's main advantages, which is the chemical specificity of the method. It will explore the fundamentals of fluorescence, how this is utilized in optical microscopy, and the mechanisms in which fluorescent molecules are joined to target proteins. The latter half of the chapter will cover the physical and mathematical derivation of the diffraction limit of optical systems in detail, and derive expression relating to the fundamental resolving power of conven-
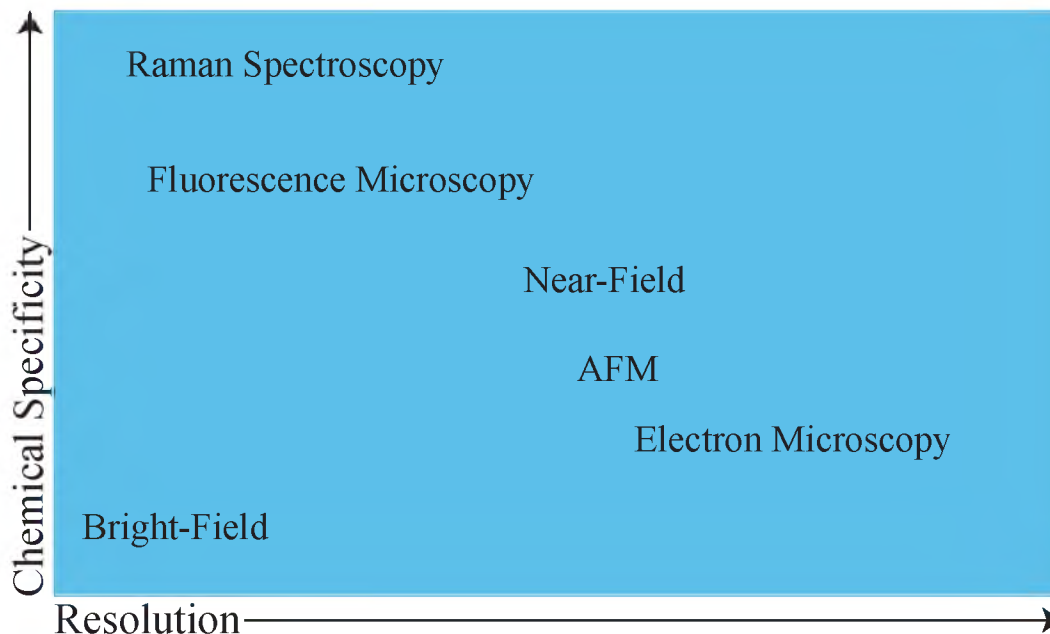
Figure 1.4. A survey of various microscopy techniques, plotted with respect to both chemical specificity (vertical axis) and their resolving power (horizontal axis).

tional optical microscopy systems.

The past 15 years of academic research, however, have seen a paradigm shift in optical microscopy, demonstrating that the resolution limit for far-field microscopy imposed by Abbe is not completely absolute.[3] The development of various "super-resolution" methodologies in the field of optical microscopy have allowed for imaging beyond the conventional diffraction limit, and the Nobel Prize in Chemistry for 2014 was awarded to three of the pioneers of this field of research. Various iterations of these methods can achieve resolution in the tens of nanometers, and have allowed for a rapid expansion in the capabilities of optical instruments.

One of these variants is known as localization microscopy. Localization microscopy utilizes time-multiplexing (isolating point-emitters in time) to allow for a statistical analysis on individual point-emitters within a sample. As will be explained in further detail in Chapter 3, this time-multiplexing allows for the spatial isolation of individual point-sources, which can then be localized to a high degree of precision, where the

---

[3]This statement obviously ignores the whole field of near-field optics, which has long been able to resolve features at the nanoscale.
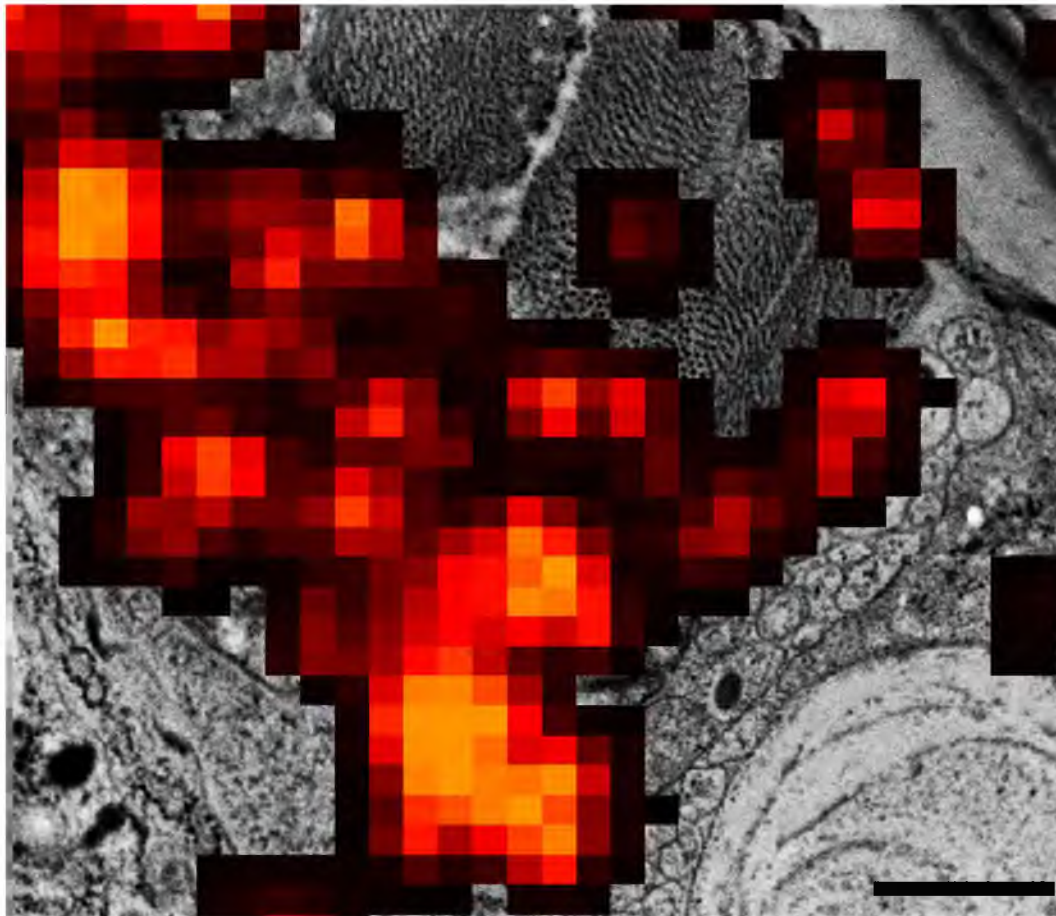
Figure 1.5. Figure representing an overlay between an optical image of individual proteins (colored features) with the structure of the cell as seen in the electron microscopy image underneath. The mage is the same image as seen in Figure 1.1, only now combined with the fluorescent image of the cross-section of a *C. elegans* whose ryanodine receptors are tagged with the fluorescent protein tdEos. The low resolving power of the fluorescent image does not allow more than a rough estimate of the protein's location within the larger framework of the host organism. However, the EM image shows fine structural detail, yet it is impossible to discern the location of individual proteins. Scale bar, 1 μm. Sample preparation and data collection by the Jorgensen Lab, University of Utah. Optical images recorded on a Zeiss Elyra single-molecule localization microscope operating in total internal reflection (TIRF) mode. Electron micrograph recorded on an FEI novaNano scanning electron microscope.

uncertainty in the location of the point-source is lower than the classical diffraction limit. The localized point-sources are then rendered as a function of the uncertainty in their location onto a single image. This technique is the most common of the super-resolution modalities, and offers an approximate increase in resolution[4] to almost an order of magnitude. The main focus of this dissertation is on methods to increase the precision with which the location of these individual point-sources may be estimated.

Chapter 3 will discuss the field of super-resolution microscopy, localization microscopy in particular, and comprehensively study its application. Chapter 4 will describe in detail how the detected emission in localization modalities may be modified to generate a higher localization precision through the use of self-interference of the emission. As is demonstrated in the chapter, this method allows for approximately three-to-five-fold increase in the precision of localization methods. In Chapter 5, a method of using the optical transfer function to measure a particle's position is discussed. This method, while differing slightly from conventional localization microscopy, illustrates a concept that improves the estimation precision by approximately a factor of two.

Finally, the concluding chapter will discuss future avenues of research, from topics discussed in Chapter 4 to returning to the concept illustrated in Figure 1.5. This idea, called correlation microscopy, aims to combine optical super-resolution methods with electron microscopy. Unlike the diffraction-limited image shown in Figure 1.5, the use of super-resolution methods allows for a much higher degree of merging of the two methods, due to the elimination of the large disparities in the level of resolution of the two methods.

Further, more detailed information is contained within the Appendices, such as the full derivation for the spatial distribution of the electric fields within a focus (Appendix A), as well as an introduction to Fisher information theory and its implications (Appendix B) for modeling a given experimental distribution. Appendices C, D and E give detailed information relating to experimental parameters contained within Chapters 4 and 5.

---

[4]Resolution in super-resolution microscopy, especially in localization microscopy, becomes a bit of a gray area. This is discussed further in Chapter 3.

1.5   References

[1] I. I. Smolyaninov, HFSP Journal **2**, 129 (2008).

[2] B. Huang, H. Babcock, and X. Zhuang, Cell **143**, 1047 (2010).

[3] B. Alberts et al., *Molecular Biology of the Cell*, Garland Science, New York, NY, 5th edition, 2007.

[4] D. E. Chandler and R. W. Roberson, *Bioimaging: Current Concepts in Light and Electron Microscopy*, Jones & Bartlett Publishers, Sudbury, MA, 2009.

[5] R. Erni, M. D. Rossell, C. Kisielowski, and U. Dahmen, Physical Review Letters **102**, 096101 (2009).

[6] J. J. Greffet and R. Carminati, Progress in Surface Science **56**, 133 (1997).

[7] G. Binnig, C. Quate, and C. Gerber, Physical Review Letters **56**, 930 (1986).

[8] U. Dürig, D. W. Pohl, and F. Rohner, Journal of Applied Physics **59**, 3318 (1986).

[9] D. Proudnikov and A. Mirzabekov, Nucleic Acids Research **24**, 4535 (1996).

[10] M. Chalfie, Y. Tu, G. Euskirchen, W. W. Ward, and D. C. Prasher, Science **263**, 802 (1994).

[11] I. D. Odell and D. Cook, Journal of Investigative Dermatology **133**, e4 (2013).

[12] S. Watanabe et al., Nature Methods **8**, 80 (2011).

CHAPTER 2

THE THEORETICAL FOUNDATIONS OF OPTICAL MICROSCOPY

As briefly outlined in Chapter 1, this chapter will give a detailed overview of two physical phenomena associated with optical microscopy, namely the principle of fluorescence and the diffraction limit. The principle of fluorescence allows for detailed studies of specific cellular components, most notably proteins. Due to the wide range of available fluorescent markers and their emission spectra, fluorescent microscopy has evolved into a robust and integral tool in the cellular and molecular biology research fields. The physical mechanism of this process will be discussed in the first half of this chapter.

The downside to fluorescent microscopy is the limitation posed by that of the diffraction limit. The latter half of this chapter is devoted to the physical and mathematical derivation of the diffraction limit, and explores the sources of this limit. The derivation the limit is first explored through the Heisenberg uncertainty relationship of electromagnetic waves, and then further explores the limitation through the mathematical framework of the angular spectrum representation. It is through this framework that the mathematical form of a diffraction-limited image of a point-source is derived.

2.1 The Principle of Fluorescence

Conventional optical microscopy creates an image by either passing light through a transparent sample or reflecting it off of an opaque sample. However, these methods do not allow for a high degree of chemical specificity, nor the ability to differentiate the specific molecular components of the cell. To achieve this, the principle of fluorescence is utilized. Fluorescence is the emission of light by a substance that has undergone absorption of light; in most instances the emission light will be of a different color than the incident light. An example of this technique can be seen in Figure 2.1, where three
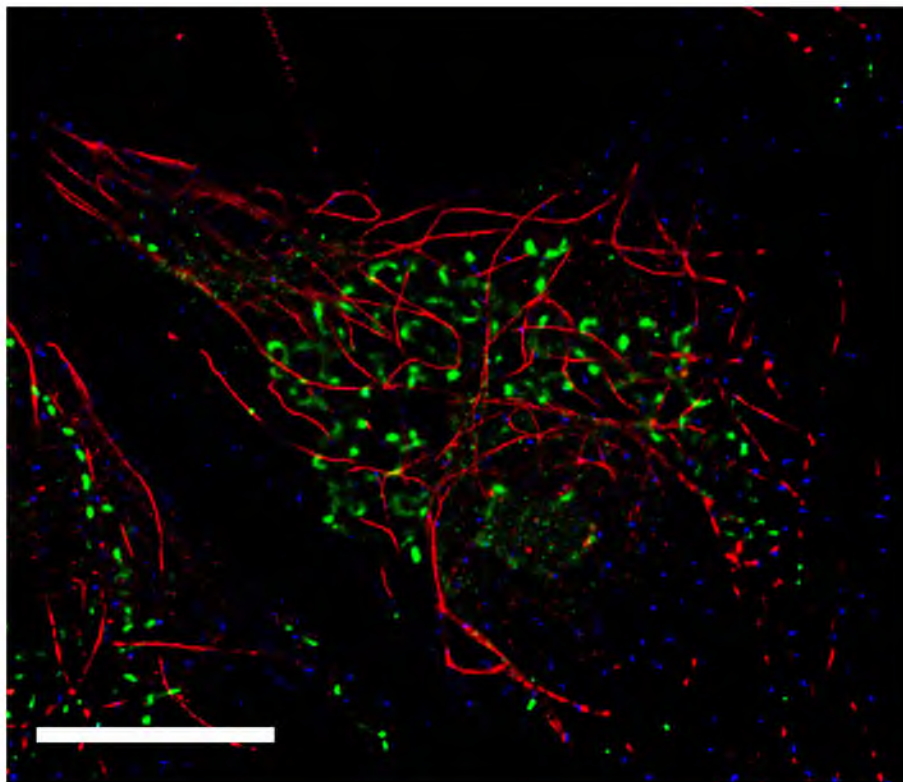
Figure 2.1. Three-color fluorescence microscopy image of a cell. Each color represents a distinct protein labeled via immunofluorescence techniques [1]. Red: tubulin (protein subunit of microtubule filaments, the cellular "highways" for motor proteins and intracellular transport). Green: TOM20 (central protein component of the TOM receptor complex present in the outer membrane of mitochondria). Blue: clathrin (protein responsible for the formation of coated vesicles within the cell). Scale bar: 10 μm. Sample preparation and data collection by the Jorgensen Lab, University of Utah. Images recorded on a Zeiss Elyra single-molecule localization microscope in epi-fluorescence mode.

distinct proteins within a kidney epithelial cell from an African green monkey (*Cercopithecus aethiops*) are labeled with three distinct fluorescent markers, each with a distinct emission spectrum. Each color can be imaged separately, using the correct filters, and the resultant images combined into a single composite three-color image.

Many substances exhibit fluorescence, usually systems where their molecular structure consists of π-orbitals, or delocalized electrons. These delocalized electrons reside across many constitute atoms, usually conjugated systems of organic molecules. Systems of conjugated molecules have proven to be immensely useful because of the simple fact that delocalized electrons in the ground state of π-conjugated systems are able to

respond to the electric field of visible light.[1] The most common forms of these found in optical microscopy are either organic dyes or fluorescent proteins. An example of the chemical structure of two such dyes, AlexaFluor 568 and Green Fluorescent Protein (GFP) may be seen in Figure 2.2. The ring structures are shown as having alternating single and double bonds, but these are actually hybridized bonds, and the electrons are delocalized over the extent of the ring.

The high chemical specificity of fluorescence when used in imaging biological samples comes from the fact that both organic dyes and fluorescent proteins can be attached to individual proteins within the cell. Organic dyes may be attached to specific proteins by the use of antibody staining techniques [1], while fluorescent proteins can be genetically inserted into the genome of the cell, and genetically encoded into the protein of interest [5]. When the sample is subjected to excitation light of the appropriate wavelengths, the fluorescent markers will absorb light and then emit light of a slightly different wavelength (color). This emission can be collected and separated spectrally from the excitation light, making fluorescence extremely sensitive even to individual molecules. It is this feature that makes optical microscopy methods so important to the biological sciences — individual protein distributions can be mapped within the cellular environment. The downside of optical methods is their relatively low resolving power. An ideal instrument for imaging of biological samples is one that is both chemically specific and offers high resolution.

2.1.1 Fluorophore Interactions with Light

When a photon interacts with a π-conjugated molecule, the photon is absorbed and an electron in the ground state (this ground state usually contains two electrons) is promoted to a higher electronic state. This promotion to a higher electronic state gives the electron a new principal quantum number, n. The interaction of the electron to the electric field of the photon is extremely fast, and occurs on the order of $\approx 10^{-15}$ s. Upon promotion to the excited state, the system can reside in either a singlet state (S_n) or a triplet state (T_n), where the electron spin configuration is either antiparallel

---

[1]For a comprehensive overview of the use of fluorescence in optical imaging, the reader is referred to reference [2].
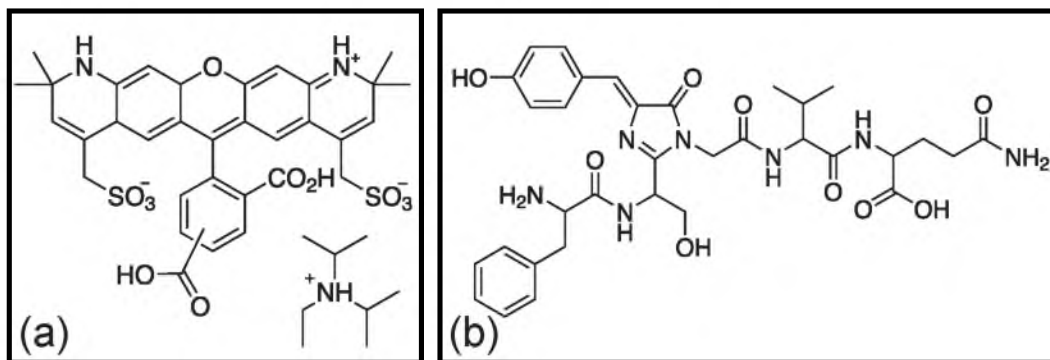
Figure 2.2. Chemical structure of two of the most common fluorophores used in fluorescence microscopy. **(a)** AlexaFluor 568, a widely used organic dye molecule [3]. **(b)** Chromophore of Green Fluorescent Protein (GFP), the first isolated protein that exhibited the property of fluorescence [4, 5].

or parallel, respectively. In a singlet state, the electron in the excited state is still paired with the remaining ground-state electron.[2] "Paired" in this context means that the two electrons have opposite spin, per the Pauli exclusion principal [6]. In the triplet state, the two electron spins are no longer paired, and are aligned. Thus, for triplet states, transitions back down to the ground state are "forbidden," since each electron would posses the same spin value. Due to the exchange interaction between the two states, the triplet state is a lower energy state for principal quantum numbers $n > 0$. Thus, the most common electronic transitions are those that involve a conservation of spin configuration (such as $S_0 \rightarrow S_n$) [7]. A Jablonski diagram is illustrated in Figure 2.3.

Being molecular systems, fluorophores posses numerous vibrational sublevels at each principal electronic energy level, due to the presence of chemical bonds linking the constitute atoms. During optical transitions from one principal electronic state to another, transitions to higher vibrational levels are allowed, and are explained via the Franck-Condon principle (discussed in Section 2.1.2). Electrons that are excited to higher vibrational levels within a principal electronic state relax quickly to the ground state of the electronic state; this process occurs on the order of $\approx 10^{-12} - 10^{-10}$ s. Electrons can also nonradiatively de-excite to a lower electronic state via a process called in-

---

[2]Electrons are fermions, which means that they each must have a unique quantum state. Every possible orbital of an atom or a molecule can hold two electrons, with the two electrons having opposite spin.
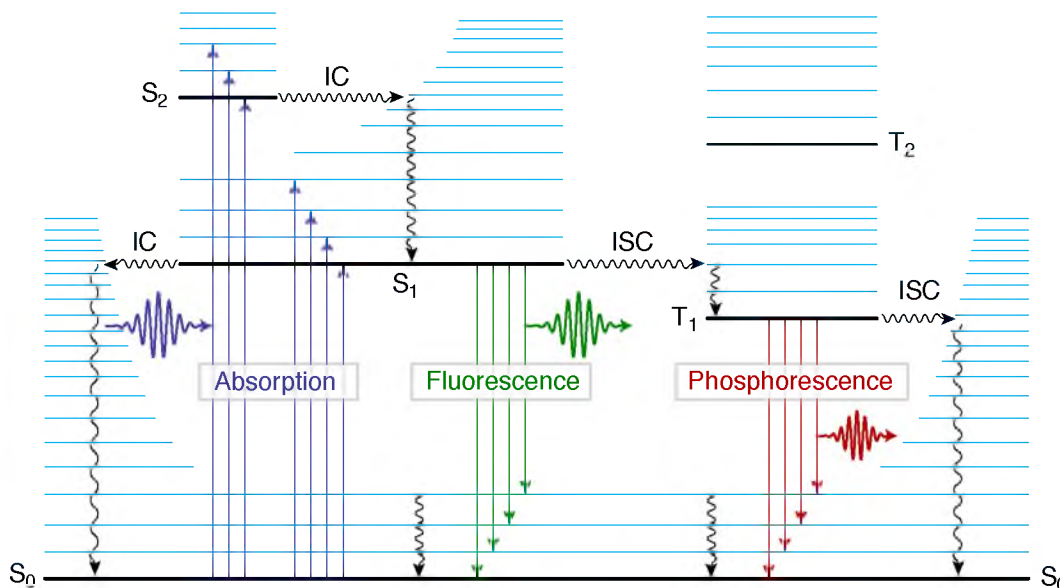
Figure 2.3. Jablonski diagram illustrating the principle of fluorescence, and the allowed transition states between electronic (black) and vibrational states (dashed blue). Both radiative (straight lines) and nonradiative (wavy lines) transitions are shown. IC = Internal conversion, ISC = Intersystem crossing, S_0 = Singlet ground state, S_n = Singlet excited state, T_n = Triplet excited state. Adapted from [7].

ternal conversion (IC) that is highly dependent on electron-phonon coupling [8]. In general, radiative decay to the ground electronic state occurs from the ground *vibrational* state of an excited *electronic* state, known as Kasha's rule [9], as is shown in Figure 2.3. Molecular systems may undergo a process known as intersystem crossing (ISC), where the spin manifolds of the excited state are exchanged. This process is mediated through spin-orbit coupling between the two states. In this way, an excited fluorophore can change from a singlet to a triplet; this process is most likely to occur when the vibrational levels of the two states overlap. In organic molecules consisting mainly of atoms with small atomic mass, the process of spin-orbit coupling is relatively weak. De-excitation to the ground state from a singlet state is the most common form of radiative decay, and occurs on the order of $\approx 10^{-9}$ s. This is known as fluorescence. Transitions from the triplet state are known as phosphorescence, and take orders of magnitude longer to decay. Most phosphorescent decay paths are on time scales of $\approx 10^{-6} - 1$ s. Since the lifetimes of the two states are so dissimilar, the triplet state is known as a "dark" state, due to the relatively long lifetime.

2.1.2 Franck-Condon Principle

The Franck-Condon principle is the collective name given to the physical explanation describing the probability of transitions in molecules developed by James Franck and Edward Condon [10–12] in the 1920's. It is used to explain the principles behind vibronic (electrical plus vibrational) transitions in molecules due to either the absorption or emission of a photon. The principle rests heavily on the Born-Oppenheimer approximation [13], which allows for a decoupling of the motion of the electrons from the vibrational motion of the nuclei of the molecule. This approximation is valid due to the approximately four orders of magnitude difference in mass between electrons and atomic nuclei. As a result, during electronic transitions the positions of the nuclei of the molecule remain unchanged, and readjust only when the electrons have adopted their final distribution [6]. Another assumption of the principle is that the processes involved happen at a low enough temperature. The consequence of this assumption is that in the principal *electronic* state, higher level vibrational energy levels are not occupied, and optical transitions occur from the ground *vibrational* state. This assumption is valid for the reason that thermal energy (kT) at room temperature is approximately an order of magnitude below the energies required for carbon-carbon double bond stretching (remembering that these bonds make up the fluorescing molecule).

Finally, the optical transitions between states, as noted earlier, are extremely fast and the nuclei are approximated as stationary during the optical transitions. Due to the increasing anharmonicity of the potential the higher the principal quantum number (electronic state), the potential wells of the excited states in the molecule have a lateral shift when represented with respect to nuclear coordinates. Keeping all of these considerations in mind, the Franck-Condon principle states that during an electronic transition, a change from one vibrational energy level to another will be more likely to happen if there is significantly more overlap between two vibrational wave functions. These optical transitions are then "vertical" transitions, as shown in Figure 2.4.

Another aspect of the Born-Oppenheimer approximation is that the total wavefunction can be factorized in an electronic ϕ_n and vibrational part $\chi_n(v_n)$, where the latter is the harmonic oscillator function with vibrational quantum number v. To further simplify matters, rotational vibrations are ignored due to their small overall contribution,
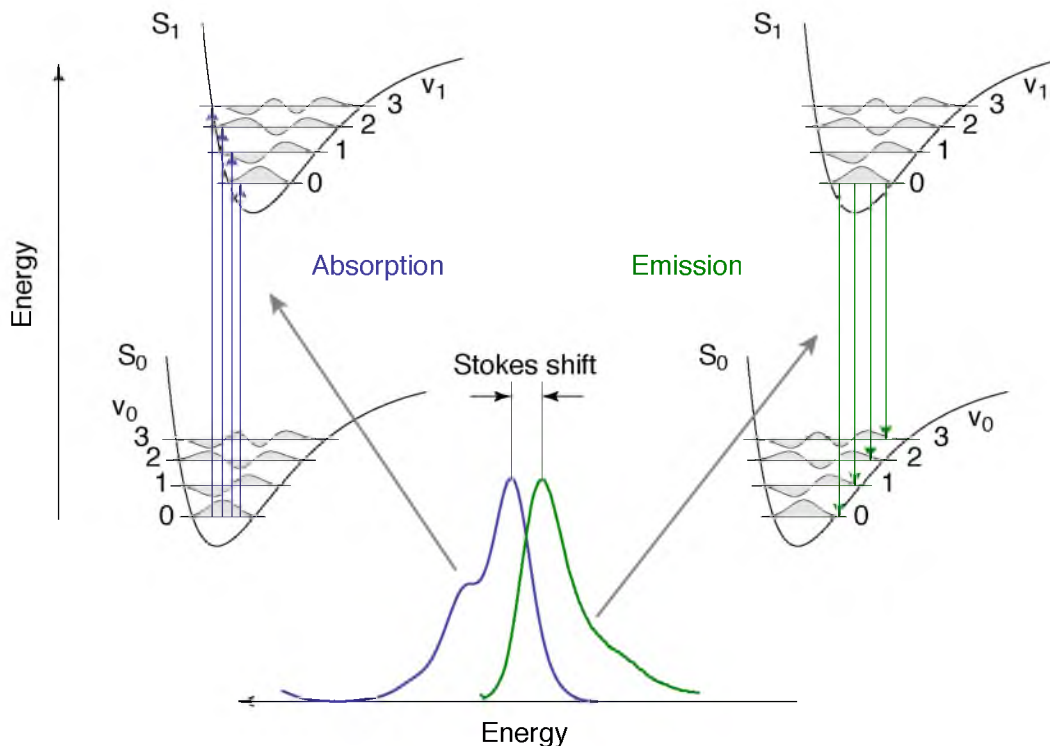
Figure 2.4. Optical transitions of a fluorescent molecule according to the Franck-Condon principle. The absorption and emission spectra shown on the bottom is that for AlexaFluor 568 (note that while energy increases to the left, wavelength increases to the right). Adapted from [14].

and the spin wavefunction is neglected. The harmonic oscillator functions of the ground and excited state are defined with respect to different zero-positions of the generalized configuration coordinate q. The transition probability $P_{v_0=0,v_1}$ from the ground state $\chi_0(v_0 = 0)$ to a vibrational level v_1 of the excited state S_1 is given by

$$P_{v_0=0,v_1} \propto \left|\langle\phi_0|\mathbf{M}|\phi_1\rangle\right|^2 \cdot \underbrace{\left|\langle\chi_0(v_0 = 0)|\chi_1(v_1)\rangle\right|^2}_{\text{Franck-Condon factor}}, \tag{2.1}$$

where $\mathbf{M} = e\mathbf{r}$ is the electric dipole moment vector, which is found by summing over all electrons. The first term in Equation 2.1 is the squared electronic dipole matrix element, which quantifies the electronic transition intensity of the system. The second term is the Franck-Condon factor that distributes this intensity between different vibrational states [15].

Following excitation to an excited electronic state, the electron will relax down to the ground vibrational state as per Kasha's rule [9]. Radiative relaxation of the fluo-

rophore then occurs from the vibrational ground state $v_1 = 0$ to any vibrational state of the ground electronic state, with the transition probabilities the highest in overlapping vibrational states. This feature is analogous to excitation, where the electron can be excited to any vibrational state of the excited state. This has the effect of causing symmetry between the excitation and emission spectra of the fluorophore, as is shown in Figure 2.4. In most cases, the molecule dissipates energy via vibrational relaxation or energy transfer, and the emission photon has less energy than the excitation photon. This shift in energy between the excitation and emission photons is known as the Stokes shift [2]. This spectral shift between excitation and emission photons is what enables the physical separation of excitation and emission light in microscope systems, with the use of wavelength selective mirrors and filters.

In summary, it is the ability to couple fluorescent molecules to particular proteins of interest in biological samples in addition to the high sensitivity enabled by the Stokes shift in emission that gives optical microscopy its high degree of chemical specificity. In principle, any protein that can be identified can be tagged with a fluorescent marker, and its physical distribution within the biological sample (cell, organism) can be investigated and studied. However, optical microscopy suffers from a fundamental drawback, one that prevents the direct imaging of proteins on physical relevant length scales. This drawback is the diffraction limit.

2.2   Resolution, the Point-Spread Function, and the Diffraction Limit

Resolution, in strictest terms, is the ability to resolve detail in an image. For astronomers, this could refer to the ability to distinguish between two stars or galaxies in close proximity. For the biologist, this could refer to two structures or two proteins close to each other within a sample of interest, or cell. With regard to imaging systems, a clear distinction must be made between magnification and resolution. Magnification refers to how much the final image is magnified with respect to the initial image. However, without a high level of resolution, continual magnification of the image will at some point produce no new information nor detail; the image can be further enlarged, but no new structural content will become apparent. At best, magnification preserves the initial resolution of the image, but can never enhance it. An example of the difference between

high resolution and low resolution may be seen in Figure 2.5. Other terms must also be distinguished from resolution, such as sensitivity and precision. When talking about how sensitive an instrument is, this most often (and the case here) refers to the ability to detect and image a small number[3] of fluorophores from a sample, taking into account inherent background signal and noise, but says nothing about the spatial resolution of the image itself. Sensitivity most often refers to the ability to detect even extremely small numbers of photons. Finally, the term precision means the ability to pinpoint the exact spatial location of a given fluorophore, but says nothing about the the ability of the system to resolve the overall distribution of fluorophores within a sample. Resolution is more about the relationship and spacing *between* distinct features of a sample, not the exact position of a *single* object or fluorophore [16]. This topic will be further touched upon in Chapter 3.

2.2.1   The Diffraction Limit

In optical microscopy, light is collected from the sample through the optical system of the microscope where it is imaged onto some form of a photon counting device, such as a camera by means of another lens. The most important element of a microscope is the objective, which sits right next to the sample.[4] The most important parameter of the objective is the numerical aperture, which is directly related to light collecting ability of the lens. Numerical aperture is function of the index of refraction through which the light is collected [5] and is defined as

$$NA = n\sin\theta. \tag{2.2}$$

See Figure 2.6(a) for a schematic illustration. The NA of a microscope is directly linked to the value of n, with $n_{air} = 1$, $n_{water} = 1.33$, and $n_{oil} = 1.51$. NA values for modern

---

[3]Ideally, even down to a single fluorophore.

[4]The assumption here is that either an oil or water immersion lens is being used. Air objectives can have longer working distances (the distance form the front of the objective to the focal plane), and be quite a few millimeters from the source. Still, the objective lens is the most crucial part of a microscope.

[5]The index of refraction n is a measure of a material's interaction with light, namely the electric field of the photon. It is important in optics because it is correlated with a material's ability to bend light rays. Technically, the index of refraction is a measure of how fast light travels through a medium, (v), compared to the speed of light in vacuum, (c). $n = c/v$.
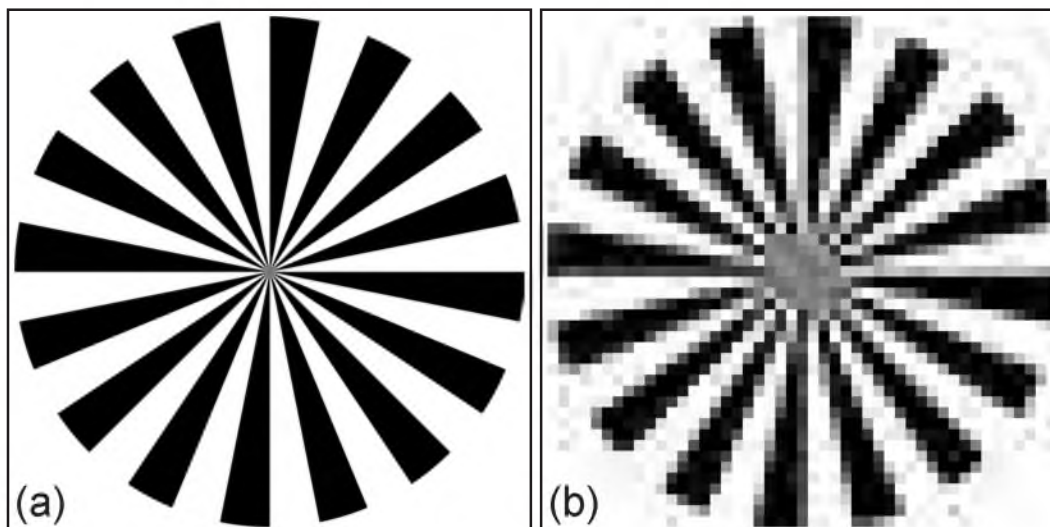
Figure 2.5. Resolution target illustration. A representation of a publicly available Siemens star, which is commonly used to determine the resolution of a system. The star in part **(a)** of the figure shows a high degree of detail, and has a high resolution. The star in part **(b)** shows a much lower level of detail, and consequently has a lower resolution. The structural information in **(a)** is higher than in **(b)**.

objectives range from ≈ 0.1 to 1.65. High-end microscopes tend to use either water or oil objectives to maximize the light collecting ability of their systems. The overall quality of the image is fundamentally limited by the diffraction limit.

As is illustrated in Figure 2.6, the ability of an imaging system to resolve fine detail is limited by how well light can be focused by a lens. The tighter the focal spot, the higher the resolution of the image produced. The actual spatial extent of the focal spot is referred to by the term *point-spread function*, or simply the PSF. The PSF can be described in terms of an excitation PSF (where an incoming light source is focused onto a sample) or the emission PSF, which is the image of an optical source on the detector. Unless explicitly stated otherwise, the term PSF will refer to the emission PSF.

Classically speaking, light is an electromagnetic wave governed by Maxwell's equations. As such, the minimal size of the focal spot produced by a lens is never infinitely small. Thus, even when light is emanating from a point-like source, the resultant image will have a finite size (hence the name point-spread function). This was first investigated by Ernst Abbe, and the limit of a microscope's resolving power to this day bears his name [17, 18]. The term *Abbe limit* refers to the resolving power of a microscope and the smallest spatial distance two points can be apart and still be discernible as distinct
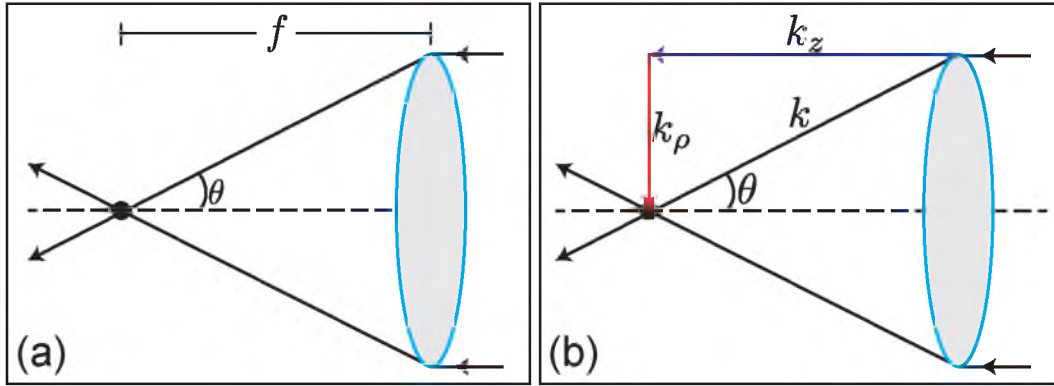
Figure 2.6. Figure illustrating the parameters of a focal spot. **(a)** A ray tracing schematic for a simple lens. If a collimated beam of light (parallel to the optic axis, dashed line) is incident onto the lens, then the ray bundles will converge at a distance f, or the focal distance, from the lens. This is the focal point of the lens. The angle θ denotes the maximum angle of rays converging to the focal spot. **(b)** Each ray bundle carries its own wave vector, denoted k. In cylindrical coordinates, k may be decomposed to k_z and k_ρ. Each wave vector carries uncertainty about its absolute value. This will be discussed further in Section 2.2.2.

objects. For light of wavelength λ, the Abbe limit is mathematically given by

$$d = \frac{\lambda}{2NA} = \frac{\lambda}{2n\sin\theta}. \tag{2.3}$$

Photons in the visible spectrum have a wavelength from 400 nm (violet) to 800 nm (red). As an example, if 500 nm light is imaged through an objective with an NA of 1.49, the resolution limit will be ≈ 168 nm. However, this is misleading because this assumes a perfect imaging system with no noise or distortions, which is never the case.[6] Practically speaking, the resolution limit in optical systems is $\approx \lambda/2$.

2.2.2 The Heisenberg Uncertainty Principle

The resolution limit can be further examined using the Heisenberg uncertainty relationship [19, 20]. In quantum mechanics, the uncertainty relationships are invoked to understand the constraints on a propagating wave function. Similar relationships hold in the case of electromagnetic waves [21], due to the fact that the Fourier-related real-space vector **x** and the momentum-space wave-vector are a pair of conjugated vari-

---

[6]In wide-field systems, where all of the light is collected and imaged onto the camera, light from either above or below the focal plane contributes to noise within the image, degrading the practical resolution.

ables [19, 22]. The optical analog of the Heisenberg uncertainty relation can then be written as [20]

$$\Delta x \Delta p_x \geq h, \tag{2.4}$$

where Δx and Δp_x represent the uncertainty in the position (x) and momentum (p_x) in the x coordinate, and h is Planck's constant. A complete description of the particle in terms of both its position and momentum is forbidden due to the uncertainty relationship. As can be seen from Equation 2.4, knowledge regarding the particle's position may be gained at the expense of knowing the particle's momentum, or vice versa. Using the de Broglie relationship $p = \hbar k$, where k is the wavenumber of the particle, $k = 2\pi/\lambda$. Using these definitions, the uncertainty relationship may be written as

$$\Delta x \Delta k_x \geq 2\pi. \tag{2.5}$$

This relationship is more meaningful, since the wave vector k is directly related to the wavelength of light. The wave vectors are shown in the schematic of Figure 2.6. In principle, if it were possible to make Δk_x infinitely large, then the uncertainty in the spatial resolution Δx could be infinitely small. In a conventional microscope, however, only a small portion of the spread Δk_x vectors are collected by the objective.[7] For a microscope objective of a given NA, only the spatial frequencies between $|k_x| = 0$ and $|k_x| = n\sin\theta\,(\omega/c)$, will be collected by the objective.[8] If the spread of wavevectors, $\Delta k_x = 2n\sin\theta\,(\omega/c)$ is inserted into Equation 2.5, and the definition of the dispersion relationship for photons is used, $\omega/c = (2\pi/\lambda)$; Abbe's formula for the diffraction limit is recovered,

$$\Delta x = \frac{\lambda}{2n\sin\theta}. \tag{2.6}$$

As stated earlier, as well as in reference [23] , only a portion of the possible wavevectors reaches the objective. Even if the objective were able to collect the wavevectors over

---

[7]A fluorophore can be accurately modeled as a radiating dipole. A radiating dipole produces a complex emission field, composed of the near-field (electric field distribution on length scales smaller than λ) and far-field (electric field distribution on length scales larger than λ). A microscope objective can never be close enough to collect the near-field distribution, limiting the resolution of the system from the start. This will be discussed in Section 2.3, as well as reference [23].

[8]ω is the angular frequency of the photons, and c is the velocity of light.

the entire range of angle, namely $\sin\theta \rightarrow 1$, only the propagating far-field wavevectors would be collected. The inability to reconstruct an image in perfect detail (a point-source is imaged as a point-source) is a direct consequence of the inability to couple the entire spectrum of wavevectors into propagating waves. The branch of nano-optics called near-field microscopy was developed for solely this reason — to lower the spatial resolution of a system by collecting a larger component of of the possible number of wavevectors from an emitting point source. The mathematical foundation for the radiating optical fields of a single point source may be studied via the concept of the angular spectrum representation. The angular spectrum representation and its role in the diffraction limit is discussed in Section 2.3 , and in references [20, 23].

2.3   The Angular Spectrum Representation

The idea of the Heisenberg uncertainty principle illustrates why it is impossible to form a perfectly tight focal spot when focusing an incoming beam of light by a lens. The diffraction limit may also be approached from the point of view of the source, and how optical fields radiate and propagate from the source to the detector. In such a context, it is helpful to view the propagation of light in a medium through the mathematical concept of the angular spectrum representation. In this representation, an optical field may be described as a superposition of plane and evanescent (exponentially decaying) waves, which are each in turn solutions to Maxwell's equations.

Specifically, the angular spectrum representation means simply a series expansion of an arbitrary optical field (coming from some source at some location in space, such as a fluorophore) in terms of plane and evanescent waves, each with a variable amplitude and propagation direction. If the assumption is made that the electric field $\mathbf{E}(\mathbf{r})$ is known at any point $\mathbf{r} = (x, y, z)$, any arbitrary value along the z-axis may be chosen and the electric field can be calculated in that particular plane. The Fourier transform of the field $\mathbf{E}$ is given by

$$\hat{\mathbf{E}}\left(k_x, k_y; z\right) = \frac{1}{4\pi^2} \iint\limits_{-\infty}^{\infty} \mathbf{E}(x, y, z) e^{-i[k_x x + k_y y]} \mathrm{d}x\mathrm{d}y, \tag{2.7}$$

where x and y are the Cartesian coordinates and k_x and k_y are the corresponding spatial frequencies. The inverse Fourier transform may be written as

$$\mathbf{E}(x, y, z) = \iint\limits_{-\infty}^{\infty} \hat{\mathbf{E}}(k_x, k_y; z) e^{i[k_x x + k_y y]} \mathrm{d}k_x \mathrm{d}k_y. \tag{2.8}$$

If the assumption is made that the medium in which the optical fields are propagating is homogenous, linear and isotropic, while having no other sources, then the time-harmonic optical field with angular frequency ω must satisfy the vector Helmholtz equation $\left(\nabla^2 + k^2\right)\mathbf{E}(\mathbf{r}) = 0$, where k is again given by $k = (\omega/c)\,n$. To determine the time-dependent solution $\mathbf{E}(\mathbf{r}, t)$, the general convention of $\mathbf{E}(\mathbf{r}, t) = \Re\{\mathbf{E}(\mathbf{r})e^{-i\omega t}\}$ is utilized.

Inserting the Fourier representation as described in Equation 2.8 into the Helmholtz equation, along with the definition

$$k_z \equiv \sqrt{\left(k^2 - k_x^2 - k_y^2\right)}, \ \ \text{with} \ \ \Im\{k_z\} \geq 0 \tag{2.9}$$

the Fourier spectrum $\hat{\mathbf{E}}$ evolves along the z-axis as [23]

$$\hat{\mathbf{E}}(k_x, k_y; z) = \hat{\mathbf{E}}(k_x, k_y; 0)e^{\pm i k_z z}. \tag{2.10}$$

Equation 2.10 illustrates that the Fourier spectrum of $\mathbf{E}$ at any arbitrary position along the z-axis, for example in the image plane, can be calculated by multiplying the spectrum in object plane, at $z = 0$, with the exponential factor $e^{\pm i k_z z}$. Inserting this result back into Equation 2.8 yields the result for any arbitrary z value [23]

$$\mathbf{E}(x, y, z) = \iint\limits_{-\infty}^{\infty} \hat{\mathbf{E}}(k_x, k_y; 0) e^{i[k_x x + k_y y \pm k_z z]} \mathrm{d}x \mathrm{d}y \tag{2.11}$$

If the optical field is propagating in a dielectric medium where no losses occur, then the index of refraction n is a real and positive quantity, which has a direct consequence on the wavenumber k_z. This wave vector is then either real or imaginary, which in turn dictates if the exponential factor $e^{i k_z z}$ yields an oscillatory function or an exponentially decaying function. Depending on the values of k_x and k_y, the solutions are either plane waves of the form $e^{\pm i|k_z|z}$ with the restriction $k_x^2 + k_y^2 \leq k^2$, or evanescent waves of the form $e^{-|k_z||z|}$ with the restriction on k of $k_x^2 + k_y^2 > k^2$.

2.3.1 Propagating and Evanescent Waves

The angular spectrum is then comprised of a superposition between oscillating plane waves, which propagate into the far-field and can be collected, and exponentially decaying evanescent waves. As demonstrated in Figure 2.7, the larger the angle between the
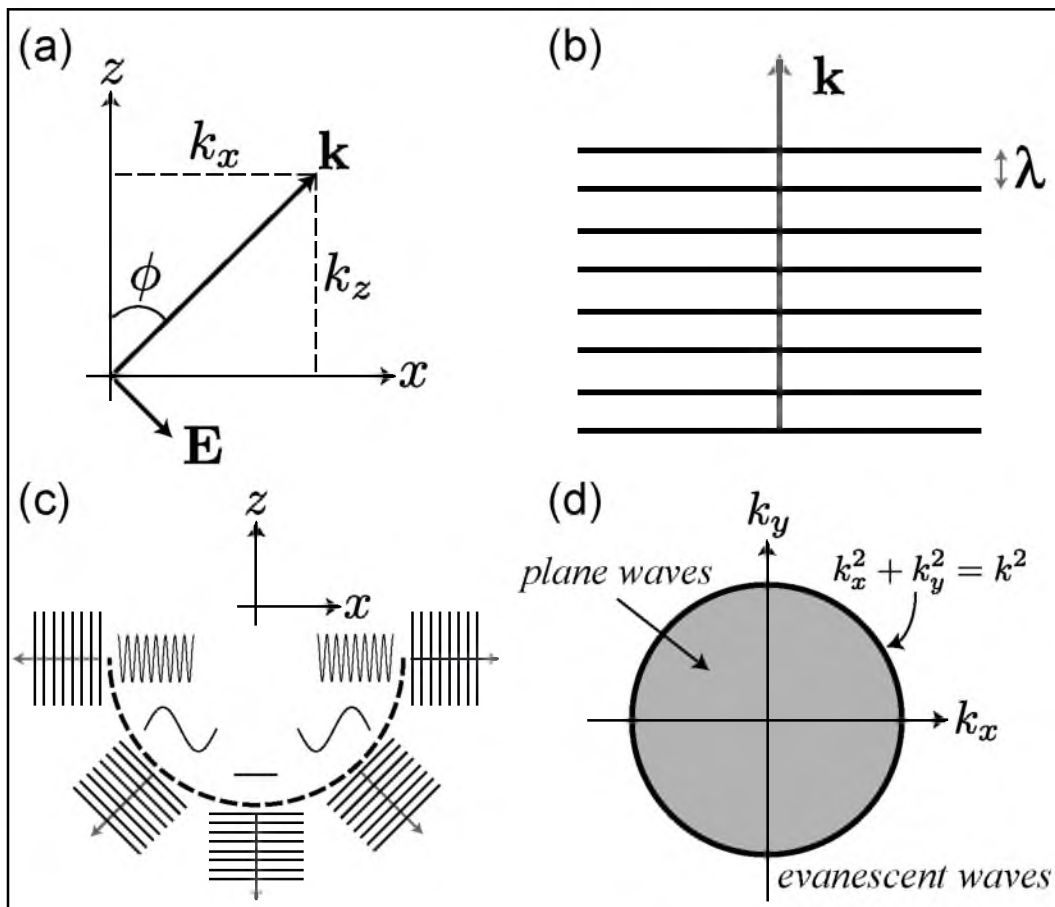
Figure 2.7. Plane wave representation of the angular spectrum. **(a)** Coordinate system definition of a single plane wave propagating at an angle of ϕ with respect to the z-axis. **(b)** Schematic representation of a plane wave. The wave propagates along the vector **k**. The spacing of the wave fronts (black lines) are the wavelength λ. **(c)** Schematic illustrating the concept that the transverse (x and y) spatial frequencies of plane waves are dependent on their incident angles. The transverse wavenumber $(k_x^2 + k_y^2)^{1/2}$ is dependent on ϕ and is limited to the range $[0 \cdots k]$. Plane waves and their propagation direction are depicted outside of the dashed hemisphere, while the projection of the plane waves onto the transverse x-axis is shown inside the hemisphere. As the figures illustrates, for plane waves traveling parallel to the z-axis, there is no modulation along the x-axis. Plane waves traveling parallel to the x-axis exhibit the highest degree of modulation along the transverse axis, up to the wave vector value k. **(d)** Illustration depicting the spatial confinement in k-space of wavevectors representing plane waves (the interior and boundary of the circle of radius k). Evanescent waves fill the region of space outside the circle. Figure adopted from [23].

k-vector and the z-axis, the larger the oscillations of wavevectors in the transverse plane. Wavevectors propagating along the z-axis have transverse components of $k_x^2 + k_y^2 = 0$, where plane waves propagating at a right angle to the z-axis have transverse components of $k_x^2 + k_y^2 = k^2$. Evanescent waves then comprise the remainder of the k-space wavevectors. However, these fields are exponentially decaying along the z-axis, and will never be collected by the microscope objective [23].

Viewed in this representation, the diffraction limit of light stems from the fact that wavevectors only up to magnitude **k** propagate into the far-field; the rest decay as evanescent waves, or are only accessible through near-field interactions.[9] In the language of the Fourier transform, a point source in the spatial domain will have infinite extent in the Fourier plane. Evanescent waves serve as a low-pass filter in the Fourier domain, meaning that the reconstruction of the point source in the image plane can *never* reproduce the original image. Since the Fourier spectrum is incomplete, the reconstructed image cannot be confined as tightly in the spatial domain as the source, because the highest frequencies, those that contribute most in creating the sharpest features of an image, have been lost. This band-width is then further limited by the inability of the microscope objective to collect the remaining spatial frequencies. For examples of techniques designed to increase the resolution of optical microscopy systems by increasing the spatial bandwidth collection ability, the reader is directed to references [24, 25].

2.4 The Airy Profile and Rayleigh Criterion

The Heisenberg uncertainty relationship and the angular spectrum representation establish why the image of a point-source is much larger than its source. However, it does not describe the shape and mathematical form that the point-spread function will assume. In order to determine the mathematical relationship governing the distribution of light in a focus, consider an ideal dipole source[10] located at the focal point of an

---

[9]This is the motivation behind the numerous methods of near-field microscopy, or near-field optics, as briefly outlined in Chapter 1. Generally speaking, these methods interact with the near-field directly at the sample, or within a fraction of a wavelength.

[10]An ideal dipole source is assumed due to the fact that the point-sources used in many microscopy experiments, such as organic dyes, behave very much like an ideal dipole. This is due to the fact that the transition moment within the fluorophore generally has a well-defined direction due to the internal structure of the molecule, as can be seen in Figure 2.2.

objective lens with a high numerical aperture, denoted NA. The objective lens will collimate the collected emission light from the dipole source, which will then propagate through space to a second lens, which focuses the light onto the detector surface located at the image plane. Such a setup is illustrated in Figure 2.8. The physical parameters of the system include the focal length f of the objective lens, the focal length f' of the second lens (which focuses the emission light onto a detector at a position of $z = 0$), and the emission source with an arbitrary dipole moment given by μ.

The framework for determining the electric field distribution within the focal point of a lens revolves around determining the transformations of the electric fields generated by the source dipole as they propagate through the objective and lens system, and are focused down to the image plane. To begin, the electric field at the position r of an arbitrarily oriented dipole μ located at r_0 is given by the dyadic[11] Green's function[12] $\overleftrightarrow{\mathbf{G}}(\mathbf{r}, \mathbf{r_0})$ [23]

$$\mathbf{E}(\mathbf{r}) = \frac{\omega^2}{\epsilon_0 c^2} \overleftrightarrow{\mathbf{G}}(\mathbf{r}, \mathbf{r_0}) \cdot \mu \tag{2.12}$$

In this derivation, it is implicitly assumed that the distance from the point source to the objective lens is much larger than the wavelength of the emitted light, which is the optical configuration of any conventional microscope. Under these assumptions, the mathematical framework from Section 2.3 holds.

For such an analysis, the Green's function must be evaluated. Since the intensity is the square of the electric field, calculating the transformations of the electric fields from source to detector is required. To simplify the calculation, it is assumed that the source is at the origin, namely $r_0 = 0$. The far-field Green's function $\overleftrightarrow{\mathbf{G}}$ is expressed in spherical coordinates, multiplied by the dipole moment vector μ to obtain the electric field. The electric field transformation is then calculated as the fields propagate through the objective and focal lens. This derivation is lengthy, and is given in full detail in

---

[11]A dyadic tensor is a second order tensor, and the term is relatively obsolete today, but it is still often used in mechanics and electromagnetism.

[12]The Green's function is a mathematical construct rendering the electric field at a point r due to a single point source, represented as a vector dipole μ located at a position r_0. Since the field at a given location r depends on the orientation μ, the Green's function must assume the form of a tensor in order to account for all possible physical orientations of μ.
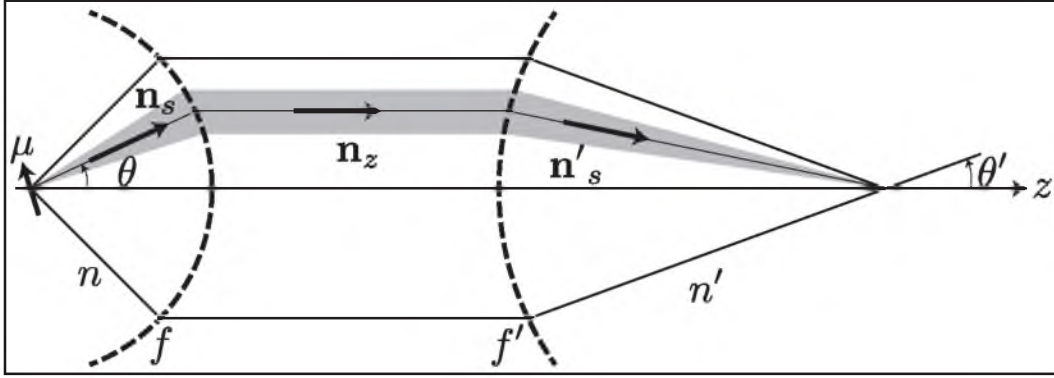
Figure 2.8. The optical configuration used in the calculation of the point-spread function. The dipole source is orientated in an arbitrary position with dipole moment μ. The radiation from the dipole is collected by objective lens with focal length f, and then focused onto the image plane by a second lens with focal length f', at the position $z = 0$ [23].

Appendix A. For brevity, the results of the full calculations are given below. The paraxial point-spread function in the image plane for a source dipole oriented along the x-axis is given by

$$\left| \mathbf{E}\left(x, y, z = 0\right) \right|^2 = \frac{\pi^4}{\epsilon_0 n n'} \frac{\mu_x^2}{\lambda^6} \frac{NA^4}{M^2} \cdot \left[\frac{2J_1\left(2\pi\tilde{\rho}\right)}{\left(2\pi\tilde{\rho}\right)} \right]^2, \tag{2.13}$$

where $\tilde{\rho} = \frac{NA\rho}{M\lambda}$, with $\rho = \sqrt{x^2 + y^2}$. The prefactors to this term are just scaling factors to the overall amplitude of the function. The term is square brackets is what determines the actual form of the PSF, which is known as an Airy profile, after George Biddell Airy [26]. The term J_1 refers to the Bessel function of the first kind. This function is plotted in Figure 2.9. Lord Rayleigh used this mathematical representation of the image of a point-source in scalar form (where the vector nature of the source is neglected) to derive his famous resolution criteria [27]. Lord Rayleigh described two separate point-sources as being resolvable if two over-lapping Airy profiles were arranged such that the maximum or peak of one profile was over the first minimum of a second profile. Relating this to the numerical aperture of a microscope objective, this relation is given by

$$\Delta x = 0.61 \frac{\lambda}{n \sin\theta} = 0.61 \frac{\lambda}{NA}. \tag{2.14}$$

The numerical prefactor in the numerator comes from the value of the first minimum of the Bessel function. This is just a theoretical limit in terms of the resolving power
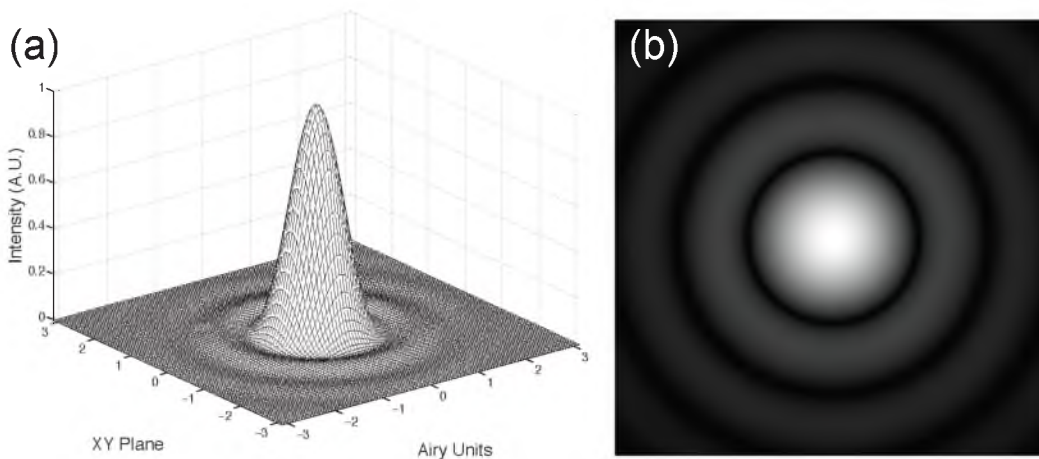
Figure 2.9. Illustration of an Airy profile, representing the image of a point-source in a diffraction-limited imaging system. **(a)** 3D representation of the Airy function. X and Y axis are scaled in Airy units, representing the distance from the peak to consecutive minima. Height represents intensity. **(b)** 2D density plot of the square root of the Airy function, to highlight the minima of the function.

of a microscope, and in practical applications, the resolving power is a convolution of both the resolving optical power of the system, along with noise in the image, optical aberrations, and signal to noise ratio [28, 29]. Thus, the above formulation is more of a theoretical best-case scenario, and not necessarily a practical representation of a microscope's performance.

The functional form of the Airy profile to describe the diffraction limit may also be derived by looking at the diffraction of light as it enters a circular aperture (say that of the objective), and the diffraction pattern the light will assume on the image plane. The Huygens-Fresnel principle can be applied over the boundary of the circle, and the summation of the total interference pattern arising from the interference effect over the boundary of the circle yields an Airy profile. Also, the diffraction limit may be viewed through the mathematical formulation of Fourier optics, where the diffraction pattern in the image plane is the Fourier transform of the scattering boundary in the Fourier plane. Taking the Fourier transform of a circular opening again leads to the Airy profile in the image plane. It should be noted, however, that these two approaches ignore the vector nature of the electric field of the incident beam, and therefore imaging of single molecules can lead to deviations from the scalar theory.

2.5 Summary

In conclusion, no microscope, especially an optical microscope, is capable of fully reproducing a point-source as an image. The microscope, and objective lens, collect only a fraction of the information regarding the position of the point-source, since only a subset of the wavevectors have propagated into the far-field. As a consequence, they are only able to partially reconstruct a representation of the point source as an image. However, the optical microscope is capable of a high degree of chemical specificity, particularly when fluorescence is utilized as the optical contrast mechanism, and is able to visualize individual proteins [30–32].

As will be further discussed in the following chapters, this fundamental limit on the resolving power of an optical instrument may be circumvented, allowing for the extraction of spatial features and information below the classical diffraction limit. These new methods rely on nontraditional imaging techniques, and are generally much more complicated than conventional imaging. What is lost in terms of ease of use is gained in the resolving power of such systems.

2.6 References

[1] A. H. Coons, H. J. Creech, and R. N. Jones, Experimental Biology and Medicine **47**, 200 (1941).

[2] J. R. Lakowicz, *Principles of Fluorescence Spectroscopy*, Springer Science & Business Media, New York, NY, 3rd edition, 2013.

[3] N. Panchuk-Voloshina et al., The Journal of Histochemistry and Cytochemistry: Official Journal of the Histochemistry Society **47**, 1179 (1999).

[4] C. W. Cody, D. C. Prasher, W. M. Westler, F. G. Prendergast, and W. W. Ward, Biochemistry **32**, 1212 (1993).

[5] M. Chalfie, Y. Tu, G. Euskirchen, W. W. Ward, and D. C. Prasher, Science **263**, 802 (1994).

[6] P. W. Atkins and R. S. Friedman, *Molecular Quantum Mechanics*, Oxford University Press, Oxford, 4th edition, 2011.

[7] B. Valeur and M. N. Berberan-Santos, *Molecular Fluorescence: Principles and Applications*, John Wiley & Sons, Weinheim, 2nd edition, 2013.

[8] M. Bixon and J. Jortner, Journal of Chemical Physics **48**, 715 (1968).

[9] M. Kasha, Journal of Chemical Physics **20**, 71 (1952).

[10] J. Franck and E. G. Dymond, Trans. Faraday Soc. **21**, 536 (1926).

[11] E. Condon, Physical Review **28**, 1182 (1926).

[12] E. Condon, Physical Review **32**, 858 (1928).

[13] M. Born and R. Oppenheimer, Annalen der Physik **389**, 457 (1927).

[14] A. Thiessen, *The influence of morphology on excitons in single conjugated molecules*, University of Utah, 2014.

[15] G. C. Schatz and M. A. Ratner, *Quantum Mechanics in Chemistry*, Courier Dover Publications, Mineola, NY, 2002.

[16] R. Heintzmann and G. Ficz, Briefings in Functional Genomics and Proteomics **5**, 289 (2006).

[17] E. Abbe, Archiv für mikroskopische Anatomie **9**, 413 (1873).

[18] E. Abbe, Journal of the Royal Microscopical Society **4**, 348 (1884).

[19] E. Stelzer and S. Grill, Optics Communications **173**, 51 (2000).

[20] J. M. Vigoureux and D. Courjon, Applied Optics **31**, 3170 (1992).

[21] J. W. Goodman, *Introduction to Fourier Optics*, McGraw-Hill, New York, NY, 2nd edition, 1996.

[22] J. T. Verdeyen, *Laser Electronics*, Prentice-Hall, Englewood Cliffs, New Jersey, 3rd edition, 1995.

[23] L. Novotny and B. Hecht, *Principles of Nano-Optics*, Cambridge University Press, Cambridge, 1st edition, 2006.

[24] S. Hell and E. H. K. Stelzer, Journal of the Optical Society of America A-Optics Image Science and Vision **9**, 2159 (1992).

[25] M. G. Gustafsson, D. A. Agard, and J. Sedat, Journal of Microscopy **195**, 10 (1999).

[26] E. Hecht, *Optics*, Addison-Wesley, San Francisco, CA, 4th edition, 2002.

[27] L. Rayleigh, Journal of the Royal Microscopical Society (1903).

[28] R. Heintzmann and C. J. R. Sheppard, Micron **38**, 145 (2007).

[29] E. Stelzer, Journal of Microscopy **189**, 15 (1998).

[30] T. Suzuki, T. Matsuzaki, H. Hagiwara, T. Aoki, and K. Takata, Acta Histochemica et Cytochemica **40**, 131 (2007).

[31] H. Sahoo, RSC Adv. **2**, 7017 (2012).

[32] K. M. Dean and A. E. Palmer, Nature Chemical Biology **10**, 512 (2014).

CHAPTER 3

CIRCUMVENTING THE DIFFRACTION BARRIER VIA
OPTICAL METHODOLOGIES

As was outlined in detail in Chapter 2, fluorescence microscopy offers the biologist an imaging modality that is highly specific and targeted in its labeling of cellular components. For instance, the technique of fluorescence in situ hybridization can detect distinct base-pair sequences on DNA and RNA molecules, while immunofluorescence methods and targeted genetic labeling with fluorescent proteins allow for imaging of distinct targeted proteins within the cell [1]. The impact that these methods have on the research performed in the biological field are extremely evident; most labs use fluorescence microscopy in numerous assays as a means of study and characterization. The result is that fluorescent images appear in a very large fraction of publications and books in biology and its numerous subdisciplines. As was equally evident in Chapter 2, however, is that the classical diffraction limit poses significant hurdles on the technique. While standard lab practices allow for labeling and detection of individual proteins, the disparity between the size of the proteins in question and the diffraction limit of light is two orders of magnitude. Proteins and protein complexes are on the order of a few nanometers for single monomer or dimer proteins and up to tens of nanometers for large complexes [2], while the diffraction limit of light, assuming the best case scenario of a high numerical aperture and low wavelength of light, is on the order of 200 nm at best theoretically, which is extremely hard to achieve in practice.

When considering linear relationship between the wavelength and resolution limit, a natural question that arises is why not use shorter and shorter wavelengths. Going to shorter and shorter wavelengths to increase the resolving power in the image means going into the ultraviolet end of the spectrum. This poses two problems in the context of biological investigations. One is that ultraviolet radiation is lethal for cells, and the

incident photons carry enough energy to destroy the chemical bonds of molecular components of the cell. The second problem is that the index of refraction, n, of materials, is a function of wavelength λ. At the shorter end of the spectrum, many of the properties that a material displays in the visible range drastically change. The lenses of the microscope become opaque, mirrors lose their reflectivity, and the optical transmission becomes extremely limited. Perhaps even more limiting is that the current range of fluorophores contains an electronic structure whose band gap energies lie within the visible spectrum (which, as outlined in Chapter 2, are comprised mainly of π-bonds) so new fluorescent probes would have to be designed. Consequently, imaging with shorter wavelengths is fairly impractical, although there are a number of recent achievements in this area [3, 4].

Optical microscopy is an invaluable tool in the study of biological systems due to its remarkable level of specificity, regardless of the limitation in the optical resolving power of such systems, codified by Abbe and Rayleigh. The past 15 years, however, have seen a remarkable advancement in the development of optical imaging methodologies, and have seen a sustained and successful effort to push optical microscopy beyond the strict resolution limit into what is now collectively known, for better or for worse, as "super-resolution microscopy." The field of super-resolution was in fact the field of research awarded the Nobel Prize in Chemistry in 2014, with the award going to Drs. Eric Betzig [5], Stefan W. Hell [6], and William E. Moerner [7] for their work to push far-field optical methods below the diffraction limit. The next section will give a brief review of the research in the field of super-resolution microscopy, but will first start with the first method to push past the limit of Rayleigh, that of confocal microscopy.

3.1 Super Resolution Microscopy in its Many Forms

Confocal microscopy, as an idea, came about in the late 1950's [8]. In a confocal microscope a focused laser beam is scanned through the sample in a predetermined path, and the emission light is collected and directed onto a photon counter. The total image is then built up pixel by pixel as the laser is scanned through the system. The confocal microscope adds two advantages to basic imaging systems. One is the ability to do optical sectioning. This is achieved by placing a pinhole in the emission path in

a conjugate image plane, which blocks out-of-focus light. This improves the contrast of the image by rejecting large amounts of background. The second advantage is the fact that the excitation volume within the sample is that of a focused laser beam (the excitation PSF), and only fluorophores within the excitation volume are excited and give off fluorescence. The emission of the sample is then confined to the spatial extent of the excitation focal spot, and the total PSF of the image is given by the product of the excitation with the emission point-spread functions. The end result is that the final point-spread function in the image plane is the square of point-spread function of a conventional image. which leads to a tighter confinement of the PSF. Mathematically, the prefactor of 0.61 in Equation 2.14 becomes approximately 0.4 as a result. The main advantage to the technique, however, is in its optical sectioning capabilities, and while the gain in the lateral PSF is marginal (the largest improvement comes in the axial confinement, which is related to the optical sectioning capabilities of these instruments), it still represents a method to move beyond what is otherwise considering the "conventional" case of the diffraction limit. One of the more common usages for confocal microscopy is in two-photon systems, where the confinement of the excitation beam is required to generate nonlinear optical responses from the sample [9]. Due to the nonlinear nature of this method, this leads to a more tightly confined emission PSF than in single-photon systems[1]

Two other methods that push beyond the classical diffraction limit deserve mention as well. These methods are similar in the sense that they increase the effective numerical aperture of a system by using a dual-objective configuration, and placing the sample between the two. 4Pi microscopy is implemented in a confocal arrangement [10–12], as discussed above, while I^5 microscopy is a wide-field configuration [13]. The main resolution improvement for these systems is in the axial direction due to the collection of emission from an opposing objectives on both sides of the sample. Since the effective NA of the system is doubled, the overall resolution of the system is lowered to $\approx$ 100-150 nm, depending on the sample. These systems are incredibly challenging to build and

---

[1]The main confinement of the emission PSF is in the axial direction, since only areas of high intensity undergo a two-photon absorption process. This confinement is slightly offset though by the fact that the excitation wavelength is twice that used in single-photon systems.

maintain in alignment, require the sample to be contained between two objectives, and are not commonly used except in specific research settings.

3.1.1 Optical Super-Resolution - Moving Beyond Abbe's Limit

As stated above, the academic community has seen remarkable advancement in the development of far-field optical methods to push further past the conventional diffraction limit of Abbe and Rayleigh. While the conventional limit of optical image formation remains in place, methods to circumvent the diffraction barrier and extract information from spatial dimensions below the diffraction limit have become routine, through various methodologies. This section will give just a cursory introduction to the methods available to optically resolve beyond the classical diffraction limit, and directs the reader to references [14–20] for in-depth optical super-resolution reviews. Broadly speaking, optical super-resolution methods that have been developed in the past generation may be broken down into three categories: structured illumination techniques, point-spread function engineering techniques, and localization, or pointillist, techniques.

3.1.2 Structured Illumination

Structured illumination is able to circumvent the diffraction barrier by illuminating the sample with an illumination profile that is harmonic in nature — usually the incident light is passed through a grating before the sample. This way, an illumination field with a distinct frequency in its illumination profile is created. This spatially varying harmonic signal is then scanned over the sample, in multiple positions and at multiple angles, and the characteristic fluorescence signal as a function of the position and orientation of the fringe pattern is recorded. Through the analysis of the signal variation as a function of the fringe location and orientation, structural features below the diffraction limit are obtained. The basic concept of the technique is that it expands the available spatial frequencies that are imaged due to the inherent spatial frequency embedded within the excitation profile. A schematic of the illustration in the frequency domain is shown in Figure 3.1. Each orientation and position of the periodic illumination profile extends the domain of a particular set of spatial frequencies. Multiple positions of the structured illumination profile are needed to expand this spatial frequency profile isotropically. Further information on this technique may be found in references [21–24]. Theoretically
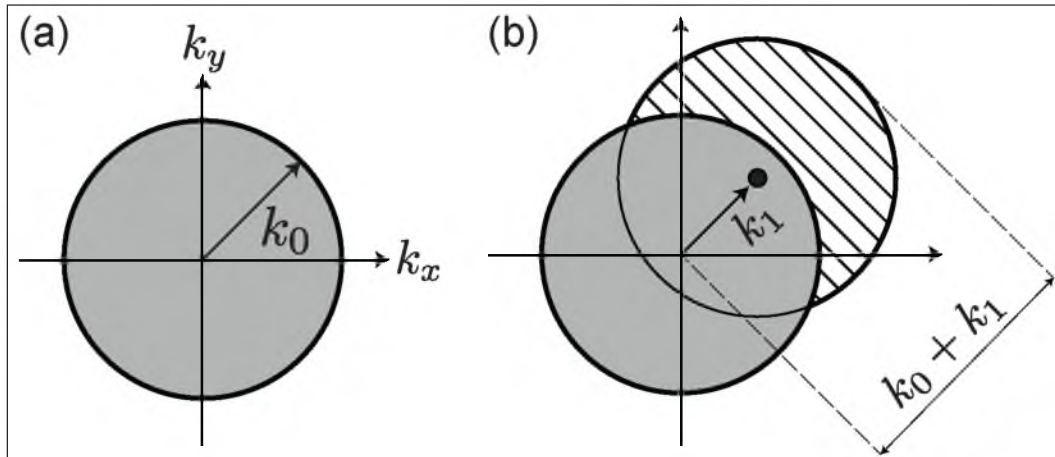
Figure 3.1. Concept of structured illumination. (a) As was seen with the angular spectrum representation, the set of observable spatial frequencies that propagate into the far-field are given by the illustrated circle with radius k_0. (b) In structured illumination, the excitation light contains contains spatial frequency k_1, and these higher frequencies may be visible as noiré fringes, as seen by the hatched circle. This region in the frequency domain has the same shape as the conventional case, but is now centered at k_1. The maximum spatial frequency that can now be observed in the image plane is now given by $k_0 + k_1$. Figure adapted from [21].

and experimentally, structured illumination enables a two-fold increase in resolving power over conventional systems.

3.1.3 STED Microscopy

STED microscopy, which stands for stimulated emission depletion microscopy, is a variant on the conventional laser scanning confocal technique. The resolving power of confocal microscopy is a function of how tightly the incident laser beam can be focused, which is limited by the focusing ability of the lens. The basic idea behind STED systems is to scan two beams over the sample. The first beam, labeled "Exc. PSF" in Figure 3.2, is a conventional focused spot excitation PSF. The second beam, the STED beam, is passed through a variable phase plate (called a vortex phase plate) such that the beam experiences destructive interference at the center of the beam profile (hence the point-spread function engineering). The phase plate is constructed such that the phase front of the laser beam undergoes a 0-2π [26] modulation in the azimuthal coordinate ϕ; every portion of the wave front is π radians out-of-phase with the diametrically opposing portion
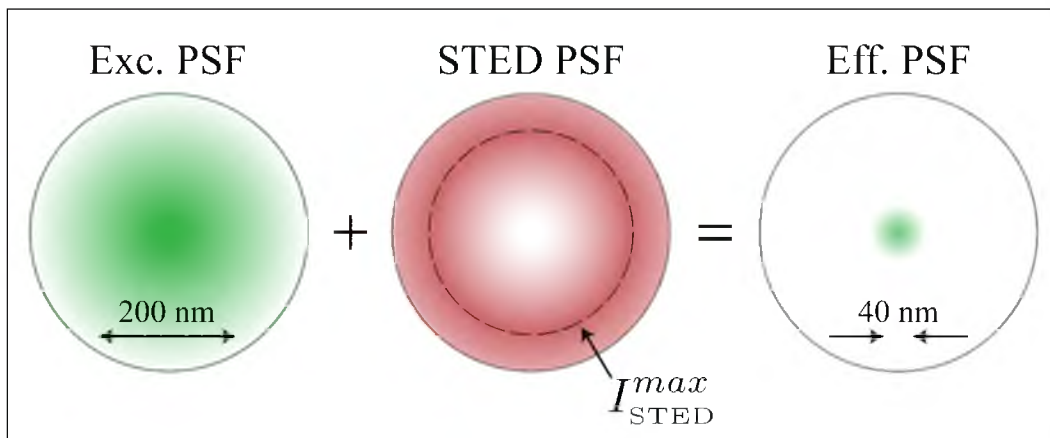
Figure 3.2. Concept of STED microscopy. The excitation point-spread function (Exc. PSF) is of the proper wavelength to stimulate the fluorophores within the diffraction-limited PSF from S_0 to the first electronic excited state, S_1 (see Figure 2.4 for reference). The STED PSF, which has a null, or region of zero intensity, at the center, is red-shifted such that it will cause the fluorophores within its spatial extent to undergo stimulated emission down to the ground state, *before* the molecules can fluoresce spontaneously. The wavelength is selected such that the transition is from the ground vibrational state of S_1 to an excited vibrational state of S_0, usually at the lowest energy region of the emission spectra. It is also chosen to have no overlap with the excitation spectra. The effective PSF (Eff. PSF) is then only composed of fluorophores that were at the null of the STED PSF, thereby creating an effective fluorescence region that is smaller than the diffraction limit. It is important to note that both the excitation and the STED PSF are diffraction-limited. By increasing the value of I_{STED}^{max}, the effective PSF can be made smaller and smaller. Figure adapted from [25].

of the wavefront, producing a null at the center of the beam.[2] The null is maintained as the STED beam is focused, and it is aligned to be centered onto the peak of the excitation PSF (so they are collinear).

The wavelength of the STED beam must be carefully considered. It is red-shifted to match the emission wavelength of the fluorophore used in the sample, but chosen such that it has zero overlap with the absorption profile.[3] When excited molecules are

---

[2]The vortex phase plates are generally made via optical lithography, where the plate becomes progressively thicker in the azimuthal coordinate, effectively increasing the optical path of the beam as a function of ϕ, i.e., $e^{i\phi}$. The beam then experiences destructive interference at the center, creating a doughnut shaped beam. It should be noted that these types of vortex phase plates are designed for beams that have circular polarization.

[3]Generally, STED beams are of extremely high intensities (in the MW/m^2 range and higher). If any portion of the absorption spectrum of the fluorophore overlapped with the wavelength of the STED beam, this would also cause molecules to transition *from* the ground electronic state *to* the first electronic excited state.

then illuminated by the STED beam, they are forced from the first excited electronic state back down to the ground state by the process of stimulated emission. Being stimulated emission, these photons propagate spatially and in phase with the depletion STED beam.[4] Only molecules at the center of the STED beam, where the intensity distribution is zero, are left in the excited state, where they then decay and fluoresce spontaneously, creating an "effective PSF." This is illustrated in Figure 3.2. STED microscopy is merely a mechanism to spatially switch off fluorophores, and limit the confinement of active, fluorescing molecules.

As an example, the excitation and STED beams can be numerically calculated [27] in the sample plane, and the effective PSF calculated as a function of the STED intensity I_{STED} and the saturation intensity I_0. This is demonstrated in Figure 3.3. The calculations for the spatial extent of the focused beams follow a similar derivation as given for a single emission dipole as outlined in Appendix A, only instead of the calculating the electric fields produced by a radiating dipole and determining their transformation through the optical system, the electric fields of an incident laser beam are used, which produces similar results. The wavelength of the excitation beam is chosen to match the absorption profile of the fluorophore, while the STED wavelength is chosen to overlap with the emission profile, to generate stimulated emission. This is shown by the difference in the colormaps of the excitation PSF and the STED PSF in Figure 3.3. As can be seen from the image, while the excitation PSF and the STED PSF are both diffraction-limited, the region of allowed fluorescence, Figure 3.3(c), can be sub-diffraction-limit in size.

Functionally, the effective resolution of a STED microscope (the effective PSF) is a function of the power of the STED beam as well the saturation intensity of a given fluorophore used in a sample. The saturation intensity is defined as the required intensity of the STED beam such that the rate of induced stimulated emission of the fluorophore by the STED beam is equal to the rate of spontaneous emission [29]. Conversely, this may also be stated at the intensity required such that the probability of fluorescence emission from the fluorophore is reduced by a factor of two [30]. At this saturation threshold, the

---

[4]Since the STED beams are extremely high power, back-reflections from optical components within the system and from the sample must still be filtered out of the emission path with the appropriate emission filters. Often times, even two identical emission filters are used to achieve adequate signal-to-noise ratios.
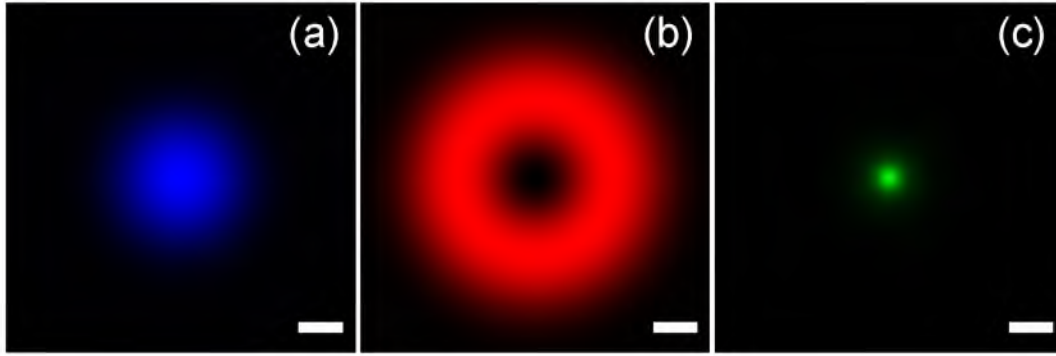
Figure 3.3. Numerical simulations [27, 28] illustrating the excitation ((**a**), blue), STED ((**b**), red) and effective ((**c**), green) PSFs in STED microscopy. For these simulations, NA = 1.4, n = 1.51, λ_{ex} = 635 nm, λ_{STED} = 760 nm, excitation intensity I_{ex} = 1 MW/m^2, STED intensity I_{STED} = 10 MW/m^2, and the saturation intensity I_0 = 1 MW/m^2. Scale bar: 200 nm.

intensity of the STED beam, I_{STED}, is equal to the saturation intensity, I_0.

The effective resolution in a STED system can be written as a modification of Abbe's criterion, taking into consideration the properties of a particular fluorophore and a given STED beam intensity. This modification can be expressed mathematically by [25, 31]

$$\Delta x \approx \frac{\lambda}{2n\sin\theta\sqrt{1+\sigma_f\tau_f I_{STED}^{max}}},$$ (3.1)

where σ_f is the absorption cross-section of the fluorophore, τ_f is the lifetime of the excited state, and I_{STED}^{max} the peak power of the STED beam. The product $\sigma_f\tau_f$ is inverse of the saturation intensity, I_0 [29], and Equation 3.1 can be rewritten as a ratio of the STED and saturation intensities

$$\Delta x \approx \frac{\lambda}{2n\sin\theta\sqrt{1+I_{STED}^{max}/I_0}}.$$ (3.2)

Since the focused beams are still diffraction-limited, the effective area in which molecules are forced down to the ground state becomes larger and larger as the intensity of the beam is increased, thereby *decreasing* the effective size of the null at the center, lowering the effective PSF of the system. Theoretically, the resolution of STED microscopy can be decreased to zero, and for certain implementations, has been experimentally verified down to a few nanometers [32].[5] Practically however, the resolution is dependent

---

[5]The sample in reference [32] was a negatively charged nitrogen vacancy point defect in diamond,

on the sample in question and the fluorophores used. Typical values are in the 30-50 nm range for well-aligned systems with the appropriate fluorophores and high-intensity laser systems.

As a final example of the dependence on resolution as a function of the ratio of the intensity of the STED beam to the saturation intensity of the fluorophore, Figure 3.4 illustrates the effect of lowering the saturation intensity I_0, while keeping the STED beam intensity the same. The effective PSF of the system, shown in green, decreases as the saturation intensity I_0 of the fluorophore is lowered by an order of magnitude in each panel. Objectively, the same effective PSF could be obtained by increasing the intensity of the STED beam by orders of magnitude.[6] Further reading on STED microscopy can be found in references [6, 33–36].

3.2   Localization Microscopy

The key attribute in both structured illumination and STED microscopy is the fact that fluorophores are selectively illuminated. The sample is either illuminated with a periodic excitation profile in structured illumination, or the region of fluorescence is confined by engineered focal fields. This idea of isolating subsets of the entire fluorophore population may be taken to its logical extreme, namely if there were only one fluorophore, or point source, within the sample.

As described in detail in Section 2.4, the mathematical form of the image of a point-source is given by an Airy profile. Imaging systems, however, are pixelated detectors with finite sampling abilities, and so the actual image of a point-source is a pixelated version of the mathematical model. Figure 3.5(a) shows the ideal version of a 2D Airy function, while Figure 3.5(b) shows an ideal image of a point-source on a pixelated imaging system. Furthermore, an image of a point-source is corrupted by the statistics involved with the process of photon counting, which are Poisson distributed (shot noise), as well as by read-out noise from the imaging system, which is Gaussian distributed [37, 38].

---

and the STED beam intensity can be increased to the maximum available power without destroying the sample.

[6]If the aim is to image a biological sample, however, the lower the amount of light going into the specimen, the better.
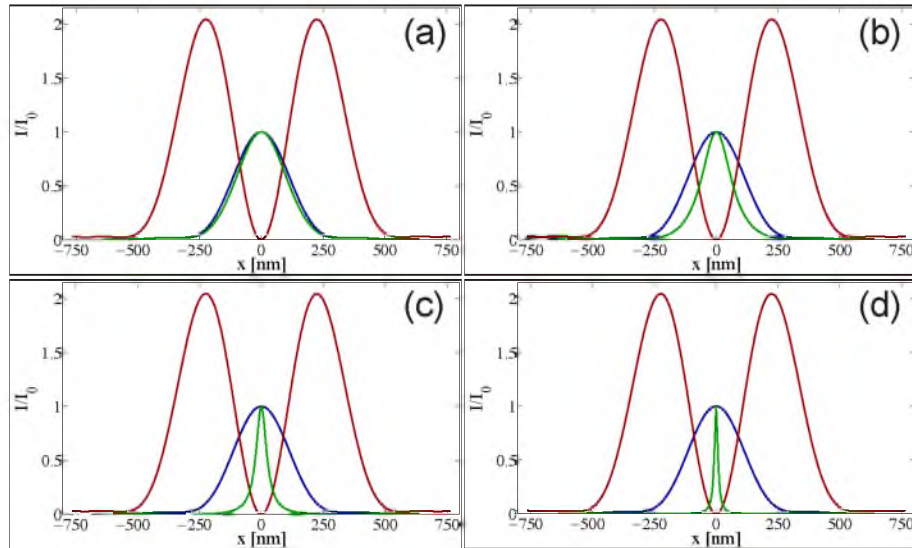
Figure 3.4. Various profiles along the x-axis of the PSFs in the case of STED microscopy for differing values of the saturation intensity, I_0. Each plot represented in this figure would represent a unique fluorophore, since each fluorophore has a unique saturation intensity I_0 (dependent on the unique absorption cross-section of each fluorophore and its intrinsic lifetime in the excited state). To benchmark the effect of varying saturation intensities, the excitation intensity is kept constant for every plot. Excitation PSF: blue. STED PSF: red. Effective PSF: green. For all plots, $I_{ex} = 1$ MW/m^2 and $I_{STED} = 10$ MW/m^2. **(a)** $I_0 = 10$ MW/m^2. **(b)** $I_0 = 1$ MW/m^2. **(c)** $I_0 = 0.1$ MW/m^2. **(d)** $I_0 = 0.01$ MW/m^2. The intensities on each plot have all been normalized to I_0.

The same image of a single point-source may be imaged on a three-dimensional plot as well, to illustrate the notion that the center of the image has the highest intensity, which corresponds to the highest number of photon counts. This can be seen in Figure 3.6. While the image of a point-source in the image plane has a much larger spatial extent than the actual point-source itself, the point-spread function still has a well defined peak. This peak has a direct correlation to the source in the image plane, and it is this fact that is the key to localization microscopy.

3.2.1 Information Extraction from the Point-Spread Function

If it is possible to isolate a single particle within a certain region of interest, the center of the PSF can be determined to with an uncertainty much smaller the width of the PSF. This fact has been exploited and used to great success in numerous particle tracking experiments [39–43]. If a single point-source can be localized, such as in particle-tracking experiments, or in samples of extremely low density, such that the point-sources are
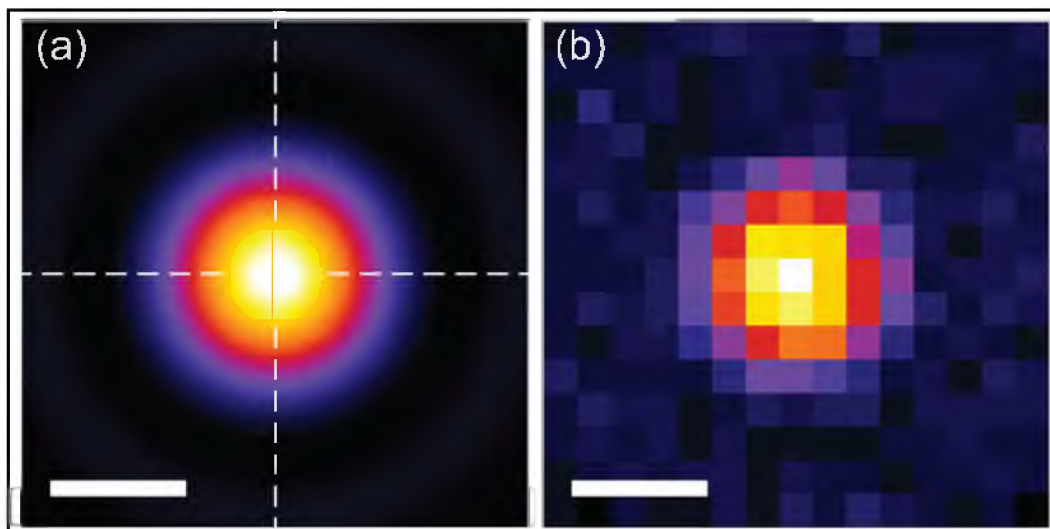
Figure 3.5. Illustration of an ideal and pixelated point-spread function (PSF). **(a)** Illustration of an ideal PSF. Recall that the ideal theoretical point-spread function is given by the Airy profile. The first minima of the function may be seen at the outer edges of the image. **(b)** Result when imaged onto a pixelated detector of finite pixel size with shot noise and readout noise added. Shot noise stems from the inherent uncertainty regarding the photon count and varies by the square root of the number of detected photons. Read noise is the inherent noise added to the signal when propagating through the camera circuitry between detection and signal to the computer. The images have been normalized, with the highest intensity of each image located in the center. The pixels sizes in this image correspond to 75 nm in the sample plane. Scale bar: 300 nm.

more than a diffraction-limited distance from their nearest neighbor, then the images can be analyzed computationally to determine the location of the source. The process is then simply reduced to performing a data-fitting analysis on the image of the point-source, and extracting a best-fit estimation for the location of the source.

As was demonstrated in Section 2.4, the profile for the image of a point-source is an Airy function. Mathematically, the Airy function can be approximated quite accurately by a Gaussian profile, which is computationally a simpler and more tractable function. The minor differences in the wings of the two functions are generally insignificant in practice, due to image corruption due to noise. Thus, the problem is reduced to determining the peak and the width of the Gaussian distribution. These can be done via numerical fitting methods, using fitting algorithms such as nonlinear least squares or maximum likelihood estimation.

Mathematically, the Gaussian function, as an approximation of the PSF, can be ex-
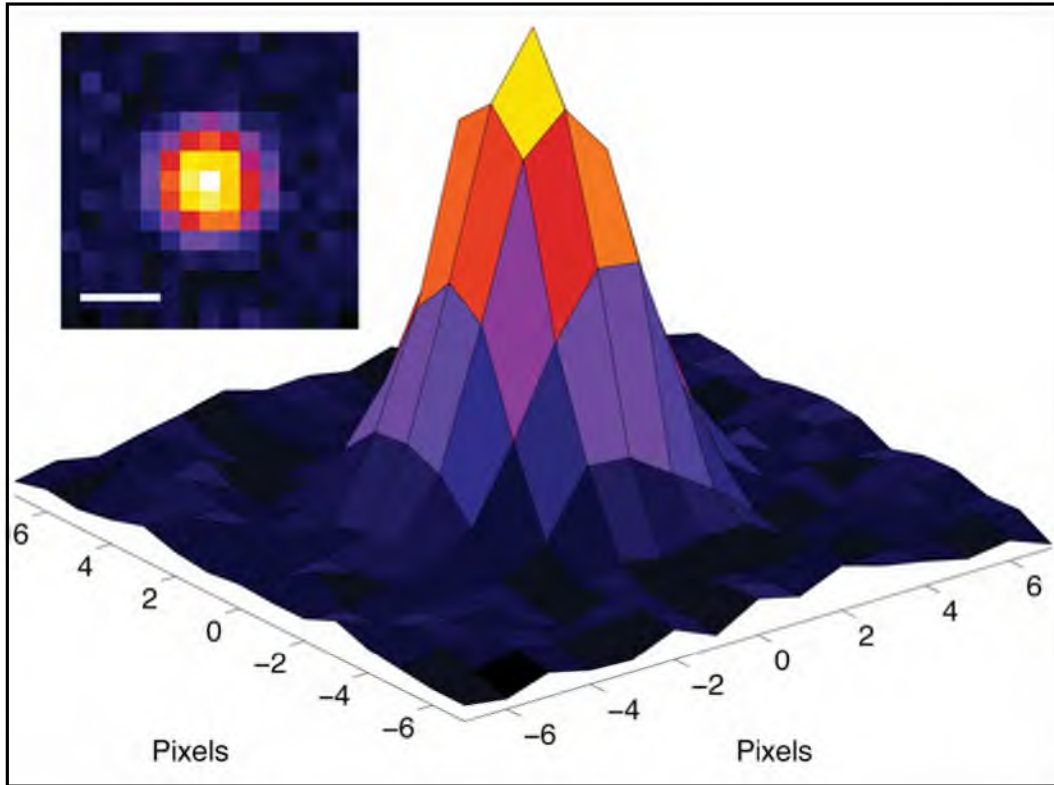
Figure 3.6. 3D Surface illustration of a pixelated PSF, as would be recorded on a camera. The height of the surface plot represents intensity; in this case, photon counts. **Inset**: 2D image of the same PSF. Scale bar: 300 nm.

pressed in two dimensions as

$$f(x) = A \cdot e^{\frac{-(x-x_0)^2}{2\sigma_x^2} + \frac{-(y-y_0)^2}{2\sigma_y^2}} + B, \tag{3.3}$$

where A is the amplitude of the PSF, x_0 and y_0 are the location of the point-source, σ_x and σ_y are the width of the Gaussian profile (the standard deviation) along the x and y axes, respectively, and B is the background. In practice, for a well-aligned microscope free of any astigmatism in the imaging optics, σ_x and σ_y can be considered equal, and just denoted as σ.

Data fitting leads to an estimation of the source position x_0 and y_0, albeit with uncertainty in the estimation. Furthermore, the finite pixel size of the detector, shot-noise in the image, and background noise must be considered. The photon shot-noise limiting case occurs when the dominant noise in each pixel is due to photons originating from the sample. The background limited case is when the dominant noise in the image is

due to other signal not from the source, such as stray light, readout error in the photon-detector, and dark current noise.

In estimating the position of the source for the shot-noise limited case, the best estimate of position is given by the average positions of the individually detected photons. For the one-dimensional case along the x-axis, the uncertainty in the estimation is common statistical formula for the standard error in the estimation of the mean [44], i.e.,

$$\langle (\Delta x)^2 \rangle = \frac{\sigma^2}{N} \qquad (3.4)$$

where Δx is the error in the localization, σ is the standard deviation of the Gaussian distribution, and N is the total number of photons collected from the source. Pixelation effects must also be considered, since pixelation results in an uncertainty in the position of the photon within a given pixel. This uncertainty is per photon, and can be added in quadrature to Equation 3.4. A pixel serves as a top-hat filter, which for a pixel of size a, has variance $a^2/12$. The uncertainty then becomes [45]

$$\langle (\Delta x)^2 \rangle = \frac{\sigma^2 + a^2/12}{N}. \qquad (3.5)$$

Pixelation effectively increases the size of the apparent PSF. Considering background noise in the analysis becomes more complicated. An estimation of the effect of background noise can be made through a χ^2 analysis, through the disparity between the actual number of photons within a pixel compared to the expected. Finding the condition for the minimum of the function $\partial \chi^2 / \partial x = 0$ will yield an equation relating the measured position in terms of x as a function of photon counts N. The derivation is lengthy, and can be found in reference [45]. The result is an extra background dominant term in Equation 3.5, and is given by

$$\langle (\Delta x)^2 \rangle = \frac{\sigma^2 + a^2/12}{N} + \frac{8\pi\sigma^4 b^2}{a^2 N^2}, \qquad (3.6)$$

where b is the background photon count per pixel. Experimentally, the background may be estimated from a frame where no point-sources are present, or from an average value of regions within a frame far from active point-sources.

The concept of localization is illustrated in Figure 3.7. The top image is a simulated point-spread function viewed on a camera detector. A best-fit Gaussian is drawn below
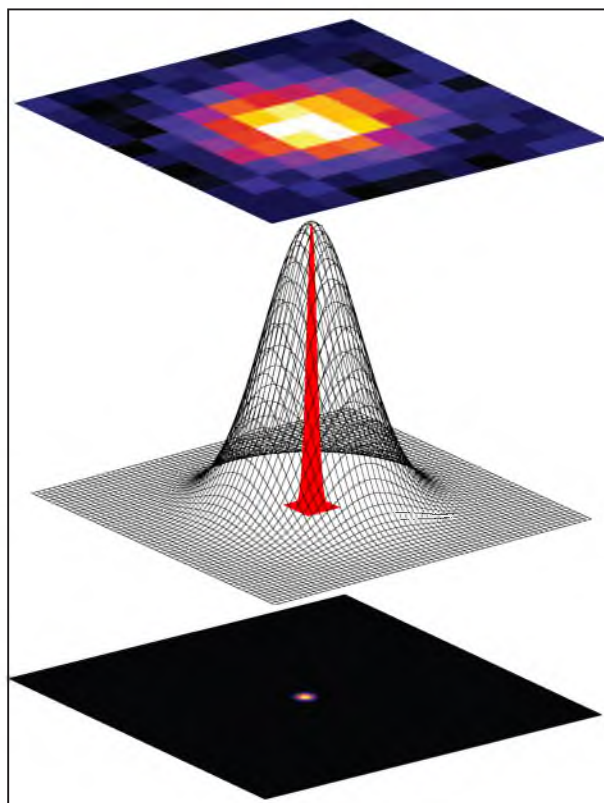
Figure 3.7. Schematic of the concept of localizing on a single point source. The top image is a diffraction-limited PSF as seen on a detector, such as a pixelated charged-coupled device (CCD). The middle image shows a mesh-image of the best-fit Gaussian (in gray) with a width of σ. The red Gaussian has a width $\bar{\sigma} = \sigma / \sqrt{N}$, where N is the number of photons with the PSF. Bottom image shows the uncertainty in the localization of the point source in the xy imaging plane. The greater the number of photons, the smaller the uncertainty.

as a gray mesh surface plot, with standard deviation σ, and an uncertainty in the position x_0 and y_0 given by $\bar{\sigma}$. Superimposed is a second Gaussian with standard deviation $\bar{\sigma}$, representing the uncertainty in the localization of the point source position. This second Gaussian is rendered in the bottom part of the figure as a two-dimensional projection in the xy plane. This is the concept of localization microscopy — for a single point-source, the location of the source may be inferred from the point-spread function to an accuracy potentially far below the diffraction limit. Depending on the fluorophores used and background values, localization methods for bright probes, which are usually used in particle tracking experiments, can yield results in the few nanometer range [41, 42]. Typical values in realistic localization microscopy methods on densely labeled biological

samples are in the 20-30 nm range. Thus, the precision with which individual fluorescent probes can be localized is typically an order of magnitude below the conventional diffraction limit.

However, the field of view of microscopes is much larger than a single point-spread function. Thus, more than one point source may be within the field of view, and if the point sources are far enough apart, their point-spread functions will not overlap. Thus, the problem becomes not one of having single sources within the field of view, but of a sparse sampling set. As long as two point sources are more than a diffraction-limited distance away, their PSFs will not overlap in the image plane, and each individual fluorophore can be isolated separately. This point is illustrated in Figure 3.8. While there are multiple point sources within the image, each point source has a distinct and nonoverlapping PSF in the image plane. A small region of interest (ROI) around each fluorophore may be extracted from the larger data set, the PSF can be localized, and each point source's location can be estimated to an accuracy below the diffraction limit. The question then becomes — how are single fluorophores isolated in a biological sample?

3.2.2 Isolating Single Fluorophores

In conventional microscopy techniques, it is impossible to isolate single molecules within a sample with densely packed fluorophores. Illuminating the sample with excitation light causes every fluorophore to react to the excitation field and undergo fluorescence. Even in STED microscopy, the effective focal spot will have numerous fluorophores within it, being an order of magnitude larger than the average size of a protein. Certain methods use the natural blinking states of quantum dots to isolate single emitters in a group ensemble, but these methods are highly impractical for conventional imaging in biological structures [46]. Even a portion of a cell a few microns in diameter can contain thousands and thousands of proteins. What is required in localization microscopy is the ability to control the state of the fluorophores, to be able to turn them from a nonfluorescent dark state to a bright active state in a manner in which only a few fluorophores are in an active state at any given time.

The ability to control the activation state of fluorescent proteins successfully came through an engineered variant on the original fluorescent workhorse, GFP [7, 47]. Termed photoactivatable-GFP (PA-GFP), this protein initially is in a dark, nonfluorescent state
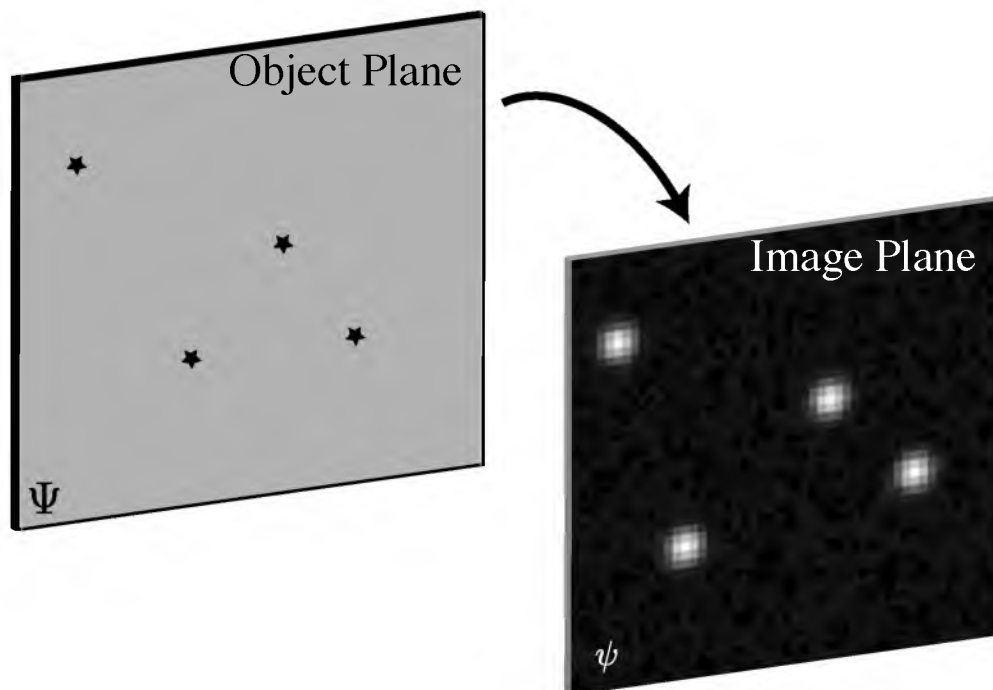
Figure 3.8. Cartoon schematic illustrating the concept of the diffraction-limit of a sparsely distributed sample. Single point-sources are represented as stars. As the image of the point sources is relayed from the object plane (Ψ) to the image plane (ψ) the diffraction-limit prevents imaging the point sources as a true point source. However, if either the number of samples is low, or the number of active "on" samples is low enough such that the nearest "on," or optically active, neighbor is greater than a diffraction-limited distance away from any given point source, each point source may be localized to a precision lower than the diffraction-limit.

when illuminated by a 488 nm laser, the standard excitation wavelength for exciting fluorescence in GFP. Upon illumination by ultraviolet light at 400 nm, the protein undergoes a conformational change within its chromophore. The conformational change involves the elimination of a carboxyl side-chain near the chromophore, allowing for a molecular rearrangement that allows for fluorescence to occur when excited with 488 nm light. This can be seen in Figure 3.9. Irradiation by 400 nm light allows for the selective activation of well-defined areas containing PA-GFP within the cell [48].

In localization microscopy using PA-GFP or similar protein variants (called photo-conversion in proteins that undergo changes in emission spectrum [50, 51]), irradiation of the sample by ultraviolet light is done at extremely low intensities. The intensity is low enough that the probability of an individual fluorophore absorbing an ultraviolet pho-
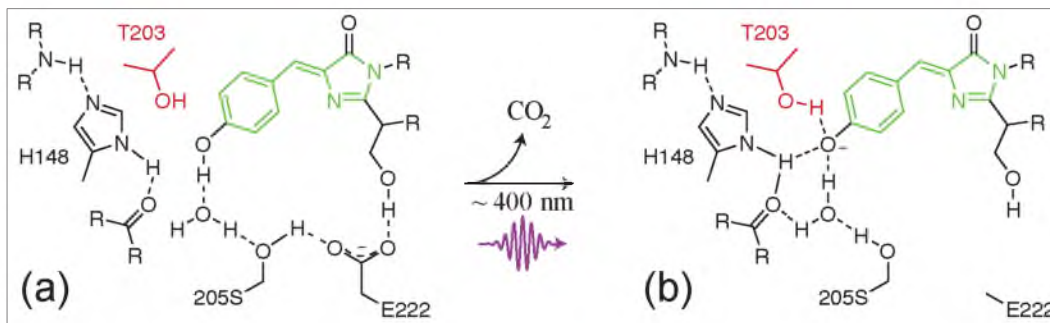
Figure 3.9. Chemical structure of photo-activatable green fluorescent protein (PA-GFP). Photo-activation is achieved by the conformational reconfiguration due to the rotation of T203 (the amino acid threonine) and the decarboxylation of of glutamic acid 222 (E222) [47, 49].

ton and undergoing photo-activation or photo-conversion is extremely low, such that at any given time, only a few individual fluorophores within the sample are in an active fluorescent state. This low density of active fluorophores (as illustrated in Figure 3.8) then allows for the computational isolation and localization of individual fluorescent proteins [5, 52].

As seen in Equation 3.6, the error in the estimation of a particle's location is given by $\approx \sigma / \sqrt{N}$ for the shot-noise limited case where background and pixel size are neglected. Recall that the variable N is the number of detected photons from the source. The higher the value of N, the lower the uncertainty will be. While fluorescent proteins are remarkably versatile and flexible in terms of the genetic labeling of a sample, their overall photon budgets are very low. Most fluorescent proteins only yield on average ≈ 100 - 500 photons before degrading [48], which is obviously a limiting factor for localization schemes.

Organic dyes, as shown in Figure 2.2(a) for Alexa 568, yield more than an order of magnitude more photons per molecule than fluorescent proteins, with average photon yields of ≈ 6000-$10,000$ [17]. Organic fluorophores can be used to label proteins as well through immunofluorescence techniques [53] and other constructs [54, 55]. The problem is to optically activate organic fluorophores, such that only a small portion are active at any given time within the sample. Fortunately, this can be done by optically shelving organic dyes.

Optically shelving of organic dyes relies on the fact that these dyes are photo-reduced

in the presence of an electron donor. While the singlet state (which is responsible for fluorescence) has a short lifetime, the triplet state is energetically stabilized (metastable) due to the fact that it is a forbidden transition. Thiols,[7] structural homologs to alcohols but containing a sulfhydryl group in place of the carboxyl group, will react with the triplet state of the fluorophores, producing a radical fluorophore. This radical fluorophore configuration is extremely stable, and can last for minutes to hours. Most importantly, the triplet and radical state of the fluorophore are "dark" states, and the fluorophore does not fluoresce. Generally, irradiation with ultraviolet light in the presence of molecular oxygen will oxidize the fluorophore and return it to its ground state, recovering fluorescence. This process is outlined in Figure 3.10. Due to the large disparity in the lifetimes of the various states involved, there is a build-up of fluorophores in these dark states, leaving only a small, random population in the bright state, which allows for the localization steps as outlined above.

3.2.3   The Methodology of Localization Microscopy

As was first demonstrated with PA-GFP [7] and various other photo-convertible fluorescent proteins [48, 50], the active state of point-sources may be controlled optically. This technique was then applied to more conventional organic dyes through photochemistry [56–58], which offer an advantage in their superior photon budget. Both methods of optical activation can be controlled through ultraviolet light, enabling experimental control of the activation density of fluorescent point sources in a given region of interest. Fluorophores will eventually photo-degrade (known as photo-bleaching) and become permanently dark. This usually involves the chemical degradation of the chromophore (usually through light-induced reactions with molecular oxygen), providing the needed deactivation of the current fluorophore subset to allow for the next round of activation. Fluorescent proteins will usually photo-bleach after yielding a few hundred photons, while organic dyes will produce upwards of 10,000 before photo-bleaching.

Localization microscopy relies on the binary control of fluorophores to work properly. By incorporating temporal control over the fluorescent state of the fluorophores

---

[7]A thiol is a chemical analog of an alcohol. The chemical composition of alcohols is $R - OH$ where R is the organic backbone to the molecule. A thiol's molecular composition is $R - SH$, where the side-chain is now a sulfur atom bonded to a hydrogen, known as a sulfdydryl group.
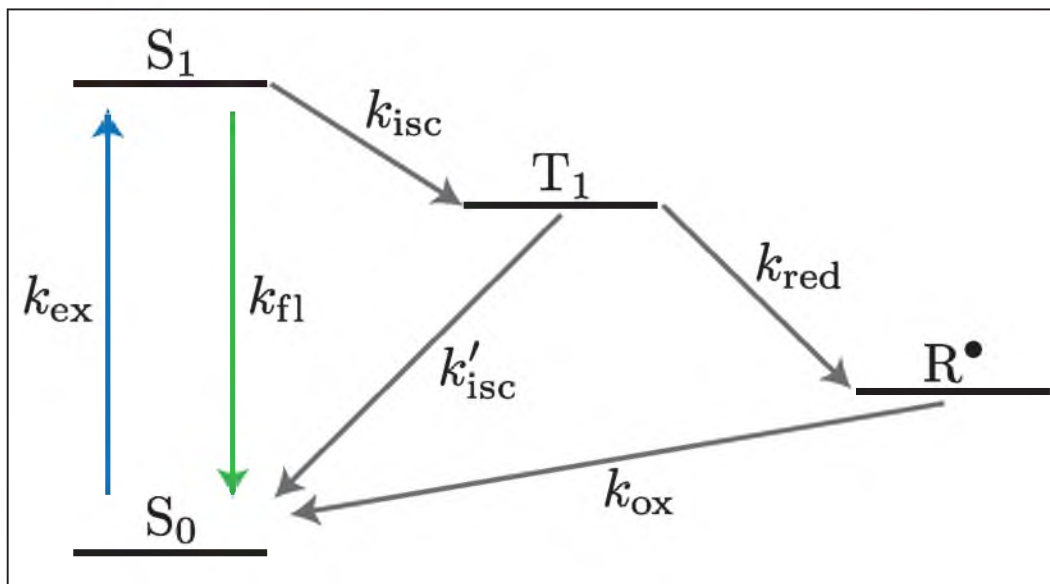
Figure 3.10. Optically shelving an organic dye. The fluorophore, Alexa Fluor 647, can either cycle between its ground state, S_0 and its excited singlet state S_1, giving off fluorescence in the process. The fluorophore can also undergo intersystem crossing, with rate k_{isc}, from the singlet state to the triplet state. Once in the triplet state T_1, the fluorophore can react with molecular oxygen (O_2) to recover the singlet ground state of the fluorophore with rate k'_{isc}, along with singlet molecular oxygen. In the presence of a thiol in the molecular environment, the triplet state can also react with the thiolate at rate k_{red} to produce the radical anion of the fluorophore ($R^{\bullet}$) and the corresponding thiyl radical (see main text). Once the fluorophore is in its radical anion state, it can react with oxygen with rate k_{ox} and return back to the singlet ground state S_0. Alexa 647 in its radical form exhibits a pronounced absorption profile at ≈ 400 nm. Radiating the sample with 405 nm excitation, for instance, will promote recovery back to the S_0. Unlike the produced thiyl radicals, the radical form of Alexa 647 is very stable and can last seconds, even in the presence of molecular oxygen. The discrepancy in the lifetimes of the various energy states leads to a build-up of fluorophores in the T_1 and $R^{\bullet}$ states, effectively leaving only a very small population of fluorophores in the active, bright state, $S_{0 \leftrightarrow 1}$. By controlling the intensity of 405 nm excitation light, for instance, the population of active fluorophores can be coarsely controlled [56].

within the sample, it is possible to gain more detail than is otherwise available conventionally. Numerous iterations are required to image each individual fluorophore within the sample. Figure 3.11 illustrates this concept. In short, localization microscopy exploits the ability to perform temporal multiplexing of the excitation and recording of individual fluorophores which allows for diffraction-limited spatial multiplexing [59].

Localization microscopy as a technique consists of activating a sparse subset of fluorophores, recording their diffraction-limited point-spread functions, photo-bleaching
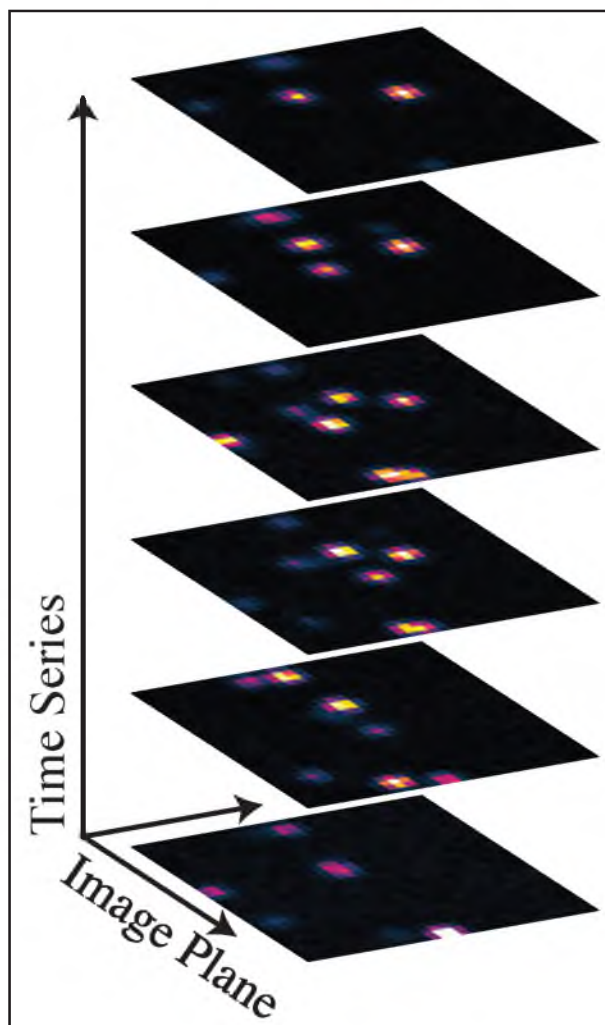
Figure 3.11. Separating fluorophore active states in time. A schematic illustrating the key feature of localization microscopy, namely the time isolation of a small set of active fluorophores. Spatial dimensions are represented horizontally ("Image Plane"), while increasing time is in the vertical direction ("Time Series"). Each slice in the image represents a unique time, in this case the acquisition time of the camera frame. During each time event, only a small fraction of the overall number of fluorophores present in the sample are in an active fluorescent state, with most on average being more than a diffraction-limited distance from their nearest fluorescent neighbor. By controlling the time and spatial multiplexing conditions within the sample, each individual fluorophore, and its PSF on the image plane, can be isolated from the larger data set and localized.

the current set of fluorophores, and repeating. After recording the data, the data are computationally analyzed where each fluorophore in each frame is isolated, extracted as a region of interest within the frame, and localized. The estimation of the position of each fluorophore is recorded, as well as the uncertainty in the estimation. A super-resolution image is then generated by computationally rendering each fluorophore in its estimated position. Figure 3.12 shows a cartoon schematic of this experimental procedure and the necessary steps involved. The image of each fluorophore is usually rendered as a Gaussian distribution, with a standard deviation corresponding to the individual point source's uncertainty in estimation [5, 52], although some methods involve plotting the localizations as a density map [60]. Since each localized point-source is rendered as a unique "point" within the computationally rendered image, localization microscopy is also referred to as pointillism microscopy [46].

As an example, Figure 3.13 is an illustration of the advantage that super-resolution can provide over classic fluorescence methods. The simulated image shows a log-spiral shape, where the central portion of the image is clearly not resolvable by conventional optical microscopy. For this simulation, each fluorophore had a conventional diffraction limited value of 200 nm. In the super-resolution image, the uncertainty in the position is an order of magnitude smaller, at 20 nm. While this is still an order of magnitude larger than the size of individual proteins, it is on the scale of protein distributed networks, such as actin filaments and microtubule networks [2].

3.2.4 Biological Examples of Localization Microscopy

As an example of localization microscopy in a biological sample, Alexa647 labeled microtubules (specifically, the α-tubulin subunit) from BSC-1 African green monkey kidney epithelial cells were imaged after methanol fixation and run through a conventional localization data collection and analysis procedure on a commercial localization microscope, a Carl Zeiss Elyra. For this system, the optical configuration is well represented by Figure 1.2. A 63x, 1.4 NA oil-immersion microscope objective was used, and the sample was excited at 647 nm wavelength excitation with the proper reducing agents (β-mercaptoethylamine, abbreviated as MEA) to allow for dark-state population build-up of the Alexa647 fluorophore. The small population subset that returns to the
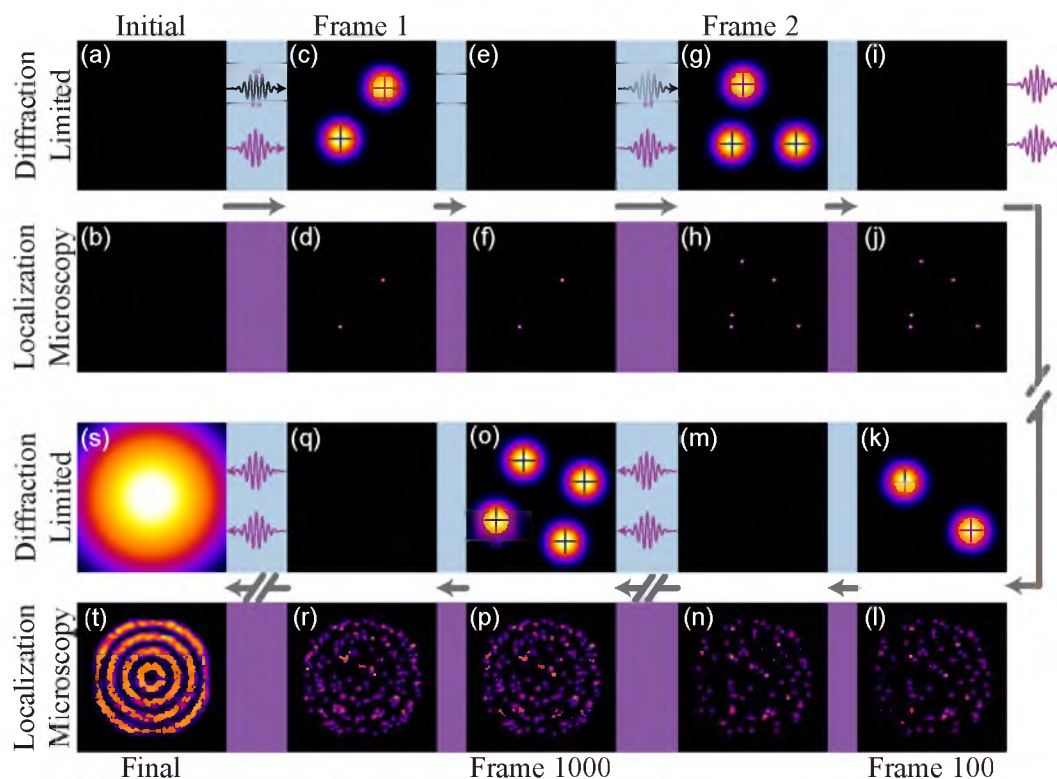
Figure 3.12. Concept of localization microscopy. **(a)** The sample is in an inactive initial state, and **(b)** no individual point-sources have been localized at this point in time. In Frame 1, the sample is illuminated with ultraviolet light at low intensity (purple light), causing a sparse subset of molecules to become active **(c)** and give off fluorescence, allowing for each point-spread function to be localized (black crosses). Once the individual molecules from each frame have been isolated and localized, their positions and uncertainties are recorded and used to build up a composite super-resolution image, **(d)** and **(f)**. After the initial subset of molecules photo-bleaches, the next sparse subset is activated with ultraviolet light, and the process repeats itself through recording, localization **(g)**, and photobleaching **(i)**. The localizations are recorded and the super-resolution image continues to build, **(h)** and **(i)**. After numerous cycles of this process (**k, m, o, q**), the super-resolution image begins to show faint structure (**l, n**). Further recording and localization (**p, r**) allow for further reconstruction of the underlying structure. Finally, after a very large number of individual molecules have been activated, recorded and localized, the super-resolution image **(t)** shows distinct subdiffraction limit features and length scales. These characteristics are not resolvable in the conventional diffraction limited image **(s)**. Broken arrows denote skipping numerous frames. All images are simulated. Figure adapted from [59].
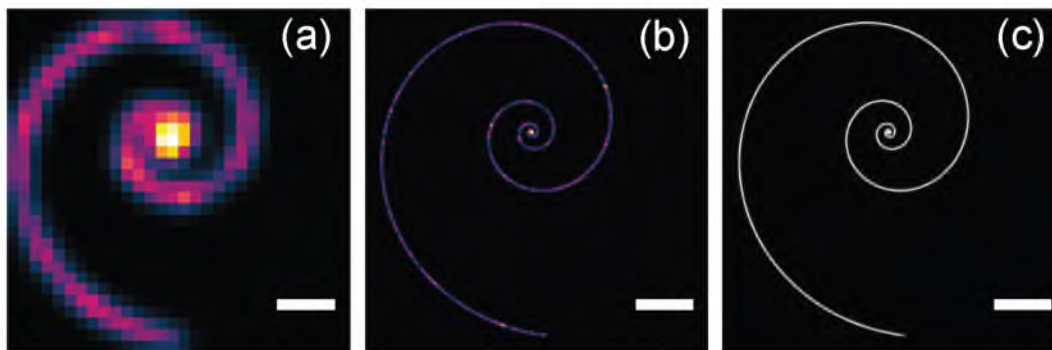
Figure 3.13. Simulation showing fluorophores distributed on a spiral shape. **(a)** Conventional, diffraction-limited image. As the spiral gets close together, the individual fluorophore's PSFs merge, and it becomes impossible to resolve small spatial details within the central portion of the spiral. **(b)** In the localization image, each individual fluorophore has been localized with an uncertainty an order of magnitude smaller than the diffraction-limited image. Each fluorophore is then rendered as a Gaussian distribution with a width (σ) an order of magnitude smaller than shown in **(a)**. As a result, the central portion of the spiral is more resolved, and the structure emerges. **(c)** The "true" shape of the spiral. Scale bar: 500 nm.

singlet state is imaged at a high enough laser intensity (≈ 10 kW/cm^2 at the sample) that the fluorophore will return to a triplet or radical dark state during a single acquisition frame (20 ms), but not before emitting thousands of photons while in the singlet state. The peak emission of Alexa647 is at 671 nm, with the emission being separated from the excitation path by the use of a wavelength selective mirror (dichroic). The emission is imaged with the proper imaging optics onto an electron-multiplying charged-coupled device (EMCCD) with a gain factor set at a value of 50.[8] The magnification of the system is such that the pixel size on the camera corresponds to a sample dimension of 100 nm. Each frame is recorded and then fed into the localization algorithm.

The localization algorithm begins with a Gaussian convolution to reduce background noise. This is accomplished by a frame-by-frame Fourier transform and multiplication of each row and column by a one-dimensional Gaussian function, followed by an inverse Fourier transform back to the spatial domain.[9] Candidate fluorophores are isolated

---

[8]The gain factor of EMCCD cameras enhances signal as well as noise, and so care must be taken in choosing an appropriate gain value so as not to mask the signal in noise. Typical EMCCD cameras have a gain range from 1 to 1000.

[9]The same mathematical transformation and image analysis could be accomplished by convolving the raw frame data with a two-dimensional Gaussian function, since convolution in the spatial domain is

based upon a threshold pixel intensity above the characteristic background values of the frame, and an ROI with a pixel radius of five (for an 11x11 extracted region) is extracted from the camera frame. Each ROI is then run through a maximum likelihood estimation routine to determine the best-fit Gaussian profile for the given fluorophore. The spatial locations, point-spread function width, estimation uncertainty, total photon count, and background are all recorded for each fluorophore, where they can then be rendered as a localization image.

Figure 3.14 shows the result. Panel **(a)** shows the image rendered as a wide-field image, where each fluorophore is rendered as a diffraction-limited Gaussian distribution, with a standard deviation of 250 nm. Panel **(b)** shows the improvement afforded by localization microscopy. Each point-source is rendered as a Gaussian distribution, with a standard deviation equal to the uncertainty in the localization of each fluorophore. On average, each fluorophore has an uncertainty of $\approx$ 20-30 nm. The localization image shows much more structure and detail that is otherwise lost within the conventional diffraction-limited image.

3.3 Localization versus Resolution

One distinction that must be made in localization microscopy is that of localization accuracy (or precision) versus resolution. In principle, STED and localization microscopy offer diffraction-unlimited imaging. If the power of the STED beam is high enough, the effective focal spot can be reduced to a nanometer scale. In localization microscopy, if a fluorophore yields enough photons and the background is low enough, it may be localized down to the nanometer scale as well. However, in the context of localization microcopy, this language is concerned with the ability with which a single point source's location may be estimated, and nothing about the ability to distinguish features within a sample.

Conventionally, the resolving power of an optical system is related to the fundamental localization ability of single point sources. Akin to the modified formalism for the Rayleigh criterion for STED microscopy, as shown in Equation 3.1, this concept can be

---

equivalent to multiplication in the Fourier domain. The latter method is used due to its computational speed over the former method, which is important when processing tens of thousands of frames of data.
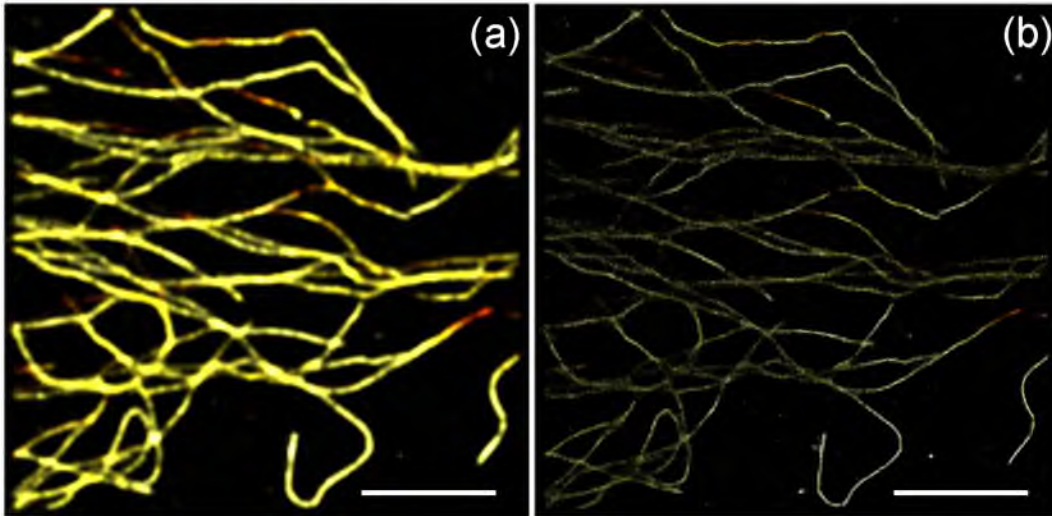
Figure 3.14. Alexa647 labeled microtubules from BSC-1 African green monkey kidney epithelial cells. **(a)** Diffraction-limited image, after intensive filtering to remove background noise and spurious data. **(b)** Localization image of the same data set. Each point is rendered as a Gaussian distribution, with a standard deviation equal to the uncertainty in the localization error. Image **(b)** shows more structural detail when compared to **(a)**. Scale bar: 5 μm.

applied to localization microscopy. Rayleigh's criterion is a resolving metric concerning *two* point sources, and the modification can be extended to include the localization accuracies of the two point-sources. The expression for this modification may be written as [61]

$$\Delta x = \frac{1}{\sqrt{4\pi A_0 \cdot (t - t_0) \cdot \Gamma_0(d)}} \cdot \frac{\lambda}{NA} \tag{3.7}$$

λ is the emission wavelength, NA is the numerical aperture of the objective, A_0 is the intensity (rate of photon detection) of the point source, $(t - t_0)$ is the acquisition time, and $\Gamma(d)$ is an expression related to the estimation ability between two unknown point sources, which takes into account both the distance between the two point sources, along with the estimation accuracy of each point source. This expression then generalizes the Rayleigh criterion for a localization microscope, but only for two point sources. For a sample with underlying structure, this formalism falls short.

In localization microscopy, numerous factors must be considered when determining the overall resolution of the image. Factors such as the physical linkage of the fluo-

rophore to the target protein must be considered,[10] as well as the underlying spatial distribution inherent to the sample. Sample dependent parameters such as the photon yields of the fluorophores, as well as ambient background signal from out-of-focus fluorescence, or even the sampling density of active fluorophores. Analysis and computational considerations must be considered as well, such as the quality of the fluorophore detection algorithms, candidate selection and the quality of the localization algorithms [62].

Ultimately, all of the above parameters directly correlate to the local labeling density. The ability to resolve structure in a sample is as much a function of labeling density as well as localization accuracy. In general, the resolution of a unique element within a sample should contain at least two data points within a specified resolution, as per the Nyquist criterion [63]. For a biological structure, however, a better definition of resolution would be that a feature of the specimen is considered to be resolvable when a feature can reliably estimated from the data [64]. One method with which to calculate an effective resolution over the sample is through the cyro-electron microscopy method of Fourier ring correlation (FRC) [65], which analyzes the correlation between two subsets of the image data in the Fourier domain. FRC evaluates the degree of correlation of two independent reconstructions of the same object in frequency space and determines the resolution threshold (the spatial frequency) at which both reconstructions are consistent and considered to be resolved [62, 66].

Realistically, the resolution of a sample depends on both the localization accuracy of the individual fluorophores comprising the image, and the labeling density and the overall distribution of the fluorophores. Qualitatively, this can be seen in Figure 3.15. Each pixel of the image of the Siemens star can be thought of as a point-source. Each of the panels in Figure 3.15(b) has an increasing number of pixels removed from the

---

[10]For example, immunofluorescence techniques use antibodies to bind to target proteins. These antibodies are known as primary antibodies, which then serve as targets for a second antibody, known as a secondary antibody. These secondary antibodies contain a conjugated fluorophore, which is what is imaged. However, the linkage of target protein to primary antibody to secondary antibody can result in a distance of $\approx$ 40 nm between the target protein and the fluorophore. In diffraction-limited imaging, this distance can be neglected, but cannot be in localization microscopy. When labeling with a fluorescent protein, the fluorescent protein is directly attached to the target protein, leaving the fluorescence marker within a few nanometers of the target protein. New techniques allow for the attachment of an enzymatic protein to the target protein of interest, which will covalently bind an organic fluorophore [54, 55].
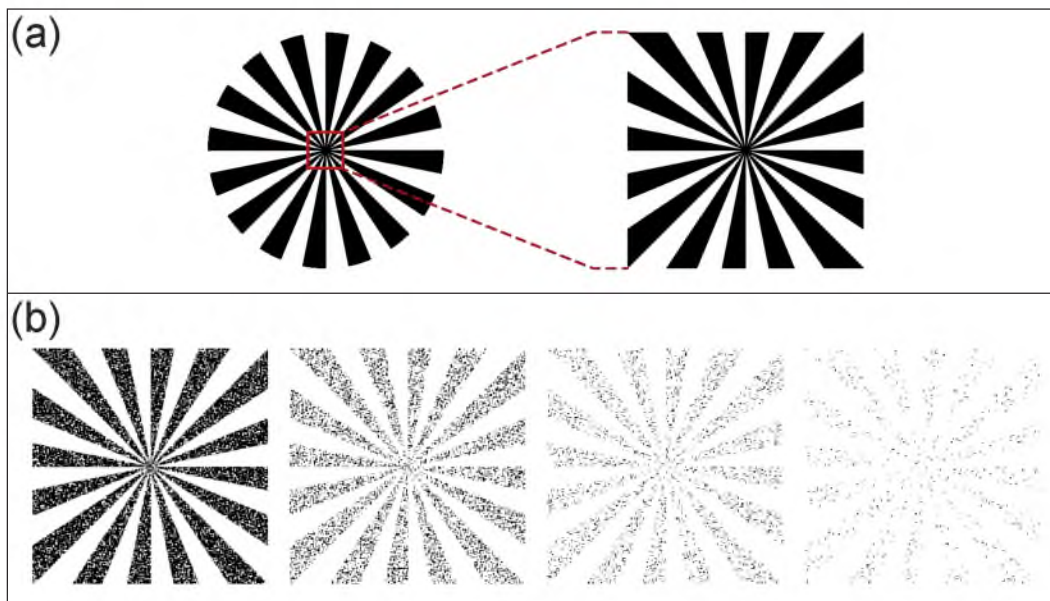
Figure 3.15. Resolution as a function of labeling density. In localization microscopy, the ability to resolve structure in a sample depends on the labeling density. **(a)** The same Siemens star that was shown in Figure 2.5, with a close-up of the center. **(b)** The effect of removing an increasing number of sampling points or pixels within the image, and its effect on the ability to resolve the detail of the structure. While each individual point in the image has a high precision in its location, unless the sampling density is high enough, there is no discernible underlying structure in the image.

image. This is analogous to a decreasing labeling density within the sample. If the labeling density is too sparse, the resolvable detail of the image is greatly diminished, regardless of how well the position of each point-source (or pixel) is known.

As an example of this in a biological sample, Figure 3.16 shows a localization microscopy image of Alexa647 labeled microtubules from BSC-1 African green monkey kidney epithelial cells. In panel **(a)**, the image is shown fully reconstructed. Using the methodology of Fourier ring correlation, and the techniques outlined in reference [62], the effective resolution of the image $\approx$ 43 nm. If only $\approx$ 57% of the data set is used in the reconstruction of the final image, as shown in panel **(b)**, the effective resolution is reduced to $\approx$ 80 nm [66]. While the localization of each sampled data point in the two images is the same (since they are taken from the same data), the resolution between the two images is different. Thus, the overall resolution is a function of both localization accuracy of each emitter within the sample being imaged, as well as the total number of samples imaged during data acquisition.
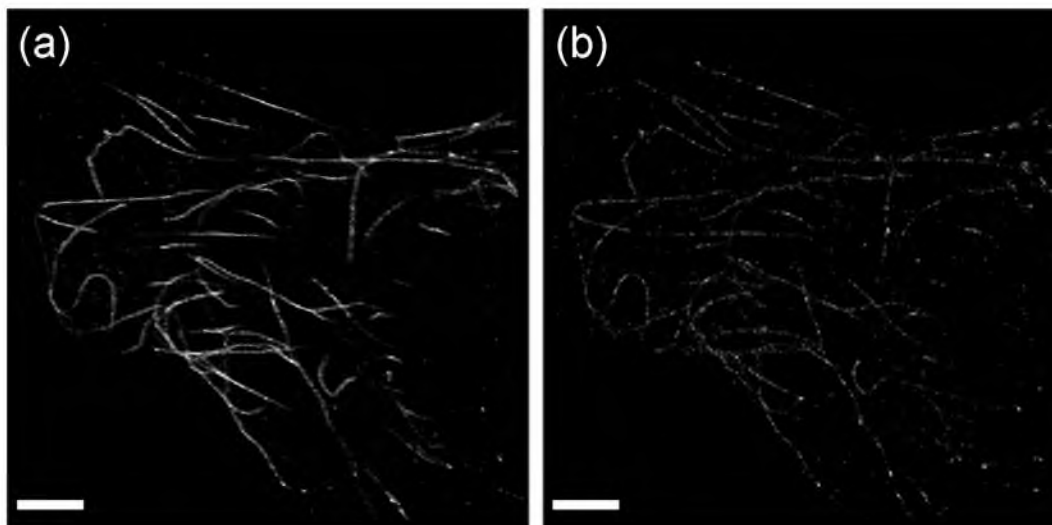
Figure 3.16. Reconstruction of imaging data from Alexa647 labeled microtubules. Sample was imaged on a Zeiss Elyra localization microscope, showing the effect of sparse labeling and its impact in image reconstruction. While the localization accuracy for each point source in the image is the same, the number of localizations in each image is different. **(a)** Image reconstructed using the entirety of the data set. **(b)** Image reconstruction using approximately 57% of the data set [66]. Scale bar: 5 μm.

3.4   Concluding Remarks

Within the last decade, the far-field performance limits codified by Abbe and Rayleigh have been circumvented by numerous methodologies. Far-field optical super-resolution techniques have had a large impact on the biological and imaging community, allowing for direct imaging of biological structures on relevant length scales. Localization microscopy has allowed for an approximate order-of-magnitude improvement in overall resolution of the image, while allowing for the large-scale determination of the spatial coordinates of each localized fluorophore in the sample. In the context of Figure 1.4, this has allowed optical microscopy to move further along the resolution axis, while still maintaining all the other benefits of the method, namely its inherently high level of chemical specificity. The technique now enables the optical characterization of biological systems at length scales more appropriate for protein interactions and function, while allowing for further statistical analysis on the distribution of proteins in three-dimensional space.

While a remarkable improvement over conventional methods, localization techniques are only able to reliably demonstrate localization ability in the tens of nanometers. The

remainder of this thesis is devoted to investigations related to improving the localization ability of single point-sources, i.e., determining the spatial position of the fluorophores. This has two consequences. One is that for a given number of photons, the localization precision will be higher, specifically enabling localization estimations within the single nanometer length scale. Secondly, fewer photons will yield the same uncertainty as in conventional cases, meaning that the acquisition rate may be increased. While the overall acquisition rate may be of little consequence in imaging fixed (i.e. dead) samples, the field of localization microscopy in both research and commercial settings is advancing towards live imaging, where acquisition speed is important due to the dynamic environment of live cells, where speed is important.

3.5 References

[1] B. N. G. Giepmans, S. R. Adams, M. H. Ellisman, and R. Y. Tsien, Science (New York, NY) **312**, 217 (2006).

[2] B. Alberts et al., *Molecular Biology of the Cell*, Garland Science, New York, NY, 5th edition, 2007.

[3] B. J. Zeskind et al., Nature Methods **4**, 567 (2007).

[4] G. Schneider et al., Nature Methods **7**, 985 (2010).

[5] E. Betzig et al., Science (New York, NY) **313**, 1642 (2006).

[6] S. W. Hell and J. Wichmann, Optics Letters **19**, 780 (1994).

[7] R. M. Dickson, A. B. Cubitt, R. Y. Tsien, and W. E. Moerner, Nature **388**, 355 (1997).

[8] M. Minsky, Scanning **10**, 128 (1988).

[9] W. R. Zipfel, R. M. Williams, and W. W. Webb, Nature Biotechnology **21**, 1369 (2003).

[10] S. Hell and E. Stelzer, Optics Communications **93**, 277 (1992).

[11] S. Hell and E. H. K. Stelzer, Journal of the Optical Society of America A-Optics Image Science and Vision **9**, 2159 (1992).

[12] H. Gugel et al., **87**, 4146 (2004).

[13] M. G. Gustafsson, D. A. Agard, and J. Sedat, Journal of Microscopy **195**, 10 (1999).

[14] S. W. Hell, Science (New York, NY) **316**, 1153 (2007).

[15] S. W. Hell, Nature Methods **6**, 24 (2009).

[16] G. Patterson, M. Davidson, S. Manley, and J. Lippincott-Schwartz, Annual Review of Physical Chemistry **61**, 345 (2010).

[17] D. Toomre and J. Bewersdorf, Annual Review of Cell and Developmental Biology **26**, 285 (2010).

[18] L. Schermelleh, R. Heintzmann, and H. Leonhardt, The Journal of Cell Biology **190**, 165 (2010).

[19] B. Huang, H. Babcock, and X. Zhuang, Cell **143**, 1047 (2010).

[20] B. O. Leung and K. C. Chou, Applied Spectroscopy **65**, 967 (2011).

[21] M. G. L. Gustafsson, Proceedings of the National Academy of Sciences of the United States of America **102**, 13081 (2005).

[22] M. G. Gustafsson, Journal of Microscopy **198**, 82 (2000).

[23] R. Heintzmann, T. M. Jovin, and C. Cremer, Journal of the Optical Society of America A-Optics Image Science and Vision **19**, 1599 (2002).

[24] M. G. L. Gustafsson et al., **94**, 4957 (2008).

[25] G. Donnert et al., Proceedings of the National Academy of Sciences of the United States of America **103**, 11440 (2006).

[26] J. Keller, A. Schönle, and S. W. Hell, Optics Express **15**, 3361 (2007).

[27] H. Xie, Y. Liu, D. Jin, P. J. Santangelo, and P. Xi, JOSA A **30**, 1640 (2013).

[28] H. Xie et al., STED3D: point spread function simulation for high numerical aperture objective and resolution evaluation, in *Bio-Optics: Design and Application*, page JT2A.39, Washington, D.C., 2013, OSA.

[29] M. Leutenegger, C. Eggeling, and S. W. Hell, Optics Express **18**, 26417 (2010).

[30] B. Harke et al., Optics Express **16**, 4154 (2008).

[31] V. Westphal and S. Hell, Physical Review Letters **94**, 143903 (2005).

[32] D. Wildanger et al., Advanced Materials , n/a (2012).

[33] S. W. Hell and M. Kroug, Applied Physics B Laser and Optics **60**, 495 (1995).

[34] T. A. Klar, S. Jakobs, M. Dyba, A. Egner, and S. W. Hell, Proceedings of the National Academy of Sciences of the United States of America **97**, 8206 (2000).

[35] T. A. Klar, E. Engel, and S. W. Hell, Physical Review E **64**, 066613 (2001).

[36] M. Dyba and S. W. Hell, Physical Review Letters **88**, 163901 (2002).

[37] N. Bobroff, Review of Scientific Instruments **57**, 1152 (1986).

[38] D. L. Snyder, A. M. Hammoud, and R. L. White, Journal of the Optical Society of America A-Optics Image Science and Vision **10**, 1014 (1993).

[39] J. Gelles, B. J. Schnapp, and M. P. Sheetz, Nature **331**, 450 (1988).

[40] H. P. Kao and A. S. Verkman, **67**, 1291 (1994).

[41] A. Yildiz et al., Science (New York, NY) **300**, 2061 (2003).

[42] A. Yildiz, M. Tomishige, R. D. Vale, and P. R. Selvin, Science (New York, NY) **303**, 676 (2004).

[43] D. Cai, K. J. Verhey, and E. Meyhöfer, **92**, 4137 (2007).

[44] J. R. Taylor, *An Introduction to Error Analysis: The Study of Uncertainties in Physical Measurements*, University Science Books, Sausalito, CA, 2nd edition, 1997.

[45] R. Thompson, D. Larson, and W. Webb, **82**, 2775 (2002).

[46] K. Lidke, B. Rieger, T. Jovin, and R. Heintzmann, Optics Express **13**, 7052 (2005).

[47] G. H. Patterson and J. Lippincott-Schwartz, Science (New York, NY) **297**, 1873 (2002).

[48] M. Fernández-Suárez and A. Y. Ting, Nature Reviews Molecular Cell Biology (2008).

[49] J. J. van Thor, T. Gensch, K. J. Hellingwerf, and L. N. Johnson, Nature Structural Biology **9**, 37 (2002).

[50] N. G. Gurskaya et al., Nature Biotechnology **24**, 461 (2006).

[51] S. A. McKinney, C. S. Murphy, K. L. Hazelwood, M. W. Davidson, and L. L. Looger, Nature Methods **6**, 131 (2009).

[52] S. T. Hess, T. P. K. Girirajan, and M. D. Mason, **91**, 4258 (2006).

[53] I. D. Odell and D. Cook, Journal of Investigative Dermatology **133**, e4 (2013).

[54] G. V. Los et al., ACS Chemical Biology **3**, 373 (2008).

[55] T. Klein et al., Nature Methods **8**, 7 (2011).

[56] S. van de Linde et al., Nature Protocols **6**, 991 (2011).

[57] S. van de Linde et al., Photochemical & Photobiological Sciences: Official Journal of the European Photochemistry Association and the European Society for Photobiology **8**, 465 (2009).

[58] J. Vogelsang et al., Chemphyschem: A European Journal of Chemical Physics and Physical Chemistry **11**, 2475 (2010).

[59] T. J. Gould, V. V. Verkhusha, and S. T. Hess, Nature Protocols **4**, 291 (2009).

[60] D. Baddeley, M. B. Cannell, and C. Soeller, Microscopy and Microanalysis **16**, 64 (2010).

[61] S. Ram, E. S. Ward, and R. J. Ober, Proceedings of the National Academy of Sciences of the United States of America **103**, 4457 (2006).

[62] R. P. J. Nieuwenhuizen et al., Nature Methods **10**, 557 (2013).

[63] H. Nyquist, American Institute of Electrical Engineers, Transactions of the **47**, 617 (1928).

[64] J. E. Fitzgerald, J. Lu, and M. J. Schnitzer, Estimation Theoretic Measure of Resolution for Stochastic Localization Microscopy, 2012.

[65] W. O. Saxton and W. Baumeister, Journal of Microscopy **127**, 127 (1982).

[66] T. Ilovitsh et al., Biomedical Optics Express **5**, 244 (2013).

CHAPTER 4

MODIFICATION OF THE POINT-SPREAD FUNCTION
THROUGH SELF-INTERFERENCE

As was demonstrated in Chapter 3, a single point-source may be localized well below the classical diffraction limit. In fact, circumventing the diffraction limit in optical microscopy has been the focus of extensive research in recent years. Much work has been accomplished in the field of single-molecule methods and microscopy [1], as well as the pioneering work in localization microscopy methods [2–4], which were able to achieve subdiffraction resolution by temporally separating adjacent emitters. Other single molecule techniques were used for particle tracking [5–7] to characterize biological structure dynamics. For the particle tracking techniques, different markers were used, such as fluorophores [5, 6, 8], and their semiconductor analogs, quantum dots [9–11]. The principle of fluorescence does not have to be used either, and direct Rayleigh scattering from metal nanoparticles can be used [12–17]. The image of a single emitter by a microscope, regardless of the emission source (fluorophore, quantum dot, metal nanoparticle), has the shape of a point-spread function. At the heart of these techniques lies the assumption that this PSF can be well approximated by a Gaussian function and the emitter can be localized to a precision well beyond the diffraction limit. In the past, most efforts have been dedicated to obtaining 3D capability [18–20], or improving the computational performance or localization precision by the choice of localization algorithms.

Localization microscopy is a data intensive methodology. Typical data sets contain tens of thousands of raw camera frames, and can contain tens of thousands to millions of unique particle localizations. Localization algorithms are important with regard processing speed, localization accuracy, and robustness. Techniques such as the fluoroBancroft algorithm [21, 22], quickPALM [23], radial symmetry methods [24], and

compressed sensing [25] all perform localization estimations without numerical data fitting. While they are inherently faster than conventional data fitting algorithms, they sacrifice localization accuracy for increases in computational speed. With regard to data fitting algorithms, traditional nonlinear least-squares is the most common algorithm. Methods such as maximum likelihood [26, 27] and K-factor filtering combined with traditional least-squares methodologies [28] produce more accurate results than traditional least-squares fitting.

Numerous studies and papers have focused on small improvements in localization ability for a given algorithm, or improvements in speed by employing graphical processor algorithms, or attempts to fit to multiply over-lapping PSFs [29, 30]. All of these methods, however, have one thing in common: the in-plane localization precision is limited to $\sigma / \sqrt{N}$ in a background free environment [31], where σ is the standard deviation of the PSF and N is the number of detected photons. This limit is the best precision one can hope to obtain given the PSF distribution and does not depend on choice of localization algorithm and instrumentation used.

This chapter will investigate a method to fundamentally improve upon this basic limit. It will demonstrate that a grating interferometer system in the detection path can be used to generate self-interference within the PSF in the real image plane, producing a modulated PSF in both scanning and wide-field modes. The modulation leads to fundamental improvement in localization, beyond the $\sigma / \sqrt{N}$ theoretical limit for the case of a Gaussian-like PSF. This approach is given the name PSF Self Interference, or PSI.

4.1 Theoretical Concept

The fundamental idea is to modify the detection PSF by utilizing self-interference within the PSF. instead of a conventional Gaussian distribution, the PSF will be modified along the axis of the interferometer. In this conception, the interferometer splits the emission along the x-axis. This modulation of the PSF changes the statistical nature of the localization procedure, allowing for a more precise localization for a given photon distribution when compared to conventional methods, as will be discussed below. A detailed look at the grating system in the detection path can be seen in Figure 4.1(a).

Light traveling through the first grating will split into two paths and then be reflected by the mirrors and combined using the second grating. The result is an interference pattern with a period that depends on the angle between the two beams when they recombine. When a point scatterer is imaged onto the second grating, the point-spread function (PSF) will self-interfere. When the pattern is imaged onto a camera, the signal profile along the horizontal (x) direction is given by [32]

$$q(x) = \text{PSF}(x) \cdot \left| 1 + \gamma \cos\left(\omega x + \phi\right) \right|, \tag{4.1}$$

γ is the fringe visibility, ω is the fringe frequency value, and ϕ is the phase value. The result is a modulated PSF shown by the green curve in Figure 4.1(b).

To determine the improvement in the localization ability, the Cramér-Rao lower-bound (CRLB) and the Fisher information matrix can be utilized to calculate the theoretical limit for localization precision in the case of PSI. These are discussed below.

4.2 Localization Ability and the Fisher Information Matrix

This section will discuss the use of the Fisher Information and its role in estimating the precision for which a parameter may be estimated with regard to a given statistical distribution. Due to the fact that the emission of photons by a source is stochastic in nature, the data collected by the detector are as well. This implies that the coordinates of the detected photons on the face of the detector are independent and identically distributed according to the density function $q(x, y)$. The estimation of the position of a single point-source is determined from the experimental data, namely the coordinates on the camera in which the signal photons are recorded. Since the process of emission and detection is a stochastic process as stated above, the estimation of the source becomes a statistical problem. If the underlying density function is known, the localization accuracy may be calculated by the use of the Fisher information matrix [33].

In characterizing the fundamental uncertainty involved with localization microscopy, various imaging parameters, such as photon counts, background noise, and camera pixel size, must be considered. The underlying fundamentals, however, entail localizing a distribution to extract an uncertainty in the mean value of the distribution. The strength of the technique does not rely on particular localization algorithms or methodologies when fitting data to a theoretical model. Calculation of the Fisher information
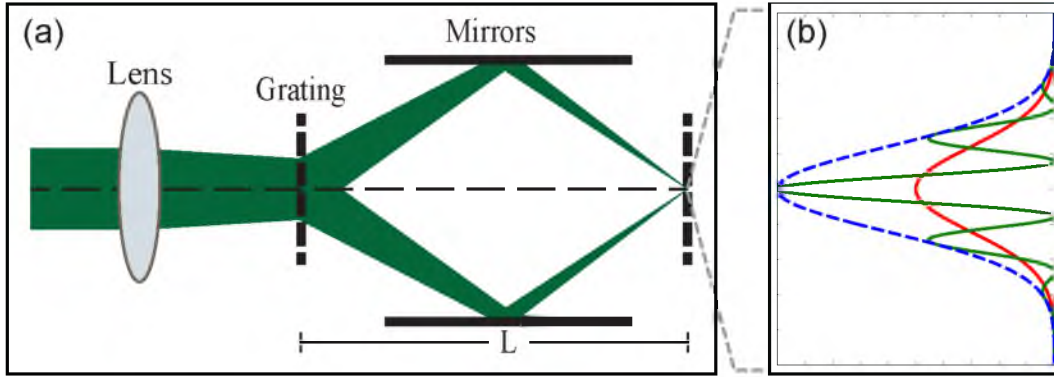
Figure 4.1. Concept of point-spread function self-interference (PSI). **(a)** PSI interferometer scheme. The lens focuses the signal onto the second grating. Splitting the beam into two and recombining it using the interferometer will impose a fringe pattern on the PSF at the second grating **(b)** Conventional Gaussian PSF (red) and PSI PSF (green). The PSI PSF is a result of the interference between the two interferometer arms. The dashed blue line shows the Gaussian envelope for PSI PSF.

matrix yields the fundamental limit of how well a particular distribution can be localized to give inherent information regarding the location of its source. In particular, the inverse of the Fisher information matrix, $I(\theta)$, provides a lower bound for the variance of an unbiased estimator, $\hat{\theta}$. More specifically, the Cramér-Rao lower bound, $\text{var}\left(\hat{\theta}\right) \geqslant I^{-1}$ [33]. If this fundamental lower bound can be calculated for a given photon distribution, then the localization limit can be derived for a particular distribution. This concept will be discussed below.

4.2.1 Derivation of the Fisher Information Matrix

For a given distribution $q(x, y)$, the Fisher information matrix may be calculated as:

$$I = N \int_{\Re^2} \frac{1}{q(x,y)} \left[\frac{\partial q(x,y)}{\partial x}, \frac{\partial q(x,y)}{\partial y} \right]^T \left[\frac{\partial q(x,y)}{\partial x}, \frac{\partial q(x,y)}{\partial y} \right] \mathrm{d}x \mathrm{d}y, \qquad (4.2)$$

where N is the number of detected photons. For a full derivation, see Appendix B. If the function $q(x, y)$ is symmetric, then the off-diagonal terms of the Fisher information matrix are zero. A generalized form of the localization accuracy, Δx, may be written as [33, 34]

$$\Delta x = \left[N \int_{\Re^2} \frac{1}{q(x,y)} \left(\frac{\partial q(x,y)}{\partial x} \right)^2 \mathrm{d}x \mathrm{d}y \right]^{-\frac{1}{2}}. \qquad (4.3)$$

The number of detected photons is the key variance in all single emitter localization schemes. When only the intensity is measured, the localization precision is inversely proportional to the square root of the number of detected photons [31, 33]. This is referred to as the Gaussian PSF case.

As can be seen from Equation 4.2, the Fisher information matrix depends on the square of the derivative of the function $q(x, y)$. Due to the spatial modulation in intensity of the modulated PSF, the value of the Fisher information matrix I is greater than for a conventional Gaussian case. Since the localization uncertainty is inversely proportional to the value of the Fisher information matrix, increasing the value of I has the effect of increasing the precision with which a given distribution may be localized. This is the effect of the interference modulation on the PSF — the PSF now has a larger area where there is a steep slope, thereby increasing the value of the Fisher information matrix.

The methods and analysis in this dissertation rely on the numerical calculation of the Fisher information matrix, which are further corroborated by Monte-Carlo simulations. However, a χ^2 analysis of the uncertainties associated with the fit parameters to a model function for a given distribution leads to the same result, that it is the areas of the function with the largest gradient that have the greatest contribution to the localization accuracy. For a detailed description, the reader is referred to reference [35].

Further information may be found in Appendix B, such as the derivation of the localization accuracy for the Airy and Gaussian[1] distributions, as well as methods for incorporating noise into the analysis.

4.3 Monte-Carlo Simulations

For an Airy or Gaussian distribution, Equation 4.2 may be calculated analytically. Due to the more complicated nature of the PSF in Equation 4.1, no analytical solution exits. However, for the given experimental parameters of γ, ω, and ϕ, the value of I may be numerically calculated. This serves as a theoretical lower-bound for the localization precision for given photon distribution in the modified PSF.

---

[1] Performing an analysis of the Fisher information matrix for a Gaussian distribution yields the familiar $\Delta x = \sigma / \sqrt{N}$, as expected.

The localization precision as a function of the number of detected photons and various values of N, for given values of γ, is shown in Figure 4.2, demonstrating that the localization precision in PSI is significantly better than that for conventional Gaussian localization. In order to corroborate the CRLB calculations, Monte-Carlo simulations were performed and compared to PSI and Gaussian localization analysis algorithms for a single emitter (details of the simulations are given in Section 4.3.1).

4.3.1   One-Dimensional Monte-Carlo Simulations

For the first set of simulations, localization error as a function of number of photons, two-dimensional figures were first generated, as shown in Figure 4.3(a), of a single emitter in random positions that were allowed to range within the central pixel on the camera. The generated figure for each emitter in the case of conventional imaging took a standard Gaussian shape, and for the case of PSI, it was a Gaussian multiplied by sinusoidal, corresponding to Equation 4.1. In this case, however, the modulation of the PSF by a sinusoidal function took place in both x and y. To simulate shot noise, measured pixel values were obtained by Poisson distribution of the integrated PSF shape over every pixel. Two thousand trials were run for each number of photons, N, and for the case of PSI the values for the fringe visibility were $\gamma = 1$ and $\gamma = 0.9$ (which corresponds to the experimental values obtained in these experiments) and fringe frequency of $\omega = 0.04$ nm^{-1}. For the simulations, a sample plane pixel size of 50 nm and objective NA of 1.0 were chosen.[2] In order to localize the point sources, a modified version of the nonlinear least-squares algorithm was used for the PSI frames, taking into account the fringe pattern. For the conventional Gaussian localization images, maximum likelihood was used since it performs better under most circumstances. The root-mean-square error, $\Delta x_{\mathrm{RMS}} = \sqrt{\langle (x_0 - \hat{x})^2 \rangle}$, was calculated, which for an unbiased estimation is the same as the localization precision [22].

The results for the uncertainty in localization accuracy along the x-axis, Δx, are shown in Figure 4.2. The localization error in the case of PSI is significantly lower, even when the fringe visibility is reduced to $\gamma = 0.9$. Comparing the simulation results to the

---

[2]This lower NA was chosen mainly due to the fact that the effective NA of the system was stopped down to avoid overfilling the transmission gratings in the interferometer.
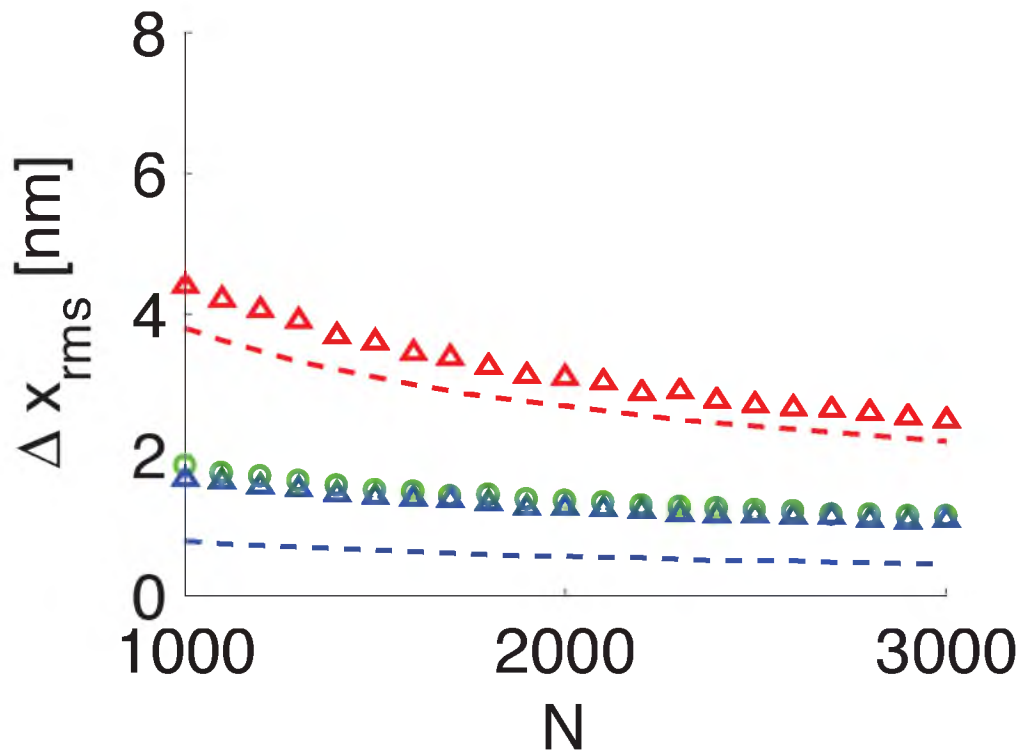
Figure 4.2. PSI Monte-Carlo simulations for localization precision versus signal photons. Simulation results for localization error of conventional Gaussian localization (red) and PSI (blue for $\gamma = 1$ and green for $\gamma = 0.9$) as a function of photon count. Dashed line: CRLB; triangles and circles: simulations.

CRLB curve for Gaussian localization shows that PSI outperforms conventional Gaussian localization regardless of the choice of localization algorithm for Gaussian localization, since the PSI Monte-Carlo simulation resulted in localization error that is below the theoretical limit of conventional Gaussian localization methods. The CRLB curve for PSI also shows that the nonlinear least-squares algorithm is not the optimal choice for this case, although it provided better results than a modified version of a maximum likelihood algorithm.

As a further step, the localization error as a function of background photons was investigated, as shown in Figure 4.4. According to these simulation results, PSI is less sensitive to background noise as shown by the smaller slope of the localization error versus background photons. In the case of PSI, the performance is barely affected by the presence of background photons. Quantitatively, PSI with $\gamma = 1$ has localization
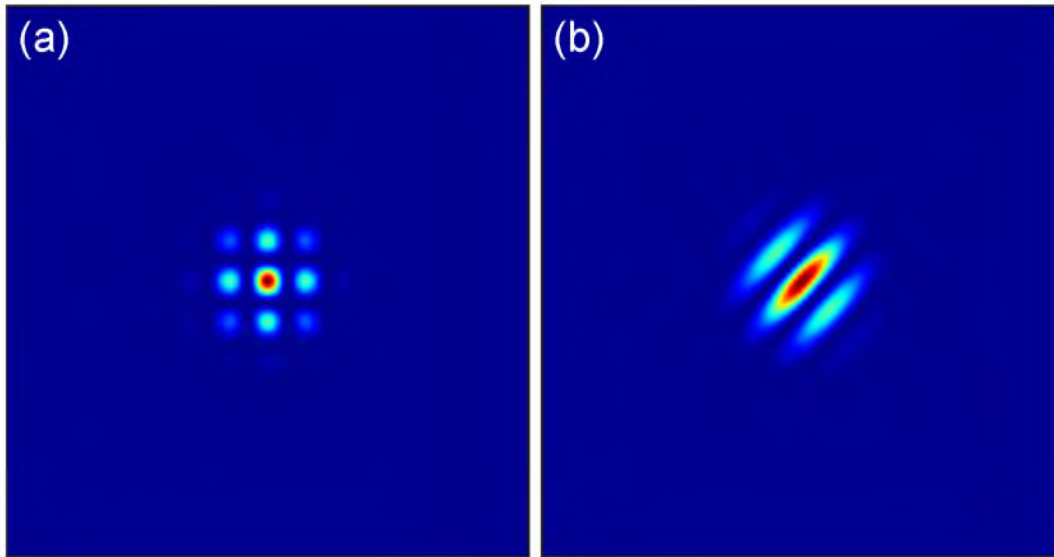
Figure 4.3. Modified PSFs for Monte-Carlo simulations. Example of a PSI PSF (simulated data). **(a)** Two-dimensional fringe pattern. **(b)** One-dimensional fringe pattern rotated at 45°. This rotated form is used in Section 4.3.2.

error that is 2.44 times lower than Gaussian localization with no background photons, where in the presence of 10 background photons per pixel, PSI outperforms Gaussian localization by a factor of 3.58.

Another important factor in PSI is the fringe visibility, which has a strong effect on performance. Results for simulations are given in Figure 4.5. The results compare the PSI localization error with the theoretical limit for Gaussian localization in the absence of background. The results indicate that even with the fringe visibility as low as 0.5, PSI gives better performance, up to a background count of 30 photons per pixel. With fringe visibility of 0.3, PSI no longer outperforms Gaussian localization, even with no background photons.

To simulate the influence of the background photons on localization error the same process was repeated, this time keeping the number of expected photons N constant (at 1000 signal photons over the PSF) while varying the number of background photons per pixel. Noise was introduced by sampling a Poisson distribution with an expectation value which corresponded to the integrated PSF shape for every pixel, including the added background value. To simulate the influence of fringe visibility, Monte-Carlo simulations with a constant N = 3000 were performed while changing the fringe visi-
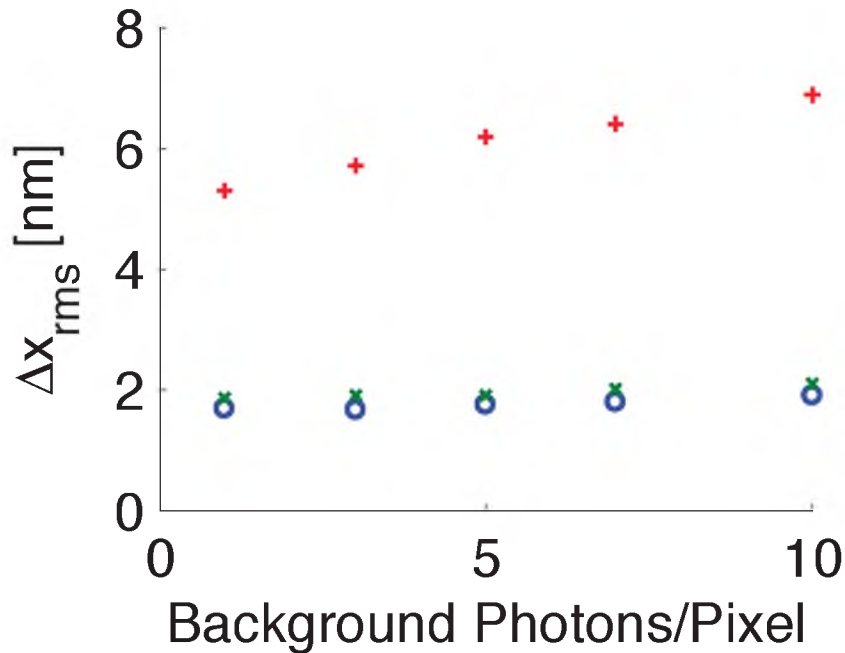
Figure 4.4. PSI Monte-Carlo simulations for localization precision versus background photons. Simulation results for localization error for Gaussian localization (red) and PSI (blue for $\gamma = 1$ and green for $\gamma = 0.9$) as a function of background photons, for $N = 1000$ signal photons.

bility between 0.3 and 1. Noise was introduced by the same method as before. These simulations were performed for different background values, and two thousand trials were used for each parameter combination.

4.3.2 Effect of Rotating the Interference Fringes by 45°

To produce localization improvement along both axes in the current configuration, the same setup may be used, but by rotating the orientation of the interference fringes by 45°. This can be obtained by rotating the first and last grating by 45°, and setting the mirrors to corresponding different heights.[3] These rotated fringes also improve the localization precision over Gaussian localization.

To analyze the performance of a one-dimensional fringe system with rotated fringes, similar Monte-Carlo simulations as those discussed above for one-dimensional PSI, but

---

[3]The gratings will diffract the emission parallel to the grating axis. Rotating the gratings then rotates the diffraction angle with respect to the optical table, since there is now a y component in the diffraction angle, i.e., $\alpha(x, y)$.
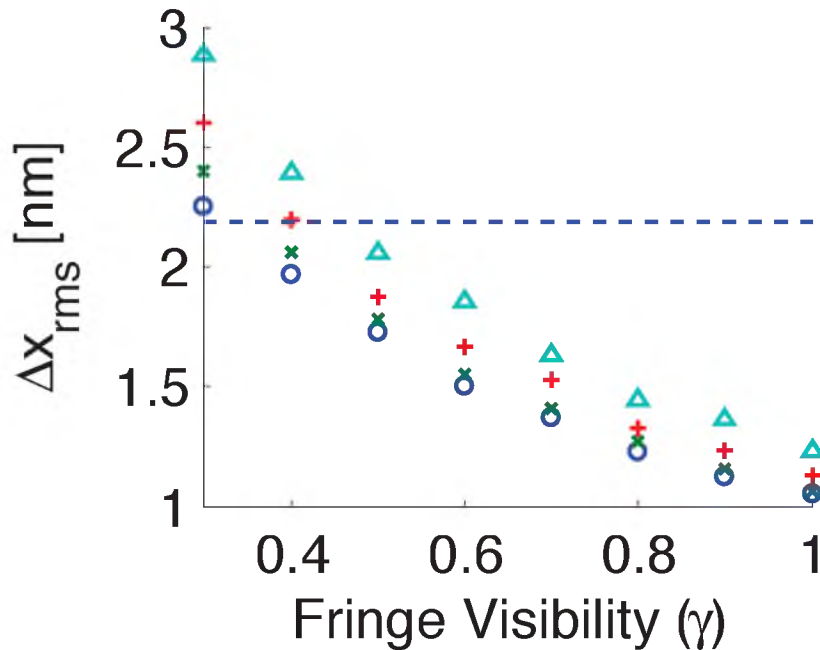
Figure 4.5. PSI Monte-Carlo simulations for localization precision versus fidelity. Theoretical limit for Gaussian localization (blue dashed line, no background photons) and simulation results for PSI as a function of fringe visibility (blue circle, green asterisk, red plus and cyan triangles for background values of 0, 10, 20, 30, respectively), for $N = 3000$ signal photons.

this time with a rotation angle of 45°, were performed. The PSF of this configuration can be seen in Figure 4.3(b). The simulation parameters were a photon count of $N = 1000$, γ equal to 0.9 and 1, and various background values. These obtained results were compared with 2D PSI and Gaussian localization, as seen in Figure 4.6. While the 2D PSI shows better performance, 1D PSI still outperforms conventional Gaussian localization and achieves localization precision better than the theoretical limit of $\sigma / \sqrt{N}$, even when the fringe visibility was $\gamma = 0.9$.

4.3.3 Monte-Carlo Simulations of Target Rings

As a final simulation, two target rings were used to generate a test pattern. The rings had a separation of 10 nm, and were 10 nm in width. Random positions on the target rings were stochastically generated, and convolved with the modified two-dimensional PSF shown in Figure 4.3(a). This image PSF was then localized, and the resulting uncertainty rendered as a Gaussian distribution, with standard deviation given by each
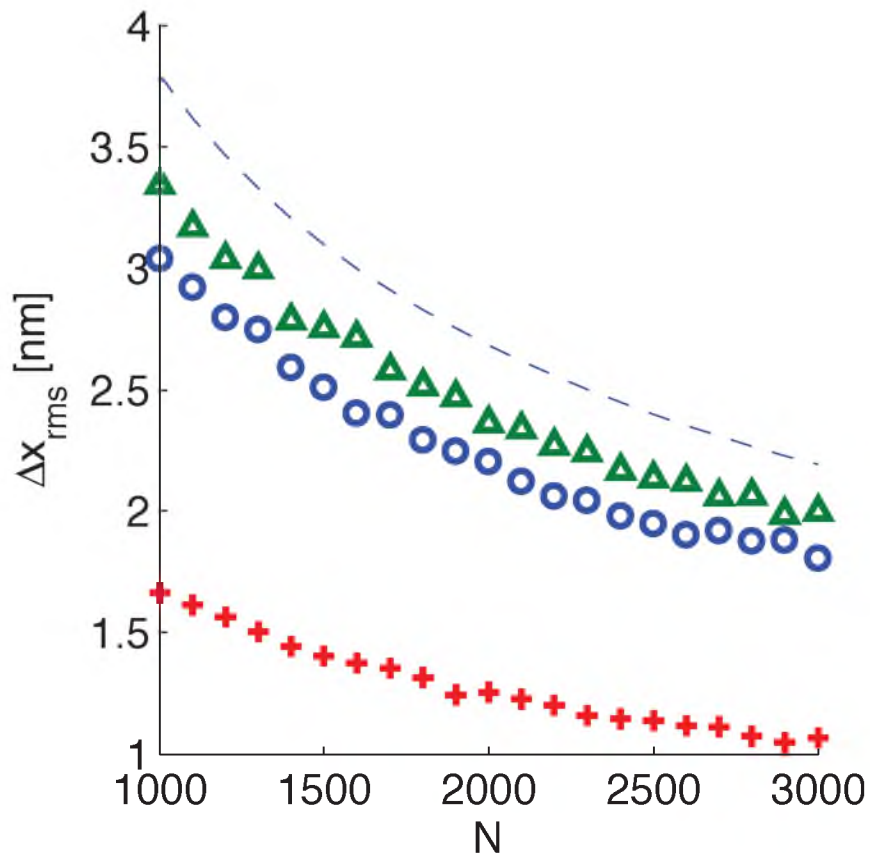
Figure 4.6. Monte-Carlo simulations for rotated 1D transmission gratings. Simulation results of the tilted fringes: Localization error as a function of number of photons, N. Dashed line: CRLB for Gaussian PSF. Green triangles and blue circles: Localization error for 1D fringes tilted at a 45° angle for $\gamma = 0.9$ and $\gamma = 1$ respectively. Red: Localization error for 2D fringes with $\gamma = 1$.

simulated particle's localization uncertainty. In these simulations, the photon yield of each source was $N = 1000$, γ was set to one, and ω was 0.04. The results can be seen in Figure 4.7. The conventional Gaussian localization is shown in part **(b)** of the figure, while the PSF case is shown in part **(c)**. The ring structure is barely discernible (if at all) in the conventional Gaussian localization case, while they are clearly visible in the case of a two-dimensional PSI.

4.4   Experimental Setup

To test experimentally the predicted improvement of localization precision for PSI, a custom microscope was designed. The optical layout used for the experiments can
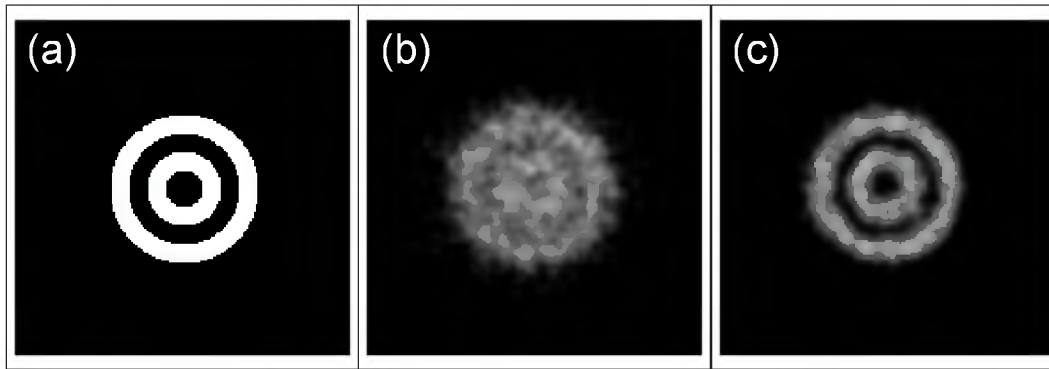
Figure 4.7. Monte-Carlo simulation of localization microscopy with a Gaussian PSF and PSI, the PSF self-interference. For this simulation, $N = 1000$ photons, and $\gamma = 1$, $\omega = 0.04$, and $\phi = 0$. **(a)** Simulated target. Separation between lines is 10 nm (Outer ring: outer radius is 40 nm, inner radius is 30 nm. Inner ring: outer radius is 20 nm, inner radius is 10 nm). **(b)** Simulation of conventional localization microscopy with a Gaussian PSF. The ring features are barely visible. **(c)** Simulation of localization microscopy with 2D PSI.

be seen in Figure 4.8. A more in-depth discussion of the optical layout and hardware of the microscope can be found in Appendix C. The system is designed in a scan/de-scan confocal configuration for fluorescence imaging with a single dual-axis scan mirror. The system has two detection paths controlled by a programmable flip mirror. One detection path directs the light onto an avalanche photo-diode (APD), and an image can be constructed as the scanning mirror directs the beam over the sample. The second detection path contains the interferometer, where a lens is positioned before the interferometer to form an imaging plane on the second grating. A lens relay system then reforms the image on the second grating onto an EMCCD camera, where this image now contains the fringe modulation over the emission PSFs. The overall magnification of the system is 400. Within the interferometer, custom manufactured transmission gratings were utilized, with a grating period of 5.97 μm, and an efficiency of 81% transmission to the ± 1 orders. The zero order is blocked, and the +1 and -1 orders self-interfere. The gratings are only along the x-axis, and were not rotated. The APD path provided a confocal mode image used to locate the nanoparticles. To form a wide field image, a lens was inserted, with the focal plane lying on the front surface of the scanning mirror, thus forming a focused spot on the back focal plane of the objective lens.

To validate this idea, gold nanoparticles were used as a scattering point source. The
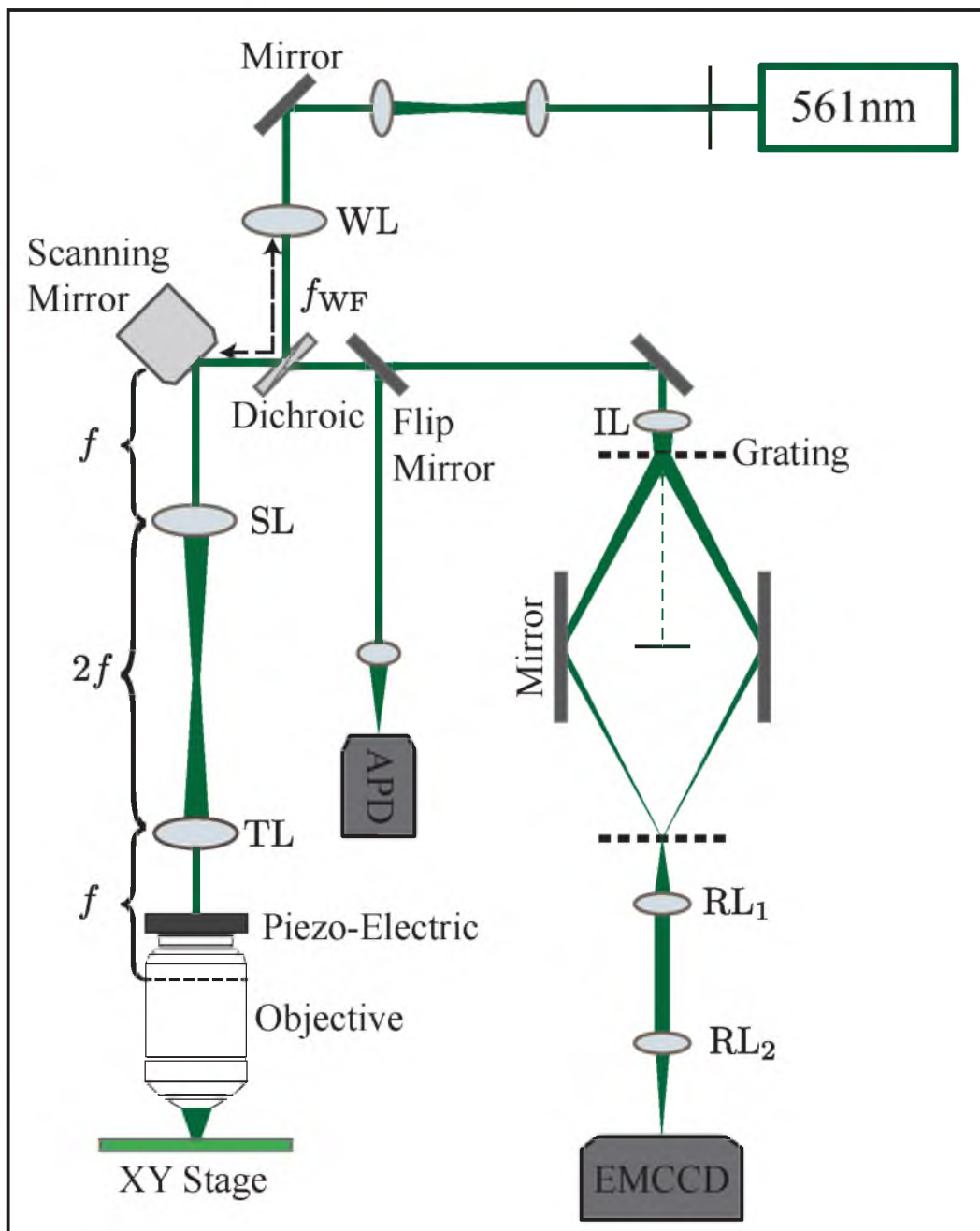
Figure 4.8. Schematic of experimental setup for modified PSF detection, with dual detection paths controlled by a flip mirror. Using the scanning mirror and APD allowed for conventional confocal scanning and imaging. The wide-field lens was introduced only to capture the wide-field image and was not used in most of the experiments. The primary image plane is formed on the second grating, which is relayed to the EMCCD. The overall magnification of the system is 400. WL = Wide-field lens. SL = Scan lens. TL = Tube lens. IL = Imaging lens. RL$_{1,2}$ = Relay lens 1,2.

gold nanoparticles will Rayleigh scatter the incident laser light, and a small percentage will leak through the dichroic, allowing for direct imaging on either the APD or EMCCD. Since the nanoparticles are sub-diffraction-limit in size, their image will appear as a diffraction-limited PSF, serving as a point-source. Since Rayleigh scattering is used to image, filtering the laser light to decrease background is not possible. In typical imaging configuration, the sample will be placed upon a glass coverslip, which is placed between the objective and sample. If there is any index of refraction mismatch as the light propagates through the objective into the sample, this will cause reflection governed by the Fresnel coefficients. For a glass-air interface, this will lead to a 4% backscatter of the incident laser light, which can be orders of magnitude larger than the emission signal.

Instead, the gold nanoparticles were imaged such that no index of refraction mismatch occurred until millimeters past the focal plane. To do so, a drop of 60 nm gold nanoparticles suspended in ethanol was deposited on a glass coverslip and left to dry. Immersion oil was then added as the surrounding medium to ensure index matching and the coverslip was covered with a glass slide. The top surface of the glass slide was painted black. An illustration of this experimental sample preparation is illustrated in Figure 4.9. When imaging in wide-field mode the same process was used but with the exception of avoided painting the slide in black, since a trans-illumination LED was used to find the nanoparticles to image onto the EMCCD.

4.5 Experimental Results

To characterize the localization improvement, a single gold nanoparticle 60 nm in diameter was imaged by focusing the excitation beam on the nanoparticle and recording the PSI pattern from the scattered light on the EMCCD. The recorded modified PSF may be seen in Figure 4.10(a). The recorded image was then projected onto the x and y axis, by summing of the columns and rows, respectively, where the x projection showed the fringe pattern and the y projection showed the standard Airy pattern, as seen in Figure 4.10(b). This allows for the direct comparison between PSI and Gaussian localization for the exact same conditions and number of photons. For all our experiments the aperture of the objective was stepped down to effective NA of 0.7 in order to prevent clipping of the signal on the gratings.
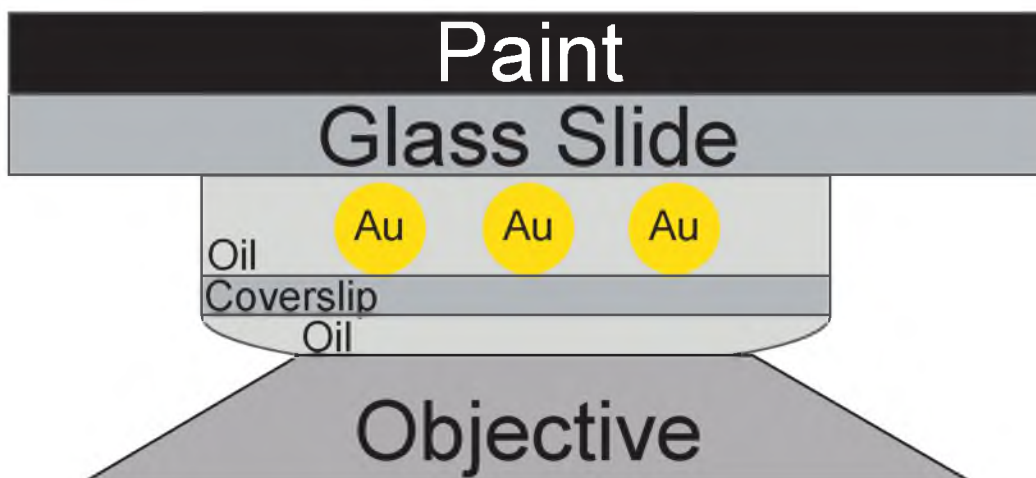
Figure 4.9. Gold nanoparticle sample preparation. The 60 nm gold nanoparticles are immobilized on a glass coverslip by evaporating the gold nanoparticles suspended in ethanol solution onto the glass coverslip. The coverslip is then coated in immersion oil, with the index of the immersion oil matching that of the glass coverslip. A glass slide is placed on top of the nanoparticles and immersion oil, and the coverslip sealed to the coverslip. Since there is no change in the index of refraction, there is no reflection of the incident laser due to index of refraction mismatch between optical mediums, and the signal received at the optical detector is primarily due to the scattering of the incident laser light from the gold nanoparticles. The glass slides are finally coated in black paint to further reduce background reflections, due to the index of refraction mismatch between the glass slide and air.

For the measurement of the localization precision of the system, the APD was used to first find a gold nanoparticle. The gold nanoparticles were then imaged onto the EMCCD camera to capture 100 frames with an integration time of 15 ms per frame. Each frame was reduced to x and y projections by summing the rows and columns of the frame, and the nanoparticle was localized. The localization along the y axis used a nonlinear least-squares localization algorithm for a conventional Gaussian PSF. For the PSI PSF, a modified version of the algorithm was employed, altered in this instance to fit to the PSI PSF model. To find the initial parameters for the nanoparticle position and standard deviation of the modified PSF, a conventional Gaussian fitting of the PSF was performed. These values were fed to the modified nonlinear least-squares algorithm localization for the modified PSI shape. This procedure then allowed for plotting the localized position in both x and y versus camera frame number. The results of this may be see in Figure 4.11.
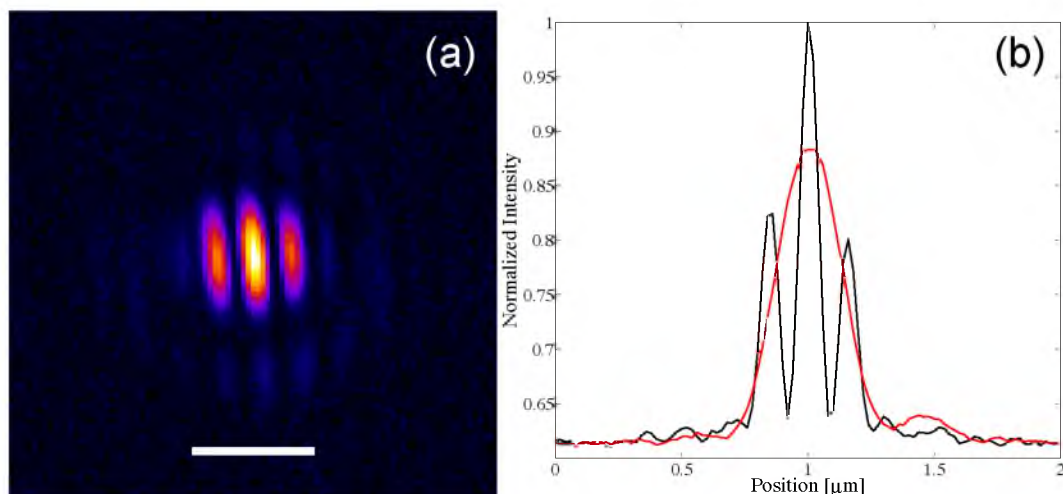
Figure 4.10. Experimentally recorded PSI. **(a)**The recorded PSI pattern from a single gold nanoparticle as seen on an EMCCD camera. As the reader can see, the fringes are easily visible. Scale bar: 0.5 μm. **(b)** Projection of the fringe pattern on the x-axis (black) and the y-axis (red) by summing the columns and rows of the recorded image, respectively. Since the modulation is one dimension only, a single bead gives both a conventional Gaussian distribution (along the y-axis) and a modified PSF (along the x-axis). This is especially useful when comparing the performance of the modified versus the conventional Gaussian cases, since it is the same bead, and hence the same signal photons, being compared against itself.

As can be seen from Figure 4.11, drift occurred in x and y, where the drift in x was oscillatory in nature. This could be due to mechanical vibrations from the equipment platform above the optical table, which could transfer vibrations to the gratings. These grating vibrations would only affect the results in x since the fringes are only along the x axis. To account for drift in the system, these results were fit to a fourth-degree polynomial and this trend line was then subtracted from the results. After this procedure, the standard deviation of localization may be calculated. As can be seen in Figure 4.11(a) and Figure 4.11(c) the drift correction for the x coordinate did not entirely account for the oscillatory behavior of this drift; therefore only part of the total data set (40 frames) was used and applied to the same correction after fitting to a fourth-degree polynomial trend line. The results of this procedure may be seen in Figure 4.11(b) and Figure 4.11(d).

Figure 4.12(a) and (b) show the histogram of extracted positions for the nanoparticle in y and x, respectively, for the full data set of 100 frames. Using only a subset of 40 frames, with the same drift correction, yields the results shown in Figure 4.12(c) and (d), for y and x, respectively.
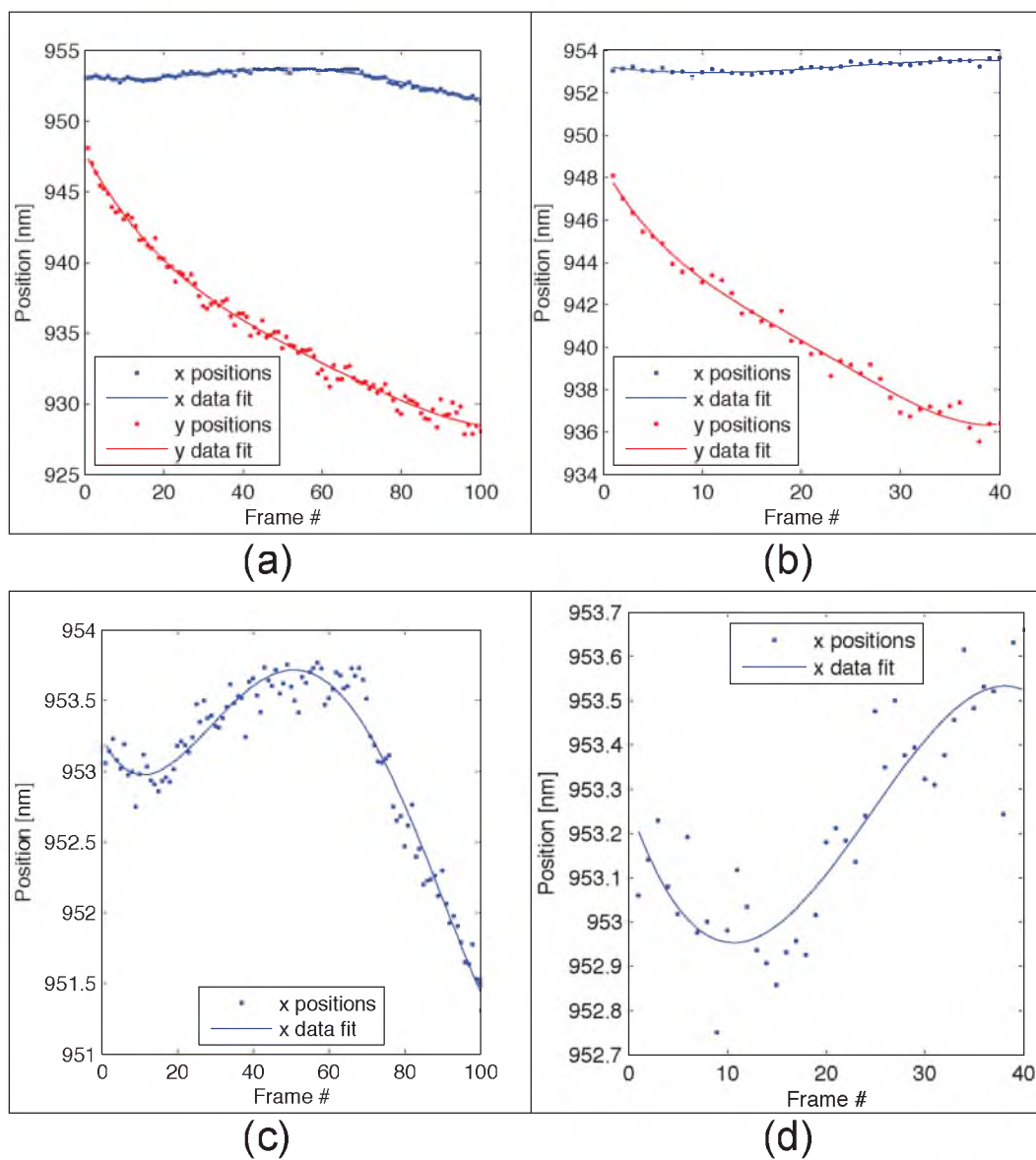
Figure 4.11. Localization results of a single stationary nanoparticle. Position in x (blue) and y (red) for **(a)** each of the 100 frames and **(b)** 40 frames out of the full data set for better fitting and drift correction. Dots: data. Solid line: fourth-degree polynomial fitting used for drift correction. **(c)** 100 frames and **(d)** 40 frames of just the x coordinate plotted on a different scale. The oscillatory behavior of the drift can be seen here.
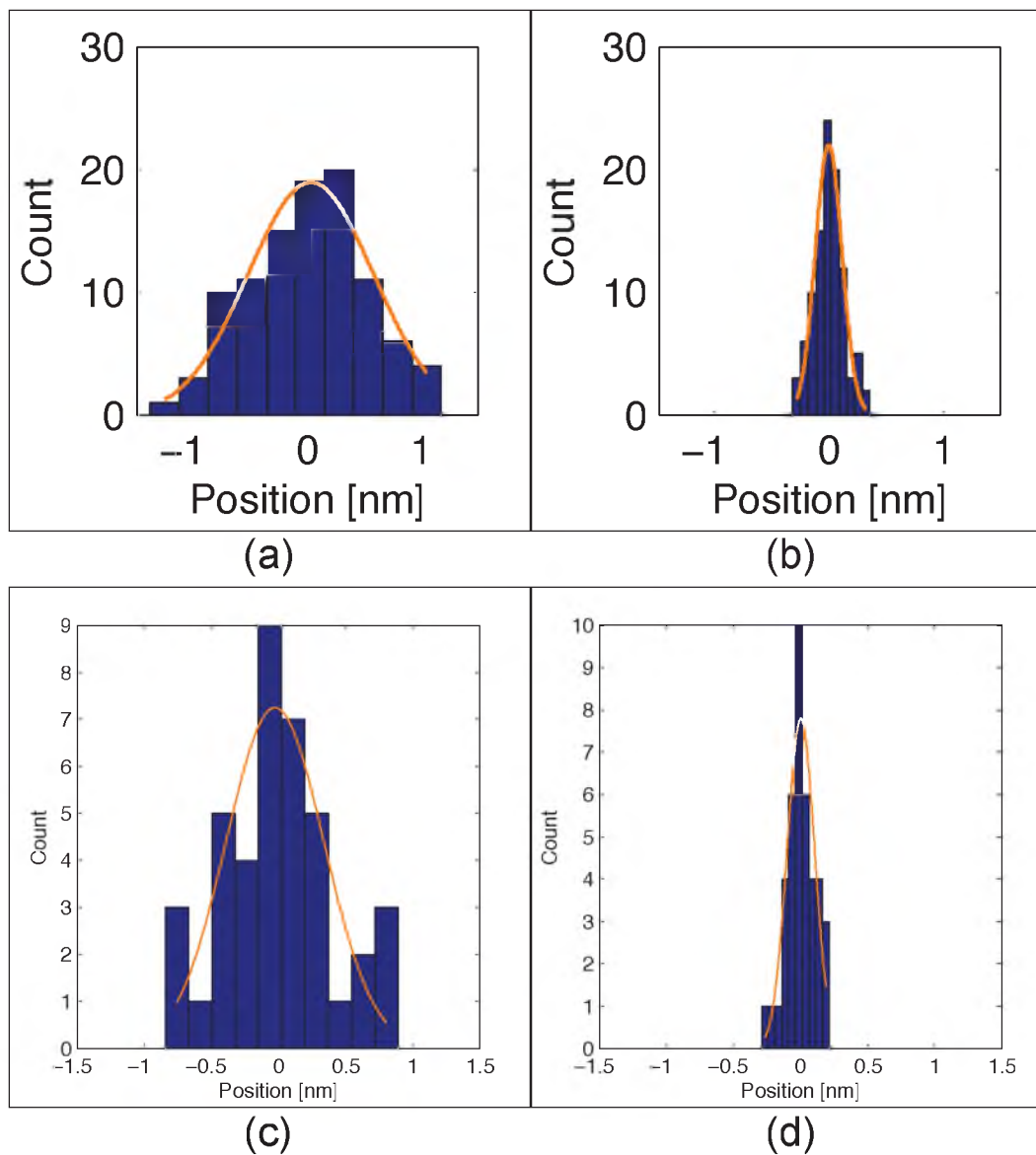
Figure 4.12. Histogram of positions of Au nanoparticle in y **(a)** and x **(b)** after drift correction. Histogram of positions in y **(c)** and x **(d)**, for drift correction of 40 frames out of the full data set.

Figure 4.13 shows the distribution of localizations for both the full data set, (a), and the partial data set, (b). Calculating the standard deviation of localization over the full data set results in localization precision of 0.52 nm in y and 0.13 nm in x. By looking only at 40 successive frames in the middle of the 100 frames, better drift correction was obtained, and hence better localization results. For the partial data set, the calculated standard deviation is 0.42 nm in y and 0.11 nm in x. Due to the large scattering signal
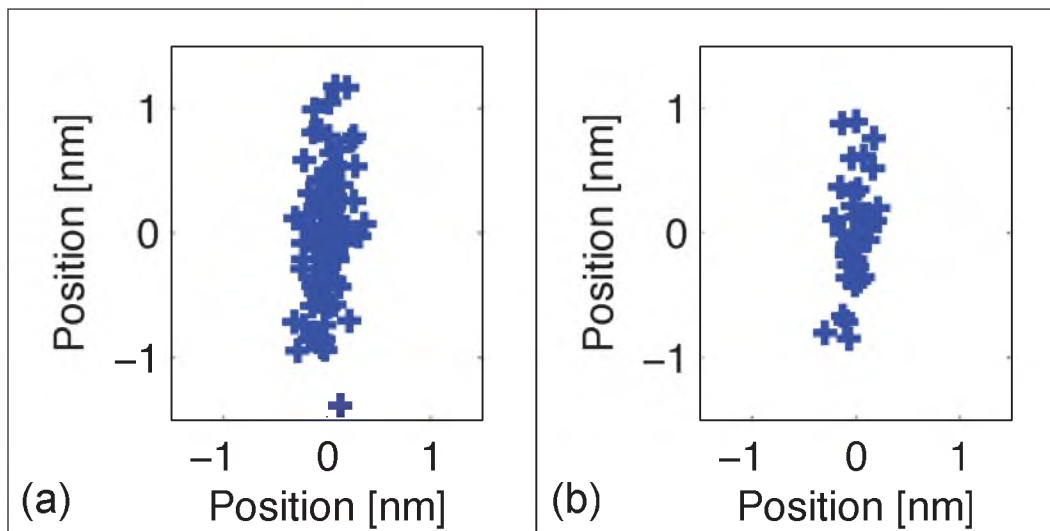
Figure 4.13. Distributions of localization results of single Au nanoparticle. **(a)** Distribution of fitted positions for the full 100 frames. **(b)** Distribution of fitted positions for a partial data set with improved drift correction.

from the gold nanoparticles, the limiting factor in localization is the signal to background ratio [31].

Using the APD to validate these finding, the signal photon count and the average background photon count were calculated. Calculating the localization precision limit in that case of data from a conventional imaging system, as well as the theoretical limit for Gaussian localization is ≈0.35 nm, in agreement with the experimental results. This indicates that PSI can suppress this theoretical limit of conventional localization methodologies.

4.5.1 Particle Tracking and Wide-field Imaging

To confirm the applicability of the method to particle tracking the scanning mirror was used to scan the excitation laser in a predetermined pattern around a stationary nanoparticle, since the position accuracy of the mirror (6 nm) is better than the stage scanning (50 nm). At each position of the mirror, a single image captured on the EM-CCD gives PSI pattern of a particular scatterer on the camera, and thus contains all the information needed to localize the nanoparticle. The nanoparticle is then localized in each frame. The localized position of the nanoparticle with respect to predetermined positions of the mirror were compared, and and the two obtained shapes were aligned

using the center of mass of coordinates. The results are shown in Figure 4.14(a), where the discrepancy between the expected position (i.e., the position set for the mirror) and the estimated position is dominated by the positioning accuracy of the mirror, which is 6 nm. In the case of the tracking experiment, it was expected that the position for the two vertical lines to be the same for all mirror positions along the vertical line. However, there was a slight error causing a diagonal line instead of a straight line. Also observed is a slight phase mismatch in the localization results, possibly due to slight sample tilt. By using this changing phase values, it was possible to correct the results by shifting the extracted position proportionally to the obtained phase value.

In many applications, such as super-resolution and particle tracking, wide-field operation mode, rather than scanning mode, has numerous benefits, including the ability to track multiple emitters, ease of finding a single emitter within the field of view, larger field of view etc. By inserting a lens which focuses the excitation beam on the back focal plane of the objective, and directing the light towards the grating, it is possible to obtain the fringe pattern in a wide-field image, as shown in Figure 4.14(b). In this image PSI PSFs are shown. One hundred such images were recorded and the nanoparticle was localized while applying drift correction as before, after subtracting a background image from each captured frame. After this, the standard deviation of localization for the two emitters were calculated, resulting in localization precision of 0.12 nm and 0.19 nm in x for the left and right nanoparticles, respectively.

4.6 Conclusions

This chapter showed that localization precision of single emitters can go beyond the theoretical limit for a Gaussian-like PSF, by a simple system modification. The results were obtained for a microscope designed primarily for fluorescence imaging, and although inefficient in gold nanoparticle detection,[4] can obtain 0.1 nm or higher localization precision. This method is most suited for single nanoparticle localization studies, for example nanoparticle tracking in biological systems. Recently, a few attempts

---

[4]The system is primarily designed for fluorescence imaging, and the detected signal, either on the APD or the EMCCD, is low due to the dichroic. For this particular dichroic, less than 1% passes through the dichroic. Changing this optic for a 50/50 beamsplitter, for example, would greatly improve detection signal.
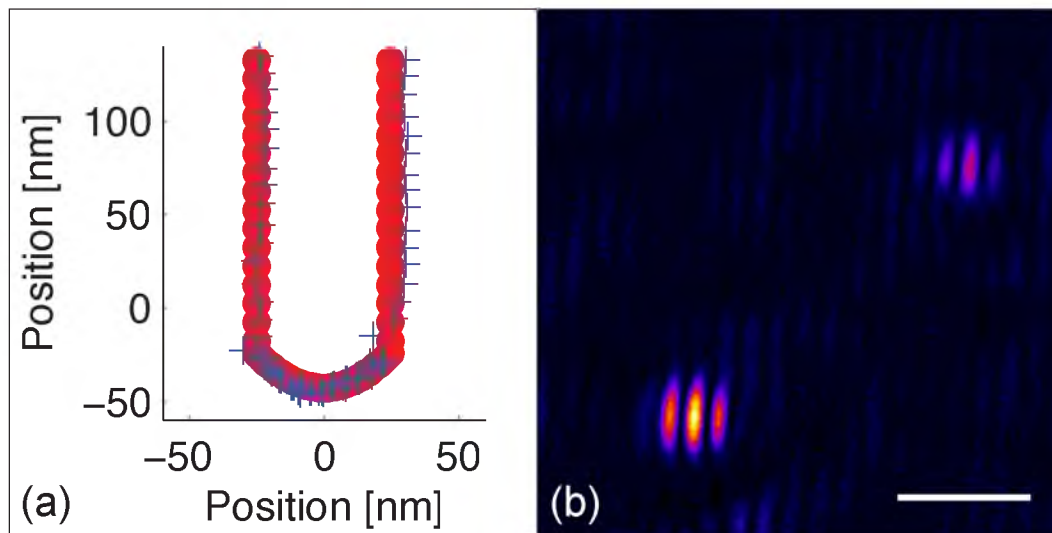
Figure 4.14. Particle tracking and wide-field image. **(a)** Particle tracking results. Red dots: Programmed scan pattern. Blue crosses: Extracted results. **(b)** Image of two gold nanoparticles in wide-field mode. Both nanoparticles can be seen to have a modified PSF. Scale bar: 0.5 μm.

were made to obtain super-resolution using metal nanoparticles (e.g., by Brownian motion sampling [36]). Although these ideas did not mature yet to nanoparticle based nanoscopy modality, PSI can obtain higher resolution in future implementations.

This method is especially applicable in high background imaging conditions, where the background impact on localization precision is smaller than Gaussian localization. This effect is demonstrated by looking at scattering of nanoparticles in brightfield mode, where partial background suppression was obtained by black paint. This shows that a special instrumentation is not required in order to obtain subnanometer localization precision, and even fluorescence microscope, while usually not adapted to imaging scattering samples, can be used to obtain subnanometer localization precision.

Another application of this method is drift correction where fluorescence super-resolution imaging and particle tracking [2–5, 8] are more appropriate. Since nanometer resolution (in certain cases [5], the localization precision is 1.5 nm) is required, drift correction with precision of 0.5 nm is not suitable, and 0.1 nm precision may be helpful. By using the metal nanoparticle as markers, sample drift can be more accurately accounted for and higher localization results can be obtained overall.

4.7 References

[1] N. G. Walter, C.-Y. Huang, A. J. Manzo, and M. A. Sobhy, Nature Methods **5**, 475 (2008).

[2] E. Betzig et al., Science (New York, NY) **313**, 1642 (2006).

[3] S. T. Hess, T. P. K. Girirajan, and M. D. Mason, **91**, 4258 (2006).

[4] M. J. Rust, M. Bates, and X. Zhuang, Nature Methods **3**, 793 (2006).

[5] A. Yildiz et al., Science (New York, NY) **300**, 2061 (2003).

[6] L. S. Churchman, Z. Okten, R. S. Rock, J. F. Dawson, and J. A. Spudich, Proceedings of the National Academy of Sciences of the United States of America **102**, 1419 (2005).

[7] J. Gelles, B. J. Schnapp, and M. P. Sheetz, Nature **331**, 450 (1988).

[8] A. Yildiz, M. Tomishige, R. D. Vale, and P. R. Selvin, Science (New York, NY) **303**, 676 (2004).

[9] X. Michalet et al., Science (New York, NY) **307**, 538 (2005).

[10] E. C. Arnspang, J. R. Brewer, and B. C. Lagerholm, PloS One **7**, e48521 (2012).

[11] S. Ram, P. Prabhat, J. Chao, E. S. Ward, and R. J. Ober, **95**, 6025 (2008).

[12] M. Lindner et al., Physical Review E **83**, 011916 (2011).

[13] R. Yasuda, H. Noji, M. Yoshida, K. Kinosita, and H. Itoh, Nature **410**, 898 (2001).

[14] A. R. Dunn and J. A. Spudich, Nature Structural & Molecular Biology **14**, 246 (2007).

[15] X. Nan, P. A. Sims, and X. S. Xie, Chemphyschem: A European Journal of Chemical Physics and Physical Chemistry **9**, 707 (2008).

[16] D. Lasne et al., **91**, 4598 (2006).

[17] H. Ueno et al., **98**, 2014 (2010).

[18] M. Badieirostami, M. D. Lew, M. A. Thompson, and W. E. Moerner, Applied Physics Letters **97**, 161103 (2010).

[19] S. R. P. Pavani and R. Piestun, Optics Express **16**, 22048 (2008).

[20] B. Huang, W. Wang, M. Bates, and X. Zhuang, Science (New York, NY) **319**, 810 (2008).

[21] S. B. Andersson, Optics Express **16**, 18714 (2008).

[22] Z. Shen and S. B. Andersson, Bias and Precision of the fluoroBancroft Algorithm for Single Particle Localization in Fluorescence Microscopy, 2011.

[23] R. Henriques et al., Nature Methods **7**, 339 (2010).

[24] R. Parthasarathy, Nature Methods (2012).

[25] L. Zhu, W. Zhang, D. Elnatan, and B. Huang, Nature Methods **9**, 721 (2012).

[26] C. S. Smith, N. Joseph, B. Rieger, and K. A. Lidke, Nature Methods **7**, 373 (2010).

[27] A. V. Abraham, S. Ram, J. Chao, E. S. Ward, and R. J. Ober, Optics Express **17**, 23352 (2009).

[28] T. Ilovitsh et al., Biomedical Optics Express **5**, 244 (2013).

[29] F. Huang, S. L. Schwartz, J. M. Byars, and K. A. Lidke, Biomedical Optics Express **2**, 1377 (2011).

[30] E. Mukamel, H. Babcock, and X. Zhuang, **102**, 2391 (2012).

[31] R. Thompson, D. Larson, and W. Webb, **82**, 2775 (2002).

[32] B. J. Thompson and E. Wolf, Journal of the Optical Society of America **47**, 895 (1957).

[33] R. J. Ober, S. Ram, and E. S. Ward, **86**, 1185 (2004).

[34] S. M. Kay, *Fundamentals of Statistical Signal Processing: Estimation Theory*, Prentice Hall, Upper Saddle River, NJ, 1993.

[35] L. Novotny and B. Hecht, *Principles of Nano-Optics*, Cambridge University Press, Cambridge, 1st edition, 2006.

[36] A. Gur, D. Fixler, V. Micó, J. García, and Z. Zalevsky, Optics Express **18**, 22222 (2010).

CHAPTER 5

INCREASED LOCALIZATION PRECISION BY
INTERFERENCE FRINGE ANALYSIS

With the modifications to the imaging system, as introduced in Chapter 4, a substantial improvement in localization ability can be achieved with a localization-based microscope. This chapter will propose another methodology that is able to overcome the conventional $\sigma/\sqrt{N}$ limit of conventional localization schemes. Unlike the imaging method presented in Chapter 4, the method presented here is based upon a scanning system, and measures not in the image plane, but in the Fourier plane.

5.1 Motivation

Conventional single particle localization [1] uses the Airy disk profile of imaged sparse single emitters to find the exact position of optical markers, and has been thoroughly discussed throughout this thesis. This chapter demonstrates an alternative to conventional localization approaches, one that involves measuring a relative phase acquired by the emitted photons through the detection interferometer, in addition to the count rate. While instruments have been designed to utilize interference [2, 3] to increase localization precision in the axial direction, those methods rely on intensity differences between optical channels to record interference effects. Several techniques modified the shape of the emitted signal to obtain precise axial position of an emitter. However, all these techniques were limited by the same theoretical limit of $\sigma/\sqrt{N}$ for the in-plane localization precision. This technique directly measures the interference fringes of the image in the Fourier plane to determine the position of a particle in the sample plane.

What is also demonstrated in this chapter is that by using the acquired phase, the theoretical limit for localization precision can be fundamentally smaller than $\sigma/\sqrt{N}$, even when viewing the Fourier plane instead of the image plane. This method has the advantage of allowing for much faster imaging or being able to image dimmer sources

with the same precision. This also was the case in the last chapter, but this method also has the ability to drastically speed up the data acquisition rate of scanning systems by reducing the sampling pixels needed to localize a single particle. Theoretical analysis through Monte-Carlo simulations were performed to validate these ideas, which were subsequently confirmed by experiment. The microscope was slightly modified from the layout discussed in both Chapter 4 and Appendix C, but still utilized the interferometer. The layout change will be discussed below. The design in this chapter is a system solely based upon a confocal design, and was used to experimentally localized the center of metal nanoparticles with a precision (standard deviation) as small as 3 nm. This Fourier-Interference-Localization Microscopy (FILM) principle is readily applied to any scanning-beam system, and is particularly useful in particle tracking.

5.2   Theory of Fourier Imaging

A lens performs an optical Fourier transform between the front and back focal positions of the lens, as is shown in Figure 5.1. In the language of Fourier relationships, the spatial location and the angular propagation of the emission beam in the Fourier plane are conjugate pairs. The relationship, in the one-dimensional case along the x-axis, is given by $F\{g(x - x_0)\} = G(\mu_x)e^{-2\pi i \mu_x x_0}$, where $\mu_x = x/\lambda f$, x_0 is the spatial location of a source in the sample plane, λ is the wavelength, f is the focal length of the lens, and F denotes the Fourier transform. The geometrical relationship between the location of a source in the sample plane, x_0, and the focal length of the objective, is given by $\sin\beta = x_0/f$. These relationships can be inserted into Fourier relationship, and written as

$$F\{g(x - x_0)\} = G(\mu_x)e^{-2\pi i \frac{x}{\lambda f} x_0} = G(\mu_x)e^{-kx\sin\beta}. \tag{5.1}$$

The focal length of the Zeiss objective used in the experiments is ≈ 2.5 mm. For a point-source located very close to the optical axis, for instance below the diffraction limit, the small angle approximation holds, and $\sin\beta \approx \beta$. Thus, a spatial offset in the sample plane is converted to an angular inclination to the optical axis in the Fourier plane by a lens. This is the principle behind a $4f$ scanning system, as is further discussed in Appendix C, Section C.2.1.
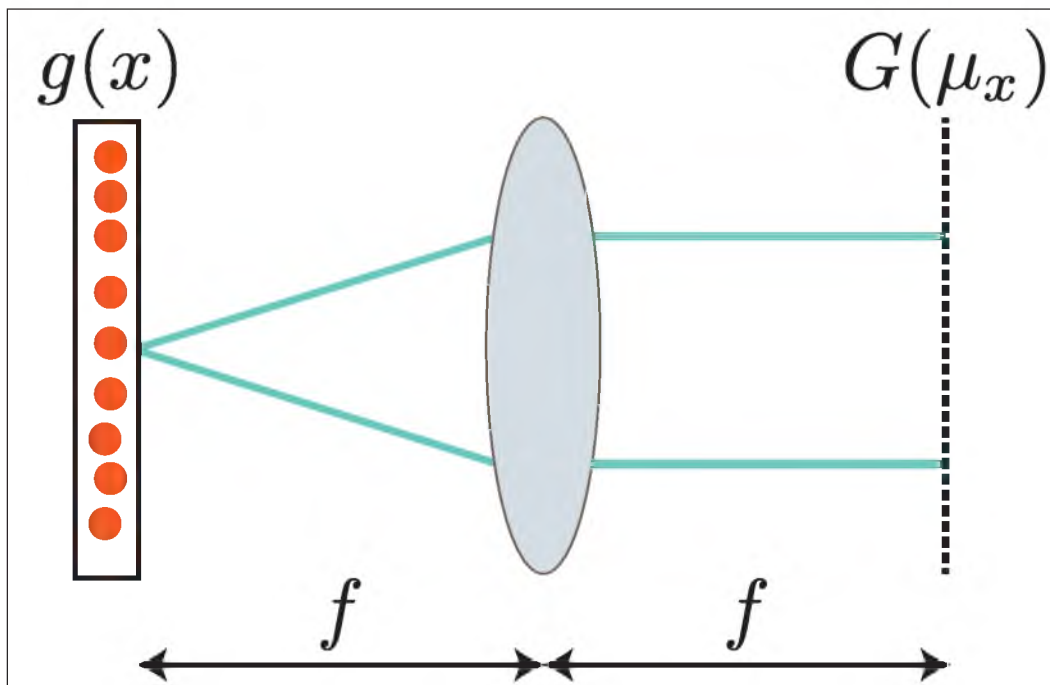
Figure 5.1. Cartoon illustrating how a lens performs a Fourier transform on a signal. The spatial plane is denoted as $g(x)$, and the Fourier plane as $G(\mu_x)$. The two planes are located at the front and back focal planes of the lens, respectively.

5.2.1 Use of Transmission Gratings in Fourier Imaging

Consider the schematic of a point-scanning imaging system shown in Figure 5.2. Photons that are emitted from a point source exactly on the optical axis will emerge propagating parallel to the optical axis after an infinity corrected microscope objective. On the other hand, if the point source were positioned off-axis, the photons would propagate at an angle to the optical axis, as indicated by the angle β from above. The propagation angle from the optical axis is proportional to the off-axis displacement of the point source, depending on the focal lengths of the lenses used in the imaging system. This angular propagation may be taken advantage of by the introduction of the transmission grating interferometer into the detection path, as was discussed in Chapter 4. The key difference between this design and that from Chapter 4 is that in this instance, the interference occurs at the Fourier plane, and not the image plane. The interferometer allows the Fourier signal to self-interfere, leading to an interference pattern on a detector placed directly at the interferometer output. The phase difference between the two arms of the interferometer depends very sensitively on the input angle
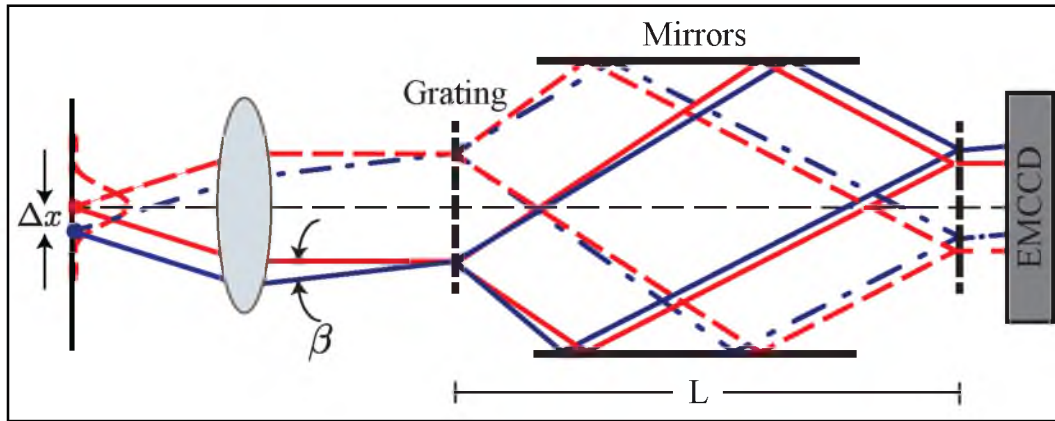
Figure 5.2. Schematic of the interferometric-based FILM. Two sources are shown in the image plane, whose Fourier transform is relayed onto the diffraction grating by the lens. Due to the Fourier transform of the lens, a spatial off-set from the optical axis results in an angular off-set into the interferometer system. Thus, the off-axis source emits photons that acquire a different phase on their individual path to the detector when compared to those from an on-axis source. By allowing each photon to interfere in the grating-mirror interferometer and capturing the interference patterns on a CCD camera, it is possible to extract the relative phase of the photons and therefore and increase the localization precision of each emitter through the use of a phase-analysis of the recorded signal.

into the interferometer, which directly maps to a lateral position in the sample plane. This interference pattern directly relates to the particle's position in the sample plane, as will be demonstrated below.

The phase gratings (for further information on their design, see Appendix D) are manufactured such that light incident along the optical axis diffracts light an angle α. Figure 5.3 shows a detailed look at monochromatic light incident on the grating, which happens to be incident at some angle β onto the grating, due to the source lying on some off-axial point in the sample plane. For light incident at angle β, the light diffracting to the bottom mirror (Path 1) will leave the grating at an angle of $\alpha + \beta$, and for light diffracting to the top mirror (Path 2), the angle will be $\alpha - \beta$.

Looking at Paths 1 and 2, the lengths of $H^1_{\alpha+\beta}$ and $H^1_{\alpha-\beta}$, or the distance from the grating to the respective mirrors, are given by:

$$H^1_{\alpha+\beta} = \frac{L\tan\alpha}{\sin(\alpha+\beta)} \tag{5.2}$$

$$H^1_{\alpha-\beta} = \frac{L\tan\alpha}{\sin(\alpha-\beta)}, \tag{5.3}$$
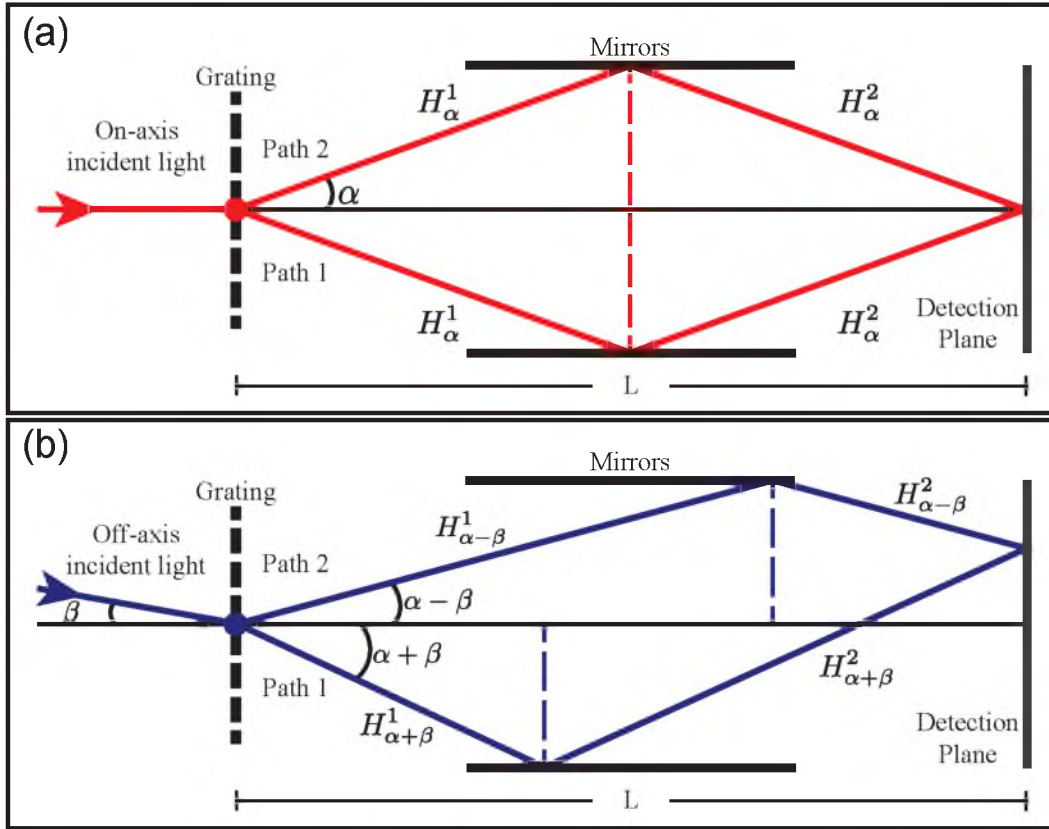
Figure 5.3. Schematic of the grating system with one transmission grating. The incoming angle of the off-axis light is given by β, and the angle that the grating will scatter monochromatic light incident on the optic axis is given by α. **(a)** The optical path for light incident on the grating along the optic axis. **(b)** The path for light incident on the grating at an angle β. The various path names are marked on the diagram. The overall path lengths of the two paths are different.

where L is the total horizontal path length from the grating to the detector. For $H^2_{\alpha+\beta}$ and $H^2_{\alpha-\beta}$ the distance from the mirrors to the detection plane is:

$$H^2_{\alpha+\beta} = \frac{L - \frac{L\tan\alpha}{\tan(\alpha+\beta)}}{\cos(\alpha+\beta)} \tag{5.4}$$

$$H^2_{\alpha-\beta} = \frac{L - \frac{L\tan\alpha}{\tan(\alpha-\beta)}}{\cos(\alpha-\beta)}, \tag{5.5}$$

The total length that the light travels for Path 1 is given by $P_1 = H^1_{\alpha+\beta} + H^2_{\alpha+\beta}$, while for Path 2 it is $P_2 = H^1_{\alpha-\beta} + H^2_{\alpha-\beta}$. The two paths within the system will give rise to an interference pattern, even in the case of a single photon event. In the case where the photons are incident along the optical axis, the interference pattern at the detector will

be at a maximum, while if the two path lengths differ by some half-integer wave-number value, then there will be a minimum in the intensity pattern at the detector.

The transmission grating interferometer produces a sinusoidal variation along the x-axis due to the wavefront of the two recombined beams not being constant across the detection plane of the interferometer; it is the interference of these two wavefronts that gives rise to the interference pattern. The resultant is then the interference pattern of two (partially) coherent beams, given by [4]:

$$q(x) = f(x) \left| 1 + \gamma \cos \left(\omega x + \phi \right) \right|, \tag{5.6}$$

where $f(x)$ is the underlying spatial distribution of the signal prior to the interferometer, γ is the fringe visibility of the interference pattern, ω if the fringe spatial frequency, and ϕ is the phase difference between the two arms of the interferometer for a particular incoming angle, β, as shown in Figure 5.2 [4]. Due to the fact the signal is in the Fourier domain, $f(x)$ has the shape of the optical transfer function (OTF) of the system.

Using the terminology from above, $g(x)$ of a confocal system is given by $g(x) = \text{PSF}(x) \cdot \text{PSF}(x)$ (see Section 3.1). Using the fact that multiplication in the sample plane is the same as convolution in the Fourier plane, $G(\mu x)$ can then be written as $G(\mu x) = F\{\text{PSF}(x)\} * F\{\text{PSF}(x)\}$. Using this, the OTF of the system may be written as [5]

$$f(x) = \frac{2}{\pi} \left[\cos^{-1} \left(\left| \frac{\rho}{\rho_0} \right| \right) - \left| \frac{\rho}{\rho_0} \right| \sqrt{1 - \left(\frac{\rho}{\rho_0} \right)^2} \right], \tag{5.7}$$

where $\rho = \frac{x}{\lambda f}$, and $\rho_0 = \frac{2NA}{\lambda}$. Here λ is the wavelength of the emission, f is the focal length of the objective lens, and NA is the numerical aperture of the objective. The relationship between the phase ϕ to the path length difference is simply

$$\phi = \frac{2\pi \left(P_1 - P_2 \right)}{\lambda}, \tag{5.8}$$

The fringe frequency ω is related to the angle by

$$\omega = \frac{2\pi}{\lambda} \left| \sin \left(\alpha + \beta \right) + \sin \left(\alpha - \beta \right) \right|. \tag{5.9}$$

This modeling of the system was used in the Monte-Carlo simulations only. In analyzing the experimental results, a calibration curve was used instead to negate any influence alignment affects would have on the experimental analysis.

5.3 Experimental Setup

Experimentally, the system was set up solely as a confocal scanning imaging system in the same scan/descan configuration, as shown in Figure 5.4. The scanning mirror, along with a scan and tube lens, are arranged in a $4f$ configuration such that the back pupil plane of the infinity corrected objective lens is conjugate to the scanning mirror plane. Using a flip mirror, light coming from the sample was then either directed to the avalanche photo-diode to obtain a conventional confocal image, or to the interferometer whose output is recorded by the EMCCD camera. The camera records the Fourier image in this instance, and not an image of the sample plane. A second $4f$ system, this time between the scanning mirror and the first transmission grating of the interferometer, is used to project a Fourier plane image onto the entrance grating of the interferometer. For further information regarding the experimental setup, see Appendix C. Appendix D contains further information regarding the design of the gratings. The aperture of the objective was stepped down to an effective NA of 0.7 to prevent clipping of the optical signal by the grating area. With knowledge of the objective properties, it is possible to numerically convert the input angle into the interferometer, β, to a displacement of the focused spot in the sample plane, as was discussed above. As was the case with Chapter 4, these preliminary experiments utilize a modulation that is one-dimensional only. With the appropriate optical design and grating construction, this principle can be extended to a two-dimensional system.

5.3.1 Experimental Results

To prove this point, an exemplary experiment was conducted. As a point source in our experiment, a 100 nm Au nanoparticle on a silicon wafer was used. The light scattered from the silicon wafer was then measured, where the nanoparticle appears as a dark diffraction-limited spot, as shown in Figure 5.5(a), due to the large extinction cross-section of the nanoparticle [6]. A measured interference pattern (CCD image of the collected light through the interferometer) is shown in Figure 5.5(b). After using the APD to isolate a single nanoparticle, the sample stage was used to position the nanoparticle relative to the center of the focus of the excitation beam. The stage was then moved in x through four 100 nm steps, thus moving the nanoparticle with respect to
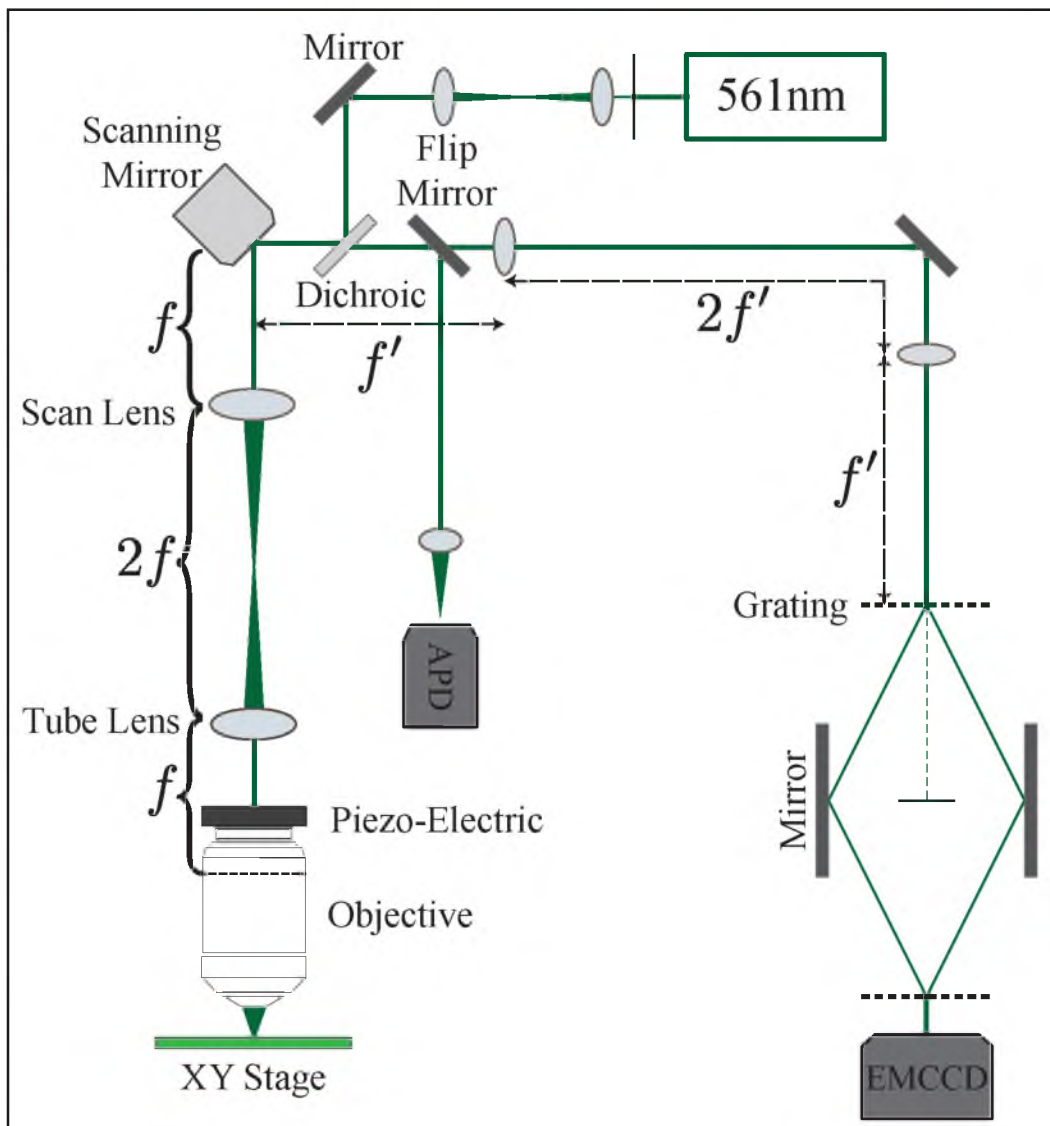
Figure 5.4. Experimental setup of the FILM system. The interferometer is set up in $4f$ configuration with the scanning mirror. Thus, the angular deviation in the Fourier plane is relayed to the interferometer.

the center of the excitation spot. Each position of the nanoparticle will give a slightly different spatial separation between the center of the excitation PSF and the location of the nanoparticle, and hence, a unique phase value ϕ is measured on the camera. For each position of the stage, 100 camera frames of the interference pattern were recorded. Each recorded frame was then projected on to the x-axis by summing the columns and fit using Equation 5.6, where for $f(x)$ a Gaussian distribution was used, since a Gaussian can well-enough approximate Equation 5.7 for modeling purposes.
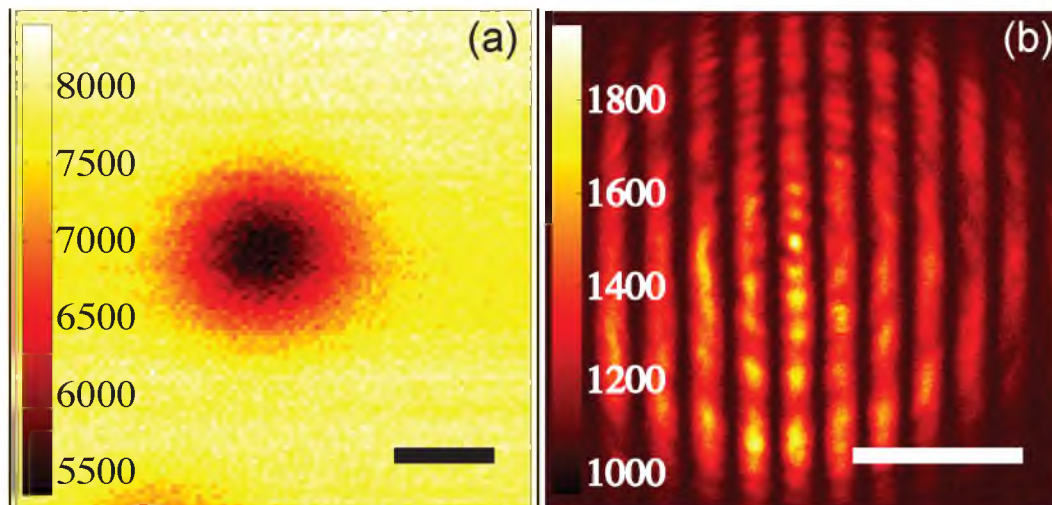
Figure 5.5. PSF versus Fourier plane image of Au nanoparticle **(a)** Single 100 nm Au nanoparticle appearing as a dark spot when imaging using an APD. Scale bar is 200 nm. **(b)** The measured interference pattern recorded on an EMCCD of photons from an on-axis beam representing a nanoparticle on the optical axis. Scale bar is 1mm. The scale for the APD image indicates photon counts. For the EMCCD image, since this is a Fourier image, the background photons cannot be counted separately from the signal photons.

To obtain accurate fitting, the initial step consisted of fitting the one-dimensional fringe signal to a Gaussian shape to extract initial values for the center of the signal, envelope width (standard deviation), amplitude and background. The signal is then divided by the fitted Gaussian and least squares fitting is used with a harmonic function to find initial values for the fringe frequency, visibility and the phase. Finally, these two sets of initial values are used as initial parameters to obtain the nanoparticle position by fitting to Equation 5.6. The extracted values of ϕ for the entire data set can be seen in Figure 5.6. As can be seen in the figure, the phase values for each stage position are constant, with a large step in value as soon as the stage is scanned. Due to the fact that this measurement is a relative phase measurement, the phase values can cycle through a maximum of 2π, which can be renormalized in the data analysis.

The parameter of ω was used to discriminate poor localizations within the data sets. In some instances, the localization did not result in small residuals. In both of these cases, a small constrained random perturbation of the initial values was applied several times, and the result with lowest residuals was selected. Averaging over each set of 100 frames for each position of the nanoparticle yields an average value for the fringe spatial
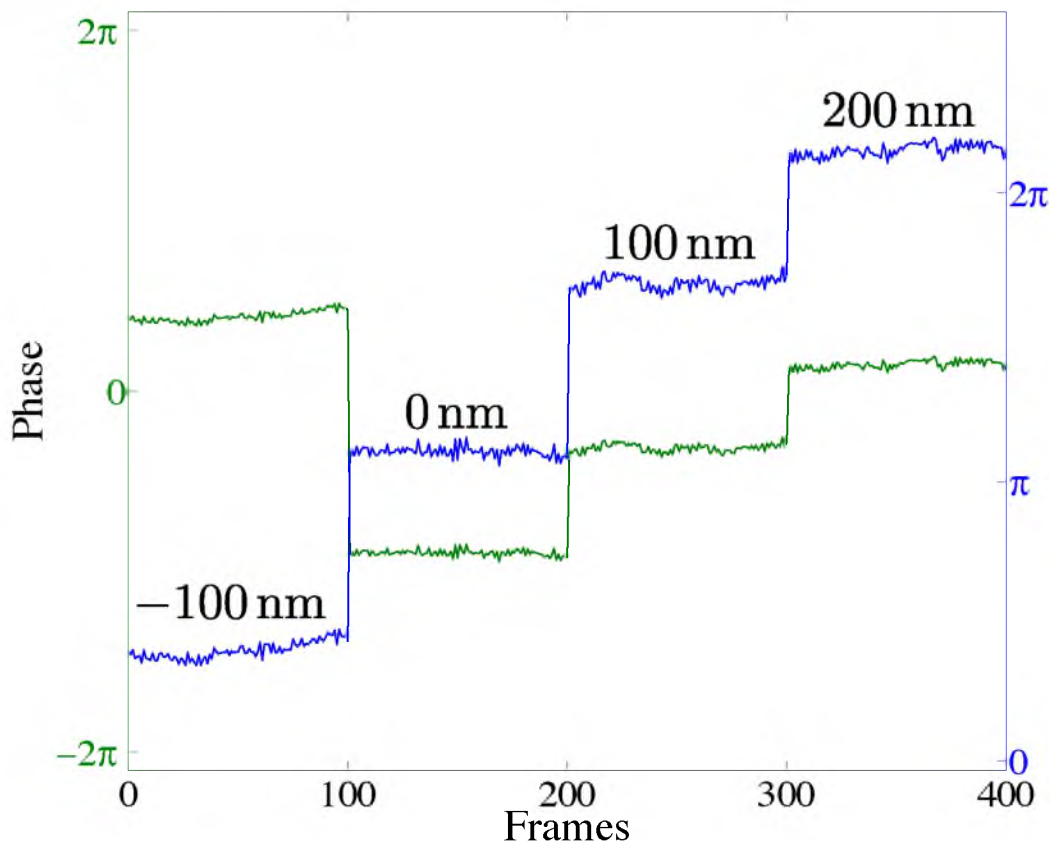
Figure 5.6. Phase values as a function of frame number. Phase values (green) and unwrapped phase values (blue) for the 400 frames captured (4 positions, 100 frames per position). The steps in the phase values correspond to the position of the nanoparticle with respect to the optical axis. Each distinct phase jump corresponds to moving the stage to a new position with respect to the optical axis.

frequency of $\omega = 0.18$ pixel^{-1} with fringe visibility of $\gamma = 0.91$. A plot of the extracted phase, ϕ, for four different stage positions, each separated by 100 nm steps, is shown in Figure 5.7. The standard deviation of measured values of ϕ at each position is $\approx 70 - 90$ mrad, and using the slope of the ϕ versus x curve (which is found by linear fitting), the corresponding localization standard deviation was calculated to be between 3 and 5 nm.

Smaller steps during this calibration experiment gave the same experimental results, thereby showing that calibration at 100 nm steps is sufficient. The same calibration is shown in Figure 5.8 for 20 nm steps sizes. The phase values show a clear trend line, whose slope is nearly identical to the one shown in Figure 5.7. The phase values are a bit noisier, and this is due to the fact that the 20 nm step sizes were below the position accuracy of the Prior xy-scanning stage used in the experiments.
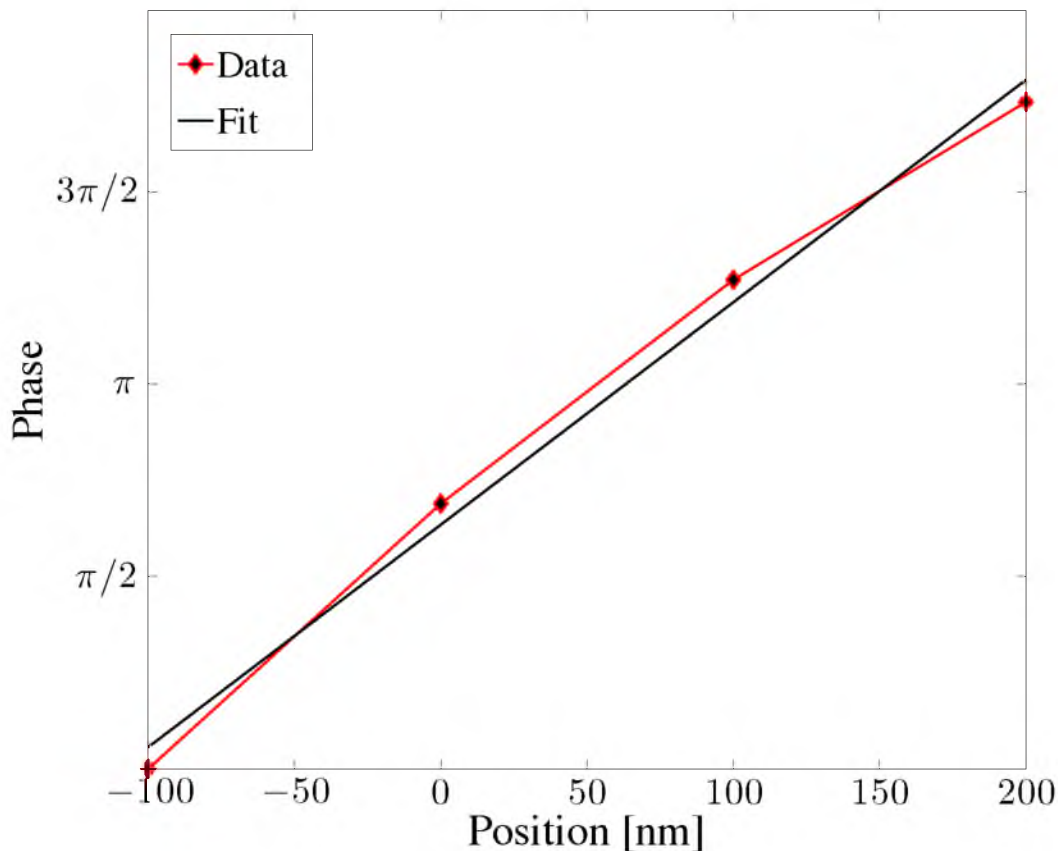
Figure 5.7. Phase values as a function of scan position. Phase extracted from the interference patterns as a function of emitter position relative to the state position (red) and calibration curve obtained by a linear fit (black). The calculated standard deviation indicates that displacements as small as 5 nm can be clearly discerned.

The fringe frequency values were also extracted by fitting in the same manner as the phase. The results are shown in Figure 5.9. The standard deviation was calculated by extracting the fringe period values for each position, and the largest standard deviation was $4.5 \cdot 10^{-6} \text{pixel}^{-1}$, which corresponds to 13.1 nm in terms of localization precision. Therefore, a precise localization cannot be obtained using this method. However, a coarse localization may be extracted from this relationship, allowing for the elimination of any possible phase ambiguity that may result. When using the fringe frequency to obtain localization, one should consider the Nyquist criterion. The highest fringe frequency that can be used is determined by the pixel size P, i.e., $2\pi/\omega > 2P$.
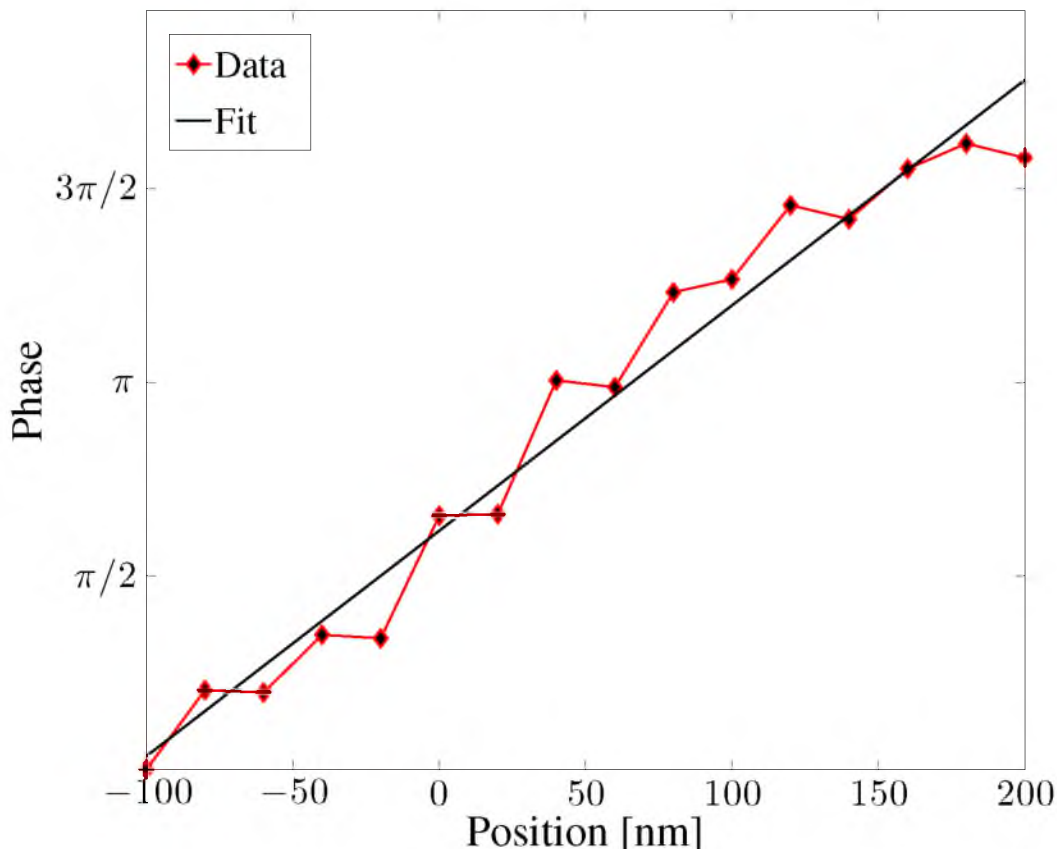
Figure 5.8. Phase values as a function of stage position for 20 nm step size (red) and calibration curve obtained by linear fit (black). The slope of this curve is 0.01829 rad/nm, versus 0.01816 rad/nm in the case of 100 nm steps. This deviation between the two values corresponds to a localization discrepancy of 2 nm over the full 2π cycle.

5.3.2   Comparison to Gaussian Localization

To compare the localization precision of FILM to that of localization using a traditional Gaussian PSF in a confocal setup, 100 frames of a single nanoparticle were acquired using the APD. A standard localization procedure was then applied to the data set by fitting these images to a Gaussian; the standard deviation of fitted Gaussian centers for these 100 measurements was ≈ 10 nm. By measuring the emitted power from the sample, a comparison between the total photon flux incident on the APD with that incident on the entrance grating of the interferometer can be made. The photon count incident on the grating was 12 % higher than that on the APD, which accounts for only $\approx 6\%$ of the more than 50% improvement in localization precision.

As can be seen in Figure 5.7(a), the value of ϕ can wrap around 2π; careful design of
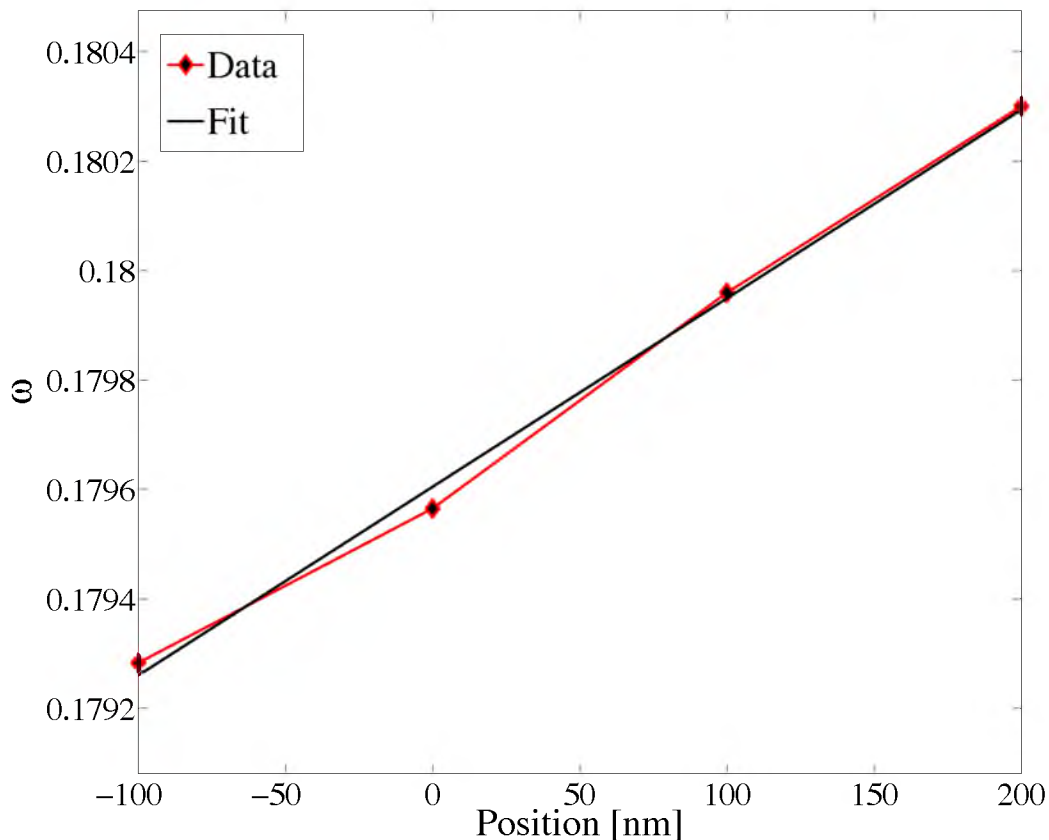
Figure 5.9. Fringe frequency values obtained by scanning the sample along the x-axis.

the system can result in phase values between 0 and 2π to eliminate ambiguity. Since the light that is incident on the gratings depends on the entrance angle β, the course position of the nanoparticle can also be extracted using the fringe frequency, as is shown in Figure 5.9. Combining the less accurate fringe frequency dependence with the fine localization obtained using the phase values also eliminates phase ambiguity, which allows for coarse-grained scanning without loss of localization precision. Such a calibration curve can be used to localize single nanoparticles given an extracted phase value from a Fourier domain interference pattern.

One has to consider the effect of a slight defocus on the obtained results. If the calibration curve and the investigated nanoparticle are obtained on the same plane, a slight defocus will have no effect. If, on the other hand, the calibration curve is obtained using an emitter, which is in a different plane than the sample, the slight defocus will cause a constant phase shift of the fringes, thus resulting in a constant shift in the acquired

position. If all the emitters have a constant shift in the estimated position, the constant shift can be eliminated by choosing an arbitrary particle as the origin and shifting all the localized locations accordingly.

5.4 Localization Precision from Interferometric Fourier Image

As was discussed in Chapter 4, the Fisher information matrix allows for the calculation of the Cramér-Rao Lower Bound (CRLB). The CRLB gives the uncertainty in the location of a single emitter, and is given by $\sqrt{I^{-1}}$, defined in Equation 4.2. Analogous to the steps outlined in Chapter 4, the localization ability of a the modified OTF may be calculated. Again, I may be calculated by inserted the FILM signal in Equation 5.6, for $q(x, y)$.[1]

When only the intensity is measured, the localization precision is inversely proportional to the square root of the number of detected photons [8, 9]. This is referred to as the Gaussian PSF case. In this approach with the modified OTF, the extra phase information allows for an enhanced precision in the localization information, due to the fact that $q(x, y)$ is a highly varying function. To elucidate this impact, the localization precision of the center of a point emitter was calculated, whose results are summarized in Figure 5.10.

The conventional Gaussian PSF fitting scenario (blue dashed line) shows the familiar $1/\sqrt{N}$ dependence. The FILM case with ideal fringe visibility, $\gamma = 1$, shows the same $1/\sqrt{N}$ dependence, but with a scaling factor that yields an increase in the localization precision, as shown by the red dashed line in Figure 5.10. For the FILM results, an interferometer length of 1 m and a grating diffraction angle of 30° were assumed. The localization error is reduced by a factor of 2 compared to the conventional PSF Gaussian fitting.

Figure 5.11 shows the dependence of the localization ability for this method as a function of background photons, when compared to the conventional Gaussian local-

---

[1]While it is general convention to do localization methods in the image plane (since the spatial distributions of the images of the sources are distinct), for single particles it is valid to do the localization in the Fourier plane as well [7]. This method only works for a single fluorophore in the field of view, since the signals are mixed in the Fourier plane. However, from analyzing the variation of the intensity gradients in the Fourier plane, it is possible to localize the position of the particle in the image plane.
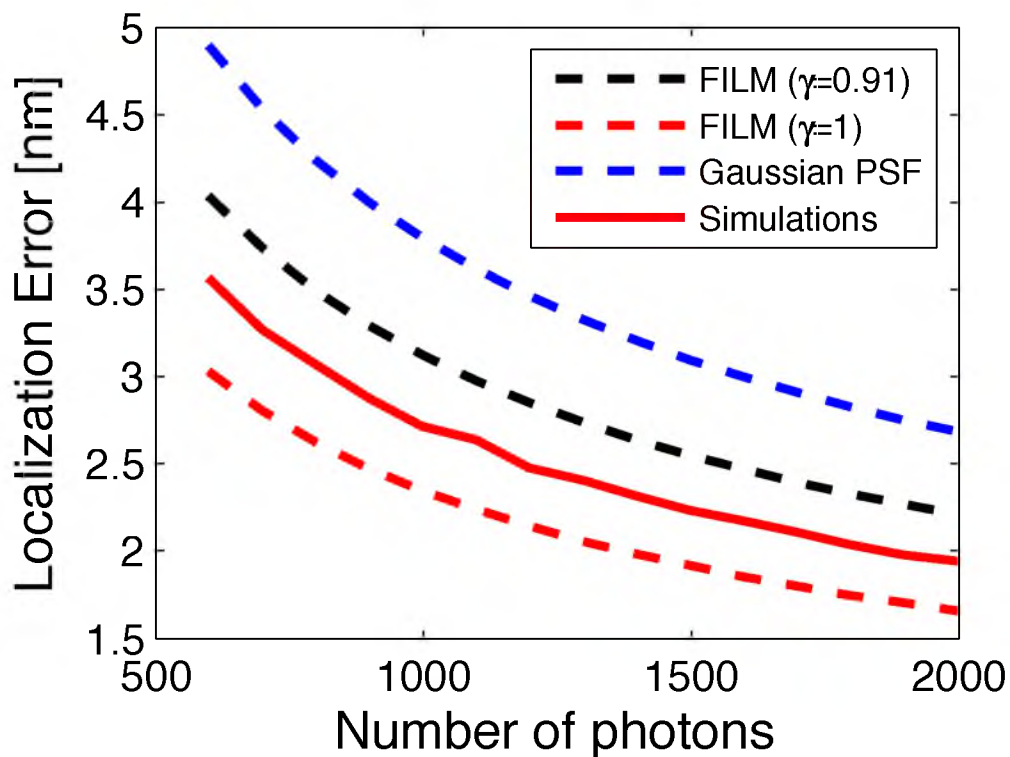
Figure 5.10. FILM versus Gaussian localization for signal photons. Theoretical analysis and simulation results of localization error of a single emitter as a function of the number of photons for the conventional case (blue dashed), FILM with ideal fringe visibility (red dashed) and fringe visibility obtained in our experiments (black dashed lines). The localization error was calculated using the Cramér-Rao Lower Bound (CRLB). Solid red line indicates the localization error obtained in our numerical simulations.

ization methodology. The Gaussian simulation shows a steeper slope than the theoretical CRLB, which is nearly flat. Localization via the FILM technique preserves this flat slope, showing the increased robustness with regard to background photons.

5.4.1   Monte-Carlo Simulations for FILM

To further test these investigations, one-dimensional Monte-Carlo simulations were performed to test the ability of FILM to improve localization precision. In these simulations, the same configuration was used for which the CRLB curve had been calculated. The first step is the generation of a calibration curve using a noise-free scenario in a range of positions from -50 nm to 50 nm. Only one single emitter was simulated at a given time, in which the signal $f(x) = \text{OTF}(x)$ is calculated and imposed the interference fringes using the derivations outlined in Section 5.2.1 for the phase and fringe period.
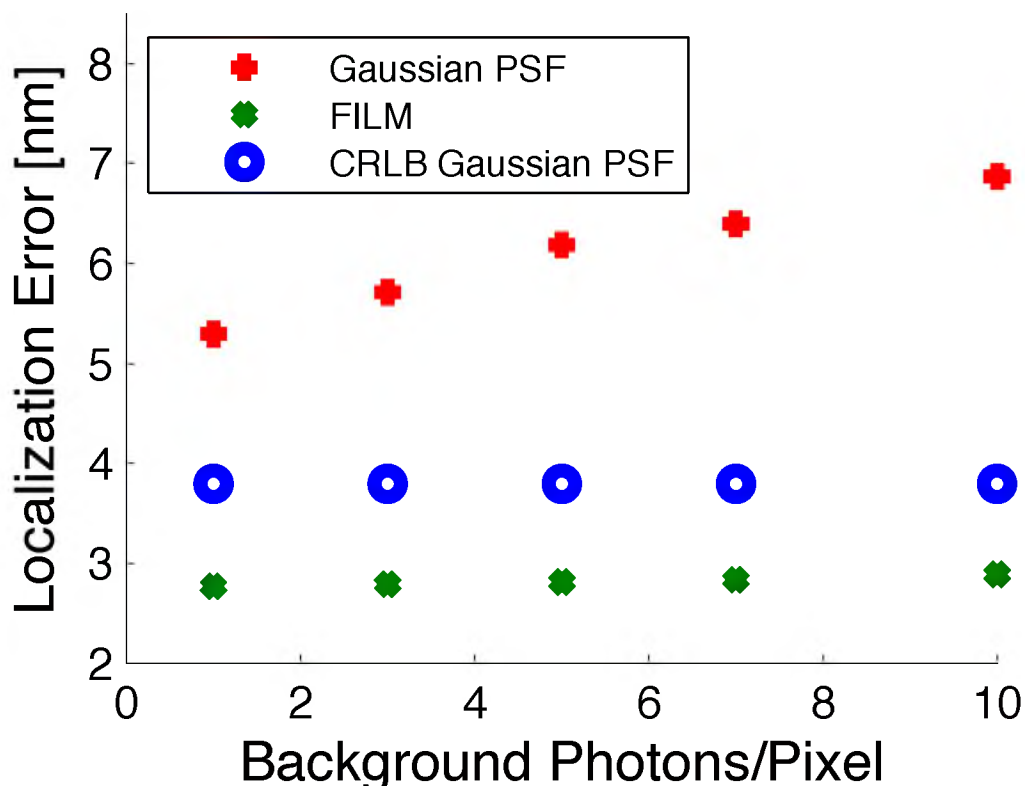
Figure 5.11. FILM versus Gaussian localization for background photons. Localization error obtained by numerical simulations of a single emitter as a function of background photons, with constant signal photons N =1000, for Gaussian PSF, FILM. For comparison, CRLB curve when N = 1000 is also shown.

Since the Fourier domain signal may be distributed over many pixels, thus decreasing the signal-to-background ratio, the image was demagnified by a factor of 6.8. This kind of demagnification can be implemented using a simple beam expander, or in the $4f$ system itself.[2]

The nanoparticle position was randomly selected between -30 nm and 30 nm for each iteration, and shot noise was added by sampling a Poisson random process with a mean value that corresponded to each individual pixel value. The localization was performed in a similar manner to that of the experimental data. Since Monte-Carlo simulations require many repetitions, accuracy was sacrificed to gain faster fitting by

---

[2] If the demagnification is to be implemented within the $4f$ system, care must be taken to not decrease the sensitivity of the system. The angular deviation of the optical beam is reduced by the same ratio as the beam diameter, as the $4f$ system is a linear transformation. This is the primary reason a one-to-one magnification in the $4f$ system was used in these experiments.

omitting the random perturbation to initial parameters when the fitting residuals were large. The localization error was calculated as

$$\Delta x_{rms} = \sqrt{E\{(\hat{x} - x_0)\}},$$ (5.10)

where x_0 is the real position of the nanoparticle, and $\hat{x}$ is the calculated position. The expectation $E\{...\}$ was taken over all of the iterations for a single photon count value. The results can be seen in Figure 5.10 as the solid red line. As seen in the figure, the localization error in FILM is smaller than the theoretical limit in the case of the conventional method of localizing a Gaussian PSF.

Background photons are known contributors to localization error [8]. To test its effect on localization precision using FILM background photons were added to each pixel and shot noise was introduced by sampling a Poisson random variable with mean that corresponds to the sum signal and background values. For the simulations, a photon count of $N = 1000$ was assumed. The single emitter was then localized using the fringe-fitting method, and compared to conventional Gaussian fitting of a single emitter in the conventional case. For the conventional Gaussian case, a pixel size of 50 nm. Figure 5.11 shows that for these simulations, the Fourier plane localization is less sensitive to background noise. This is seen by inspecting the slope of the curves. Further, at $N = 1000$, even when the background is 10 photons/pixel, the localization error is lower in the case of FILM than the CRLB limit for Gaussian PSF.

5.5   Localizing Single Particles

To show that it is possible to localize actual single emitters using the proposed technique, the next step involved imaging three nanoparticles separated approximately 2 μm from each other, as shown in Figure 5.12, top. Using a calibration curve, the position of each nanoparticle relative to the illumination center could be determined from the measured phase values as the sample was scanned along the axis connecting the three nanoparticles. The actual nanoparticle position was then determined by $\hat{x} = \hat{x_0} + mL$, where $\hat{x_0}$ is the estimated position relative to the illumination beam (i.e. position within the scanning pixel), m is the scanning pixel index and L is the scanning step. The scanning step (pixel) for this measurement was 1 μm, and 25 frames were averaged for each position.
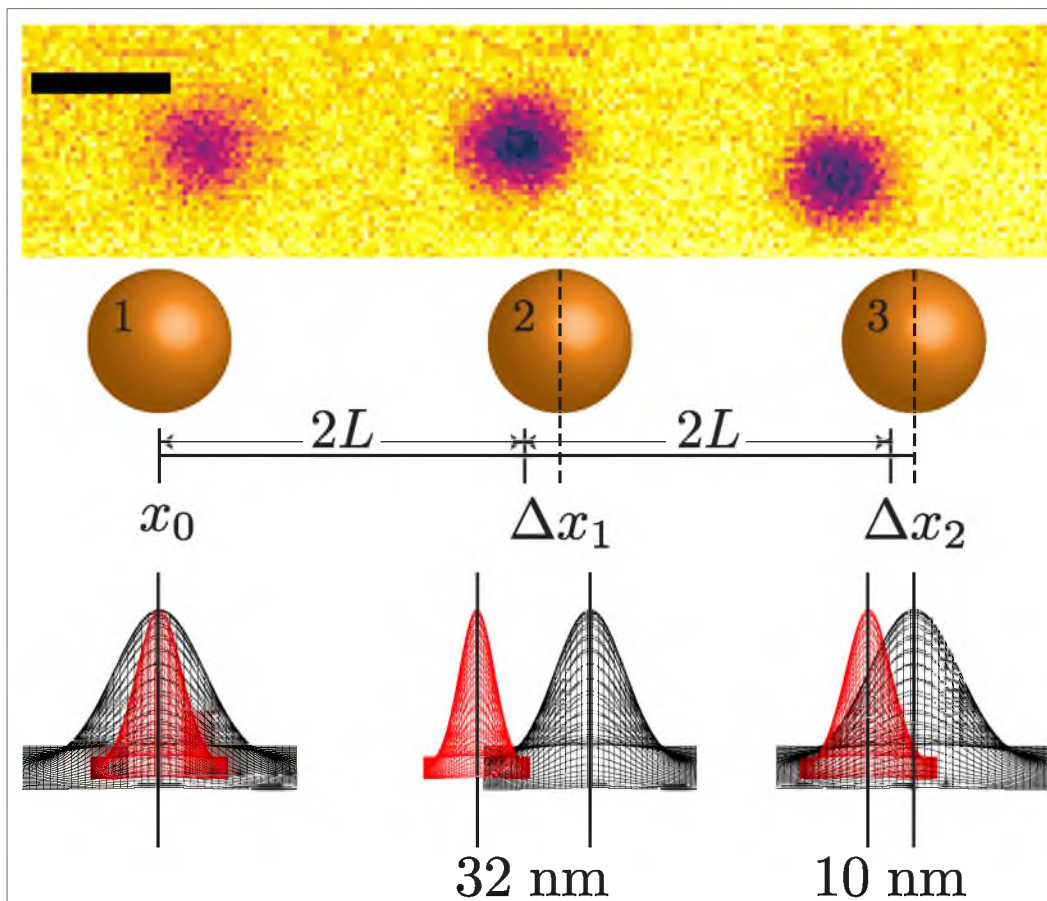
Figure 5.12. Localization of three nanoparticles (yellow spheres, not drawn to scale), at positions x_0, $2L+x_1$, $2L+x_2$, where L is the scanning pixel (step) size, using conventional Gaussian method (gray) of the nanoparticles from the APD image, and FILM (red). The values obtained by conventional fitting of the Gaussian PSF from the APD image are 0, 2067 nm, and 4160 nm. For the phase fitting using the FILM technique, the values are 0, 2099 nm, and 4150 nm. The widths of the Gaussian profiles correspond to the expected standard deviations of localization using both methods. **Top**: APD image. Scale bar is 1 μm.

To calculate the positions of the three nanoparticles, the left nanoparticle was used as the reference point, $x = 0$. A calibration curve was then used to find the position of the middle and right nanoparticles relative to the left nanoparticle. For comparison, the three nanoparticles were scanned conventionally in confocal mode (with 40 nm step size) and imaged onto the APD. A conventional Gaussian localization algorithm was then applied to the image data, again using the position of the left nanoparticle as a reference. The results of the two fitting techniques are shown in Figure 5.12 and demonstrate good agreement with each other, indicating that the FILM scheme can be

used to localize single emitters. Slight discrepancies in values between the two methods can be attributed to the position of the scanning stage, which has positioning accuracy of 50 nm. Importantly, the phase-sensitive approach yields more precise localization even though the sampling density for the scan was very low (1 μm step size), compared to the conventional confocal localization with 40-nm step size. In the case of the APD, the scan covered an area of 7 μm by 2 μm, with a 40 nm scanning pixel size and 1.5 ms pixel dwell time, for a total image acquisition time of $\approx$ 13 s. Measuring the position via the phase value of the fringes in the FILM signal, only 7 frames of the EMCCD were acquired over the 7 micron scan along the x direction, as only one data point per single nanoparticle is needed to estimate the position. At a 50 ms frame rate, the acquisition time was 350 ms, over an order of magnitude faster than that with the APD.

In the above measurements, backscattering of the laser from the sample leads to a specific fringe pattern, which is altered by the presence of a nanoparticle in the laser focus. To determine which scan positions have nanoparticles, the flip mirror was used to deflect the collected signal onto an APD to acquire a conventional confocal image of the scan area. At scan positions corresponding to nanoparticle locations, the fringe pattern image of the scan area exhibits a clear shift in phase relative to the Gaussian envelope function that defines the interference zone. For dark-field or fluorescence imaging, where the signals are expected to be positive (larger than background) the use of an APD would be completely redundant since the fringe pattern would appear on the camera only when the scattering nanoparticle is within the laser focus.

5.6 Fourier Imaging Localization Conclusions

This chapter showcased that localization precision for isolated scatterers/emitters could be enhanced by extracting phase information from the scattered/emitted photons. The phase can be measured by allowing photons to interfere in a Mach-Zehnder interferometer positioned between the microscope objective and detector. By combining such a phase measurement technique with conventional localization schemes, the achievable precision of localization-based techniques can be increased significantly. Alternatively, the same localization precision can be achieved with fewer detected photons, which will allow for fast imaging of low quantum-yield samples. Furthermore, this

technique allows scanning of the sample with larger scanning steps than conventional scanning systems, allowing for faster scanning. For example, the total scanning time that was required to generate the APD image in Figure 5.12 was approximately 15 seconds, compared to 350 ms required to scan the same 7 μm range via the FILM method. This scanning speed corresponds to 300 μm for a full 15 s scan time. This technique also shows that regardless of scanning pixel size, which was 1 μm, nanoparticles or a single point source may be localized to extremely high precision. Furthermore, localization techniques using phase extraction from Fast Fourier Transform methods of the interference fringes may allow significantly faster localization estimations without the need for computationally intensive numerical fitting routines. For more on this method, see Appendix E.

This technique also can be applied for particle tracking of single metal nanoparticles (or any monochromatic scattering/absorbing point source). Extending the technique to super-resolution microscopy requires adapting the proposed method to previously suggested nanoscopy methods using metal nanoparticles [10–12]. In addition, applying the same principles to noncoherent fluorophore emission by allowing the broad-band beams to interfere in the same place by applying optical-path-length correction, which may be a subject of future work, which can result in Fourier domain super-resolution imaging technique with enhanced resolution of more conventional fluorescent microscopy fluorophores. To extend this principle to two-dimensional localization, two-dimensional gratings are required, with two additional mirrors that will reflect the light back to interfere on the camera, in the same manner as in one dimension. One can then find the phase shift in x and y independently to obtain the x and y position of the single emitter. Since the localization in x and y is done independently (separability of the Fourier transform), the theoretical analysis is valid for two-dimensional localization.

5.7   References

[1] N. G. Walter, C.-Y. Huang, A. J. Manzo, and M. A. Sobhy, Nature Methods **5**, 475 (2008).

[2] G. Shtengel et al., Proceedings of the National Academy of Sciences of the United States of America **106**, 3125 (2009).

[3] D. Aquino et al., Nature Methods **8**, 353 (2011).

[4] B. J. Thompson and E. Wolf, Journal of the Optical Society of America **47**, 895 (1957).

[5] J. W. Goodman, *Introduction to Fourier Optics*, McGraw-Hill, New York, NY, 2nd edition, 1996.

[6] P. K. Jain, K. S. Lee, I. H. El-Sayed, and M. A. El-Sayed, The Journal of Physical Chemistry. B **110**, 7238 (2006).

[7] B. Yu, D. Chen, J. Qu, and H. Niu, Optics Letters **36**, 4317 (2011).

[8] R. Thompson, D. Larson, and W. Webb, **82**, 2775 (2002).

[9] R. J. Ober, S. Ram, and E. S. Ward, **86**, 1185 (2004).

[10] A. Gur, D. Fixler, V. Micó, J. García, and Z. Zalevsky, Optics Express **18**, 22222 (2010).

[11] T. Huang, L. M. Browning, and X.-H. N. Xu, Nanoscale **4**, 2797 (2012).

[12] X. Cheng, D. Dai, D. Xu, Y. He, and E. S. Yeung, Analytical Chemistry **86**, 2303 (2014).

CHAPTER 6

OUTLOOK AND FUTURE DIRECTIONS

This dissertation has demonstrated, within the field of localization microscopy methods, that through the use of an transmission-based interferometer system in the detection path, that it is possible to localize the position of a point-source beyond the conventional $\sigma/\sqrt{N}$ dependence that is standard for conventional Gaussian fitting. Of the two methods, the modification of the PSF of point-sources will prove most adaptable to conventional localization methods, since most localization-based methodologies are wide-field systems that are flexible in their detection configuration. Numerous techniques for improving the localization ability of systems involve complicated optical set-ups. Systems that aim to increase resolution by increasing the effective numerical aperture of the instrument usually do so via two opposing objectives, which makes aligning, and maintaing proper alignment, extremely difficult. STED microscopy, which produces sub-diffraction-limit confinement at the sample, are extremely complicated optically to build and maintain. STED systems require high-power lasers, increasing their cost, and the alignment of the two beams must be carefully maintained.

The systems described here, by contrast, are relatively simple. In the case of the PSF self-interference, the grating system is reliable and easy, and with the proper engineering, could easily be attached to a conventional microscope body. As is always the case with localization methods, the localization algorithm is an important factor. It is important in both the speed at which data can be processed and also the accuracy involved with candidate detection and isolation within individual frames, and the localization accuracy of the algorithm itself. The modification to conventional algorithms to incorporate the fringe modulation in the data fitting process has proven to be more of a challenge in terms of speed, but not in its accuracy.

The remainder of this chapter will be focused on two main points. The first are

improvements to the grating system from its current configuration and design. The second is more general in scope, and discusses methods with which to combine optical super-resolution methods with those of electron microscopy, of which preliminary results will be presented.

6.1 Improving the Transmission Grating Interferometer

While Chapters 4 and 5 discussed methods to localize point-sources below the conventional localization limit for Gaussian distribution sources, they were limited by two key factors. The first of these is that the current form of the interferometer is purely monochromatic. While interferometers offer extremely precise detection capabilities, and are used in numerous branches of research and academic settings, they are generally a monochromatic implementation. In the experimental results highlighted in this dissertation, each instance used Rayleigh scattering from gold nanoparticles of $\lambda = 561$ nm. The numerous methods that have been devised to incorporate fluorescent markers into biological systems, and the advantages they offer, become extremely limited if the marker is a large, bulky nanoparticle.

The second is the fact that the increase in the localization precision is only along the grating axis. In these experiments, the localization improvement occurs only along the x-axis, while the y-axis follows conventional Gaussian localization statistics. Monte-Carlo simulations showed that while localization accuracy was improved for both x and y cases when the one-dimensional gratings were rotated at a 45° angle, the improvement was not nearly as large for gratings that offered modulation in both the x and y axes. In real biological samples, which follow their own internal organizational structure and not those imposed by an external axis on a detector, the limited availability of more isotropic (i.e., two- or three-dimensional) localization improvement is limited in scope. While the types of systems that are suitable for study are limited, one such type would be the study of molecular motors in *in vitro*-type experiments. The reason that these would be useful biological systems to study is that molecular motors travel along microtubule filaments and follow a quasi-one-dimensional path, which can be oriented along the axis of the gratings of the interferometer.

6.1.1 Broadband Diffraction Grating System

The first of these improvements to the grating system is illustrated in Figure 6.1(a). By replacing the mirrors with appropriate gratings, shown as G2 and G3 in the figure, the system can be simply modified to become a multiwavelength interferometer. Each wavelength will diffract from the first grating, G1, at a unique angle α_λ. They will then diffract at G2 and G3 (see caption for details) and recombine at the last grating in the system, G4. Each wavelength will have its own unique optical path length, which is not the case in the current configuration. In the current layout of the interferometer, only the wavelength of light that the system is aligned to, λ_0, will recombine at the second grating, or image plane. Since the angular deviation of the emission incident on the first grating is wavelength dependent, the spatial position of the image plane is wavelength dependent as well. As a result, for $\lambda < \lambda_0$, the focal position is before the second grating, and for $\lambda > \lambda_0$, after the second grating. This shift in the focal position can be mostly filtered out in the lens relay system, thereby increasing the fidelity of the signal. By replacing the mirrors with gratings, the focal plane at grating G4 becomes wavelength *independent*. Thus, the grating system can be manufactured to image broadband, fluorescent sources, while still modifying the PSF.

As an example of the ability to use fluorescence to produce a modified PSF, two fluorescent samples were imaged through the interferometer. If the spectral bandwidth is kept to as narrow a bandpass as possible, the current configuration of the interferometer system can image fluorescent sources. These modified PSFs can be seen in Figure 6.2. In both instances, a spatial filter was placed within the lens relay system to block the spectral bandwidth of the emission incident onto the camera.[1] Since the spectral bandwidth is narrowed to such a small window, the emission signal incident onto the camera is greatly reduced. The first such sample was a very dense fluorescent dye sample placed upon a coverslip, with the spatial location of the emission coming from the confinement of the focused excitation beam. The fringes are clearly visible. In part **(b)**, a single fluorescent bead, 100 nm in diameter, was imaged. While dim,

---

[1]Since the focal position within the interferometer system is wavelength dependent, the out of focus light may be blocked by the appropriate use of spatial filters within the lens relay system. One filter was placed before the first relay lens, and one placed in the middle of the lens relay. These were adjusted until maximum fidelity was observed.
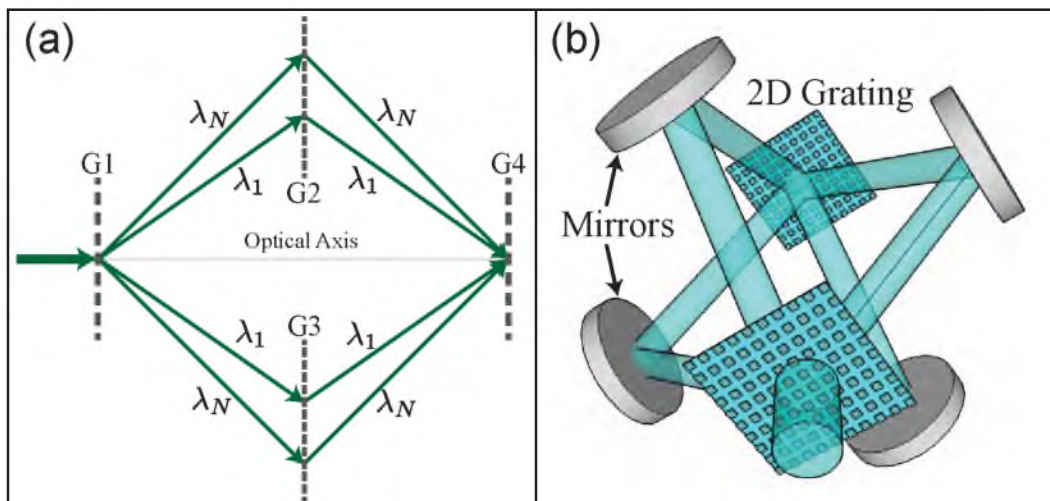
Figure 6.1. Two methods to improve the grating system. **(a)** Four grating system to allow for the use of broadband sources. The use of a further two gratings (G2 and G3) in place of mirrors allows for the use of broadband fluorescent sources. Each wavelength has its own unique optical path through the system, and will recombine at the second grating. G2 is optimized for the +1 order, while G3 is optimized for the -1 order. **(b)** Two-dimensional grating system for use in Rayleigh scattering experiments. Here, the first and last gratings are two-dimensional gratings to split the signal into x and y components. The signals recombine at the second grating, producing a modulation in the PSF in both the x and y directions.

the fringes are still visible. The PSFs of the two images are elongated along the x-axis. Again, this is a function of the wavelength dependence of the focal position within the interferometer.

6.1.2 Two-Dimensional Grating System

Another improvement for the system can be the generation of gratings that diffract the signal not only along the x-axis, but along the y-axis as well. Two-dimensional gratings will offer the advantage of improvement in the localization ability in both the x and y directions in the sample plane, making the imaging modality much more convenient and relevant for biological imaging. Such a setup may be see in Figure 6.1(b).

Recall that the simulations from Chapter 4 utilized a PSF that was modified along both the x and y axis. This was shown in Figure 4.7. As shown in Figure 6.1(b), the system is constructed with four mirrors, indicating that this iteration is monochromatic. This does not have to be the case; the mirrors can be replaced with the appropriate gratings, to produce a broadband grating system that is capable of imaging fluorescent
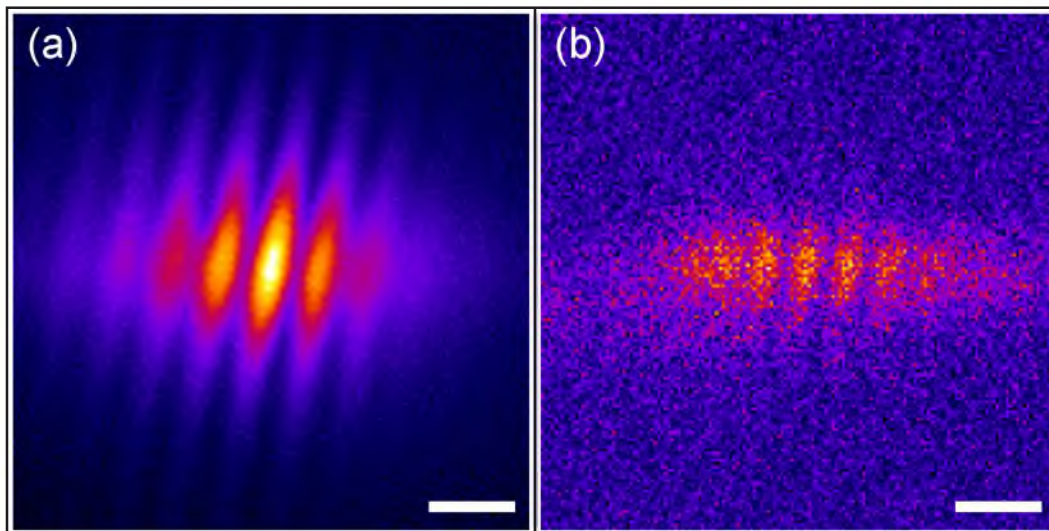
Figure 6.2. Two examples of interference observed over the PSF within the interferometer configured in imaging mode (as presented in Chapter 4). **(a)** EMCCD image of a dense fluorescent dye. The fringes are noticeable. Due to the density of the sample, the PSF shape originates from the focused excitation beam. **(b)** EMCCD image of a single fluorescent latex bead, 100 nm in diameter. While dim, the fringes are noticeable. For both images, the spectral bandwidth was reduced by a spatial filter in the lens relay system. This also has the effect of drastically reducing the signal incident on the camera. The dense bead sample in **(a)** provides an incredibly strong signal. The single bead in **(b)** is difficult to image due to the large reduction in the spectral bandwidth of the emission reaching the detector. Scale bar: 0.5 μm.

markers. Of course, the downside to this is that signal is lost at every grating used, so the overall signal will be weaker, but capable of imaging bright fluorescent samples with localization improvement along both the x and y axes. Construction of a two-dimensional grating system is basically reduced to an engineering and optimization problem.

6.2 Correlation Fluorescence and Electron Microscopy

Due to the nature of the method, localization microscopy is best suited for imaging fixed samples. Since the active state of the fluorophores is extended in time (recall Figure 3.11), the acquisition times required for imaging cycles are longer than conventional methods. This limitation makes live-cell imaging more of a challenge. For cells or samples that have been fixed and immobilized, and do not move, shift, or change shape

like a live sample would, the acquisition time required is not significant.[2]

Another drawback to localization methods is that to produce an image with definable resolution and features, the marker proteins must form a quasi-continuous structure. This is why microtubules and actin filaments are so often used as benchmarks for localization microscopy images, and as test samples for new methodologies within the field. They form well-defined, long structures that easily lend themselves to characterization. If the protein target in question is a protein that is sparsely distributed, or localized only around certain structures in the cellular architecture, then the localization image will be reduced to an image of distinct areas of marker clusters.

The problem with such images is that they can lack context, and fail to put the target proteins within the larger framework of the cellular environment. Since the only signal is coming from the proteins of interest, the associated structure and environment surrounding the protein is left unresolved. As was shown in the opening chapter, electron microscopy provides an excellent imaging method to view the structure and environment of the cell. In a sense, electron microscopy and fluorescence microscopy are complimentary methods. Electron microscopy offers very little in the ability to tag and image specific target proteins, but gives a beautifully detailed image of the components of a cell or sample. Optical microscopy is only selective to target proteins, and highlights their location, while failing to give the over-arching picture of the host environment.

As a (perhaps) crude analogy, imagine a bird's eye-view of the campus of the University of Utah. A satellite image of campus would give the location of the buildings, their proximity to one another, and their size. Students would be seen walking between buildings, and from the image, it would be possible to estimate on the number of students on campus, or the buildings that receive the heaviest amount of student traffic. If the goal was to isolate the physics or biology majors from the larger group of students, however, the satellite image would not offer that ability.

On the other hand, if the physics and biology majors could be monitored by say a GPS locator, their movements and location could be followed. Such an "image" would

---

[2] Furthermore, localization microscopy methods use high laser intensities, which cause photo-damage and photo-toxicity in live samples. For a fixed sample that is no longer living, this is not as much of an issue.

reveal their location, but not their environmental surroundings. The students could be filtered from the larger crowd of University of Utah students as well. What is most useful, however, is the combining of both types of imaging. The satellite imagery gives the structure, organization, and layout of the campus. GPS tracking could isolate the physics and biology majors, and allow for their location to be pinpointed on the overall image of the campus. Localization microscopy offers the ability to tag individual proteins, while electronic microscopy gives a detailed image of the structure of the cell. Combining the two types of imaging would allow for the direct placement of proteins within the organizational superstructure of the cell. Combining the two methods is collectively known as correlation microscopy.

6.2.1 Methodology of Correlation Microscopy

In order to perform correlation microscopy, the same sample must be imaged in both an optical localization microscope, and on an electron microscope, either a scanning or transmission microscope. The actual experimental preparation to allow for imaging in both types of instruments is complicated, but is possible with the correct sample preparation and imaging parameters. [1] For imaging on an electron microscope, the sample must be dehydrated (since electron microscopy is done in vacuum), embedded in a plastic resin, and coated with either an electrically conducting material (scanning electron microscopy) or a electron dense material (transmission electron microscopy). For a sample using fluorescent proteins, this step would usually denature the proteins within the sample, thus destroying their fluorescence capabilities. Using organic dyes in the place of proteins is possible as well, but care must be taken since the dyes are added to the sample prior to imaging, where they bind to the target protein. Fortunately, the resins used to encase the samples for electron microscopy are permeable to the buffer solution required for to cause blinking (see Section 3.2.2).

If the sample is imaged optically first, kept partially hydrated, and the final steps required for electron microscopy imaging done after optical imaging, localization microscopy is possible. Since samples for electron microscopy are extremely thin (on the orders of tens of nanometers), the optical images from electron micrograph samples

can be quite good, since there is low background from out-of-focus fluorescence.[3] The sample can then be prepared for electron microscopy, and imaged.

The problem then becomes — how are the two images registered to each other? The field of view of the optical microscope and the electron microscope will not be identical, nor will the orientation of the samples within the respective instruments. Also, the final steps required for imaging in an electron microscope subtly distort the sample, since it is being dehydrated and then coated.[4] This issue is overcome by the use of fiducial markers that are visible in both the optical and the electron microscopy images, where either latex beads or gold nanoparticles may be used as fiducial markers. These are placed upon and adhered to the sample before imaging them on a microscope.

6.2.2   Fiducial Markers and Error Registration

Latex beads or gold nanoparticles[5] offer long-lasting, bright sources of fluorescence. With the proper selection of beads, or size of gold nanoparticles, their emission fluorescence may be in a spectrally distinct bandpass than the emission signal from the sample. For electron microscopy, the latex beads will appear as bright regions within the image,[6] while gold nanoparticles will appear as dark circles within the image since they are electron dense. Since the latex beads and the gold nanoparticles will appear in both images, and in the same position, they serve as fiducial markers between the two images. If the coordinate transformation to map the fiducial marker locations from the optical image to the electron image can be calculated, then the whole optical image can be transformed to map to the coordinate system of the electron micrograph image.[7] Such

---

[3]Using organic dyes is harder, since it is more difficult to remove excess dye from the sample completely. If fluorescent proteins are used, this is not a problem. Fluorescent proteins, however, do not have the photon yield of organic dyes.

[4]Scanning electron microscopy coats the sample in a carbon powder film, while transmission electron microscopy coats with a thin-layer of a heavy metal.

[5]With the correct size and the correct excitation wavelength, gold nanoparticles can fluorescence through resonant frequency excitation of surface plasmons.

[6]Latex beads will accumulate charge, and hence repeal any incident electrons.

[7]The optical image is mapped onto the coordinate system of the electron micrograph because the sample undergoes deformations during the sample preparation stage. Also, the optical localization image contains much less structure within the image than the electron micrograph, and suffers less as a result

a procedure will then map the fluorescence from the sample onto the cellular structure imaged by electron microscopy.

The transformation algorithm that maps the optical image to the coordinate system of the electron micrograph uses an affine transformation. In an affine transformation, the x and y dimensions may be scaled and sheared independently, while also allowing for translation. It is a linear transformation, and the mathematical relationship is given by

$$[u, v] = [x, y, 1] * T^{-1}, \tag{6.1}$$

where the vectors u and v are the transformed, target coordinate system, x and y are the base coordinate system, and T is a 3x2 transformation matrix. An example of this transformation may be seen in Figure 6.3.

The uncertainty in the calculation of the matrix T is dependent on the number of fiducial markers in the sample, and their spatial distribution within the sample itself. To calculate the uncertainty in the transformation, the error for a given fiducial marker (A - E, shown in Figure 6.3) is calculated by removing that particular fiducial marker from the image registration algorithm, and running the registration algorithm with the remaining fiducial markers in the data set. The difference in location between the two markers is then calculated, and the geometric distance between the two is reported. This gives an estimation for the local error between the optical and electron micrograph images within the region of a given fiducial marker. Figure 6.4 illustrates the error associated with each of the fiducial markers shown in Figure 6.3.

Figure 6.5 shows the result of mapping the diffraction-limited optical signal onto the low magnification cross section of the *C. elegans*. Part **(a)** of the figure is the low magnification electron micrograph, while part **(b)** shows the overlay of the transformed diffraction-limited optical signal overlaid on top of the image. The tagged protein is a protein associated with the calcium channels of muscle cells, and localizes to the muscle tissue shown along the side of the worm, as can be seen in the figure. The fluorophore used is tdEos.[8]

of the transformation.

[8]Photo-convertible proteins undergo a color conversion in their emission upon excitation by ultravio-
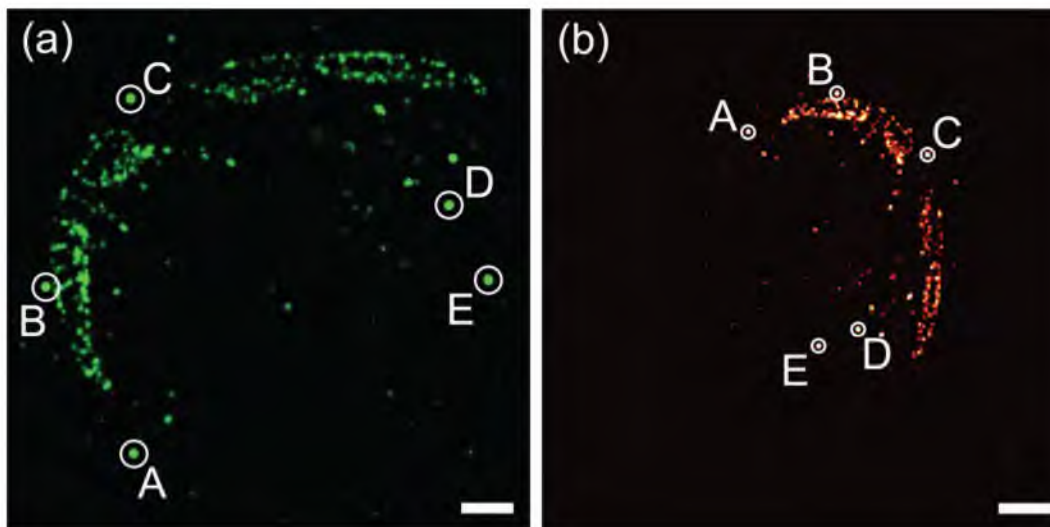
Figure 6.3. Images of the diffraction-limited fluorescence image from a cross-section of a *C. elegans* nematode. This is the entire diffraction-limited optical signal from the sample (of only which a part is shown in Figures 1.5 and 1.3). The signal is coming from ryanodine receptors (calcium channels) that are tagged with the fluorescent protein tdEos. Fiducial markers within the two images are circles in white, and correspondingly labeled A - E. Note the change in the values of the scale bar in the two images. **(a)** The original diffraction-limited optical image. Scale bar: 10 μm. **(b)** The same optical image as in **(a)**, but now transformed by an affine transformation to map onto the coordinate system of the electron micrograph sample specimen, derived from the coordinate transformations of the fiducial markers. As the reader can see, the image is both rotated and scaled. Scale bar: 20 μm. Sample preparation and data collection by the Jorgensen Lab, University of Utah.

In the top right of Figure 6.5, three high magnification images were taken, which are overlaid onto the low magnification image. Figure 6.6 shows a close-up view of one of these high magnification images. Part **(a)** of the figure shows just the high resolution electron micrograph, without any fluorescence overlay. Part **(b)** shows the diffraction-limited optical image super-imposed. Due to the disparity in resolution between the two, the underlying electron micrograph is obscured. If the localization microscopy image is used instead, as is shown in **(c)**, then the mapping of the optical signal to the electron micrograph can be better resolved. A further closeup may then be seen in part **(d)**. However, care must be taken in the information taken from this image. The area of this image is near fiducial marker "C", from Figures 6.3 and 6.4, which has $\approx$ 275 nm of

let light. Thus, they can be isolated temporally and spectrally, instead of just temporally as in the case of PA-GFP.
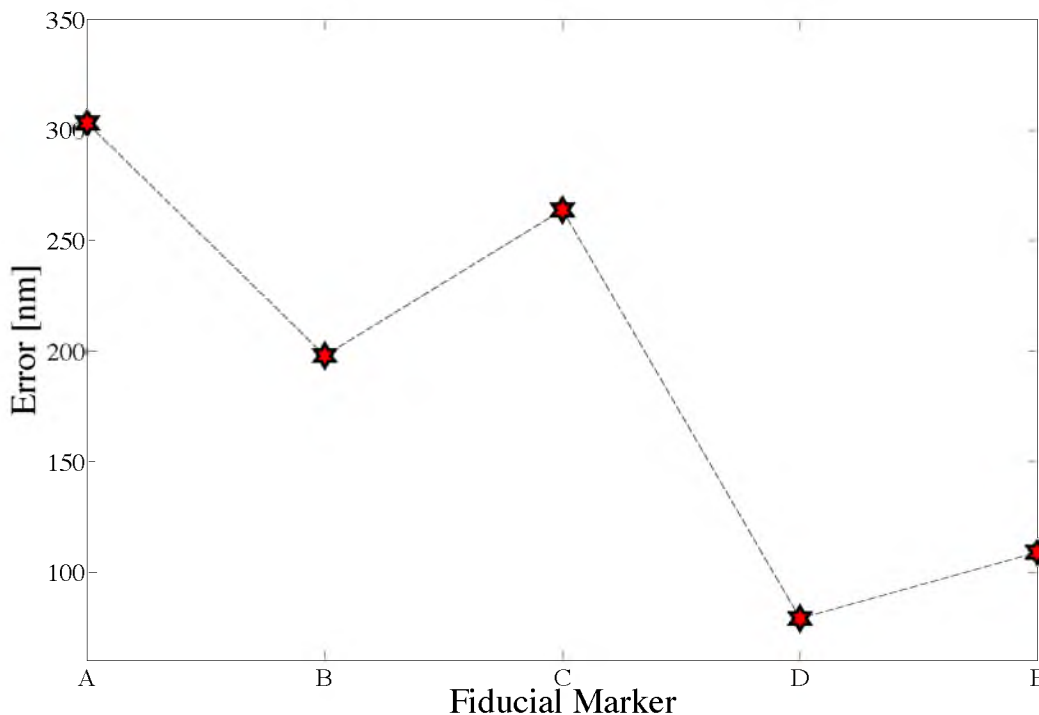
Figure 6.4. Error in the optical and electron micrograph image registration (in nanometers) between the optical and electron micrograph registration for each fiducial marker. The calculation of the error is described in the main text. As can be seen from the plot, the error is quite large, well above the localization uncertainty for the fluorophores in the optical image. Since the actual number of fiducial markers used in this example was only five over ≈ 80 μm, it can be expected that the error would be large. Further error is exacerbated by the fact that the low magnification electron image suffers from lateral distortions. This is due to the fact that the scan size that this image required is extremely large for a scanning electron microscope, and the field correction for such a large field of view is not entirely homogenous. Electron microscopes, since they use electrons instead of photons, must use electromagnetic "lenses" to steer the electrons, which are harder to engineer for a flat field of view than conventional glass lenses for light.

error associated with the optical and electron micrograph images. This large amount of error is associated with the image being near the edge of the low magnification electron micrograph, where the distortion effects are the greatest. Due to the low number of fiducial markers, it is difficult to calculate a proper transformation matrix.

Further work through members of the Jorgensen lab has been done in the area of increasing the fiducial marker density within the samples (data not shown). One method is to use fiducial markers whose fluorescence signal is outside of the spectral region of interest for the sample. That way, the fluorescence signal from the fiducial markers will
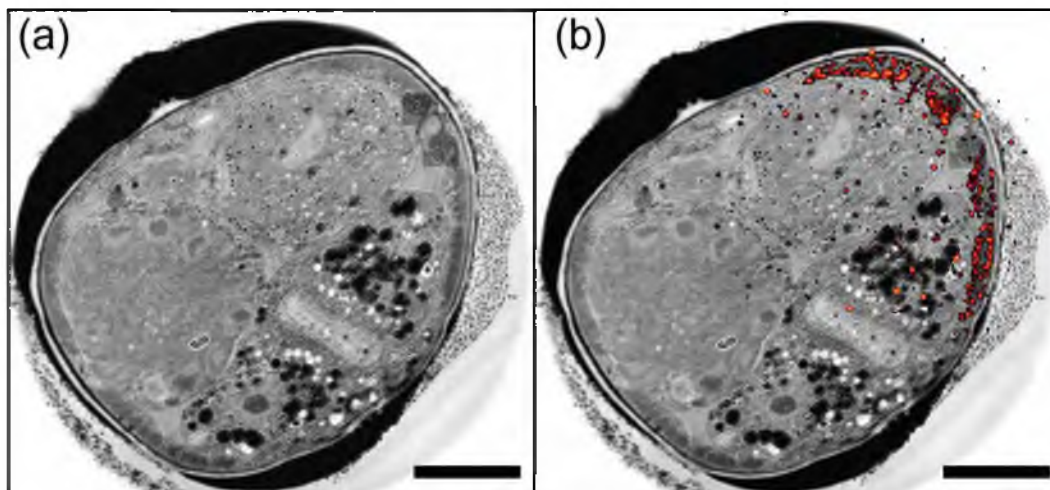
Figure 6.5. Correlation optical and electron microscopy image at the diffraction limit. Low magnification images of the cross-section of the *C. elegans* sample taken on a scanning electron microscope. This is a relatively large field of view for a scanning electron micrograph. **(a)** Electron micrograph of the entire cross-section. Three high magnification images may be seen in the top right of the cross-section. **(b)** Same electron micrograph, with the diffraction-limited optical signal super-imposed on top. Scale bar: 20 μm. Sample preparation and data collection by the Jorgensen Lab, University of Utah.

not mask the underlying signal from the sample.[9] The higher number of fiducial markers will increase the precision of the alignment registration. Another method is to take numerous high magnification images, and to stitch them all together into a composite image. The field distortions for each individual image will be greatly reduced, further improving image registration.

Figure 6.7 illustrates an example of this technique. Three high magnification images (as seen as the region of higher contrast in the top right of the images in Figure 6.5) are shown having undergone an autocorrelation routine to superimpose the images on top of each other. The data acquisition is as follows. A low magnification image is taken to identify a specific region of interest for high magnification imaging. Due to the smaller field of view of the high magnification images, multiple images must be stitched together to form a large field of view that is useable for correlation studies. The high magnification images are taken such that there is a slight overlap between the fields of

---

[9]The sample shown throughout this chapter suffered from the fiducial fluorescence and the fluorescent protein used (tdEos) having similar emission spectrums. If the density of the fiducial markers had been too high, then they would mask a large percentage of the region of interest.
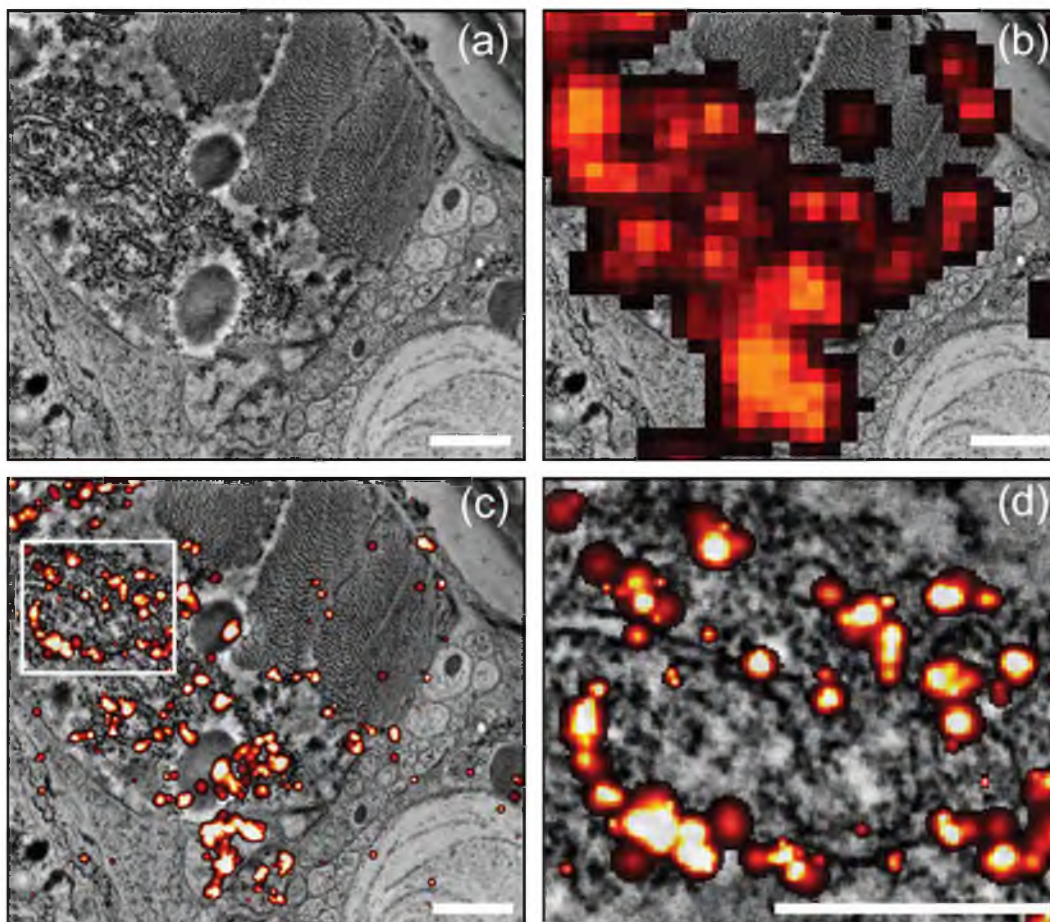
Figure 6.6. Correlation optical and electron microscopy image using localization microscopy. Close-up detail of Figures 6.3 and 6.5. **(a)** Detailed image of a high magnification electron micrograph of a section of the *C. elegans*. **(b)** Same close-up section with the diffraction-limited signal super-imposed. Due to the diffraction limit, the optical signal just masks and hides the underlying structure, giving little useful information regarding the localization of the fluorescent proteins in relation to the electron micrograph sample. **(c)** Super-resolution image of the signal from **(b)**. The location of the proteins may now be better discerned, giving more information regarding the location and functionality of the protein in question. **(d)** Image of the section of the image outlined by the white box in part **(c)**. Scale bar: 1 μm. Sample preparation and data collection by the Jorgensen Lab, University of Utah.

view of successive images. Due to the common imaging region, two fields of view may be stitched together into a composite image, and further images subsequently added.

The images are registered to each other via a normalized cross-correlation algorithm. Generally speaking, a cross-correlation is a comparison between the values of a parent image, $A(M_A, N_A)$, and a template matrix, $B(M_B, N_B)$, where B either partially or completely overlaps onto A. It is mathematically computed as
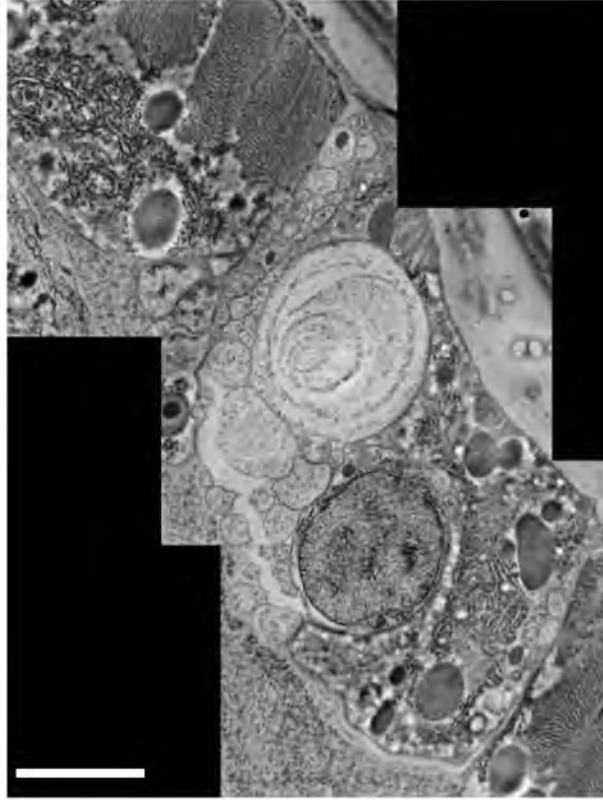
Figure 6.7. Composite image of three high magnification electron micrograph images. The field distortions are much lower when using a scanning electron microscope at high magnification, since the range of scan angles is much smaller. To compensate for the smaller field of view, multiple high magnification images may be stitched together. This is done through image cross-correlation. Slight contrast differences exist due to regions being imaged twice. Since the field distortions are minimized when using high magnification scans, the registration between the optical and election micrograph images will be more precise, and the error correspondingly lower. Scale bar: 2 μm.

$$C\left(i,j\right) = \sum_{m=0}^{M_A-1} \sum_{n=0}^{N_A-1} A\left(m,n\right) B^*\left(m+i,n+j\right), \tag{6.2}$$

where $0 \le i < M_A + M_B - 1$, and $0 \le j < N_A + N_B - 1$. $C\left(i,j\right)$ has its maximum value for given indices i and j when the two matrices are aligned such that they are shaped or overlap as much as possible. The template B is indexed over the parent image A, and C computed for each value of i and j. Generally speaking, the more structure and features present in an image, the greater the correlation values will be. Fortunately, electron micrographs images are rich in structure, and well suited to correlation studies.

To account for intensity variations between two images, it is customary to calculate the normalized cross-correlation. The normalized cross-correlation may be calculated

as 5

$$\gamma(\mu,v) = \frac{\sum_{x,y}[f(x,y)-\bar{f}_{\mu,v}][t(x-\mu,y-v)-\bar{t}]}{\left(\sum_{x,y}[f(x,y)-\bar{f}_{\mu,v}]^2 \sum_{x,y}[t(x-\mu,y-v)-\bar{t}]^2\right)^{\frac{1}{2}}},\qquad(6.3)$$

where f corresponds to the image in question, $\bar{t}$ is the mean of the template, and $\bar{f}_{\mu,v}$ is the mean of $f(x,y)$ in the region under the template. As is illustrated in Figure 6.7, this method works quite well for the high resolution images.

6.2.3 Synaptic Function Studies

The focus of the sample shown in this chapter has been on the localization of a single protein within the context of the cellular environment, namely that given by the context of an electron micrograph image. A further advantage of localization microscopy is the ability to determine and quantify the spatial coordinates of two proteins with respect to each other. This can be achieved by tagging two distinct proteins with two different fluorescent markers that have nonoverlapping emission spectra. The emission signal of the two can be spectrally separated, and viewed independently. As an example of this ability, consider the example shown in Figures 6.8 and 6.9 of a synaptic junction within a *C. elegans* nematode.

The images shown in Figure 6.8 are those of a chemical synapse, showing a synapse formed between a neuron and a muscle cell. The synaptic cleft is the extracellular space between a presynaptic terminal (neuron) and postsynaptic cell (muscle), into which the chemical cargo from the axon is released. The postsynaptic cell contains chemical receptors within its cell membrane that detect the chemical cargo released from the axon. Structures called synaptic vesicles within axons transport these neurotransmitter chemicals, and release their cargo upon interaction with the cellular membrane near a structure called the dense projection. The dense projection is located within an area of the neuron known as the active zone.[10] The typical spacing of the synaptic cleft is $\approx$ 20-40 nm, while synaptic vesicles are $\approx$ 30 nm in size.

---

[10]The active zone is the region of the axon membrane where synaptic vesicles interact with the cellular membrane and release their cargo.
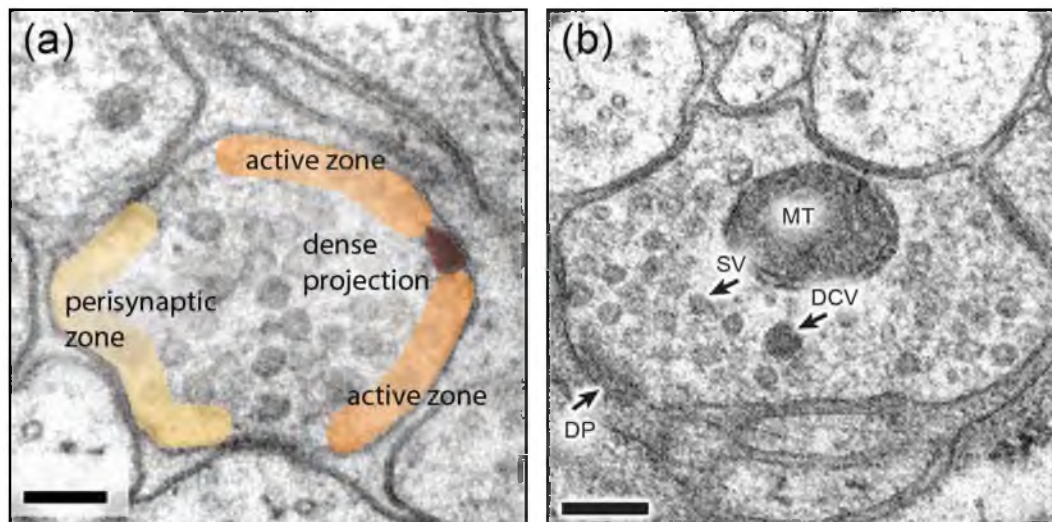
Figure 6.8. Electron micrographs of a neuromuscular junction in a *C. elegans* nematode. **(a)** Electron micrograph with cartoon illustration of key structural components. Synaptic vesicles within a synapse fuse with the plasma membrane proximal to the dense projection, releasing their cargo into the synaptic cleft. The chemical cargo is detected by receptors on the postsynaptic cell, in this case a muscle cell. **(b)** Key components of the active zone of a synapse. MT: mitochondria. SV: synaptic vesicles. DCV: dense core vesicle. DP: dense projection. Scale bar in all images: 100 nm. Sample preparation, data collection and images by the Jorgensen Lab, University of Utah.

Synaptic vesicles interact with the plasma membrane through interactions with synaptic vesicle and plasma membrane proteins, where they dock and fuse[11] with the plasma membrane and release their cargo. The dense projection appears to be the organizing center of the synapse and may be the home of presynaptic calcium channels and the major site of synaptic vesicle fusion. This interaction provides a system that can be well studied through the use of two-color investigations. Figure 6.9 shows a localization microscopy image of an interaction between two proteins associated with synaptic vesicles and the dense projection. The worm strain used in the images in Figure 6.9 is a strain where the native synaptotagmin-1 (snt-1) gene has been replaced with a modified variant of synaptotagmin-1 fused with a SNAP tag (synaptotagmin-1::SNAP) and with the orange organic dye TMR-Star (synaptotagmin-1::SNAP::TMR-Star).[12] Synaptotagmin is

---

[11] The actual model is still under investigation.

[12] Recent techniques, SNAP [2] and HALO [3], use suicide enzymes conjugated to the target protein in place of fluorescent proteins. Organic dyes are introduced to the cellular environment, where they bind to the suicide enzymes. The dye is then washed from the cell, leaving only dye attached to the target protein.
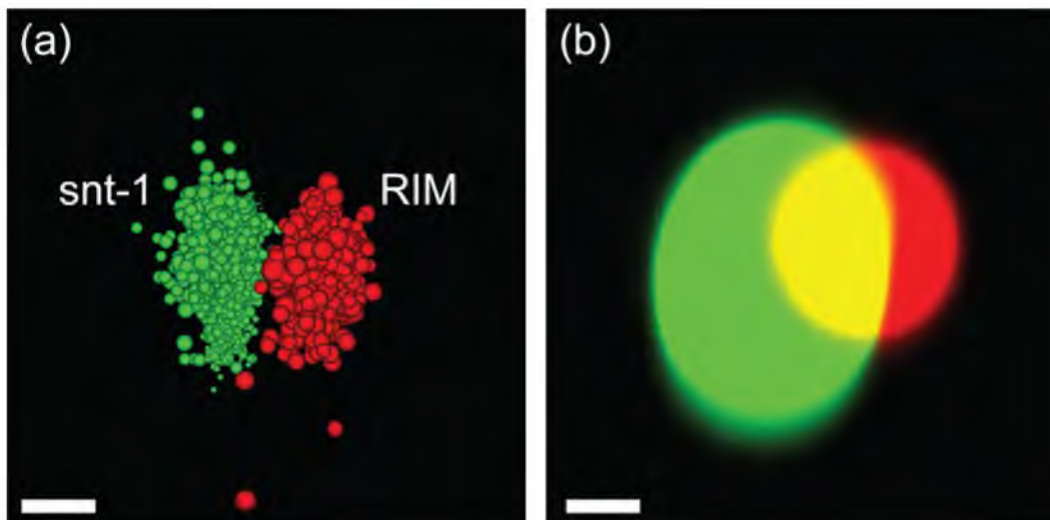
Figure 6.9. Localization images of the structure of a synapse in *C. elegans*. **(a)** Localization microscopy image of two proteins associated with the dense projection and synaptic vesicles, synaptotagmin-1 [snt-1] (green circles) and RIM (red circles). Synaptotagmin is the calcium sensor protein present in the membrane of synaptic vesicles. RIM is the dense projection protein required for the regulation of synaptic vesicle exocytosis. The image is rendered such that each individual localization is scaled as a spherical object with radius equal to the uncertainty in localization. The clear spatial distinction between the two proteins, within two adjacent and touching biological structures, is clearly visible. **(b)** "Diffraction-limted" image of **(a)**. Unlike part **(a)**, each localization is rendered as a 250 nm sphere. The size of each sphere causes them to merge together, effectively blurring and lowering the resolution of the image. The boundary between the two proteins is no longer discernible. Scale bar in all images: 100 nm. Sample preparation and data collection by the Jorgensen Lab, University of Utah.

the calcium sensor for synaptic vesicle and is an integral synaptic vesicle membrane protein. The second modification to the worm strain is an insertion of the dense projection protein RIM fused with a Halo tag (RIM::Halo). This protein localizes exclusively to the dense projection. RIM::Halo is labeled with the dye SiR (RIM::Halo:SiR), a near-IR fluorescent dye. Both proteins of interest now have two different color dyes attached, and can be individually localized simultaneously in the same specimen.

The image in Figure 6.9(a) shows a single presynapse imaged in an intact *C. elegans* labeled with synaptotagmin-1::SNAP::TMR-Star and RIM::Halo::SiR. The localization image is rendered such that each individual localization of the fluorophore is displayed as a sphere. The green circles are synaptotagmin-1::SNAP::TMR-Star (the synaptic vesicle protein) and the red circles are RIM::Halo::SiR (the dense projection protein).

The spatial boundary between the two proteins can be clearly seen in the figure. Due to the extremely close proximity between the two proteins, conventional diffraction-limited imaging would not be able to resolve this level of detail and organization of the two proteins with respect to each other.

These types of two-color imaging are prime candidates for correlation studies. Mapping the fluorescent images to the spatial map of the electron micrograph image would give direct evidence of the spatial location of the docking location of the synaptic vesicle at the dense projection. The two color channels can be registered to each other[13] and then mapped to the spatial coordinate system of the electron micrograph, showing in detail the fluorescence distribution over the cellular structure.

6.3   Summary and Final Conclusions

At the beginning of this dissertation, Figure 1.4 illustrated various types of microscopy by their respective chemical specificity as a function of their resolving power. While fluorescence microscopy is extremely flexible in terms of what sort of target proteins may be tagged and imaged, the resolving capabilities of optical microscopy is limited. Methods to circumvent the diffraction-limit of light[14] have enabled researchers the ability to visualize and quantify fluorescent emission below the conventional diffraction-limit codified by Abbe and Rayleigh. Collectively known as "nanoscopy," these methods have opened up a new era in biological imaging and study.

Figure 6.10 gives an updated variant on Figure 1.4. Replacing "fluorescence microscopy" with "nanoscopy," the methods available through optical means move further along the resolving axis, while maintaining its high levels of chemical specificity, a characteristic that made it such a popular medium in the first place. Ultimately, the weak-link of optical microscopy has been augmented and circumvented, while allowing the strengths that made optical microscopy extremely advantageous to biological

---

[13]Multicolor fiducial markers can allow for registration and calibration of the spatial shift, if present, between color channels on an optical instrument.

[14]The field of super-resolution microscopy is full of acronyms for the various differing modalities, which have been avoided in this dissertation. As a brief example, there is STED [4], GSDIM [5], PALM [6], FPALM [7], iPALM [8], STORM [9], dSTORM [2], SIM [10], I^5M [11], 4Pi [12], FIONA [13], SHREC [14], and DOPI [15].
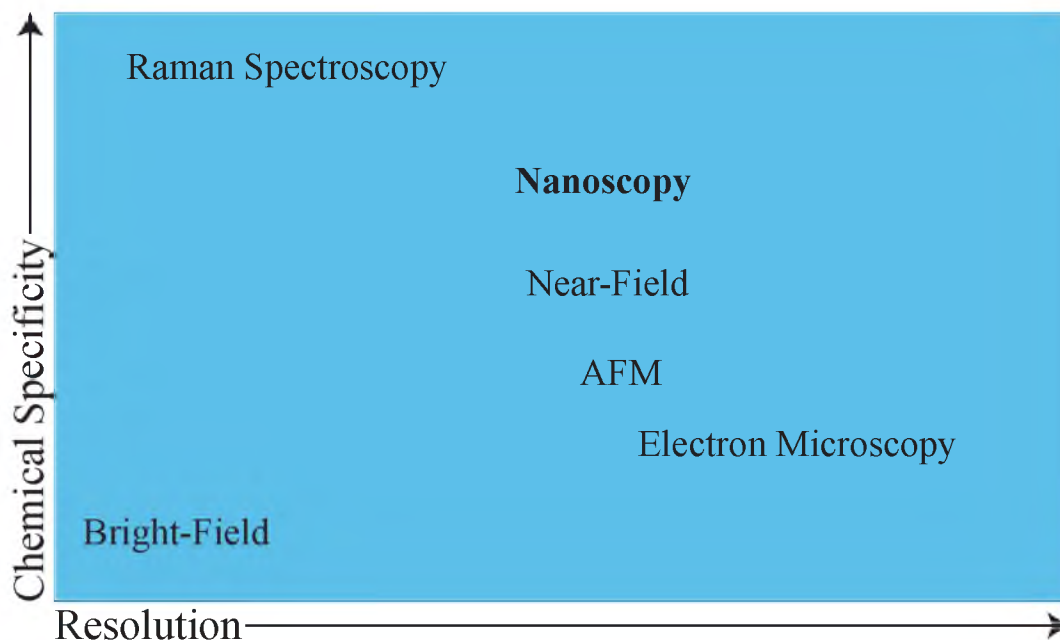
Figure 6.10. Updated chart of microscopy methods and their resolving power plotted as a function of chemical specificity. Using the collective word "nanoscopy" to denote any super-resolution optical technique, these methods move further along the resolution axis, while still preserving their high chemical specificity.

research to be preserved.

6.3.1   Advantages of Differing Super-Resolution Modalities

As was outlined briefly in Chapter 3, the field of super-resolution microscopy encompasses numerous techniques. From a practical standpoint, there are tradeoffs between the methods, and depending on the sample or experiment at hand, some are more advantageous than others. Multiple color studies generally eliminate STED microscopy methods, due to the complexity of the optical configuration and spectral requirements of the dyes used; even two-color imaging requires a lot of work in STED. Structured illumination and localization microscopy, on the other hand, are able to image three or four different colors within a single sample quite easily.

From the point of view of sample preparation, super-resolution methods such as structured illumination [10] (Section 3.1.2) require little to no change in the sample preparation techniques, while STED [4] microscopy (Section 3.1.3) requires only specific fluorescent tags. Localization microscopy requires more complicated and involved sample preparation techniques, but generally offers the best resolving power of the various

super-resolution techniques.

With the availability of open-source localization microscopy software packages, localization microscopy offers the easiest implementation of super-resolution microscopy, even with its more complicated sample preparation. The optical configuration is extremely simple, and does not require the complexity of STED or structured illumination. STED offers "instant" super-resolution, with the acquired raw images needing no post-processing unlike the heavy data analysis of structured illumination and localization microscopy.

6.3.2 Three-Dimensional Super-Resolution

The techniques illustrated in this paper solely discuss two-dimensional imaging. Numerous methods have been employed to determine axial positioning of a point-source below the diffraction-limit as well. The width of a PSF is generally about twice as large in the axial direction as in the lateral dimensions. Methods to encode axial information onto the emission PSF include using a cylindrical lens in the emission path to produce an asymmetric PSF whose shape depends on the axial location of the point-source [16], imaging two focal planes simultaneously within the sample [17], the generation of a double-helix-shaped emission PSF whose azimuthal rotation depends on the distance from the coverslip [18], and through the use of interference when imaging samples in a 4Pi configuration (using two opposing objectives, Section 3.1) [8, 19].

6.3.3 Further Developments in Optical Microscopy

Optical microscopy is also undergoing other rapid advancements, this time focused on drastic improvements in not spatial resolution, but temporal resolution. Recent breakthroughs in imaging hardware have allowed for faster and faster temporal resolution due to the introduction of scientific-grade CMOS cameras (sCMOS). These new cameras offer drastically larger fields of view and frame rate speeds than electron-multiplying CCD cameras, allowing for substantial increases in imaging speed, which is especially suited for live-cell imaging. Furthermore, sCMOS cameras offer a higher effective quantum yield than EMCCD cameras.[15] This is due to the fact that they do not amplify noise

---

[15]The signal amplification process of electron multiplying CCD cameras effectively doubles the noise level in the signal, since the amplification process affects both signal and noise. This has the combined

like an EMCCD, and with the correct noise characterization, produce better localization results than EMCCD cameras [20].

The focus of these new techniques are on live-cell imaging. Numerous new methods aim to combine fast imaging of whole biological specimens (whole cells, embryos, and organisms) using these new sCMOS cameras with optical configurations that limit the excitation laser intensity within the specimen. Photo-toxicity in live-cell imaging can cause biological and chemical damage to the specimen, especially if imaged over hours or days. Such methods include imaging samples with light sheets instead of either wide-field, where the entire sample is illuminated simultaneously, or confocal, which scans a focused, high intensity laser through the sample. Two objectives are used, and are placed at a 90° angle with respect to each other. One objective is used to deliver the excitation, while the second objective is used to collect the fluorescence emission. This allows for rapid imaging with minimal photo-toxicity to the sample. Numerous examples of light-sheet microscopy methods are given in references [21–26].

6.3.4   Final Thoughts

Optical microscopy is an extremely flexible tool, and has developed into an essential method for numerous biological investigations. A tool as simple as a piece of glass first allowed for the direct viewing of samples that were too small for the unaided eye to see, and such pieces of glass are still making a profound impact on biological research. While the techniques have become increasingly complex, the sensors better and faster, the light sources cheaper, stronger, brighter and more compact, and the analysis more computational, optical microscopy at its core is about pieces of glass collecting light and forming an image. The various capabilities available through those pieces of glass have become more intricate over time, and perhaps even more impactful than they were 400 years ago.

However, as was outlined in Chapters 2 and 3, there were always scientific questions that remained beyond the limits of what optical microscopy could provide. If the direct goal was the precise spatial arrangement of fluorophores within a sample, the diffraction limit of light set a boundary two orders of magnitude larger than the physical size of the

---

effect of halving the signal-to-noise, which effectively lowers the quantum efficiency in half.

proteins being studied. With the realization of the de Broglie wave theory of particles, scientists in the early part of the 20th century turned to using electrons instead of photons to push the bounds of resolution. This is the theory behind electron microscopy, which in practice is able to resolve structure on the nanometer scale. Unlike fluorescence microscopy, electron microscopy could neither label targets with the specificity of optical instruments, nor perform dynamic studies. Its high level of resolution, however, ensures that it will remain a staple in the imaging world for a long time to come.

It is hard to think of a single piece of imaging technology that has the ability to give the wide-range of investigative tools that fluorescence microscopy can and routinely does, even when considering diffraction-limited imaging. The revolution of super-resolution microscopy was to bring optical microscopy down to more appropriate spatial scales of the proteins and molecular machinery of the cellular environment, and to be able to combine it with the inherent advantages of the technique in general. The work presented in this dissertation is my attempt to push the boundaries of the field even further by attempting to maximize as much as possible the information content of the recorded signal, and to further push the precision with which the true spatial location of the cellular target may be identified. The use of this technique to further the incorporation of optical and electron microscopy is perhaps the most realistic implementation, with the intended aim of giving as a realistic interpretation of the spatial distribution of proteins within a biological system as possible, and to combine that with the ultrastructure given by an electron micrograph image.

It is currently an exciting time of development and research within the microscopy world, with many novel techniques and methods to pioneer. It is my hope that this work provides a stepping point for perhaps some of those projects to come.

6.4   References

[1]   S. Watanabe et al., Nature Methods **8**, 80 (2011).

[2]   T. Klein et al., Nature Methods **8**, 7 (2011).

[3]   G. V. Los et al., ACS Chemical Biology **3**, 373 (2008).

[4]   S. W. Hell and J. Wichmann, Optics Letters **19**, 780 (1994).

[5]   S. W. Hell and M. Kroug, Applied Physics B Laser and Optics **60**, 495 (1995).

[6] E. Betzig et al., Science (New York, NY) **313**, 1642 (2006).

[7] S. T. Hess, T. P. K. Girirajan, and M. D. Mason, **91**, 4258 (2006).

[8] G. Shtengel et al., Proceedings of the National Academy of Sciences of the United States of America **106**, 3125 (2009).

[9] M. J. Rust, M. Bates, and X. Zhuang, Nature Methods **3**, 793 (2006).

[10] M. G. Gustafsson, Journal of Microscopy **198**, 82 (2000).

[11] M. G. Gustafsson, D. A. Agard, and J. Sedat, Journal of Microscopy **195**, 10 (1999).

[12] S. Hell and E. H. K. Stelzer, Journal of the Optical Society of America A-Optics Image Science and Vision **9**, 2159 (1992).

[13] A. Yildiz et al., Science (New York, NY) **300**, 2061 (2003).

[14] L. S. Churchman, Z. Okten, R. S. Rock, J. F. Dawson, and J. A. Spudich, Proceedings of the National Academy of Sciences of the United States of America **102**, 1419 (2005).

[15] E. Toprak et al., Proceedings of the National Academy of Sciences of the United States of America **103**, 6495 (2006).

[16] B. Huang, W. Wang, M. Bates, and X. Zhuang, Science (New York, NY) **319**, 810 (2008).

[17] M. F. Juette et al., Nature Methods **5**, 527 (2008).

[18] S. R. P. Pavani and R. Piestun, Optics Express **16**, 22048 (2008).

[19] D. Aquino et al., Nature Methods **8**, 353 (2011).

[20] F. Huang et al., Nature Methods **10**, 653 (2013).

[21] C. J. Engelbrecht and E. H. Stelzer, Optics Letters **31**, 1477 (2006).

[22] P. J. Verveer et al., Nature Methods **4**, 311 (2007).

[23] M. Weber and J. Huisken, Current Opinion in Genetics & Development **21**, 566 (2011).

[24] T. A. Planchon et al., Nature Methods **8**, 417 (2011).

[25] Y. Wu et al., Nature Biotechnology **31**, 1032 (2013).

[26] B.-C. Chen et al., Science **346**, 1257998 (2014).

APPENDIX A

MATHEMATICAL DESCRIPTION OF THE
POINT-SPREAD FUNCTION

This Appendix will discuss the mathematical framework associated with focusing the emission signal from a radiating source by a lens onto a detector. It will discuss the emission properties of the source and their transformations due to the optical elements, as well as the full vectorial nature of the focusing fields. This is in constrast to the scalar approximations usually given in optical textbooks, such as those given in References [1–3]. Instead, this Appendix will follow more of the format outlined in References [4–6]. To delve further into the problem, one must look at the transformations of the electric fields due to refraction at the interface of the objective lens with the medium of the dipole source. Before that is accomplished, however, another look at the angular spectrum representation of the electric field is required.

A.1   The Angular Spectrum Representation of the Far-Field

The angular spectrum representation mathematically describes how a local field distribution in the plane containing the origin $(z = 0)$ is mapped onto other planes $(z = z_0)$, and more generally, how the field propagates through space. The inverse of this is what is the field distribution if a far-field field is focused onto an image plane. Recall that the angular representation is given by [4]

$$\mathbf{E}(x, y, z) = \iint\limits_{-\infty}^{\infty} \hat{\mathbf{E}}(k_x, k_y; 0) e^{i[k_x x + k_y y \pm k_z z]} dk_x dk_y. \tag{A.1}$$

The far-field approximation to the field is what is of interest in this derivation, namely what is the behavior at the point $\mathbf{r} = \mathbf{r}_\infty$. To do so, it is appropriate to use a unit vector $\mathbf{s}$ that maps in the direction of $\mathbf{r}_\infty$, given by

$$\mathbf{s} = (s_x, s_y, s_z) = \left(\frac{x}{r}, \frac{y}{r}, \frac{z}{r}\right), \tag{A.2}$$

where, as usual, $r = \sqrt{x^2 + y^2 + z^2}$ in the direction of $\mathbf{r}_\infty$. Calculating the far-field, $\mathbf{E}_\infty$, requires the substitution $r \to \infty$. This result may now be used in Equation A.1. Since it is the far-field signal in question, evanescent waves do not contribute to the resultant electric field, and can be ignored. This entails looking only at the wavevectors up to k. The result is now

$$\mathbf{E}_\infty\left(s_x, s_y, s_z\right) = \lim_{kr \to \infty} \iint_{\left(k_x^2 + k_y^2\right) \le k^2} \hat{\mathbf{E}}\left(k_x, k_y; 0\right) e^{\left. ikr \right| \frac{k_x}{k} s_x + \frac{k_y}{k} s_y \pm \frac{k_z}{k} s_z \right|} \mathrm{d}k_x \mathrm{d}k_y. \tag{A.3}$$

This result is complicated, and requires an in-depth analysis using the method known as stationary phase. For an extended derivation of the result, the reader is directed to Reference [7]. The result of may be expressed as [4]

$$\mathbf{E}_\infty\left(s_x, s_y, s_z\right) = -2\pi i k s_z \hat{\mathbf{E}}\left(k s_x, k s_y; 0\right) \frac{e^{ikr}}{r}. \tag{A.4}$$

The qualitative meaning of this equation is that the far-fields are entirely defined by the Fourier spectrum of the fields $\hat{\mathbf{E}}\left(k_x, k_y; 0\right)$ in the object plane, dependent on the substitutions $k_x \to k s_x$ and $k_y \to k s_y$. The result of this is that the unit vector $\mathbf{s}$ fulfills the relationship

$$\mathbf{s} = \left(s_x, s_y, s_z\right) = \left(\frac{k_x}{k}, \frac{k_y}{k}, \frac{k_z}{k}\right). \tag{A.5}$$

The ability to use the concept of geometrical optics stems from the fact that only one plane wave with a particular wavevector k of the angular spectrum at a position $z = 0$ contributes to the far-field along a point located in the direction of a unit vector denoted by s. All other plane waves are canceled along this vector s due to destructive interference. The immediate result of this is the fact that the far-field may be represented as a collection of individual rays, with each ray characterized by a unique plane wave. Combining Equation A.4 and Equation A.5, one obtains

$$\hat{\mathbf{E}}\left(k_x, k_y; 0\right) = \frac{i r e^{-ikr}}{2\pi k_z} \mathbf{E}_\infty\left(k_x, k_y\right). \tag{A.6}$$

Inserting this expression into the Equation A.1, the result is [8]

$$\mathbf{E}(x, y, z) = \frac{i r e^{-ikr}}{2\pi} \iint_{\left(k_x^2 + k_y^2\right) \le k^2} \mathbf{E}_\infty\left(k_x, k_y\right) e^{i\left[k_x x + k_y y \pm k_z z\right]} \frac{1}{k_z} \mathrm{d}k_x \mathrm{d}k_y. \tag{A.7}$$

A.2 The Focusing of Electric Fields

In dealing with the mathematical derivation of the electric fields of an optical beam, it is necessary to look at the boundary conditions that exist between the lens focusing the light and the incident optical field [9, 10]. In this treatment, the first assumption is that the fields near an optical lens are treated as dictated by geometrical optics, and that an aplanatic lens is being used in the system. An aplanatic lens obeys both the sine condition and the intensity law. The sine condition, as shown in Figure A.1(a), states that every optical ray, either emerging from or converging to the focal point of an aplanatic system, intersects its conjugate ray at a sphere concentric with the focal point with radius f, where f is the focal length of the lens. The term conjugate ray refers to a ray that is traveling parallel to the optical axis. If the conjugate ray is diverting at an angle of θ, the distance the ray is from the optical axis is $h = f \sin \theta$. In other words, the sine condition is merely the refraction of the light rays at the surface of the lens.

The second condition of an aplanatic system is merely another manner in which to write the conservation of energy. The geometrical representation deals with the optical field as a collection of light rays, and the energy propagating along each ray through the optical system (neglecting losses at each optical element) must remain constant. Therefore, the energy that is incident on a lens is equal to the energy that leaves the lens. As detailed in Figure A.1(b), the fields before and after the lens must obey [9]

$$|\mathbf{E}_2| = |\mathbf{E}_1| \sqrt{\frac{n_1}{n_2}} \sqrt{\frac{\mu_2}{\mu_1}} \cos^{1/2} \theta. \tag{A.8}$$

Since the magnetic permeability for materials that are used in optical systems (at optical
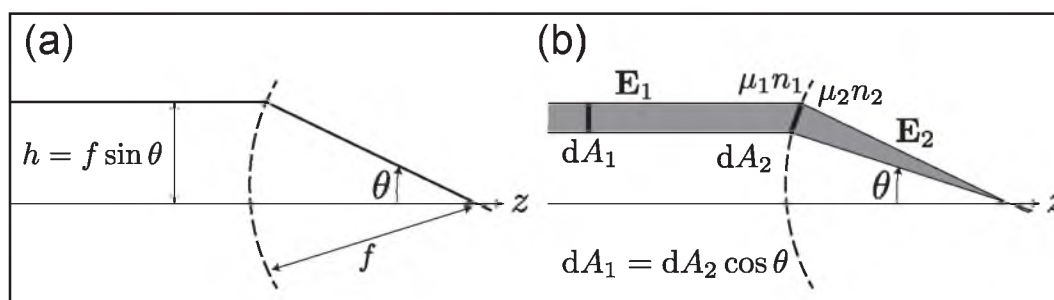
Figure A.1. Schematic of optical geometry through a focusing lens. For a system obeying geometrical optics: **(a)** Sine condition. **(b)** Intensity law; the energy content of a single ray must stay constant. Adapted from [4].

frequencies) is equal to one, it can be ignored in further considerations. With all of these considerations, the aplanatic system may be represented as shown in Figure A.2. Incident rays are refracted at the sphere of radius f, whose intersections are denoted as $(x_\infty, y_\infty, z_\infty)$. The focusing lens transforms a system in cylindrical coordinates to one into spherical coordinates. The cylindrical system is described through the unit vectors $\mathbf{n}_\rho$ and $\mathbf{n}_\phi$, while the spherical coordinate system is described through the unit vectors $\mathbf{n}_\phi$ and $\mathbf{n}_\theta$. For convenience, the incident field $\mathbf{E}_{\text{inc}}$ is decomposed into orthogonal components $\mathbf{E}_{\text{inc}}^{(s)}$ and $\mathbf{E}_{\text{inc}}^{(p)}$, where (s) and (p) stand for s and p-polarization, respectively. Expressing these terms as unit vectors, the results are given by [4]

$$\begin{aligned} \mathbf{E}_{\text{inc}}^{(s)} &= \left| \mathbf{E}_{\text{inc}} \cdot \mathbf{n}_\phi \right| \mathbf{n}_\phi \\ \mathbf{E}_{\text{inc}}^{(p)} &= \left| \mathbf{E}_{\text{inc}} \cdot \mathbf{n}_\rho \right| \mathbf{n}_\rho. \end{aligned} \tag{A.9}$$

These two orthogonal components of $\mathbf{E}$ will interact differently at the boundary of the lens. The unit vector $\mathbf{n}_\phi$ is not affected by the refraction of the incident field, whereas the unit vector $\mathbf{n}_\rho$ is mapped to the unit vector $\mathbf{n}_\theta$. The refracted electric field, far from the lens, may then be described as [4]

$$\mathbf{E}_\infty = \left| t^s \left| \mathbf{E}_{\text{inc}} \cdot \mathbf{n}_\phi \right| \mathbf{n}_\phi + t^p \left| \mathbf{E}_{\text{inc}} \cdot \mathbf{n}_\rho \right| \mathbf{n}_\theta \right| \sqrt{\frac{n_1}{n_2}} \cos^{1/2}\theta, \tag{A.10}$$

where, for completeness, the Fresnel coefficients t^s and t^p have been included.
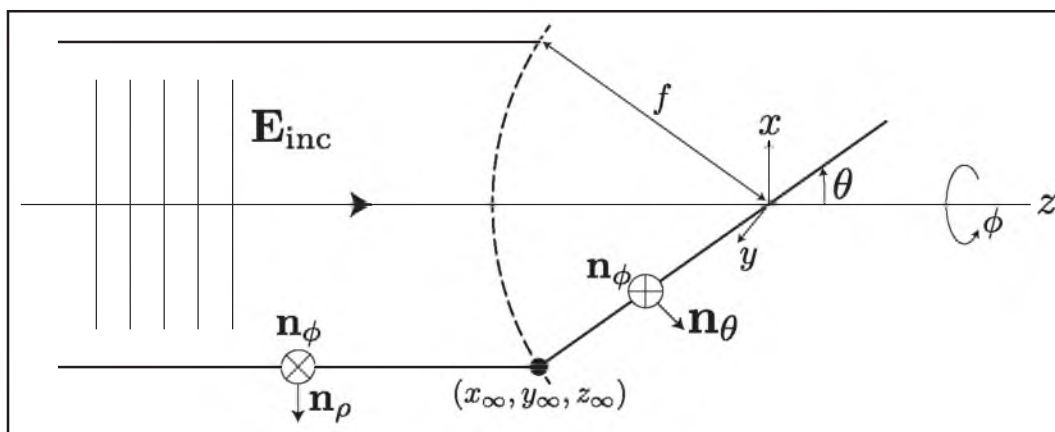
Figure A.2. Geometrical representation and definition of coordinates for an aplanaptic lens system. Adapted from [4].

The unit vectors $\mathbf{n}_\rho$, $\mathbf{n}_\phi$, and $\mathbf{n}_\theta$ can now be expressed in terms of their Cartesian counterparts $\mathbf{n}_x$, $\mathbf{n}_y$, and $\mathbf{n}_z$. Using the spherical coordinates θ and ϕ, the result is

$$\mathbf{n}_\rho = \mathbf{n}_x \cos\phi + \mathbf{n}_y \sin\phi$$

$$\mathbf{n}_\phi = -\mathbf{n}_x \sin\phi + \mathbf{n}_y \cos\phi \tag{A.11}$$

$$\mathbf{n}_\theta = \mathbf{n}_x \cos\theta \cos\phi + \mathbf{n}_y \cos\theta \sin\phi - \mathbf{n}_z \sin\theta.$$

Inserting these into Equation A.10, the field just after the focusing lens becomes [4]

$$
\mathbf{E}_\infty \left(\theta, \phi \right) = t^s \left(\theta \right) \left[\mathbf{E}_{\text{inc}} \left(\theta, \phi \right) \cdot \begin{pmatrix} -\sin\phi \\ \cos\phi \\ 0 \end{pmatrix} \right] \begin{pmatrix} -\sin\phi \\ \cos\phi \\ 0 \end{pmatrix} \sqrt{\frac{n_1}{n_2}} \cos^{1/2}\theta
$$
$$
+ t^p \left(\theta \right) \left[\mathbf{E}_{\text{inc}} \left(\theta, \phi \right) \cdot \begin{pmatrix} \cos\phi \\ \sin\phi \\ 0 \end{pmatrix} \right] \begin{pmatrix} \cos\phi\cos\theta \\ \sin\phi\cos\theta \\ -\sin\theta \end{pmatrix} \sqrt{\frac{n_1}{n_2}} \cos^{1/2}\theta. \tag{A.12}
$$

Furthermore, $\mathbf{E}_\infty$ may be expressed in terms of the spatial frequencies k_x and k_y using the substitutions $k_x = k\sin\theta\cos\phi$, $k_y = k\sin\theta\sin\phi$, and $k_z = k\cos\theta$. Consequently, the far-field can be expressed in a form of $\mathbf{E}_\infty$ and inserted into Equation A.7, meaning that the fields at the focus of the lens are entirely due to the far-field components. Due to symmetry, it is best to describe the fields in terms of θ and ϕ. Using the transformations $x = \rho\cos\phi$, $y = \rho\sin\phi$, and the differential element transformation of $\frac{1}{k_z}dk_x dk_y = k\sin\theta d\theta d\phi$, the angular spectrum representation of Equation A.7 may be written as [4]

$$
\mathbf{E}\left(\rho, \varphi, z \right) = \frac{ikfe^{-ikf}}{2\pi} \int_0^{\theta_{\text{max}}} \int_0^{2\pi} \mathbf{E}_\infty \left(\theta, \phi \right) e^{ikz\cos\theta} e^{ik\rho\sin\theta\cos(\phi-\varphi)} \sin\theta d\phi d\theta. \tag{A.13}
$$

where φ represents a point in the focal field, while ϕ represents a point on the focusing lens. Also, r has been replaced by the focal length of the lens, f, and the limits of integration in θ represent the physical limitations of the lens itself. If the incident electric field $\mathbf{E}$ is known, along with the physical properties of the lens, such as the numerical aperture NA and focal length f, the focal field may be calculated.

A.3   The Point-Spread Function

Now that the means for describing the electric field at a focal point as a result of a far-field electric field being transformed by a lens are defined and available, the electric field

produced by a single point source is needed. To begin, the mathematical framework of the Green's function $\overset{\leftrightarrow}{\mathbf{G}}$ can be expressed in spherical coordinates (r, θ, ϕ) as [4]

$$\overset{\leftrightarrow}{\mathbf{G}}_\infty(\mathbf{r}, 0) = \frac{e^{ikr}}{4\pi r} \times \begin{bmatrix} \left(1 - \cos^2\phi \sin^2\theta\right) & -\sin\phi\cos\phi\sin^2\theta & -\cos\phi\sin\theta\cos\theta \\ -\sin\phi\cos\phi\sin^2\theta & \left(1 - \sin^2\phi\sin^2\theta\right) & -\sin\phi\sin\theta\cos\theta \\ -\cos\phi\sin\theta\cos\theta & -\sin\phi\sin\theta\cos\theta & \sin^2\theta \end{bmatrix} \quad \text{(A.14)}$$

To obtain the electric field, $\overset{\leftrightarrow}{\mathbf{G}}$ is then multiplied by the dipole moment μ. To account for refraction at the objective of focal length f, and again at the focusing lens with focal length f', the transformations used above in mapping $\mathbf{n}_x$ and $\mathbf{n}_y$ to $\mathbf{n}_\theta$ and $\mathbf{n}_\phi$ are used. If the discussion is limited to a dipole aligned along the x-axis, $\mu = \mu_x \mathbf{n}_x$, the electric field just after the second (focusing) lens becomes

$$\mathbf{E}_\infty^{(x)}(\theta, \phi) = \frac{\omega^2 \mu_x}{\epsilon_0 c^2} \frac{e^{ikf}}{8\pi f} \times \begin{bmatrix} (1 + \cos\theta\cos\theta') - (1 - \cos\theta\cos\theta')\cos 2\phi \\ -(1 - \cos\theta\cos\theta')\sin 2\phi \\ -2\cos\theta\sin\theta'\cos\theta \end{bmatrix} \sqrt{\frac{n\cos\theta'}{n'\cos\theta}},$$

$$\text{(A.15)}$$

where $\sin\theta' = (f/f')\sin\theta$, and $\cos\theta' = \sqrt{1 - (f/f')^2\sin^2\theta}$, due to the sine condition and conservation of energy, respectively. While the current derivation is strictly looking at a dipole oriented along the x-axis, the principle of the derivation remains the same for a dipole oriented in any arbitrary manner. The resultant electric field would be a linear combination of the electric field due to dipoles oriented along the x, y, and z axes, i.e., $\mathbf{E}_\infty(\theta, \phi) = \mathbf{E}_\infty^{(x)} + \mathbf{E}_\infty^{(y)} + \mathbf{E}_\infty^{(z)}$. Now that the electric field has been calculated, all that remains is to plug the expression for the electric field into the expression given by Equation A.13.

To simplify the expression, the assumption $f \ll f'$ is made, which allows one to ignore the contribution of $\cos\theta'$, and to make the approximation $\left|1 \pm (f/f')^2\sin^2\theta\right|^{1/n} \approx 1 \pm \frac{1}{n}\left(\frac{f}{f'}\right)^2\sin^2\theta$. Armed with this information, the analytic result may be written as

$$\mathbf{E}(\rho, \varphi, z) = \frac{\omega^2}{\epsilon_0 c^2} \overset{\leftrightarrow}{\mathbf{G}}_{\text{PSF}}(\rho, \varphi, z) \cdot \mu, \quad \text{(A.16)}$$

where the dyadic point-spread function $\overset{\leftrightarrow}{\mathbf{G}}_{\text{PSF}}$ is given by the expression

$$\overset{\leftrightarrow}{\mathbf{G}}_{\text{PSF}} = \frac{ik'}{8\pi}\frac{f}{f'}e^{i(kf - k'f')} \begin{bmatrix} \left(\tilde{I}_{00} + \tilde{I}_{02}\cos 2\varphi\right) & \tilde{I}_{02}\sin 2\varphi & 2i\tilde{I}_{01}\cos\varphi \\ \tilde{I}_{02}\sin 2\varphi & \left(\tilde{I}_{00} - \tilde{I}_{02}\cos 2\varphi\right) & 2i\tilde{I}_{01}\sin\varphi \\ 0 & 0 & 0 \end{bmatrix} \quad \text{(A.17)}$$

with the integrals $\tilde{I}_{00} - \tilde{I}_{02}$ defined as [4, 6, 10]

$$\tilde{I}_{00}\left(\rho, z\right) = \int_{0}^{\theta_{\max}} \cos^{1/2}\theta \sin\theta \left(1 + \cos\theta\right) J_0\left(k'f/f'\rho\sin\theta\right) g\left(\theta\right) \mathrm{d}\theta \qquad \text{(A.18)}$$

$$\tilde{I}_{01}\left(\rho, z\right) = \int_{0}^{\theta_{\max}} \cos^{1/2}\theta \sin^2\theta J_1\left(k'f/f'\rho\sin\theta\right) g\left(\theta\right) \mathrm{d}\theta \qquad \text{(A.19)}$$

$$\tilde{I}_{02}\left(\rho, z\right) = \int_{0}^{\theta_{\max}} \cos^{1/2}\theta \sin\theta \left(1 - \cos\theta\right) J_2\left(k'f/f'\rho\sin\theta\right) g\left(\theta\right) \mathrm{d}\theta \qquad \text{(A.20)}$$

where $g\left(\theta\right) = e^{ik'z\left[1 - 1/2(f/f')^2\sin^2\theta\right]}$. Again, φ describes a point at the focal field, while ϕ represents the field at the lens element. Furthermore, as in Figure 2.8, the prime designation indicates the index of refraction of the medium at the focal field.

The derivations presented here are the full vectorial solutions. In $\overleftrightarrow{\mathbf{G}}_{\text{PSF}}$, for instance, the columns represent the field of a dipole oriented along the x, y, and z axes. In this instance, since the assumption was made that $f \ll f'$, the longitudinal field E_z is zero.

Equations A.18 - A.20 describe the vectorial mapping of the electric field of a source emitter to the focal point in the image plane. The final result depends on the numerical aperture of the lens, $NA = n\sin\theta_{\max}$, since the limits of integration in the identities $\tilde{I}_{00} - \tilde{I}_{02}$ depend on $\theta_{\max}$. The magnification of the system is defined as $M = \frac{n}{n'}\frac{f'}{f}$. Since the intensity of an optical field is given by the square of the electric field, and this is what an optical detector responds to, the calculation of the PSF will depend on the square of the electric field. Again, simplifications may be made to create a first-order analytic approximation. Firstly, the assumption may be made that the dipole is parallel to the x-axis, and that $\theta_{\max}$ is small enough to warrant the approximations of $\cos\theta \approx 1$ and $\sin\theta \approx \theta$. Furthermore, in the image plane the exponential terms in Equations A.18 - A.20 are of order unity, and J_2 goes to zero for small values of θ. All that remains is the integral for $\tilde{I}_{00}$, which may be integrated analytically using the identity $\int xJ_0\left(x\right)\mathrm{d}x = xJ_1\left(x\right)$. With these approximations in hand, the paraxial point-spread function may be written as [4]

$$\lim_{\theta_{\max} \ll \pi/2}\left|\mathbf{E}\left(x, y, z = 0\right)\right|^2 = \frac{\pi^4}{\epsilon_0^2 nn'}\frac{u_x}{\lambda^6}\frac{NA^4}{M^2}\left[2\frac{J_1\left(2\pi\tilde{\rho}\right)}{\left(2\pi\tilde{\rho}\right)}\right]^2, \qquad \text{(A.21)}$$

where $\tilde{\rho}$ is defined as $\tilde{\rho} = \frac{NA\rho}{M\lambda}$. Thus, the image of a point source imaged by an objective and focusing lens produces a point-spread function whose overall shape is governed by the Airy equation. The more conventional scalar form given in optical text books of the diffraction of a beam passing through a circular aperture again yields the Airy profile, but is purely a scalar result. Furthermore, such a derivation does not take into consideration the parameters discussed in this Appendix, such as the emission profile of the point source, the propagation of fields from the source to the image plane, and the coordinate transformations of the electric field due to the objective and focusing lens. The actual function derived here is dependent on the orientation of the dipole, which means that the functional form of the focus spot is different for differing oriented dipoles.

A.4 References

[1] G. R. Fowles, *Introduction to Modern Optics*, Courier Dover Publications, New York, NY, 2nd edition, 1989.

[2] E. Hecht, *Optics*, Addison-Wesley, San Francisco, CA, 4th edition, 2002.

[3] A. Lipson, S. G. Lipson, and H. Lipson, *Optical Physics*, Cambridge University Press, Cambridge, 4th edition, 2010.

[4] L. Novotny and B. Hecht, *Principles of Nano-Optics*, Cambridge University Press, Cambridge, 1st edition, 2006.

[5] M. Born and E. Wolf, *Principles of Optics: Electromagnetic Theory of Propagation, Interference and Diffraction of Light*, Cambridge University Press, Cambridge, 7th edition, 1999.

[6] C. J. R. Sheppard and T. Wilson, Proceedings of the Royal Society of London. Series A. Mathematical and Physical Sciences **379**, 145 (1982).

[7] L. Mandel and E. Wolf, *Optical Coherence and Quantum Optics*, Cambridge University Press, Cambridge, 1995.

[8] E. Wolf, Proceedings of the Royal Society of London. Series A. Mathematical and Physical Sciences **253**, 349 (1959).

[9] B. Richards and E. Wolf, Proceedings of the Royal Society of London. Series A. Mathematical and Physical Sciences **253**, 358 (1959).

[10] J. Enderlein, Optics Letters **25**, 634 (2000).

APPENDIX B

FISHER INFORMATION THEORY

This Appendix will discuss the use of the Fisher Information and its role in estimating the precision for which a parameter may be estimated with regard to a given statistical distribution. Due to the fact that the emission of photons by a source is stochastic in nature, the data collected by the detector are as well. This implies that the coordinates of the detected photons on the face of the detector are independent and identically distributed according to the density function $f_\theta(r)$. The estimation of the position of a single point-source is determined from the experimental data, namely the coordinates on the camera in which the signal photons are recorded. Since the process of emission and detection is a stochastic process as stated above, the estimation of the source becomes a statistical problem. If the underlying density function is known, the localization accuracy may be calculated by the use of the Fisher information matrix [1].

In characterizing the fundamental uncertainty involved with localization microscopy, various imaging parameters such as photon counts, background noise, and camera pixel size, must be considered. The underlying fundamentals, however, entail localizing a distribution to extract an uncertainty in the mean value of the distribution. The strength of the technique does not rely on particular localization algorithms or methodologies when fitting data to a theoretical model. Calculation of the Fisher information matrix yields the fundamental limit of how well a particular distribution can be localized to give inherent information regarding the location of its source. In particular, the inverse of the Fisher information matrix, $I(\theta)$, provides a lower bound for the variance of an unbiased estimator, $\hat{\theta}$. More specifically, the Cramér-Rao lower bound, $\mathrm{var}\left(\hat{\theta}\right) \geq I^{-1}$ [1]. If this fundamental lower bound can be calculated for a given photon distribution, then the localization limit can be derived for a particular distribution. This concept will be discussed below.

B.1 Derivation of the Fisher Information Matrix

For single-molecule microscopy, the counting process is denoted by $N(t), t \geqslant 0$. For every detected photon, the spatial coordinates are independent and identically distributed random variables, governed by the density function $f_\theta(r) = \left(1/M^2\right)\left(r/M - \theta\right)$, where r spans all space, f is the function describing the photon distribution on the detector surface, M is the magnification of the optical system, and θ is the position of the point-source in the object plane. The overall optical efficiency of the system at hand is denoted by Γ.

Following the convention of [2–4], the Fisher information matrix is given by the following expression:

$$\mathbf{I}(\theta) = E\left[\left(\frac{\partial \mathscr{L}\left(\theta|z_1, \cdots, z_K\right)}{\partial \theta}\right)\left(\frac{\partial \mathscr{L}\left(\theta|z_1, \cdots, z_K\right)}{\partial \theta}\right)^T\right], \tag{B.1}$$

where $E[\cdot]$ is the expectation operation with respect to the underlying density function f_θ. The log-likelihood function is then given by

$$\mathscr{L}\left(\theta|z_1, \cdots, z_K\right) = \ln\left|p\left(T_1 = t_1, \cdots, T_K = t_K | Z(t) = K\right)\right| + \ln\left|P\left(Z(t) = K\right)\right| \sum_{k=1}^{K} \ln\left|f_\theta\left(r_k\right)\right|. \tag{B.2}$$

In the above expression, $z_1, \cdots, z_K$ represent the observed data with the definition $z_k = \left(r_k, t_k\right)$, where $r_k = \left(x_k, y_k\right)$ are the spatial coordinates of the kth detected photon, t_k the arrival times, $0 < t_1 \leqslant t_2 \leqslant \cdots \leqslant t_K$, and $k = 1, \cdots, K$. Furthermore, $Z(\cdot)$ represents the counting process describing the photon counting process [1].

Assuming a density function f_θ satisfies the regularity conditions [2, 3], the Fisher information matrix may be written then in the following form:

$$\mathbf{I}(\theta) = \Gamma E\left[N(t)\right] \begin{bmatrix} \int\limits_{\Re^2} \frac{1}{q(x,y)}\left(\frac{\partial q(x,y)}{\partial x}\right)^2 \mathrm{d}x\mathrm{d}y & \int\limits_{\Re^2} \frac{1}{q(x,y)}\frac{\partial q(x,y)}{\partial x}\frac{\partial q(x,y)}{\partial y}\mathrm{d}x\mathrm{d}y \\ \int\limits_{\Re^2} \frac{1}{q(x,y)}\frac{\partial q(x,y)}{\partial x}\frac{\partial q(x,y)}{\partial y}\mathrm{d}x\mathrm{d}y & \int\limits_{\Re^2} \frac{1}{q(x,y)}\left(\frac{\partial q(x,y)}{\partial y}\right)^2 \mathrm{d}x\mathrm{d}y \end{bmatrix}, \tag{B.3}$$

with the assumption that the counting process N is a Poisson process with rate A. Thus, $E[N(t)] = At$. If the distribution at hand is symmetric, then the off-diagonal elements go to zero. The expression in Equation B.3 can then be used to derive the fundamental limit in which a given distribution can accurately localized.

B.2 Derivation of Airy and Gaussian Profile Localization Estimation Values

In this section, the Fisher information matrix will be calculated for the Airy and Gaussian profiles. These two profiles are significant because the Airy profile describes the true mathematical distribution of the PSF in the image plane, while the Gaussian is the approximation used in most localization algorithms, due to the increase in computational speed.

B.2.1 Airy Profile

For the Airy profile, the PSF is given by

$$q(x,y) = \frac{J_1^2\left(\alpha\sqrt{x^2+y^2}\right)}{\pi\left(x^2+y^2\right)} \tag{B.4}$$

where $\alpha = (2\pi n_a)/\lambda_{em}$ and J_1 denotes the Bessel function of the first kind. The off-axis elements of the tensor in Equation B.3 are zero, i.e., $[\mathbf{I}(\theta)]_{12} = [\mathbf{I}(\theta)]_{21} = 0$. The derivative then of the PSF function q with respect to the x coordinate is given by [1]

$$\frac{\partial q(x,y)}{\partial x} = \frac{-2\alpha x}{\pi} \frac{J_1\left(\alpha\sqrt{x^2+y^2}\right)}{\sqrt{x^2+y^2}} \frac{J_2\left(\alpha\sqrt{x^2+y^2}\right)}{\sqrt{x^2+y^2}}. \tag{B.5}$$

Using recurrence relations and integral identities of Bessel functions [5], the Fisher information along the x coordinate may be written as, using the definitions $x = \rho\cos\phi$ and $y = \rho\sin\phi$:

$$
\begin{aligned}
[\mathbf{I}(\theta)]_{11} = [\mathbf{I}(\theta)]_{22} &= \Gamma E\left[N(t)\right] \int_{\Re^2} \frac{1}{q(x,y)} \left(\frac{\partial q(x,y)}{\partial x}\right)^2 \mathrm{d}x\mathrm{d}y \\
&= \Gamma E\left[N(t)\right] \int_{\Re^2} \frac{1}{\frac{J_1\left(\alpha\sqrt{x^2+y^2}\right)}{\pi\sqrt{x^2+y^2}}} \left[\frac{\partial}{\partial x}\left(\frac{J_1^2\left(\alpha\sqrt{x^2+y^2}\right)}{\pi\left(x^2+y^2\right)}\right)\right]^2 \mathrm{d}x\mathrm{d}y \\
&= \frac{4\Gamma At\alpha^2}{\pi} \int_{\Re^2} \frac{x^2 J_2^2\left(\alpha\sqrt{x^2+y^2}\right)}{\left(^2+y^2\right)^2} \mathrm{d}x\mathrm{d}y \\
&= \frac{4\Gamma At\alpha^2}{\pi} \int_0^{2\pi} \cos^2\phi\mathrm{d}\phi \int_0^\infty \frac{J_2^2(\alpha\rho)}{\rho} \mathrm{d}\rho \\
&= \Gamma At\alpha^2
\end{aligned}
\tag{B.6}
$$

Utilizing the fact that the quantity $\Gamma A t$ is simply the number of photons, N, remembering that $\alpha = (2\pi n_a)/\lambda_{em}$, and the definition of the uncertainty in localization $\delta_x = [\mathbf{I}(\theta)]^{-1}$, the result is given by the expression [1]

$$\delta_x = \frac{\lambda_{em}}{2\pi n_a \sqrt{\Gamma A t}} = \frac{\lambda_{em}}{2\pi n_a \sqrt{N}} \qquad (\text{B.7})$$

B.2.2 Gaussian Profile

The same analysis may also be performed for a Gaussian distribution, which is useful since it often serves as an approximation to the PSF. The form of the Gaussian distribution is given by

$$q(x,y) = \frac{1}{2\pi\sigma_g^2} e^{-\left(x^2+y^2\right)/\left(2\sigma_g^2\right)}, \qquad (\text{B.8})$$

where again the off-diagonal elements are zero, x, y are elements of the real numbers, and σ_g is the standard deviation of the Gaussian function. The Fisher information matrix is then given by the expression [1]

$$
\begin{aligned}
[\mathbf{I}(\theta)]_{11} = [\mathbf{I}(\theta)]_{22} &= \Gamma E\left[N(t)\right] \int_{\Re^2} \frac{1}{q(x,y)} \left(\frac{\partial q(x,y)}{\partial x}\right)^2 \mathrm{d}x\mathrm{d}y \\
&= \frac{\Gamma A t}{\sigma_g^4} \left(\frac{1}{\sqrt{2\pi}\sigma_g} \int_{\Re^2} x^2 e^{-x^2/\left(2\sigma_g^2\right)} \mathrm{d}x\right) \times \left(\frac{1}{\sqrt{2\pi}\sigma_g} \int_{\Re^2} x^2 e^{-y^2/\left(2\sigma_g^2\right)} \mathrm{d}y\right) \quad (\text{B.9}) \\
&= \frac{\Gamma A t}{\sigma_g^2}.
\end{aligned}
$$

And as before, using the result of the Fisher information matrix, the limit of localization accuracy for the Gaussian profile along the x-axis (the same expression holds for the y-axis as well) can be defined as the familiar term

$$\delta_x = \frac{\sigma_g}{\sqrt{\Gamma A t}} = \frac{\sigma_g}{\sqrt{N}}. \qquad (\text{B.10})$$

B.3 Modifying the Intensity Distribution

As seen in the sections above, the actual uncertainty for any given statistical uncertainty is based upon the underlying form in question; an Airy profile has a slightly different uncertainty in the mean than that of a Gaussian. This idea can be taken a step further and the question can be asked of what is the underlying uncertainty for a given

photon distribution with a much larger structural content and variation in the function. Since the calculation of the Fisher information matrix requires analyzing the derivative of the function representing the optical signal, a signal with a greater variation in the function will lead to a drastically different results.

An interference pattern may be imposed upon a given photon distribution through the analysis of partial coherence, and the use of an transmission grating interferometer (as presented in Chapters 4 and 5). Since the experimental configuration produces an interference pattern solely along the x-axis, the expression for the intensity distribution along the x-axis only needs to be calculated. The result may be written down as [6]:

$$q(x) = f(x) \left| 1 + \gamma \cos\left(\omega x + \phi\right) \right| \tag{B.11}$$

where $f(x)$ is the intensity distribution of the signal, γ is the fidelity of the inference and ranges between 0 and 1, ω is the frequency of the fringe pattern, and ϕ is the phase shift of the fringe pattern over the intensity distribution. This expression holds for an arbitrary signal $f(x)$.

Before the Fisher information matrix can be calculated, the equation for $q(x)$ in Equation B.11 needs to be normalized such that the integral of the distribution is equal to one. The Fisher information matrix assumes a priori that the distribution in question is normalized to integrate to one, such that the integral over the distribution does not have any effect on the sample density factor, in this case N, the number of photons collected. If the image $q(x)$ did not integrate to one, this would introduce a sampling bias into the calculation, effectively weighting the sampling density. Thus, Λ needs to be solved for, such that $\Lambda \int f(x) \left| 1 + \gamma \cos\left(\omega x + \phi\right) \right| \, \mathrm{d}x = 1$ over all space and for all value of γ, ω, and $f(x)$. To do this, the functional form of $f(x)$ must be determined.

B.3.1   Modification of the PSF

In Chapter 4, the grating interferometer was used to modify the PSF of the emission source, which was gold nanoparticles in this case. Thus, the PSF may be modeled as a Gaussian function, and use this for the functional $f(x)$. Then, the intensity distribution $q(x)$ is given by

$$q(x) = A \cdot e^{-x^2/2\sigma^2} \cdot \left| 1 + \gamma \cos\left(\omega x + \phi\right) \right|. \tag{B.12}$$

The normalized form of this equation is found to be

$$q(x) = \frac{e^{-x^2/2\sigma^2} \cdot \left| 1 + \gamma \cos\left(\omega x + \phi\right) \right|}{\sqrt{2\pi}\sigma \left(1 + e^{-\sigma^2\omega^2/2} \cos\left(\omega\phi\right) \right)}. \tag{B.13}$$

The expression for $q(x)$ may then be inserted into the expression for the Fisher information matrix, Equation B.3, and the expression for $\mathbf{I}(\theta)$ may be calculated. With this modified form of the information matrix, a direct comparison against standard Gaussian localization accuracies can be calculated. Due to the functional form of $q(x)$, however, this expression does not yield an analytical result, and must be computed numerically.

B.3.2 Modification in the Fourier Domain

Chapter 5 utilized the grating interferometer in a different manner, and looked at the Fourier domain of the signal. Thus, the model of the signal $f(x)$ is based upon the optical transfer function (OTF) of the microscope [7]

$$f(x) = \frac{2}{\pi} \left[\cos^{-1}\left(\left| \frac{\rho}{\rho_0} \right| \right) - \left| \frac{\rho}{\rho_0} \right| \sqrt{1 - \left(\frac{\rho}{\rho_0} \right)^2} \right], \tag{B.14}$$

where $\rho = \frac{x}{\lambda f}$, and $\rho_0 = \frac{2NA}{\lambda}$. Here λ is the wavelength of the emission, f is the focal length of the objective lens, and NA is the numerical aperture of the objective.

Using this normalized approximation of the modified Fourier domain signal, again the function $q(x)$ can be written down and inserted into Equation B.3. With this result, the ratio of the localization accuracies for the modified Fourier domain signal to the standard Gaussian PSF can be calculated. Since an analytical solution to the Fisher information matrix for the modified Fourier domain signal is not obtainable, numerical approaches again must be utilized. This approach will allow for a direct comparison between the localization ability of a standard Gaussian PSF and the modified Fourier domain signal. Since $\sqrt{I^{-1}(\theta)} = \Delta x$, I can be numerically calculated for both models, which allows for two separate but related methodologies for computing the localization precision of an optical source.

B.4   The Effect of Pixelation and Noise in the Image

In the world of experiment, however, imaging detectors are not ideal. They have finite sampling size (pixels) and have noise associated with the image as well, due to

the statistical nature of the imaging process (Poisson noise) and readout noise from the detector (Gaussian). Assuming that the detector has C_K pixels, and treating the Poisson and Gaussian noise as additive, the acquired image can be written as $\mathscr{I}$, where $\mathscr{I}_{\theta,K} = S_{\theta,K} + B_K + W_K$. In this definition, K is the data from the kth pixel and θ denotes the unknown position of the particle in question. $S_{\theta,K}$ denotes a Poisson distributed random variable with a mean determined by the intensity distribution $q(x)$, i.e., $\mu_\theta(k) = \gamma A t \int q_\theta(x) \, dx$. The two remaining terms deal with the noise of the image. B_k is the shot noise factor, which obey Poisson statistics. Namely, B_k has a mean of $b_k t$, where t is the acquisition time of the image. The final term W_k represents the read noise of the system, with mean value η_k and variance σ_k^2. The last assumption is that these variables are all independent [1].

B.4.1 Noise Free Case

The Fisher information matrix can be rewritten (still for a noise-free case) for Poisson random variables [4, 8] as

$$\left| \mathbf{I}(\theta) \right|_{ij} = \sum_{k=1}^{K} \frac{1}{\mu_\theta(k)} \frac{\partial \mu_\theta(k)}{\partial \theta_i} \frac{\partial \mu_\theta(k)}{\partial \mu_j}, \quad i, j = 1, 2. \tag{B.15}$$

B.4.2 Poisson Noise Case

In dealing with Poisson noise, each pixel is corrupted by noise with a mean value of $b_k t$. The value that each pixel records is then $\mu_\theta(k) + b_k t$, for $k = 1, \cdots, K$. No assumption is made regarding the dependence of noise with regard to its source. Therefore the location of the particle should have no influence on the noise statistics. The Fisher information matrix may then be written, in the case of Poisson noise, as a simple modification to Equation B.15, given by [1]

$$\left| \mathbf{I}(\theta) \right|_{ij} = \sum_{k=1}^{K} \frac{1}{\mu_\theta(k) \, b_k t} \frac{\partial \mu_\theta(k)}{\partial \theta_i} \frac{\partial \mu_\theta(k)}{\partial \mu_j}, \quad i, j = 1, 2. \tag{B.16}$$

B.4.3 Poisson and Gaussian Noise Case

The final, and most complicated, case involves looking at the contributions to the Fisher information matrix from both Poisson noise stemming from photon counting statistics, and camera readout noise, which is Gaussian in nature. The derivation is lengthy, but can be summarized in a few steps, neglecting intermediate steps. For this,

an estimate for the log-likelihood function, $\mathcal{L}$, as is used in Equation B.1, can be found for this case in reference [8]. The result for $\mathcal{L}$ is then inserted into Equation B.1. The end result of such a process is given by:

$$\left|\mathbf{I}\left(\theta\right)\right|_{ij} = \sum_{k=1}^{K} \frac{\partial \mu_\theta\left(k\right)}{\partial \theta_i} \frac{\partial \mu_\theta\left(k\right)}{\partial \theta_j} \times \left(\int_{\Re} \frac{\left(\sum_{l=1}^{\infty} \frac{\left[\mu_\theta\left(k\right)+b_k t\right]^{l-1} e^{-\left(\mu_\theta\left(k\right)+b_k t\right)}}{\left(l-1\right)!} \times \frac{1}{\sqrt{2\pi}\sigma_k} e^{\frac{-1}{2}\left(\frac{z-l-\eta_k}{\sigma_k}\right)^2}\right)^2}{\left(\sum_{l=0}^{\infty} \frac{\left[\mu_\theta\left(k\right)+b_k t\right]^{l} e^{-\left(\mu_\theta\left(k\right)+b_k t\right)}}{l!} \times \frac{1}{\sqrt{2\pi}\sigma_k} e^{\frac{-1}{2}\left(\frac{z-i-\eta_k}{\sigma_k}\right)^2}\right)^2} dz - 1\right)$$

(B.17)

This result is obviously quite complicated, but can be handled by numerical techniques when determining the effects of noise in localization precision in Monte-Carlo simulations.

B.5   References

[1] R. J. Ober, S. Ram, and E. S. Ward, **86**, 1185 (2004).

[2] R. C. Rao, *Linear Statistical Inference and its Applications*, Wiley Series in Probability and Statistics, Wiley, Hoboken, NJ, 2nd edition, 1973.

[3] S. Zacks, *The Theory of Statistical Inference*, Wiley, New York, NY, 1971.

[4] S. M. Kay, *Fundamentals of Statistical Signal Processing: Estimation Theory*, Prentice Hall, Upper Saddle River, NJ, 1993.

[5] G. N. Watson, *A Treatise on the Theory of Bessel Functions*, Cambridge University Press, Cambridge, 2nd edition, 1966.

[6] B. J. Thompson and E. Wolf, Journal of the Optical Society of America **47**, 895 (1957).

[7] J. W. Goodman, *Introduction to Fourier Optics*, McGraw-Hill, New York, NY, 2nd edition, 1996.

[8] D. L. Snyder, A. M. Hammoud, and R. L. White, Journal of the Optical Society of America A-Optics Image Science and Vision **10**, 1014 (1993).

APPENDIX C

MICROSCOPE DESIGN AND LAYOUT

This Appendix will discuss and give an overview of the layout, construction, and components of the custom microscope that the experiments in this dissertation were carried out on. The system is a custom built microscope built to be a multiwavelength system with broad capabilities. It is designed in two parts, with the laser excitation sources on one optical table, and the body of the microscope on a second optical table. The light is delivered from one table to the other by means of a fiber optic cable, where it is delivered to the sample. Emission is collected, and imaged via either a conventional method or through an interferometer system. The system is composed of numerous pieces of controllable hardware, which are operated through the LabVIEW programming environment.

C.1   Lasers and Laser Coupling

The four laser sources are Coherent solid-state laser diode systems, and are comprised of a 405 nm, 488 nm, 561 nm, and 649 nm lines. The 405 and 649 nm lasers are the Coherent Cube model, and the 649 nm as an output of 160 mW, while the 405 nm has a power output of 100 mW. The 488 and 561 nm are the Coherent Sapphire model, and the 488mW has an output of 150 mW, and the 561 nm has an output of 200 mW. The lasers can be seen in the bottom part of Figure C.1.

The lasers are directed with mirrors into a common optical path. This can be seen as well in Figure C.1, highlighted by the individual color lines. The black boxes at the top of the figure were repurposed from a Till Photonics microscope. They contain two mirrors to steer the laser beam, and a long-pass dichroic. The dichroic mirrors are wavelength selective, depending on the requirements needed for a given optical system. In this case, the dichroics are long-pass mirrors, which means that they will pass all wavelength
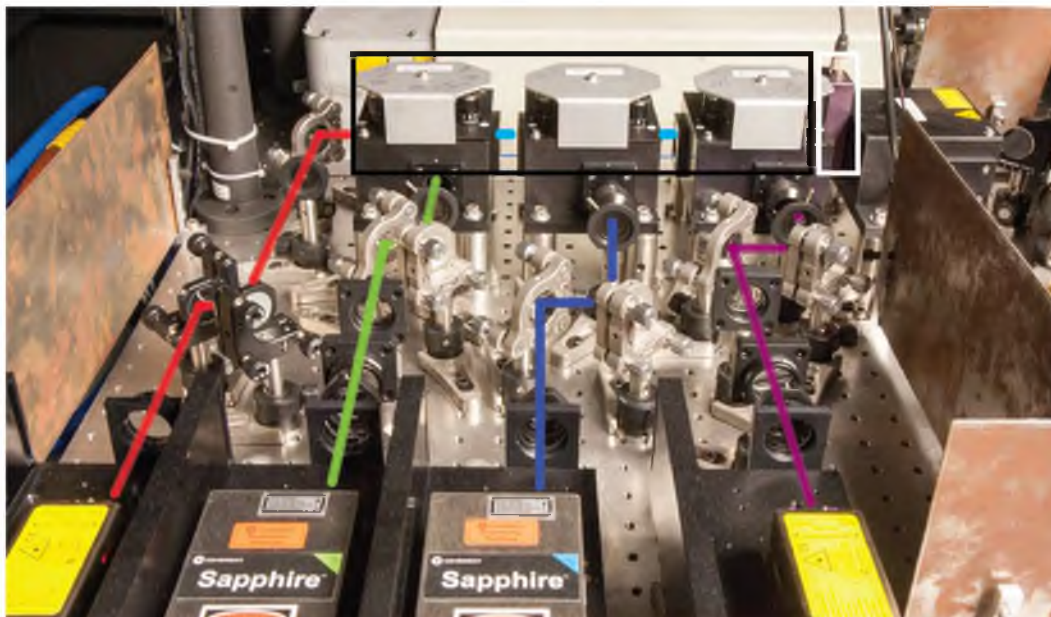
Figure C.1. Layout of the laser launch, collimation optics, and mechanical shutter. The lasers, from left to right, are 649 nm, 561 nm, 488 nm, and 405 nm. The black box surrounds custom collimation optics repurposed from a Till Photonics microscope. These boxes contain dichroic mirrors that are wavelength specific, allowing the lasers, which are at distinct wavelengths, to be collinear along a common optical beam path. The white box indicates the mechanical shutter, which is cycled on and off during system operation via software control.

values above a certain threshold, and reflect wavelengths below that cutoff. In this way, multiple lasers of multiple wavelengths may be combined onto a single, common optical path. Since the dichroics are long-pass dichroics, the longest wavelength laser is on the left, or the 649 nm, and they progress down to the shortest wavelength, the 405 nm laser. For example, the first black box on the left (for the 561 nm, green) has the red 649 nm light incident from the left. The 649 nm will pass through the dichroic, while the 561 nm light is reflected. The two beams are now collinear after this piece in the optical pathway. This process repeats for the 488 and 405 nm lines, until all lasers are combined on a common optical path.

Once the lasers are all combined along a single optical path, they pass through a mechanical shutter from Till Photonics, outlined by the white box in Figure C.1. This shutter is used to block the lasers when the system is not actively scanning or imaging. It is operated by a TTL pulse input, which is controlled through the user software interface, and has a response time of $\approx$ 500 ms.

C.1.1 Modulating Laser Intensity with an AOTF

The next component in the optical path is embedded within the black box (outlined by the white rectangle in Figure C.2), and is an acousto-optic tunable filter (abbreviated AOTF) from AA Optoelectronics, model AOTFnC-400-650. AOTF's are electro-optical devices that serve as an electronically tunable filter that allow for the simultaneous control of the transmitted intensity and wavelength of multiple collinear laser lines. The construction of an AOTF is based a birefringent crystal, usually Te)$_2$, whose optical transmission properties are altered when the crystal is subjected to a propagating acoustic wave.To generate an acoustic wave, a piezo-electric transducer is bonded to the crystal. Application of a radio-frequency electrical signal to the piezo-electric causes oscillatory expansion and contraction of the material. The oscillatory movement sends a high-frequency acoustic compression wave along the crystal, which generates a periodic modulation of the index of refraction throughout the crystal structure, along the propagation axis of the acoustic wave.

The periodic alteration of the index of refraction of the crystal has the effect of turning the crystal into a transmission grating, or a mobile phase grating. Incident wavelengths of light which meet the appropriate phase-matching (conversely, momentum-matching) conditions of the given periodic modulation within the crystal are diffracted into a first-order diffraction beam. For any given acoustic driving frequency, only a limited band of spectral frequencies will satisfy this phase-matching condition and become diffracted. While similar to a transmission grating, the diffraction of the incident laser beam does not occur at a planar interface, but rather over the entire crystal volume. Variation in the driving frequency allow for selective tuning of the wavelengths to the first-order diffraction beam, and the intensity of the acoustic wave throughout the crystal determines the amount of light diffracted into the first-order beam. Mathematically, the spectral output is given by

$$\lambda_{center} = V \cdot \frac{\Delta n}{v},$$
(C.1)

where V is the velocity of the acoustic wave, Δn is the birefringence of the crystal, and v is the frequency of the acoustic wave. Thus, an AOTF can modulate the output power and wavelength of a multiple wavelength input. The response times of AOTFs are in the
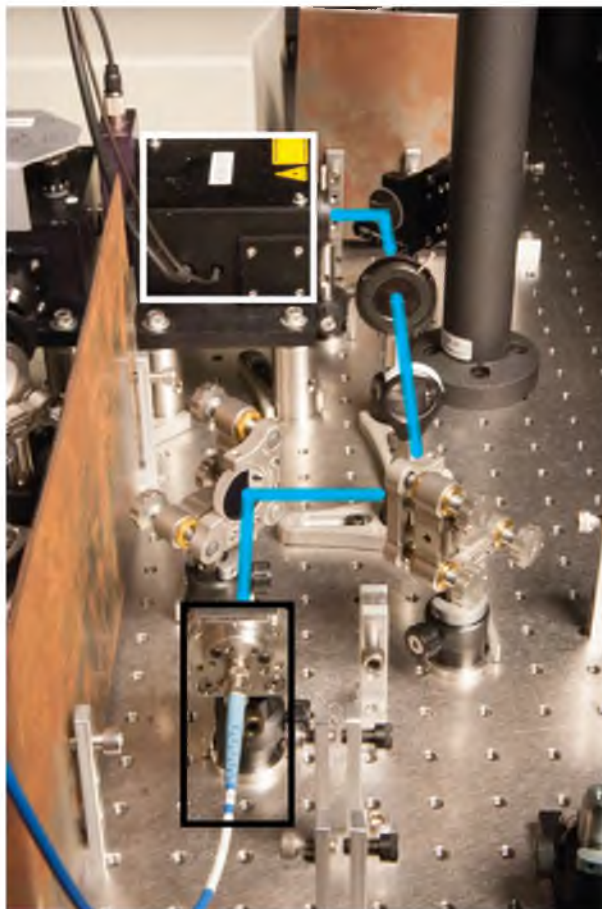
Figure C.2. AOTF and coupling optics. White box indicates the cover housing the AA Optelectronics AOTF (see text for description). Mirrors steer the laser beam into the achromatic fiber coupler. There is a weakly focusing lens to help compensate for the long beam path (since the laser beams will have slightly diverged). The fiber is an achromatic polarization maintaining single-mode fiber.

nanosecond range, and allow for quasi-simultaneous transmission of multiple continuous wave laser sources by rapid switching of the driving frequency. For a well-aligned system, transmission into the first-order diffracted beam can reach up to 85%, allowing for an efficient and convenient intensity and wavelength selective filter.

C.1.2   Coupling Into a Single-Mode Fiber

After passing through the AOTF, the undiffracted beam is blocked (by a razor blade, and then an aperture to minimize scattered light leakage) while the first-order diffracted beam is coupled into the fiber. In practice, the angular separation between the two beams is just a few degrees; the beams need to propagate a few centimeters before

they have diverged enough to block the undiffracted beam. The first-order beam is shown leaving the AOTF housing unit in Figure C.2, and being directed towards the fiber coupler, a Thorlabs PAFA-X-4-A model achromatic fiber coupler, outlined by the white box.

The input beam is steered via mirrors and adjustments on the fiber coupler mount and focused down to the core of the optical fiber, where it is coupled into the fiber and propagates to the microscope body. A polarization maintaining fiber is used to ensure that the output beam contains a Gaussian intensity profile (i.e., it is a TEM_{00} order beam). Larger multimode fibers allow for self-interference within the wave front due to higher-order propagating modes, and the output is a nonhomogenous intensity distribution due to this self-interference.

Single-mode polarization maintaining fibers require careful consideration of the incident beam profile and size to ensure adequate coupling efficiency. The core of a single-mode fiber (through which the light propagates) is only a few μm in size, which makes coupling a challenge. The core of multimode fibers can be hundreds of μm in size in comparison. To ensure proper coupling into a single-mode fiber, the beam waist of the incident laser beam as it is focused onto the core of the fiber must at least match the core in size, and if possible, be slightly smaller. The size of the waist of a Gaussian beam, using the paraxial approximation, can be given by

$$D_{\text{waist}} = \frac{4\lambda f}{\pi d_{\text{beam}}}. \tag{C.2}$$

D_{waist} is the waist size of the focused beam, λ is the wavelength of a particular laser, f is the focal length of the lens focusing the beam onto the fiber, and d_{beam} is the diameter of the incident laser beam. The larger the diameter of the beam, or the shorter the focal length of the focusing lens, the smaller the diameter of the focal spot.

In Equation C.2, the term D_{waist} also represents the size of the core of the single mode fiber, D_{core} . For the achromatic single-mode fiber shown in Figure C.2, that size is 3.3 μm. The focal length for the collimation lens is 4 mm. Thus, the parameter d_{beam} for each laser line should be such that $D_\lambda \approx D_{\text{core}}$. In Figure C.1(a), the 561 and 405 nm lasers can be seen to have a beam expansion configuration with the two lens pairs in each optical path. This is to ensure that the beam size for those two lasers give an optimal value for d_{beam}, ensuring that D_λ is the correct value. The beam sizes of the

649 and the 488 nm lasers did not require any modification. For a well-aligned system going into a single-mode fiber, the coupling efficiency can be close to 70%, and is $\approx 65\%$ in this setup for the 488, 561, and 649 laser lines. The 405 is near the cut-off transmission value for the optical fiber, and its transmission efficiency is reduced by a factor of ≈ 2.
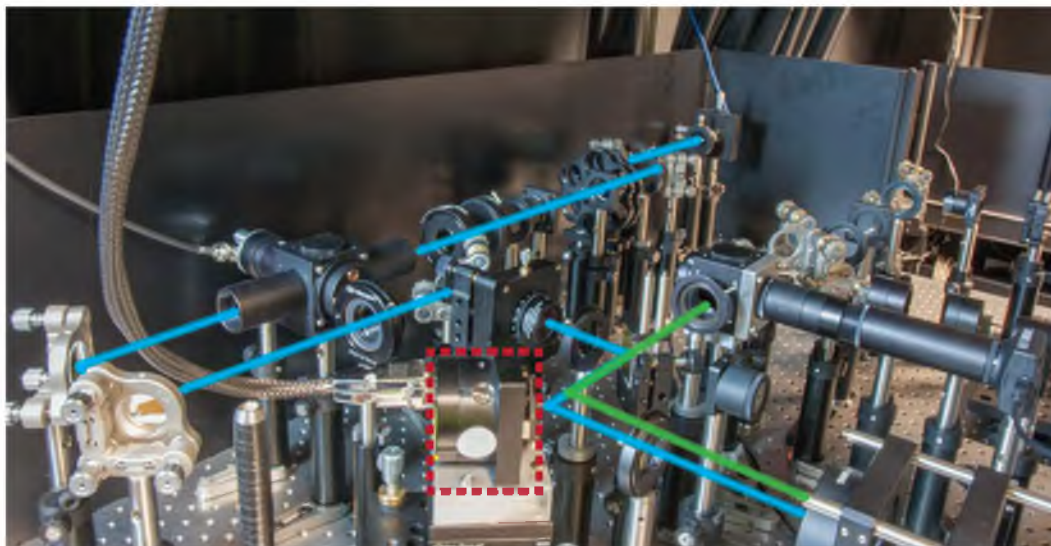
C.2 Excitation Path

For the excitation path, the laser light is re-collimated by an achromatic objective, where it is directed through a beam lens relay to expand the beam to fill the back aperture of the imaging objective, which is 7.2 mm in diameter. The output diameter of the beam is given by $D = 2fNA$, where f is the focal length of the collimation objective, and NA is the effective numerical aperture of the *optical fiber*, since it is the fiber core size which dictates the angular spread of the light coming from the fiber. The focal length of the collimation objective is 18.2 mm, and the optical fiber has an effective NA of 0.12, giving an output beam diameter value of ≈ 4.4 mm. The beam is then expanded by a factor of 1.6 in the lens relay to just match the diameter of the back aperture of the objective. The filling factor of the back aperture of the objective is an important parameter, since as was seen in Equation C.2, the larger the beam diameter, the smaller the focal spot diameter will be. This initial part of the excitation path can be seen in Figure C.3.

The beam goes through a beam sampler, which is an angled piece of glass that is lacking an antireflection coating on one side.[1] Approximately 4% of the beam is then directed onto a photodiode, whose voltage output is then proportional to the incident amount of light. This output can be calibrated by measuring the power with an optical power meter to give real-time incident power readings. This is important for photo-bleachable samples, namely any sample that uses fluorescence, instead of Rayleigh scattering as in the case of gold nanoparticles.

After the beam sampler, the light is directed onto a quad-band dichroic mirror, a Semrock Di01-R405/488/561/635-25x36. This dichroic mirror will reflect the four laser

---

[1]All modern optics use antireflection (AR) coatings, which are dielectric layers deposited on top of optical elements to minimize back reflections governed by the Fresnel equations. The dielectric layers are designed to be achromatic over a fairly large spectral window. For example, visible-range AR coatings are effective from 400 - 750 nm, while near-IR AR coatings are effective from 750 - 1100 nm.

Figure C.3. Initial portion of the excitation path, indicated by the cyan beam. The laser is recollimated from the optical fiber by an achromatic air objective, and sent through expansion optics to expand the laser beam to match the clear back aperture of the objective (objective not shown). The beam goes through a beam sampler for power measurements, and is redirected onto the surface of the scanning mirror (red dashed box). The lens before the scanning mirror can be taken in and out depending if confocal or wide-field mode is needed. The beam is shown entering into the scan lens. The emission path is indicated by the green beam. The two paths are split at the wavelength sensitive mirror, or dichroic.

lines, yet be transparent to emission from fluorophores excited by any given laser. For example, the fluorescent protein GFP has an emission peak of 510 nm when excited by 488 nm light. The quad-band dichroic will reflect the 488 nm light, but be transparent to the 510 nm peak emission, thereby separating the emission from excitation light within the microscope, allowing for the detection of the emission.

For the experiments highlighted in Chapters 4 and 5, scattered light from the gold nanoparticles was imaged. The dichroic is not perfectly efficient, and allows $\approx 1\%$ of the back-reflected laser light through. For scattering experiments, that amount of light is still incredibly high compared to the fluorescence yield from fluorescent samples. For experiments using fluorescence to image, back reflection and leaked laser light must be further filtered out by the use of emission filters. Emission filters are similar to dichroics, but have extremely large (10^7 or 10^8) extinction ratios between the targeted transmitted and reflected spectral ranges. An emission filter would be used in conduction with a dichotic to further filter out any leaked laser leakage through the dichroic.

C.2.1 4*f* Scanning System

The final part of the excitation path is the scan/descan 4*f* system, comprised of the scanning mirror, scan lens, tube lens, and finally the objective. In a scan/descan arrangement, the emission light from the sample completely retraces the optical path of the excitation, regardless of the position of the scanning mirror. The emission beam will leave the scanning mirror along the optical axis of the detection path, since every angular position is descanned upon reversal through the system.[2] A picture of the physical system may be seen in Figure C.4, while a cartoon schematic of a 4*f* system may be seen in Figure C.5. In Figure C.4, the scan and tube lens are on a rail system to help with alignment, and a 45° mirror folds the light vertically into the back aperture of the objective. While the objective cannot be seen in Figure C.4, it is directly above the 45° mirror. It is on a linear translation stage to coarsely adjust the position of the objective at the correct focal height for a given sample. The 45° mirror is adjustable as well, to ensure that the light enters the back aperture of the objective orthogonal to the back focal plane, allowing for proper alignment of the system.

The scanning mirror used is an Optics in Motion biaxial 100 series (OIM101) scanning mirror. Unlike more conventional scanning systems, which are based upon a galvanometer design and thus only operate along a single axis,[3] the scanning mirror in the system is capable of biaxial movement. The face of the scanning mirror can then be placed a focal length away from the scan lens, and scanned in any orientation.

The objective used is a Zeiss Plan-Apochromat 63x magnification, 1.40 NA oil iris objective with variable back aperture. With the back aperture stopped down to its minimum position, as was the case for the experiments in Chapters 4 and 5 to avoid overfill-

---

[2]While scanning systems can be fast, they are orders of magnitude slower than the lifetime of fluorescent molecules. Fluorescent lifetimes are on the order of nanoseconds, while the scan time of a single pixel of most systems is in the high μs to ms time range. Systems that push the envelope on speed can reach low μs pixel dwell times, or for specialized resonant scanning systems, hundreds of nanoseconds. This is still well above the lifetime of fluorophore, thereby ensuring that the emission is always returned along the same optical path.

[3]Systems that use galvanometers require care in their construction, due to the fact that scanning the angle of the first galvanometer changes the beam position on the second galvanometer. They are either manufactured such that the two galvanometers are very close together, minimizing beam walk-off, or in a 4*f* configuration of their own, thereby increasing the number of optical elements the excitation, and therefore emission, must travel through.
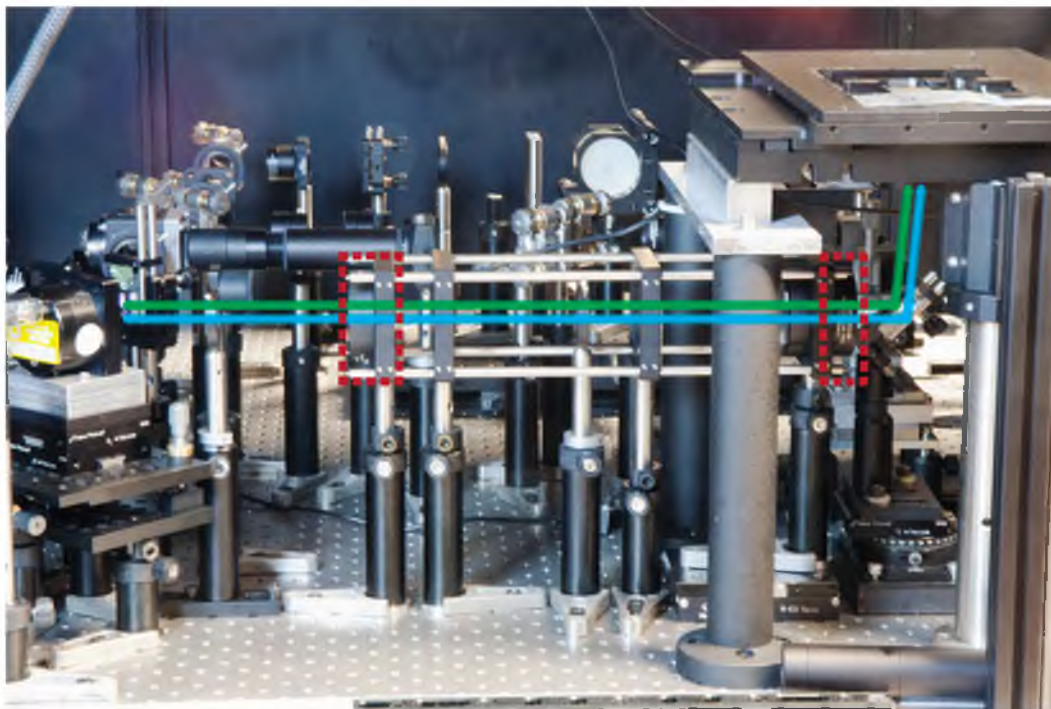
Figure C.4. Side view of the layout of the $4f$ scanning system. The scan (red dashed box, left) and tube lens (red dashed box, right) are matched lenses, and are one focal length away from the scanning mirror and back aperture of the objective, respectively. The two lenses are a distance of $2f$ apart from each other. The excitation light (cyan) is folded from a horizontal path to a vertical path by a 45° mirror, and enters the back aperture of the objective (not shown due to stage blocking the view). The emission light (green) retraces the optical path and reflects off of the scanning mirror along the same optical path as the excitation light, passes through the dichroic to the detection path.

ing the transmission gratings, the effective NA is 0.7. The focal length of the objective is 2.53 mm, and the back focal plane of the objective is located 19.4 mm from the front shoulder of the objective body, meaning that the effective location of the back focal plane of the objective is located within the objective itself. This is accounted for in the positioning of the objective with respect to the tube lens.

The objective is mooted on a Physik Instrumente P-725 PIFOC 400 μm travel range objective piezo-scanner for precise positioning of the objective at nanometer accuracy. The objective and PIFOC are placed on Newport 460P-X-05 linear travel stage, which is coarsely moved to an in-focus position and locked. This setup allows for flexibility in the samples and sample holders that may be imaged on the system. The samples are housed on a Prior H117IX3 fast xy scanning stage, which allows for easy placement of
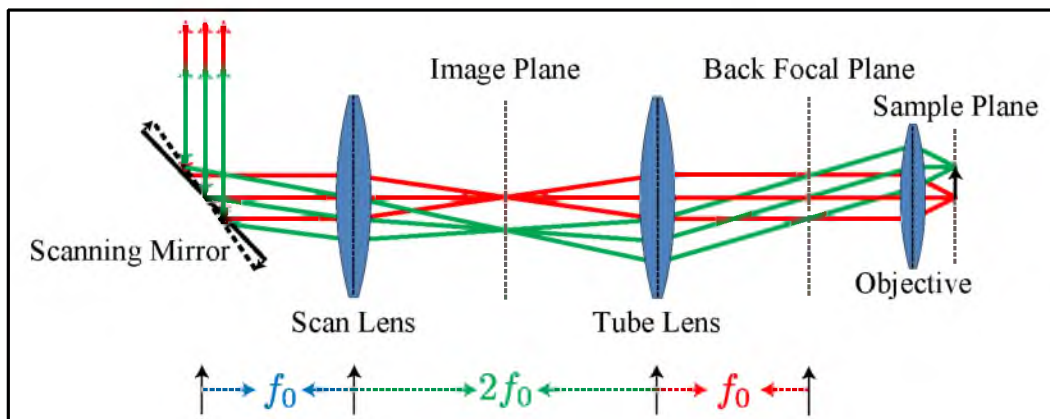
Figure C.5. Schematic of a $4f$ system. In a $4f$ system, the scanning mirror is one focal length away from the scan lens, which is a distance of $2f$ from the tube lens. The tube lens is then a distance of one focal length away from the back focal plane of the objective. The principle of this setup is to relay the angle of the beam, dictated by the angle of the scanning mirror, into the back aperture of the objective, while keeping the spatial location of the beam at the back aperture of the objective constant. The scanning mirror changes the input angle, α_{SL}, into the scan lens, which changes the focal position in the image plane. The tube lens then collimates the light, and due to the spatial offset in the image plane, the collimated light comes into the back focal plane of the objective at an angle, α_{TL}. If the focal lengths of the scan and tube lens are equal, $f_{SL} = f_{SL}$, then $\alpha_{SL} = \alpha_{TL}$. If they are not equal, the ratio of the angles is the same as the ratio of the two focal lengths of the two lenses. If the light into the objective is at an angle, the light is focused at a different spatial position within the sample plane. Thus, the angle of the scanning mirror controls the focal position in the sample. As this figure demonstrates, regardless of the angle of the scan mirror, the location of the beam at the back focal plane of the objective is stationary.

the samples over the objective.

C.3   Detection Path

The system is designed to have two detection paths, controlled by an electronically controlled mirror. As seen in Figure C.6, the conventional confocal detection path delivers the emission light down the middle of the optical table, while the lower path is for the interferometer. A custom transillumination device can also be seen in the top part of Figure C.6. This consists of a 735 nm LED light source, and is used to find a region of interest in the sample, be it nanoparticles or cells. This is accomplished through the use of a Thorlabs CMOS camera in the initial part of the detection path (not shown). A beam pick-off analogous to the one in the excitation path samples the emission, and creates an image on the camera, conjugate to the sample plane. This camera is also used to find
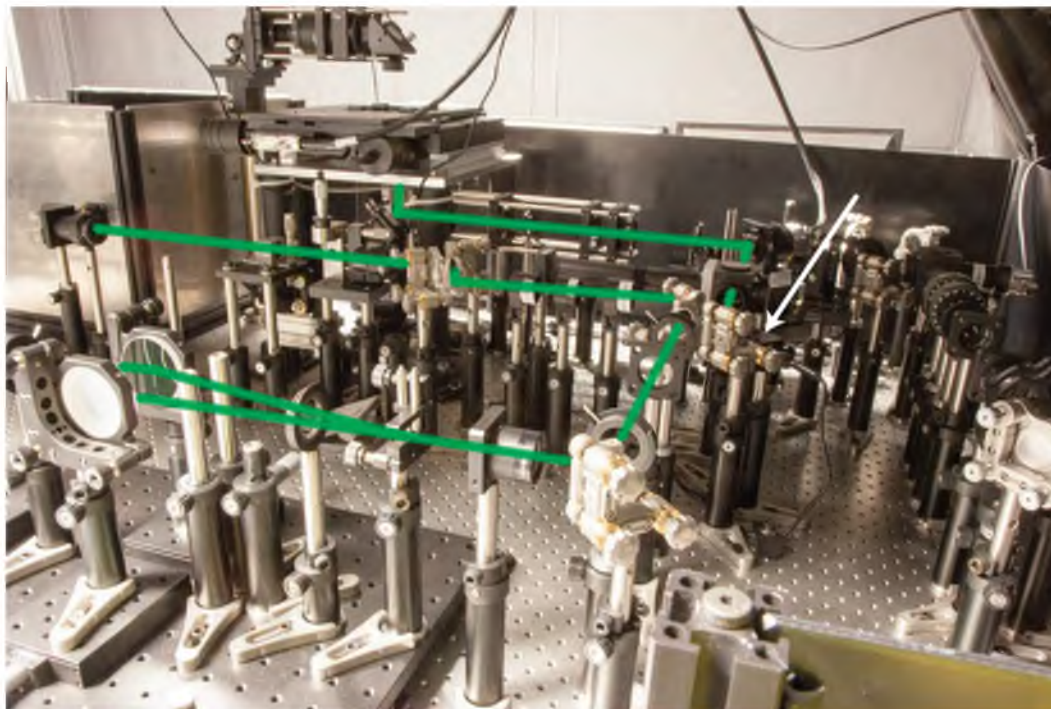
Figure C.6. Full detection path of microscope system, shown with the emission light leaving the objective and going through the $4f$ system. The white arrow indicates the position of the programmable flip mirror (in the down position in this photo) the controls the detection path the emission will take. The emission light can either go to the conventional imaging path and onto the APD (not shown, in silver box at the left of the photo) or to the interferometer system (shown in the bottom of the photo).

the focus when positioning the objective and sample together, as the back reflection from the laser will create a focal spot on the camera.

The conventional confocal optical path goes into a silver light-tight box behind the stage, and is focused onto an avalanche photo diode (APD) from Micro Photon Devices, a model PDM with a 50 x 50 μm square detector surface. This APD has $\approx 45\%$ quantum efficiency at 561 nm. The APD is in a conjugate image plane to the sample, and is used to measure photon counts for every position of the scanning mirror. The APD detection path has an overall magnification of 60, and therefore the detector surface is ≈ 0.8 Airy units wide. This allows for an optimal balance for collection of light only within the focal position of the objective, rejecting out of focus background light for a higher signal-to-noise ratio than a wide-field system.

The bottom detection path is that of the custom interferometer, and can be seen in Figure C.7. The interferometer has two transmission gratings, which are discussed in

Appendix D. The transmission gratings are highlighted by the white boxes in Figure C.7, and are positioned $\approx$ 45 cm apart along the optical axis. The mirrors recombine the two interference beams at the second grating. The imaging lens can be seen on the right edge of Figure C.7. A lens relay is placed between the second transmission grating and the camera, as seen on the optical rails. This lens relay reforms the image plane on the camera, an Andor electron-multiplying charged coupled device (EMCCD) camera, model iXon DV885. The overall magnification on the EMCCD is 400. The EMCCD has pixels 8 x 8 μm in size, and is a 1000x1000 pixel array sensor. The quantum efficiency for this camera is similar to the APD, and is $\approx$ 50%.

C.4   LabVIEW Software Control

The system is controlled through custom LabVIEW programs, giving electronic control to the mechanical shutter, the AOTF, the scanning mirror, stage, piezo control, and APD. The Andor camera is controlled through software provided by Andor, and will not be discussed here. LabVIEW is a graphical programming environment, which allows for rapid software/hardware integration.

The AOTF is controlled by a custom LabVIEW routine, shown in Figure C.8(a). Each laser has its own on/off ability and intensity control. It also has the capability to open and close the mechanical shutter, turn the transillumination LED on and off, and the ability to control the electronic flip mirrors. The AOTF, which can handle all four laser lines simultaneously, is controlled by sending a string command to the electronic driver, which interprets the signal and sends the appropriate RF signal at the appropriate amplitude to the AOTF. The objective piezo is controlled by the routine shown in Figure C.8(b). The objective piezo is controlled as well by string commands fed into the electronic controller, which feeds a high voltage input to the piezo-electric.

The Prior xy stage can also be controlled via the LabVIEW routine, as seen in Figure C.9. The stage has custom controls to move relative or absolute coordinates. The stage allows for custom scanning routines as well, which was used in Chapter 5. The stage scanning method is a scan/rescan configuration: the stage scans from x_{min} to x_{max}, with pixel size Δx, and then returns to the x_{min} position. The stage increments Δy, and repeats, scanning from y_{min} to y_{max}. During stage scanning, at each stage position,
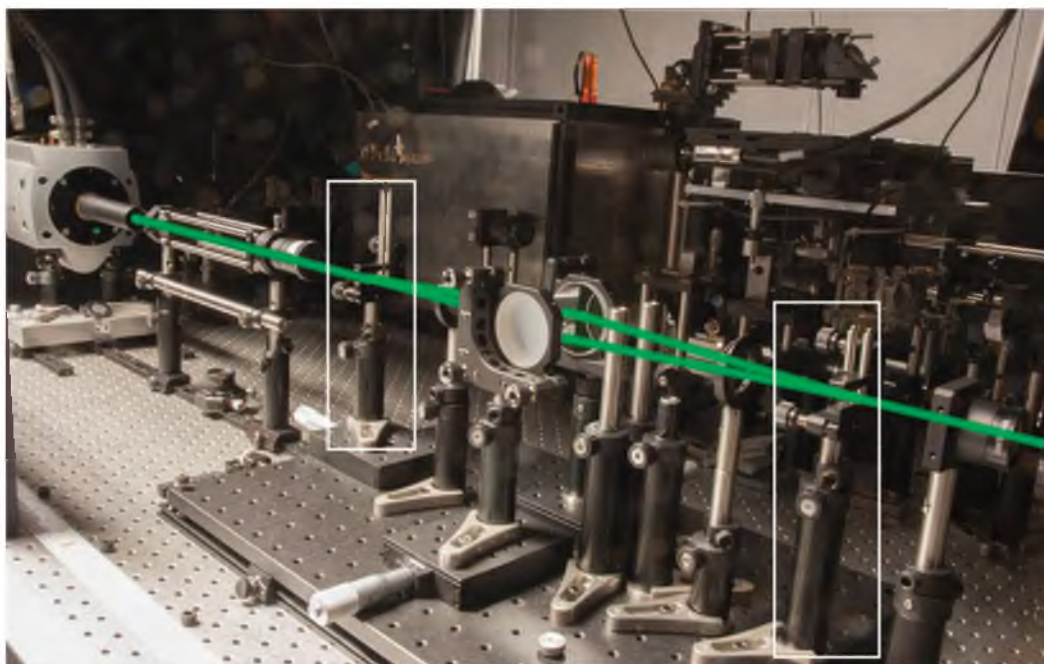
Figure C.7. Detection path through the interferometer (set up as the optical configuration as presented in Chapter 4). The two transmission gratings are in the optical holders highlighted by the white boxes. The emission is split by the first transmission grating, and the mirrors recombine the beam path onto the second grating, which forms the primary image plane. The lens relay system then transfers the image plane onto the EMCCD. The black tubes on the front of the EMCCD shield the sensor from stray ambient light, reducing background.

the stage sends an external TTL trigger to the camera, allowing for stage control over the camera frame acquisition.

The scanning and imaging routine is shown Figure C.10. The program routine controls the scanning mirror and reads the output from the APD through an National Instruments data acquisition card. The program has controls for the scan range and scan time, as well as the ability to import custom scan routines, park the laser at a particular location, and do multiple scan routines. The scanning configuration is similar to the stage scanning technique, which is a scan/rescan method. To form an image, the APD sends a TTL output for each photon that is detected, and these are counted by the National Instruments data acquisition card and binned for every pixel location of the scanning mirror. The scan/rescan across the x-axis is averaged, and this line-by-line readout is then displayed on the software until a full scan is completed. For imaging a single bead through the interferometer, for example, the laser beam can be parked at the
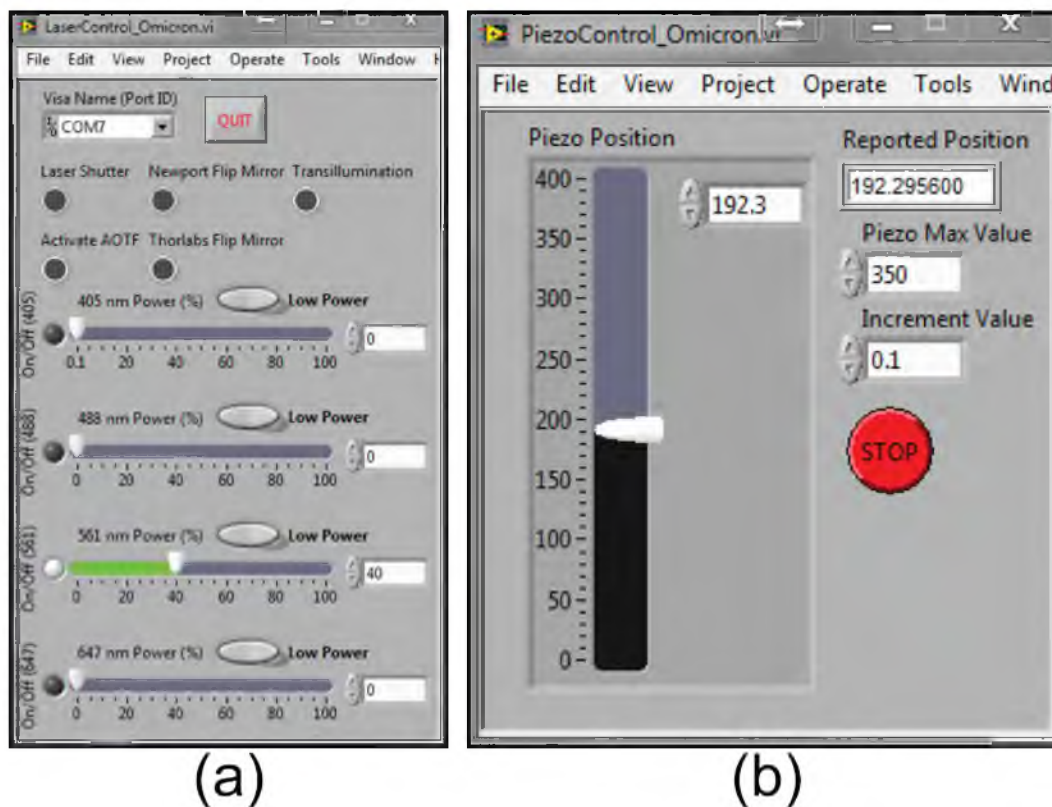
Figure C.8. Custom laser and piezo control software. **(a)** Image of the custom software for the laser lines, the flip mirrors within the microscope, and the transillumination system. Each laser line has individual control over its intensity, as well as if it passes through the AOTF or not. **(b)** The software control for the piezo is shown, indicating the focal position, as well as controls for focal position increments, and position stops to prevent the objective from moving into the sample.

center of a bead, as is shown in Figure C.10, and the data collection handled by sending TTL trigger signals to the EMCCD through the Prior stage control.
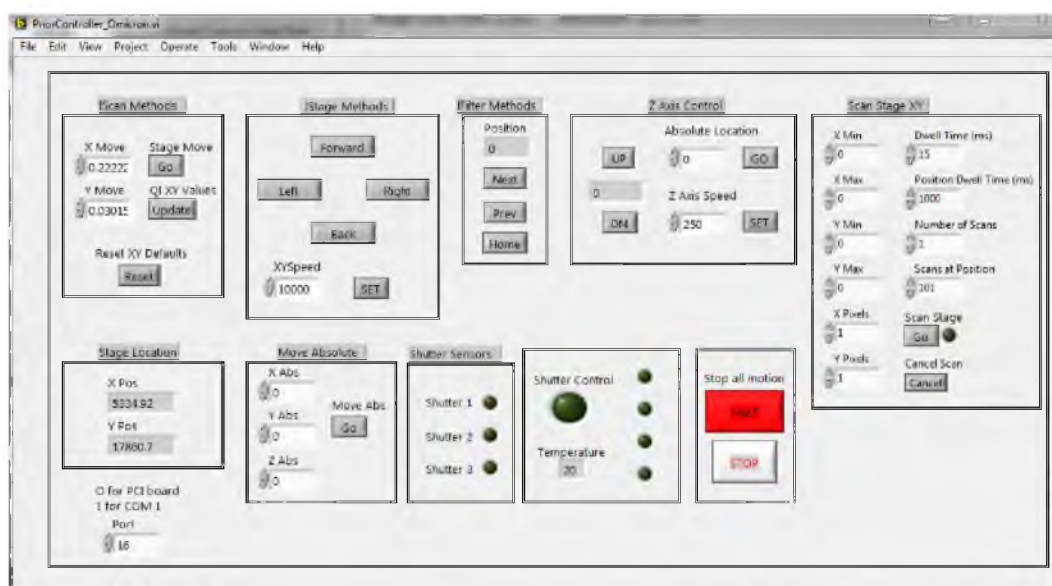
Figure C.9. Image of the custom software used to control the Prior xy stage. Independent controls of the relative and absolute stage position are shown, as well as the ability to scan the stage in a predetermined scan pattern (controls on the right).
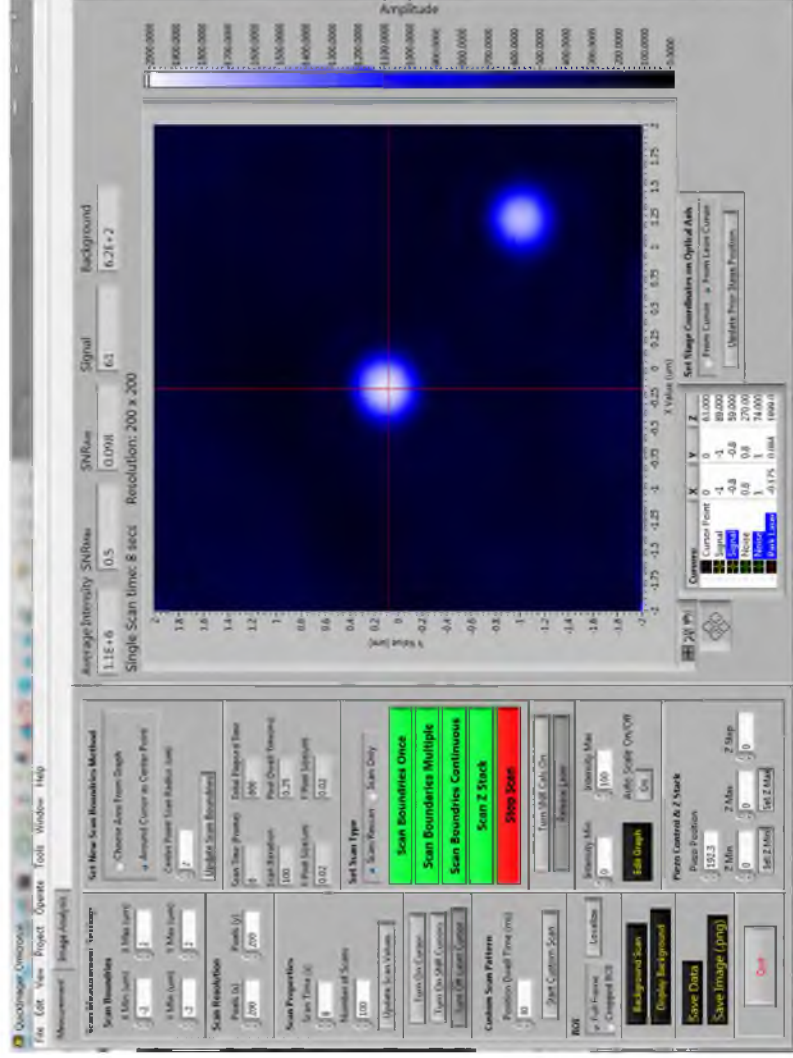
Figure C.10. Image of the custom software used to control the scanning mirror and create an image. The software has controls for scan range, pixel size, and overall scan time. The software also allows for custom ROI determination, centering the laser on a given particle's center-of-mass, as well as custom arbitrary scan pattern positions. The image shown on the software here is that of the 60 nm gold nanoparticles used for the analysis from Chapter 4. As can be seen in the image, the gold nanoparticles produce a diffraction-limited PSF (the total ROI is 4 x 4 μm in size), and the system is well aligned, as evidenced by the symmetrical PSFs.

APPENDIX D

DESIGN OF BINARY PHASE GRATING

This Appendix will discuss the mathematical details of the design of the binary gratings that were used for the experiments conducted in this dissertation.

D.1   Mathematical Description of Binary Phase Grating

The current grating system, shown in Figure D.1 is designed around a wavelength of $\lambda = 520$ nm, with a $\Delta\lambda = 20$ nm from each side.[1] The wavelength resolution of the system is $\delta\lambda = 1$ nm.

A unit cell of the grating, as shown in Figure D.2, can be described mathematically as

$$u_{\text{cell}}(x) = \text{rect}\left(\frac{x}{b}\right) * \delta\left(x + b/2\right) + \text{rect}\left(\frac{x}{b}\right) * \delta\left(x - b/2\right) e^{i\phi} \tag{D.1}$$

where $*$ denotes convolution. The entire grating with an infinite number of periods is given by:

$$u(x) = \left[\text{rect}\left(\frac{x}{b}\right) * \delta\left(x + b/2\right) + \text{rect}\left(\frac{x}{b}\right) * \delta\left(x - b/2\right) e^{i\phi}\right] * \text{comb}\frac{x}{\Lambda} \tag{D.2}$$

where the function $\text{comb}\left(...\right)$ is defined as

$$\text{comb}\left(y f_x\right) = \sum_{m=-\infty}^{\infty} \delta\left(f_x - \frac{m}{y}\right) \tag{D.3}$$

The far field can be calculated by using the Fourier transform

$$u(f_x) = \left|\text{sinc}\left(b f_x\right) e^{i2\pi b f_x/2} + \text{sinc}\left(b f_x\right) e^{-i2\pi b f_x/2} e^{i\phi}\right| \text{comb}\left(\Lambda f_x\right) \tag{D.4}$$

---

[1] The wavelength specifications of the gratings were designed for a different wavelength range than the primary one used in the experiments presented in this dissertation, namely 520 nm (design) versus 561 nm (experiment). The only major issue with dealing with a wavelength out of the design range is the efficiency of the system, but since Rayleigh scattering from gold nanoparticles was used, this was not a major concern. The next generation will incorporate four gratings, and will be used for broad-band fluorescence samples.
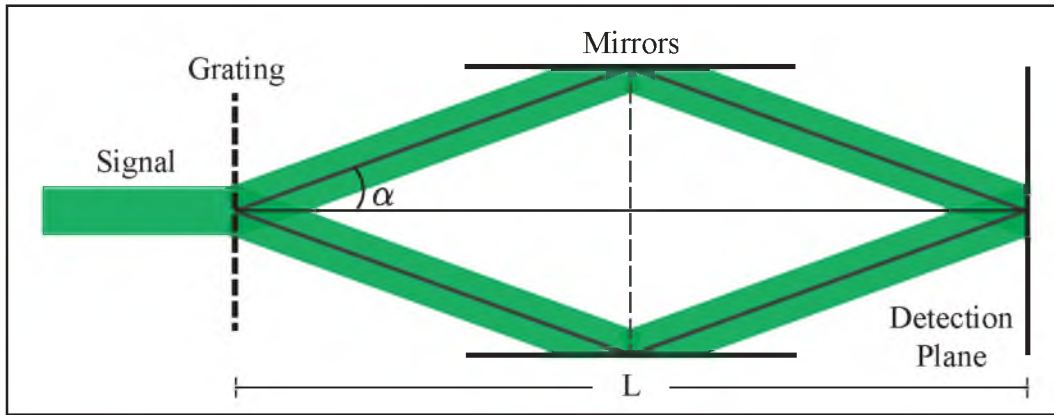
Figure D.1. The grating system showing an input signal split into the +1 and -1 orders, and recombining at the detection plane. Not shown is the central order and corresponding beam block, or higher diffraction orders.

where the constant amplitude coefficients have been neglected, and $f_x = \frac{x}{\lambda z}$. If $b = \Lambda/2$ and a phase $\phi = \pi$ are used, the expression becomes:

$$u(f_x) = \frac{\sin(\pi b f_x)}{\pi b f_x} \left| e^{i\pi b f_x} - e^{-i\pi b f_x} \right| \text{comb}(2b f_X).$$ (D.5)

Using the definition of the comb function in Equation D.3, for $\text{comb}(2b f_x)$, the expression then is given by

$$\text{comb}(2b f_x) = \sum_{m=-\infty}^{\infty} \delta\left(f_x - \frac{m}{2b}\right).$$ (D.6)

This function is nonzero at $f_x = m/2b$. Substituting these values into Equation D.5, the result is

$$u(f_x) = \frac{2i \sin(\pi m/2)}{\pi m/2} \sin(\pi m/2),$$ (D.7)

which equals zero for the even diffraction orders. For the odd orders, $u(f_x) = \frac{1}{\pi m}$, and the intensity is $I = \frac{1}{\pi^2 m^2}$. Therefore, for $m = 1$, an efficiency of 81% is obtained. For a limited number of periods, N, the grating function is given by

$$U(x) = \text{rect}\frac{x}{N\Lambda} \left[\text{rect}\left(\frac{x}{b}\right) * \delta(x + b/2) + \text{rect}\left(\frac{x}{b}\right) * \delta(x - b/2) e^{i\phi} \right] * \text{comb}\left(\frac{x}{\Lambda}\right)$$ (D.8)

and the far field is

$$U(f_x) = \text{sinc}(N\Lambda f_x) * \left| \text{sinc}(b f_x) e^{i2\pi b f_x/2} + \text{sinc}(b f_x) e^{-i2\pi b f_x/2} e^{i\phi} \right| \text{comb}(\Lambda f_x).$$ (D.9)
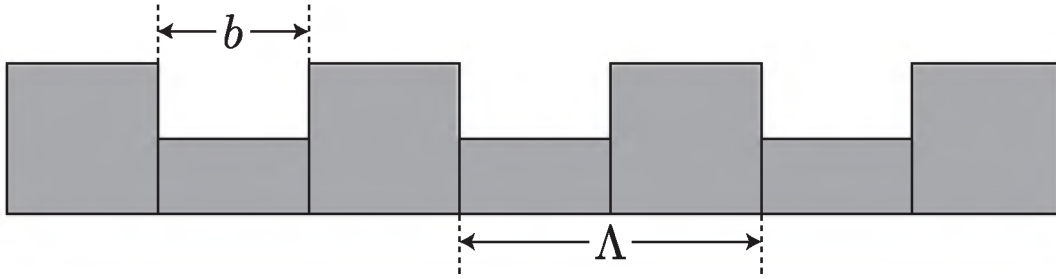
Figure D.2. Sketch of the grating system. Λ denotes the length of a full period, and b is the length of the step.

Again, if $b = \Lambda/2$ and a phase $\phi = \pi$ are used, while assuming as before that $f_x = m/2b$, the expression is

$$U(f_x) = \text{sinc}\left(N\Lambda f_x\right) * \frac{2i \sin\left(\pi m/2\right)}{\pi m/2} \sin\left(\pi m/2\right). \tag{D.10}$$

D.2   Grating Design

The grating is designed around a wavelength of $\lambda = 520$ nm, and the center wavelength will have a diffraction angle of $\theta = 5°$. Using the diffraction equation, the period of the grating equals

$$\Lambda = \frac{m\lambda}{\sin\theta} = 5.97\mu\text{m}, \tag{D.11}$$

where the diffraction order $m = 1$ was selected.

If this system is to be used for a broadband source spectrum, the angular spread of the first diffraction order cannot overlap the angular spread of the other orders. Since the grating is designed to have odd diffraction orders only for $\lambda = 520$ nm, care must be taken to ensure that the first diffraction order not does overlap the second. For the first diffraction order the most extreme angle is at $\lambda = 540$ nm and for the second at $\lambda = 500$ nm. Thus,

$$\theta_{max,m=1} = \arcsin\left(\frac{\lambda_{max}}{\Lambda}\right) = 5.19° \tag{D.12}$$

$$\theta_{min,m=2} = \arcsin\left(\frac{2\lambda_{min}}{\Lambda}\right) = 9.64° \tag{D.13}$$

D.3   Number of Periods and Grating Size

The resolvable angle of the system is determined by the first order diffraction spot size. This is determined by the width of the main lobe of the envelope in Equation D.10, i.e.,

$$U(f_x) = \text{sinc}\left(N\Lambda f_x\right) = 0 \tag{D.14}$$

Therefore, $N\Lambda\pi\frac{x}{\lambda z} = \pi$, and the width of the main lobe is $\delta x = \frac{\lambda z}{N\Lambda}$. Since a wavelength spacing of $\delta\lambda = 1$ nm is required, the relationship

$$\sin\left(\theta + \delta\theta\right) = \frac{m\left(\lambda + \delta\lambda\right)}{\Lambda} \tag{D.15}$$

is used, where $\delta\lambda$ may be calculated, i.e., $\delta\lambda = 16.83 x 10^{-4}$. Using the relationship $\left(x + \delta x\right)$ $= z\tan\left(\theta + \delta\theta\right)$, the required spacing in the x direction is found to be $\delta x \approx 17\,\mu$ m. Using the relationship $\delta x = \frac{\lambda z}{N\Lambda}$ once more, the number of periods for the grating are found to be $N > 1064$. The minimum width of the grating is therefore $N\Lambda = 6.4$ mm.[2]

---

[2]This value is a minimum. New gratings have to be larger than this value so the back aperture of the objective can be fully opened.

APPENDIX E

INCREASED LOCALIZATION PRECISION BY
INTERFERENCE FRINGE ANALYSIS
SUPPLEMENTAL

This appendix will present further analysis and experimental details from Chapter 5.

E.1   Fast Extraction of Phase Value

To initially validate the ideas presented in Chapter 5, a custom transmission grating interferometer was setup as follows. A single-mode Research Electro-Optics, Inc. helium-neon laser operating at 543 nm served as the light source, and was imaged onto an Andor Clara Interline 1392x1040 pixel CCD, with a pixel size of 6.45 μm. The same custom manufactured transmission gratings were utilized, with a grating period of 5.97 μm, and an efficiency of 81% transmission to the $\pm$1 orders. The zero order was blocked. To control the incident angle of the laser onto the grating, a $4f$ scanning configuration was constructed, with the grating in the final imaging plane of the system. The Optics In Motion biaxial fast scanning mirror served as the scanning control. The $4f$ system was constructed using two 50 mm focal lengths lenses from Thorlabs (Part AC254-050-A-ML). The $4f$ scanning configuration can be seen in Figure E.1. The interferometer was constructed using matched mirrors from Thorlabs (Part BB1- E02). The mirrors served to recombine the +1 and -1 orders from the grating, and the two orders were recombined at the surface of the CCD.

To determine the phase values corresponding to different particle locations, the laser spot was recorded for a series of small scan angle steps. Each step in scan angle corresponded to a shift in the sample plane of 20 nm, which was calibrated using a custom confocal microscope with a scan and tube lens each with a focal length of 150 mm, and a 63X Zeiss oil-immersion objective with an NA of 1.4 and a nanofabricated calibration
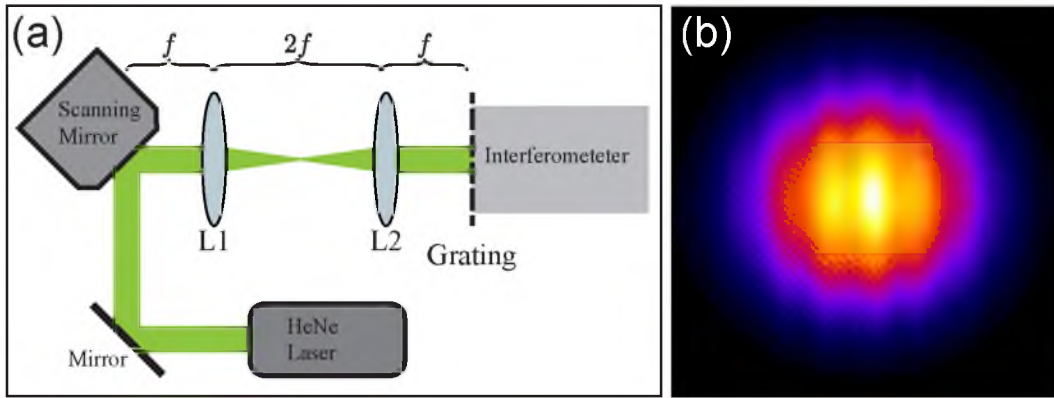
Figure E.1. Wavefront modification through the interferometer. **(a)** Schematic of $4f$ scanning configuration. A 543 nm HeNe laser was directed onto a scanning mirror, whose scanning angle determined the angle of incidence onto the grating. The lenses used were 50 mm focal length achromatic doublets. **(b)** Image of the modulation produced at the output of the interferometer over the wavefront of the laser beam.

AFM grid, with a pitch variation of 5 μm. The angular step size corresponding to a 20 nm step size in the sample plane was 7.67 μrad, which was above the stated accuracy of 2 μrad of the Optics In Motion scanning mirror.

In order to extract the phase values of the beam after propagating through the interferometer, the image was recorded onto an Andor Clara interline CCD and analyzed as follows. Since we are only concerned with the movement of the phase front with respect to the x-axis, the fringe pattern was collapsed along the y-axis to generate a one-dimensional image. This image was then analyzed in a custom MATLAB (The Mathworks, Natick, MA) routine that found the best-fit parameters for γ, ω, and ϕ. The same image was then also analyzed by Fourier decomposition via the method of Takeda, et al. [1] to extract the value of ϕ. To do so, note that the modulation component given in Equation 5.6 can be rewritten as an exponential function and simplified down to:

$$q(x) = f(x) + f(x)\frac{\gamma}{2}e^{i\phi} + f(x)\frac{\gamma}{2}e^{-i\phi}e^{-i\omega x} \tag{E.1}$$

Here, γ is the interference fidelity (between 0 and 1), ω is the spatial frequency of the interference pattern, and ϕ is the phase of the fringe pattern. If we take a Fourier transform into the frequency domain, which we can then denote as $Q(x)$, we end up with three distinct terms — one related to the underlying signal which can be filtered, and two terms solely containing the frequency, and hence phase, information. To find this

phase value, the central peak of the Fourier domain is filtered, along with the positive peak corresponding to the second term of Equation E.1. Only the negative peak, or the last term in Equation E.1, is then transformed back to the spatial domain, which we can denote now as $iQ(x)$. We exclude the positive peak to ensure that the inverse Fourier transform has both real and imaginary components. While either the negative or the positive peak may be selected for analysis, we chose the negative peak to ensure that the slope of the phase versus position is the same sign as the slope extracted from the numerical fitting routine. The underlying phase value can then be extracted from these two components as follows:

$$\phi = \tan^{-1}\left(\frac{\Im\left[iQ(x)\right]}{\Re\left[iQ(x)\right]}\right) \qquad (E.2)$$

This expression for the phase across the image is only a relative value; a global phase can be imposed by choosing any arbitrary reference point (in this case the phase from a particular pixel) and subtracting that value from the relative phase. These values can then be compared to the phase values extracted from the numerical fitting routine; both of these are shown in Figure E.2 for the numerical fitting method (top) and the Fourier analysis (bottom). While the particular values are different for the phase value at a given scan angle, and hence sample position, this is due to the choice of the relative offset value chosen in the Fourier analysis. However, the trend is the same between the two methods, and hence the sensitivity of the approach. As can be seen readily from the plots, the phase value of the image varies extremely rapidly, and can be used to give an independent measurement of the central position of the emitting probe. This phase value is sensitive to the length of the interferometer and angle in which the two beams combine. The angle of the two beams, or the length of the interferometer, can be varied to have the phase go through one cycle of 2π across the image.

E.2   References

[1] M. Takeda, H. Ina, and S. Kobayashi, Journal of the Optical Society of America **72**, 156 (1982).
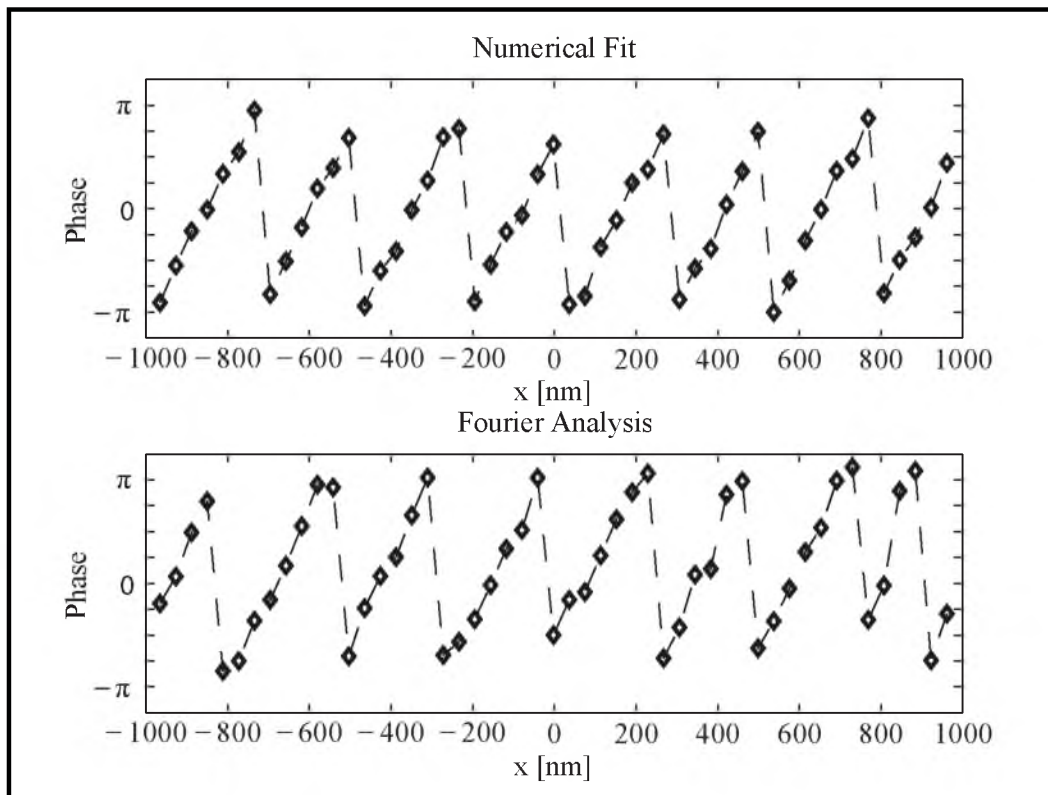
Figure E.2. Plot of extracted phase values from numerical fitting (**top**) and Fourier analysis (**bottom**). The x-axis of each plot represents the corresponding displacement in the sample plane for a given scanning angle. While the absolute values differ, this is merely due to the choice of a reference value in the Fourier analysis. The trend, and therefore the sensitivity, between the two methods is equal.